INFORMATION TO USERS

This manuscript has been reproduced from the microfilm master. UMI films the text directly from the original or copy submitted. Thus, some thesis and dissertation copies are in typewriter face, while others may be from any type of computer printer.

The quality of this reproduction is dependent upon the quality of the copy submitted. Broken or indistinct print, colored or poor quality illustrations and photographs, print bleedthrough, substandard margins, and improper alignment can adversely affect reproduction.

In the unlikely event that the author did not send UMI a complete manuscript and there are missing pages, these will be noted. Also, if unauthorized copyright material had to be removed, a note will indicate the deletion.

Oversize materials (e.g., maps, drawings, charts) are reproduced by sectioning the original, beginning at the upper left-hand corner and continuing from left to right in equal sections with small overlaps. Each original is also photographed in one exposure and is included in reduced form at the back of the book.

Photographs included in the original manuscript have been reproduced xerographically in this copy. Higher quality 6" x 9" black and white photographic prints are available for any photographs or illustrations appearing in this copy for an additional charge. Contact UMI directly to order.

UMI

A Bell & Howell Information Company
300 North Zeeb Road, Ann Arbor MI 48106-1346 USA
313/761-4700 800/521-0600

Experimental and Numerical Analysis of Abrasive Waterjet Drilling of Brittle Materials

by

Zihong Guo

A dissertation submitted in partial fulfillment
of the requirement for the degree of

Doctor of Philosophy

University of Washington

1998

Approved by _____
(Co-Chair of Supervisory Committee)

_____
(Co-Chair of Supervisory Committee)

Program Authorized to Offer Degree *Mechanical Engineering*

Date 8/21/98

In presenting this dissertation in partial fulfillment of the requirements for the Doctoral degree at the University of Washington, I agree that the Library shall make its copies freely available for inspection. I further agree that extensive copying of this dissertation is allowable only for scholarly purposes, consistent with "fair use" as prescribed in the U.S. Copyright Law. Requests for copying or reproduction of this dissertation may be referred to University Microfilms, 1490 Eisenhower Place, P.O. Box 975, Ann Arbor, MI 48106, to whom the author has granted "the right to reproduce and sell (a) copies of the manuscript in microform and/or (b) printed copies of the manuscript made from microform."

Signature 

Date 8/21/98

University of Washington

Abstract

Experimental and Numerical Analysis of Abrasive Waterjet Drilling of Brittle Materials

by

Zihong Guo

Chairs of the Supervisory Committee: Professor Mamidala Ramulu
Professor Michael G. Jenkins

Department of Mechanical Engineering

The interaction between abrasive waterjet (AWJ) and brittle materials, as well as related machining mechanisms, was studied using a hybrid experimental - numerical analysis approach. First, the machineability of ceramic materials, such as alumina, silicon nitride, silicon carbide, and titanium diboride, was studied by varying the AWJ input parameters. The AWJ machining forces on these materials were measured and discussed. First, an SEM study was conducted to investigate the AWJ machining mechanisms on continuous fiber-reinforced ceramic composites (CFCC). Second, a moiré interferometry experimental setup and procedure were developed, as well as a 3-D finite element model. The measured surface displacement distributions were used to drive the finite element modeling. In this inverse problem, the measured reaction forces of the specimen during AWJ drilling were matched the reaction forces from the finite element simulation. Three pressure loads of the AWJ exerted on the cavity were assumed for the FEA model, and their effects on the surface displacement distribution were studied through numerical experiments. The verification of the finite element model was carried out by studying a statically loaded specimen, both experimentally and numerically, in which the moiré fringe patterns from the experiments and the displacement contour plots from the FEA were compared.

The test results from the machineability study indicated that structural ceramics can be machined by AWJ at a reasonable material removal rate. Under certain conditions a threshold supply pressure exists. The impact force on a specimen by pure waterjet is about 20% greater than that by an AWJ. There exists a basic fluctuation frequency that is low in value and associated with the AWJ system. The material removal mechanisms for AWJ cutting on CFCC consist of a combination of bending, shearing, micromachining, and erosion. The micro-mechanisms associated with AWJ drilling are micro-fracture of fibers and matrix, delamination, and fragmentation of fiber bundles. The results from the numerical experiments demonstrated that the shear applied on the kerf surface, simulating the AWJ return flow, most profoundly affects the surface displacement distribution. The optical experimental data from both polycarbonate and alumina indicated that the horizontal strain, ε_x increases as the depth of hole is increased. The AWJ drilling process was numerically modeled reasonably well with the three assumed pressure loads, i.e. jet pressure, normal pressure, and shear. The numerical modeling demonstrated that the principal stresses at the bottom of the hole increase as the depth of hole increases. The material removal mechanism is a process of micro crack initiation, micromachining and erosion, as proposed by Ramulu[17]. This can be substantiated quantitatively by the study results. The micro-crack can be activated by the impingement of the AWJ by the condition of $K_I \geq K_{Ic}$.

TABLE OF CONTENTS

LIST OF TABLES

LIST OF FIGURES

ACKNOWLEDGEMENT

I would like to express my sincere appreciation to my advisor Professor Mamidala Ramulu for his insightful guidance, his inspiration and vision, his patience, his encouragement, and his support throughout the preparation and writing of this dissertation. I am deeply grateful to him for the weekend meetings during the years of my part-time study, which were essential to the completion of this research. Without all of his support this dissertation would have been impossible. I want to thank Professor Michael Jenkins, the co-chair on my supervisory committee, for his wise guidance and advice. I am grateful to Professor Kobayashi for serving on my reading committee and providing me with his valuable comments on my thesis, and for his generosity in allowing me to use the optical apparatus in his research lab. Gratitude is also extended to Professor K.Y. Lin and Dr. Ed. Ting of Flow International Inc. for taking the time to serve on my supervisory committee, and for their guidance and input to my research and this dissertation.

I have been very fortunate in having a number of friends who have helped me in different ways in the past five years. Professor F. X. Wang had been a great help during the initial stage of my research. I am indebted to Dr. Zhikai Guo and his wife Qiong for their support and help throughout my graduate study, both academically and in my life. Grateful acknowledgment must be paid to Mr. Duc Tran for his exceptional support and friendship, his generosity, his masterful help with my experiments, and his constructive discussions on my research. Many other people in the Department of Mechanical Engineering deserve a thank you for their assistance, notably Mr. Leong Ma and Dr. Omori for their valuable discussions; Dr. D. Arola for sharing his experimental expertise; and Tom Collin in the machine shop for helping with fixture machining needs. Especially, I would like to express my deep gratitude to Dr. V.

Chandrasekran at Boston Scientific Corporation for his mentorship, continuing support, and understanding. His drive for scientific excellence has pushed me to aspire for the same.

I am deeply grateful to my wife, Yan, and my parents-in-law for their understanding and support during the last few years. My son Kevin also deserves a thank you. He has been an inspiration for me to complete the research work. Finally, I am greatly indebted to my mother, my late father, my brothers, and sister for their unwavering support and their unselfish sacrifices for my education and my entire life. It would have been impossible to get through all this without them.

Financial support from National Science Foundation is acknowledged.

Dedication

To my mother

CHAPTER 1
INTRODUCTION

1.1 BACKGROUND

High pressure water has been in use for centuries as a processing technology[1]. Since the advent of waterjet machining technology in the early 1970s, waterjet has been used in cutting wood, plastic, and other soft materials[2]. Significant improvements were achieved on the overall reliability of the high pressure system in the next decades. With the introduction of the first abrasive waterjet machine in the early 80s, in which particles of garnet or silica sand were entrained into the waterjet stream, this cutting technology became more capable of machining harder materials. High speed abrasive waterjet exhibits a high potential in the field of machining brittle materials, such as ceramics, ceramics composite, glass, and some polymers, etc. To further advance this technology, experimental and analytical techniques are employed in this study to investigate the interaction between AWJ and these brittle materials, with particular emphasis on polycarbonate and ceramics[3].

1.2 PROPERTIES OF CERAMICS AND THEIR APPLICATIONS

Ceramic is a brittle material that has been used in human endeavors since ancient times. Under normal use conditions ceramics do not oxidize, and they expand or contract relatively little under extreme weather conditions. Current classification of ceramics includes not only traditional materials that are made by heating natural substances, but also the highly refined and synthesized materials that are engineered for modern chemical, mechanical, electrical, optical and magnetic properties. Traditional ceramics are largely made from natural raw materials, which are separated physically and reduced

in size. Advanced ceramics generally require chemical conversion of raw materials into intermediate compounds, which lead to purification and subsequent chemical conversion into the final desired form [4]. However, all ceramics comprise a very complex material system, which have poor uniformity, reproducibility, and machineability. Even though the technical problems associated with the production and fabrication of advanced ceramics have hindered the growth in development, ceramics are slowly taking hold in specialized applications because of their special properties.

Ceramics and their composites make up a diverse group of inorganic non-metallic brittle materials with a wide range of compositions and properties. Advanced ceramics are either monolithic or composite. Any of the monolithic forms can be reinforced by particles, whiskers, or fibers. The physical and mechanical properties of ceramic materials are strongly dependent on their composition and microstructure, and on the history of manufacture. Some of the typical mechanical properties of the ceramic and other metallic materials are given in Table 1.1.

Ceramic materials have a variety of unique engineering properties, such as extreme high-temperature stability, hard and wear-resistant surfaces, low thermal expansion, and high stiffness to weight ratio. Advanced ceramics have very desirable use characteristics, including high temperature strength, and resistance to oxidation, creep, corrosion, and erosion[5]. They also exhibit resistance to crack propagation under compression. Today these materials can be found in many daily life, industrial, and scientific applications. For example, advanced ceramics are used as turbine blades, prosthetics, ceramics bearings, etc.[3] The advent of missiles and the space age has produced exceptional demands for materials that will withstand extremes in temperature and other environmental conditions. Advanced ceramics, such as carbide and graphite based systems, are being used in some rocket nozzles where temperatures exceed 2700°C. Magnetic ceramics include cores for computer memories and permanent magnets for

electric motors. Because of their extreme hardness, especially at high temperatures., advanced ceramics are widely used as cutting and grinding tools in industry.

Even though ceramics have so many special properties and attractive applications, the commercialization of advanced ceramics has not occurred as rapidly as anticipated. Advanced ceramics are still very expensive because they continue to be difficult to manufacture. Thus, it is an emergent task to find a more economical and efficient way to manufacture ceramics.

1.3 MACHINING OF BRITTLE MATERIALS

Brittle materials, such as polycarbonate, ceramics, and their composites, have the potential to offer superior performance when compared to metals. However, brittle materials do not exhibit appreciable plastic deformation as metallic materials do. Ductile materials can undergo a large plastic deformation long before fracture, thus allowing them to deform into the required shape and join to structure. Often, ceramic materials must be used in the shape in which they emerge from the factory. In order to expand the possible applications of these materials and gain wide acceptance in industry, net-shape processing of ceramics is necessary. In practical engineering applications, post-sintering machining of ceramics is needed for dimensional control and production optimization. At the present time, machining of ceramics to the final shapes costs up to 80% of the total manufacturing cost, due to the brittle nature and inherent hardness of the ceramics[6]. Therefore, machining methods must be developed to allow for successful fabrication of ceramic component parts.

Ceramic components can be machined by using mechanical, chemical, and thermoelectric energy. Complicated three-dimensional ceramic shapes can be made with a modified milling center for creep-feed grinding of ceramics[7]. During machining processes, surface flaws or cracks can be generated that contribute to the variable

performance of advanced components. Currently, conventional machining methods for structural ceramics include surface grinding and single point cutting [6,8,9,10] which mostly generate rough and uncontrollable surfaces. In the worst case these methods would fracture the part. The most economical, and technically the most controllable machining process is sought to finish ceramics. Machining processes must be improved to develop cost-effective and production-viable processes.

Of all the non-conventional machining processes, abrasive waterjet (AWJ) machining is most widely accepted as the most economical way to machine ceramics[11,12,13]. Research has demonstrated that a high-energy beam is ideal for shaping materials[6]. This beam should have a definitely small cross section, and precisely controlled depth and direction of penetration, and it should not cause any detrimental effects on the generated surface[14]. Abrasive waterjet machining is defined as the serving of a material by a high pressure collimated jet of water in which the abrasive particles are entrained. Abrasive waterjet cutting offers several distinct advantages over alternative processes. It produces a quality surface, is relatively inexpensive and environmentally sound, and its material removal rate is reasonably high. However, abrasive waterjet machining of advanced ceramics is a very complex process. The effect of machining on brittle materials, and advanced ceramic materials in particular, have not yet been very well understood. The present research investigates the effect of abrasive waterjet machining on ceramics. The study will increase the general understanding of the machining phenomena for more successful application of abrasive waterjet machining on brittle materials. Conclusions from this study will serve as the basis for designing an optimized AWJ nozzle assembly and AWJ machine.

1.4 ORGANIZATION

The goal of this research is to investigate the interaction between the AWJ and the workpieces of polycarbonate, ceramics, and ceramic composites, which is outlined in Chapter 2. The dissertation starts in Chapter 3 with a comprehensive review of the current secondary machining methods for ceramics, and with concentration on abrasive waterjet machining. The fundamental erosion theory and machining mechanisms for abrasive waterjet machining on ceramics are also presented in this chapter. In Chapter 4 the AWJ machining system and the test procedures for a parametric study are described, and the machineability for both ceramics and continuous fiber-reinforced ceramic composites (CFCC) are experimentally studied. The AWJ machining micromechanisms of these materials are discussed, and the test results are reported and analyzed. Chapter 5 is dedicated to the optical experimental setup and procedures of the moiré interferometry displacement measurement. The finite element analysis (FEA) is also detailed in this chapter. A numerical experiment studying the effect the different pressure loads of the AWJ and an experimental-numerical simulation of the specimen under static loading are discussed in Chapter 6. The results from both optical experiments and numerical modeling of AWJ drilling on test specimen are reported in Chapter 7. The surface displacement distributions from optical experiments of a polycarbonate specimen during abrasive waterjet machining are used to drive the numerical modeling under the similar boundary conditions, followed by a discussion in Chapter 7. The important findings from the current research are reported in Chapter 8, and the recommendations for future research are included in Chapter 9.

Table 1.1 Mechanical Properties of Ceramics and other Materials [5, 15]

Materials	METALS				CERAMICS			
	4041 Steel	SEA 316 Stainless Steel	6061 T6 Aluminum	Tool Steel	AD90 Nom. 90%Al_2O_3	TiB_2	Silicon Carbide (Hot Press)	Silicon Nitride (Hot Press)
Density (g/cm^3)	7.8	7.87	2.7	7.5-8.0	3.60	4.5-4.54	3.23	3.18
Young's Modulus (GPa)	207	207	69	210-235	276	514-574	440	311
Tensile Strength (@2%GPa)	827	578	310	--	221	700-1000		900
Yield Strength (GPa)	655	241	276					
Poisson's Ratio	.32	0.33		--	0.22	0.09-0.13		0.24
Stiffness/Weight ($GPa/g/cm^3$)				27-30	77			64
Compressive Strength (GPa)	827	578		1000-2000	2482			
Hardness (GPa)	165	158	95	6.4-	10.4	15	24.5	17
Fracture Toughness K_{1c}				50-80	3-4	6-8	3.9	6
Max. Temperature (°C)		760		760	1500			1200
Corrosive Resistance (Weight Loss $mg/cm^2/day$)	H_2SO_4 @20°C	--		--	0.03			
Coefficient of Thermal Expansion ($10^{-6}/°C$)	25-1000°C			6.0	8.1	8.1	4.55	3.3

CHAPTER 2
OBJECTIVES

2.1. APPROACH OF THIS STUDY

The goal of this research is to investigate the mechanics of AWJ piercing of brittle materials, including polycarbonate and advanced ceramic materials. Therefore it is essential to understand the stress and strain state in the materials associated with the AWJ drilling process. The stresses and strains can be either calculated analytically and numerically, or obtained experimentally. A hybrid experimental - numerical analysis approach advanced by Kobayashi [16] is adopted in this study, which leads to a critical task of recording the transient state of stress or strain in the impingement zone of the target material during the AWJ piercing process. Photoelasticity was used by Ramulu[17] to study the abrasive waterjet machining micromechanisms for transparent brittle polymer materials. In that case the average stress distributions were observed from the photoelastic fringes. However, for opaque ceramic materials, photoelasticity techniques can not be utilized. In addition, the deformation induced by the abrasive waterjet machining in ceramic materials is expected to be very little due to its high hardness and brittleness. Thus another optical technique, moiré interferometry, is used to investigate the stress and strain state in the ceramic material during AWJ piercing. The first step in the process is to measure the whole-field surface displacements in a ceramic material, by using the moiré interferometry technique while the specimen is being pierced by high pressure AWJ. The machining force exerted on the specimen by the AWJ, or the reaction force of the specimen, is also measured by using a specially designed force dynamometer. Finally, the state of stresses in the machined specimen is numerically analyzed by using a commercial finite element analysis (FEA) code. The machining pressure loads used in the FEA model, simulating the action of the abrasive waterjet, are determined by

matching the surface displacements from the FEA modeling with those from the experiments. The matching process of the pressure loads is by trial and error. Similar boundary conditions in the optical testing condition will be applied to the FEA model.

2.2. OBJECTIVES

The abrasive waterjet machining process involves wave propagation, tensile and shear fracture, erosion, cratering, and large scale cracking enhanced by pressure[18]. However, very limited research on the mechanics of the AWJ and workpiece material interaction has been reported[19] to date. The displacement and stress distributions, and the fracturing behavior of the material under dynamic conditions have not been understood. This research tends to characterize the material removal mechanisms during the abrasive waterjet machining process. The specific objectives of this investigation include the following:

(1) To understand the effect of machining conditions, namely, the supplied pressure, abrasive size and flow rate, traverse speed, etc., on abrasive waterjet machining of brittle materials, such as ceramics and ceramic fiber reinforced composites, by parametric studies.

(2) To develop an experimental setup and procedure for studying the displacement distributions generated in the AWJ piercing process, and to construct an AWJ drilling numerical model.

(3) To determine the quasi-static state of stresses surrounding the micro-cracks generated in the impingement zone of target material during AWJ piercing process, and to compare experimentally obtained displacement fields with that of the numerical model.

CHAPTER 3
LITERATURE REVIEW

3.1 CERAMICS MACHINING PROCESSES

Advanced ceramics have been increasingly applied in optical, electronic, mechanical, and biological industry due to their inherent superior high temperature strength, hardness, wear resistance, as well as their proved electrical, optical, thermal, and magnetic properties[2,3,5]. However, secondary machining processes are needed for ceramics to meet their product shape, size, finish design, and surface quality requirements. The high hardness of the ceramics makes conventional machining a slow and expensive process. In order to achieve the complex shapes and surface finish, various other machining processes have been utilized.

Generally, ceramics machining processes can be classified into two machining process categories: abrasive and non-abrasive. During both machining processes, energy is transferred from a source to the part that is to be machined in order to remove stock and create new surfaces [20]. Machining processes that utilize abrasives to accomplish energy transfers are referred to as abrasive machining methods. Abrasive machining and surface finishing methods include grinding, lapping, honing, polishing, abrasive fluid jet machining, and ultrasonic machining. Methods that result in such energy transfer without the use of abrasives are non-abrasive machining methods. Non-abrasive machining methods include laser beam machining, electrical discharge machining, ion-beam machining, electron-beam machining, chemical machining, and electrochemical machining. Detailed machining processes for brittle materials are presented in Appendix A. Unfortunately, most of them are not very efficient or economical for machining of ceramics. The most conventional machining technique for ceramics uses diamond

machining, and it contributes to the high cost and poor reliability of ceramics. In order to make ceramics a cost-effective alternative to existing materials, an innovative ceramics machining technique should be developed and utilized.

Much recent research has proved that the abrasive waterjet machining has a number of merits in ceramics machining[21]. There are no problems with it in terms of cutting tool degradation or thermal stresses, and it generates low machining forces on work pieces. In addition, compared to other traditional and non-traditional techniques, AWJ is very efficient in machining hard and brittle materials like ceramics.

3.2 ABRASIVE WATERJET MACHINING SYSTEM

3.2.1 Principles of Abrasive Waterjet Machining

In abrasive waterjet machining, high-velocity water is used to entrain and accelerate abrasive particles, such as garnet or silica sand, to achieve the performance needed for machining of metals, ceramics and composites. A conventional AWJ system typically includes: high pressure pump, nozzle assembly, abrasive delivery system, catcher system, motion system, and control unit. A Diagram of the AWJ system is shown in Figure 3.1[22].

3.2.2 Components of Abrasive Waterjet Machine

The high pressure pump supplies high pressure water necessary for machining. A core part in the pump is a hydraulically driven high pressure intensifier, as shown in Figure 3.2. This is a reciprocating plunger type pump. The pressurized hydraulic oil from a hydraulic piston pump is fed into the intensifier pump. Because the area of the piston in the oil side is about twenty times larger than the area of the piston in the water

side, the intensifier is able to pressurize water up to 400 MPa. The output water pressure is controlled by adjusting the hydraulic oil pressure.

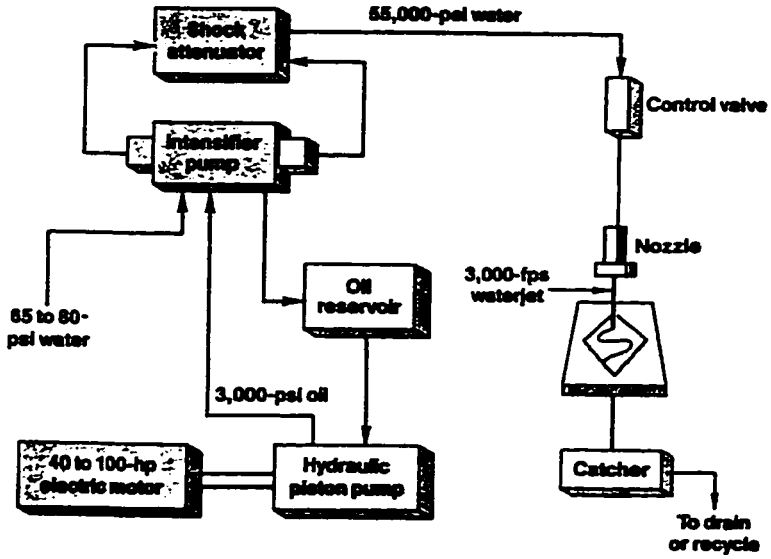

Figure 3.1 A Diagram of the AWJ System

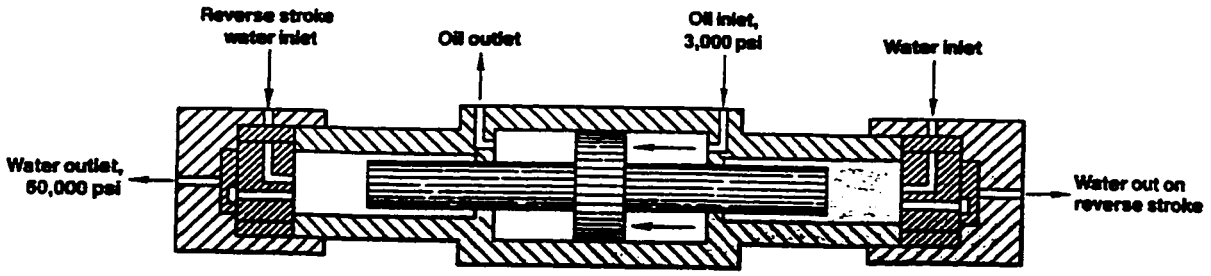

Figure 3.2 A Diagram of the High Pressure Intensifier

The nozzle assembly houses the waterjet orifice and mixing tube, and provides coherence and direction to the jet streams at an estimated speed of 900 m/s. As shown in Figure 3.3, a sapphire jewel assembly is used to adjust the diameter of the emitted jet stream. The diameters of sapphire jewel range from 0.076 mm to 0.51 mm. Abrasives are fed into the mixing chamber. The mixture of water and abrasives is further mixed and accelerated in the tungsten carbide focusing nozzle. This coherent AWJ is ready to machine the hard-to-machine materials.

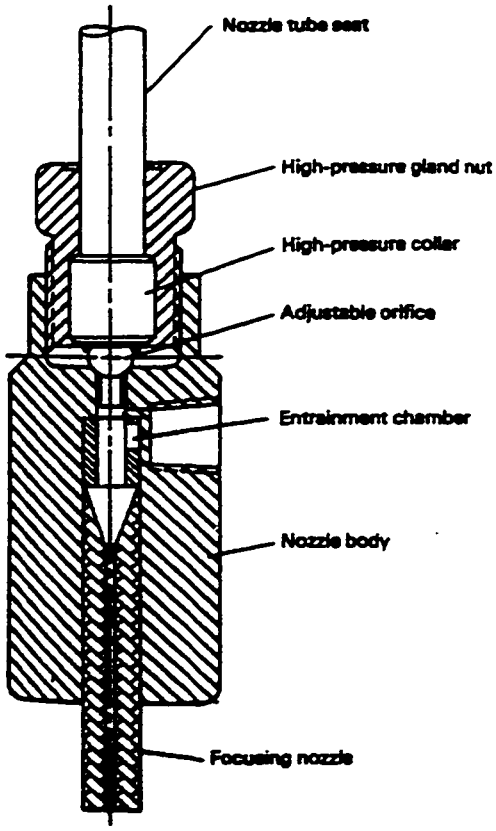

Figure 3.3 Cross Section View of a Nozzle Assembly[23]

The abrasive delivery system consists of an abrasive hopper, a flow rate control valve and delivery hose. A catcher system dissipates the residual energy of the jet and collects the waste. Two types of catchers are commonly used. One is a tank catcher filled with steel balls, and the other is a point catcher. The motion configurations of the AWJ system decide what type of catcher is appropriate. The motion system is used to move either the workpiece while the nozzle assembly is kept stationery, or vise versa.

Waterjet cutting consists of accelerating water in a nozzle in excess of 1000 m/sec and aiming the nozzle at a target point. As the jet flow hits the impingement zone, the velocity of the water radically drops to near 0 m/sec or to the velocity of the deformed workpiece. This results in the creation of a high stress on the workpiece surface. If the pressure is sufficient, the fluid/workpiece interface moves and cutting occurs. If the stresses created in the deformed zone are less than the deformation threshold, cutting is impossible. Adding abrasive particles to the waterjet changes the cutting dynamics. The water hammer effect at the collision site results in the development of pressure exceeding the static pressure of water in the impingement zone, and results in the subsequent removal of a small portion of the workpiece materials.

3.3 AWJ MACHINING OF BRITTLE MATERIALS

3.3.1 Machineability of Ceramics and Composite with AWJ

Abrasive waterjet machining is an erosive technique for cutting or drilling hard materials, which uses a direct stream of abrasive particles at high velocity. Several parameters affect abrasive waterjet cutting performance and machining results. These parameters can be divided into two groups: operational parameters and physical parameters. Operation parameters are those related to machining requirements, which include traverse rate, number of passes, standoff distance, impingement time for drill,

rotation speed for turning, and lateral feeding speed for milling. Physical parameters are those related to the controlling factors of the process, and can be categorized as follows[24]:

1. Hydraulic parameters (water pressure, flow rate)
2 Abrasive parameters (abrasive material, particle shape and size, abrasive flow rate and their condition (dry or slurry)
3. Mixing parameters (waterjet orifice diameter, diameter and length of mixing tube)

These can be summarized in Table 3.1:

Table 3.1 Abrasive Waterjet Cutting Process Parameters[25]

No.	Category	Parameters
1	Hydraulic	1. Waterjet Orifice Diameter 2. Waterjet Pressure
2	Abrasive	1. Grain Size 2. Flow Rate 3. Abrasive Material
3	Abrasive Nozzle	1. Nozzle Diameter 2. Nozzle Length 3. Nozzle Material
4	Cutting Process	1. Traverse Speed 2. Standoff Distance 3. Angle of Attach 4. Number of Pass
5	Workpiece	1. Hardness 2. Surface finish

Similarly, the abrasive waterjet cutting results or output are listed below:

1. Depth of penetration
2. Kerf width
3. Geometrical and dimensional accuracy
4. Surface roughness
5. Volume of material removal

Many parametric studies have been performed in abrasive waterjet machining on ductile materials and brittle materials. Hocheng and Chang [26] studied the machineability of ceramics by AWJ in terms of material removal rate, kerf shape, and surface roughness in a series of slot cutting experiments on aluminum oxide and silicon nitride ceramics. They concluded that AWJ is effective in machining of modern ceramics. The material removal rate is mainly controlled by the hydraulic pressure and abrasive flow rate. The traverse speed affects the kerf width and taper ratio by altering the specific cutting energy input. Also there exists an optimum combination between narrow cuts and uniform kerf taper. Faster passing of jet causes clear wall striations.

Material property is one of the most important factors determining the modes and rate of machining by abrasive waterjet[27]. The material hardness (H, or Vicker's hardness number) is the most relevant material property to the cutting wear mode. On the other hand, the modulus of elasticity (E) correlates well with the material removal in deformation wear. The empirical model was obtained to calculate the depth of cut (h) as a function of material properties.

$$h = \frac{A}{\sqrt{H}} + \frac{B}{E + C} \qquad (3.1)$$

where *A*, *B* and *C* are process constants that depend on AWJ parameters and the traverse rate.

Hamatani and Ramulu[28] also studied machineability on high temperature composite by abrasive waterjet. They used two-particulate reinforced ceramics, TiB_2/SiC and metal SiC/Al matrix composites in their piercing and slot cutting experiments. They found that: 1)abrasive waterjet machining of the ceramic matrix composite TiB_2/SiC was feasible, since better holes with minimal damage could be produced in ceramic composite at low standoff distance. 2) SiC/Al composite was easily machinable by AWJ, and good surface-finish could be produced, and 3) slotted edge damage in metal matrix composite was larger than in ceramic composite. Another study focused on the damage to plastic samples during abrasive waterjet machining[29]. It was revealed that under non-optimum conditions of excessive cutting speed, high standoff distance, low water pressure, and small nozzle diameter (which are considered non-optimum), the surfaces displayed signs of fiber debonding, pull-out, matrix chipping, and delamination. Roughness readings revealed that surface quality improved with larger diameter nozzle and at low machining speeds.

In another parametric study of abrasive waterjet piercing, Hunt, et. al.[30]analyzed material removal rate in terms of water pressure, abrasive flow rate, material thickness, material type, and material mechanical properties. They also investigated the machineability of aluminum oxide ceramics piercing and cutting with high pressure abrasive waterjet. They observed that the machining efficiency was determined by three major abrasive properties: abrasive material type, particle roundness (shape), and particle size. The results indicated that the cutting time with waterjet machining could significantly be reduced in comparison with the traditional methods of ceramic cutting. There were no mechanical or thermal loads directly applied to the workpiece, thereby eliminating chatter, vibration, surface distortion, and surface damage of the workpiece. *It*

was found that the sharp edges of an abrasive particle acted as a micro-cutting tool, which enhanced the probability of erosive failure initiation of the workpiece. Therefore, sharp edged abrasive grains were much more effective than round shaped abrasives. The researchers also chose garnet as the most economical and efficient abrasives for micro-cutting and piercing in comparison with silica sand, aluminum oxide and silicon carbide. It was found that there exists a threshold abrasive flow rate and jet pressure. Above the pressure threshold, further increase did not reduce the piercing time anymore. The general trend fit for abrasive flow rate, and was more dependent on material. The experimental results showed that (1)workpiece governs the mode of material removal, (2)material hardness is one of the most important properties for waterjet processes, and (3)the piercing time increases as the modulus of fracture increases. The results also implied that there was a third material parameter, a micro-structural parameter, which would encompass both brittle and ductile materials for abrasive waterjet processes.

It was found that a threshold ratio of particle-to-target material hardness needed to be exceeded for efficient cutting. The relevant material properties depended on the range of traverse rate if other process parameters were kept unchanged[31].

3.3.2 Standoff Distance Effect in a Waterjet Machining Process

Standoff distance plays a very important role in the jet machining capability, and it appears that there exists an optimum standoff distance for cutting metals [32]. Konig and Wulf[33] studied the influence of standoff distance and feed rate on kerf geometry. They demonstrated that the widening of kerf is a linear function of standoff distance. In other words, increasing the standoff distance results in an increased kerf width of the cut in a linear fashion.

3.3.3 Surface Finish Analysis in an Abrasive Waterjet Machining Process

The AWJ machined surfaces on high temperature composites (SiC whisker/2124 Al_2O_3) has rendered relatively smooth surfaces coupled with minimum subsurface microstructural damages[34]. Hunt, Kim, and Reuber [35] conducted a parametric study on the surface finish optimization for abrasive waterjet cutting. An experimental study was conducted to develop a method for optimizing the abrasive waterjet cutting the surface finish, of abrasive waterjet machined workpiece by means of process kinetic parameter, namely the workpiece reactive force. It was found that the workpiece reactive force could be used as a control parameter for optimizing the abrasive waterjet process. Mohan, et al compared the machined surface texture to AWJ and laser machining[36]. In an experimental study by Burnham and Kim [37], the surface finish associated with high pressure abrasive waterjet processes was ascertained in a statistical approach. The results revealed that the surface roughness could be predicted by the statistical manipulation of certain process parameters, and by the workpiece reactive force. In another study, Kovacevic, et al[38] characterized abrasive waterjet cut surface using static and dynamic characterization techniques. They concluded that the abrasive waterjet cut surface profile was predominantly Gaussian in nature. Primary and secondary wavelengths were responsible for the surface profiles. In an AWJ machining of steel and titanium, Chao[39] noticed that the waterjet generated surface was separated into smooth and striation zones. The striation influence was negligible in the smooth zone, which had a random, moderately isotropic texture with the height distribution nearly Gaussian. The roughness of the cut surfaces was strongly related to the depth of cut and cutting speed for the striation zone of an abrasive waterjet cut surface. The roughness parameters *Ra* and *Rq* increased rapidly as depth of cut or cutting speed increased. It was noted that vibration of an abrasive waterjet machining system played an important role in the generation of striation marks on the machined surface[40]. Another work by Hashish[41] demonstrated that the particle size as one of the most dominant parameters also affects the surface finish.

Even though the machining of advanced materials with AWJ could result in minor but controllable surface texture effects, the surface integrity was not affected by particle deposition, delamination, gouging, microstructural changes, cracking, chipping, work hardening, and heat-affected zones. Kovecevic, et al[42] investigated the possibility by linking the dynamic workpiece normal force and the quality of the machined surface.

3.3.4 AWJ Pressure and Abrasive Particle Size

In a separate study, Hashish investigated the effect of pressure in abrasive waterjet cutting, and the interaction between water pressure and various operational and physical parameters [43]. He found that as the waterjet pressure increased, the jet coherency was reduced, which reduced the effectiveness of jets' machining capability at the same pressure. Increasing the waterjet pressure increased the material removal rate. However, this method not only raises the machining cost, but also lowers the machining quality. Fragmentation of abrasive particles occurs as they flow through the narrow mixing tube of the AWJ. At higher pressures the degree of fragmentation increases, which affects the mixing efficiency and the effectiveness of cutting. This explains the earlier results by Hunt, et al regarding threshold pressure. As flow pressure reached its threshold, the abrasive particles became fragmented, and the cutting efficiency was reduced. Further increase of pressure did not increase the rate of material removal.

Momber, et al[44] investigated the correlation between the size and size distribution of wear particles generated during abrasive waterjet cutting processes on cast iron and the general mechanism, as well as an energy absorption and the efficiency of material removal. The average diameter of the removed wear particles dropped with rising pump pressure following the relations:

$$D(p)=A^{4} * p^{-1/5} \qquad (3.2)$$

where D is the average diameter of the removed wear particles and is a function of pressure p; *and* A is a material constant that depends on both work material and the abrasives. *They found that about 2% of AWJ input energy was absorbed due to the generation of the wear particles. The material removal mechanism did not depend significantly on the pump pressure applied, but the pump pressure influenced the efficiency of the material removal process.* Geskin, et al [45] studied the abrasive particle distribution in the abrasive waterjet stream. The experimental results showed that the average particle density within the jet remains constant and is not influenced by any other parameters. Hence the particle distribution is not a concern and has no effect on the machining results. More experimental results indicated that an optimum abrasive grain size distribution produces the maximum cut quality at a fixed process condition[46].

3.3.5 AWJ Machining Energy, Force and Thermal Effect

In abrasive waterjet machining processes, much of the energy from the pressurized water is dissipated by water. Part of the input energy is converted into friction induced heat [47]. However, there is no significant temperature rise at the machining zone[48], because most machining-induced heat is absorbed and cooled by the excessive water.

Li, et al. [49] studied the dynamic force within the workpiece in the impingement zone by using piezoelectric transducers and strain gauges. They concluded that at a constant stagnation pressure, the momentum of jet stream, and the corresponding forces generated in the impact region, are partially determined by the water flow rate. Focusing tube diameter, abrasive flow rate, and abrasive size also have secondary effects on the variation of flow momentum. At some conditions, these variables can substantially change the flow development. There is a limit of the forces generated in the machining process while changing the standoff distance. Furthermore, the variation of the forces

caused at different standoff distances is not significant (around 10-15%). Momber[50] developed a mathematical model for estimation of the energy absorption capability of materials during abrasive waterjet machining. The energy absorption depends on the depth of cut following a second order equation.

3.3.6 Precision Machining of AWJ

In a study on the machineability of aluminum oxide ceramics piercing and cutting with high pressure abrasive waterjet, Kim, et al [51] suggested that a more extensive investigation would be needed to apply this new technology to ceramic machining applications. The material removal process by the abrasive waterjet can be optimized if one can control the traverse speed and the position, as a function of the nozzle wear, to achieve significant productivity improvement and cost saving. Ansari, et al[52] investigated the influence of abrasive waterjet parameters on the volume removal rate in abrasive waterjet turning. The volume removal trends in abrasive waterjet turning were similar to those in linear cutting with abrasive waterjet. Increasing waterjet pressure, orifice diameter, and abrasive flow rate generally resulted in an increased volume removal rate. Due to the abrasive waterjet limit or volume sweep rate limit the volume removal rate leveled off. Many studies [53, 54, 55, 56, 57, 58] have also been conducted for linear cutting, milling, turning, and cutting using the abrasive waterjet machining technique. For example, Hashish, et al[59] compared AWJ to laser beams for precision hole drilling on a ceramic that was coated with thermal barrier coating. High quality holes could be obtained with abrasive waterjet drilling without fracture or chip. Holes of size ranging from .016 to .025 inch could be drilled, and the hole size could be controlled. Hashish[60] also investigated composite material trimming with abrasive-waterjet. It was shown that the machining accuracy with abrasive-waterjet could be 0.025 mm, which allowed accurate control of the machining process. An experimental investigation of rectangular pocket milling with abrasive water was conducted by Paul, et al[61]. The depth of the

pocket could be controlled to a value of 0.04 mm with an acceptable surface finish, and the variation of the depth of pocket seemed to decrease at higher transverse feed, lower water pressure, and increased mass flow rate of the abrasive particle.

It was concluded that the AWJ technique offers great machining advantages for many materials, especially hard-to-machine alloys and composites, in a wide variety of machining operations. An optimal range of parameters for machining materials should be used to avoid adverse effects and to maximize material removal rate. However, the machining precision needs to be improved.

3.3.7 Effects of Material Hardness and Jet Impact Angle

The work material hardness and the abrasive hardness strongly affect the material removal rate. A study by Wada[62] has shown that the wear mechanisms and the wear rates of the worn ceramics, such as Si_3N_4 , SiC, Al_2O_3, are a function of the ratio of the abrasive hardness to the hardness of the target ceramics. The fracture toughness of the target materials also plays a role in determining the material removal rate.

Wong, et al[63] and Wada, and Kumon[64] studied the effect of the jet impact angle on the cutting quality. It appeared that the material removal rate was strongly affected by the secondary wear for SiC abrasives on Si_3N_4 ceramics. They confirmed that a 90 degree angle of the jet produced the most uniform groove depth and width for Si_3N_4 materials[64].

3.4 EROSION THEORIES AND MECHANISMS

3.4.1 Abrasive Waterjet - Workpiece Interaction

In the abrasive waterjet machining process, either an abrasive mixed waterjet stream or liquid droplets collide with a solid surface at a high velocity. The process of high pressure waterjet machining differs from traditional methods of material machining

in the use of an abrasive entrained waterjet as a cutting tool. The waterjet exiting the nozzle can be supersonic. In the complex jet cutting process, chip removal, particle separation, and gradual material destruction are achieved as a result of the motion of the jet at the machined surface. The action of the high-speed waterjet on the workpiece creates an impact[65]. After impact, the stresses quickly increase to their critical levels in the machined material. These result in brittle fracture, where the rupture strength appears to be smaller than the yield limit, or $\frac{d\varepsilon}{dt} > \frac{\sigma}{\xi}$, where ε is the maximum strain, t is the duration of loading, σ is the fracture stress, and ξ is a coefficient of internal bonding. The mechanics of fracture in brittle materials during abrasive waterjet cutting can vary due to the initiation and propagation of micro-cracks.

Following is a discussion of the mechanisms during abrasive waterjet cutting and abrasive waterjet drilling . A schematic of the interaction of an abrasive waterjet with a workpiece in the cutting process is illustrated in Figure 3.4[65]. The high speed AWJ flows along the arrow V_j, while the machined material moves in the direction of arrow. There are three types of jet action on the machined material, namely impact jet, slipping jets, or slanting jets. Since the waterjet diameter is very small compared with the thickness of the machined material, all three types of jet actions are involved during the interaction of the waterjet with the machined material in the cutting zone.

The abrasive waterjet cutting process develops in three different stages, i.e. development (entry) stage, developed cutting stage, and exit stage [66]. The entry stage is the initial cutting stage before the jet reaches the maximum depth of cut. At a certain point when the maximum cutting depth is reached, the developed cutting stage begins. Right after a full kerf of cut is formed, a cyclic dual substage procedure starts. In the first substage, abrasive particles attack the kerf wall at a sharp angle, thus initiating the cutting wear mode, as termed by Bitter[67]. In the second substage, particles collide with the kerf

wall and remove material at large angles. This is the deformation wear mode. The waterjet-material interface curvature increases as the depth of cut increases, due to deflected particles, reduced angle of attack, and decelerated particles. Both substages may exist in abrasive waterjet machining. However, the impact angles in both substages are very small on a local level, and hence the cutting mode should be the predominant mechanism in both substages.

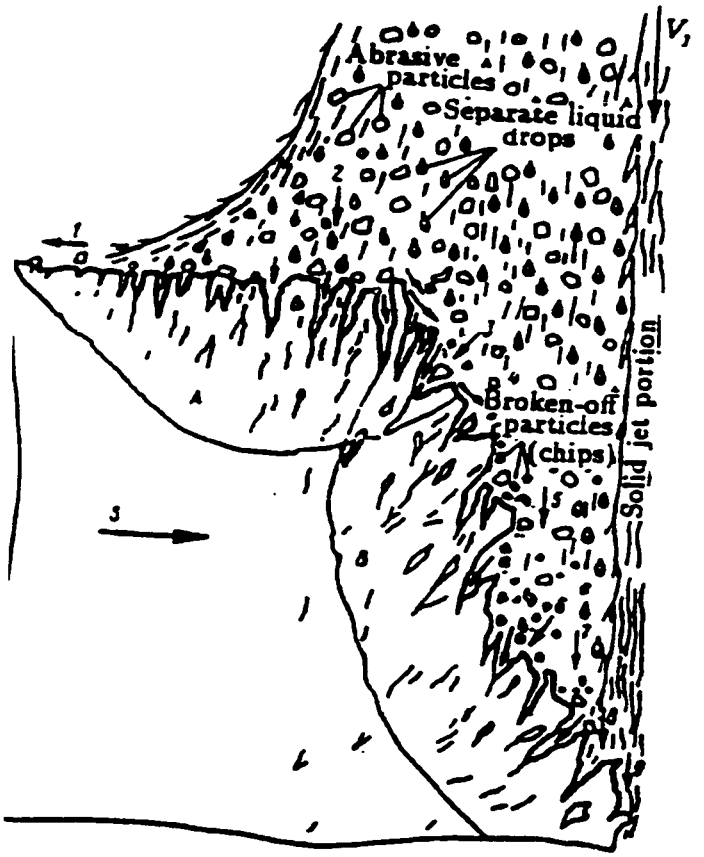

Figure 3.4 Schematic of the AWJ-Workpiece Interaction during Cutting [65]

Directions of the jets are indicated by arrows noted below:

(2) and (8)	impact jet
(1), (4), (5) and (9)	slipping jet
(3), (6), and (7)	slanting jet respectively

The abrasive waterjet machining mechanism in drilling is somewhat different from that in the cutting discussed above. In order to examine the mechanism involving high-speed waterjet drilling, a representation of the flow pattern of AWJ drilling is illustrated in Figure 3.5. In abrasive waterjet drilling, only impact jets' and slipping jets' actions are prevalent, and slanting jet does not exist. This is because the flow reverses direction after impact with the machined material, and flows out of cavity after it reaches the stagnation point. The stagnation point is denoted by *"0"* in the sketch, where it suffers direct impact by the abrasive waterjet. The reverse flow results in considerable shear stress in the immediate vicinity of the stagnation point. This shear force has relatively less impact on the failure of the material than the oncoming flow. The oncoming flow is retarded by the back flow before it hits the cavity. However, further bombardment on the material surface of the cavity by the oncoming flow jet removes a new layer of material, and creates a new and deeper cavity. The AWJ penetrating capability decreases as the depth of the drilled hole increases, due to the decreasing AWJ net kinetic energy that is available for eroding the workpiece [68].

3.4.2 Erosion Mechanisms in Material

A gradual material loss from a surface in the form of small particle or fragments occurs due to the repeated dynamic or impulsive forces acting on a solid surface. This phenomenon is called erosion. The erosion mechanisms are not the same for ductile materials and brittle materials. The erosion mechanism for ductile materials can be classified into seven categories [69]:

1. Cutting
2. Extrusion
3. Micro-flaking (or deformation wear)

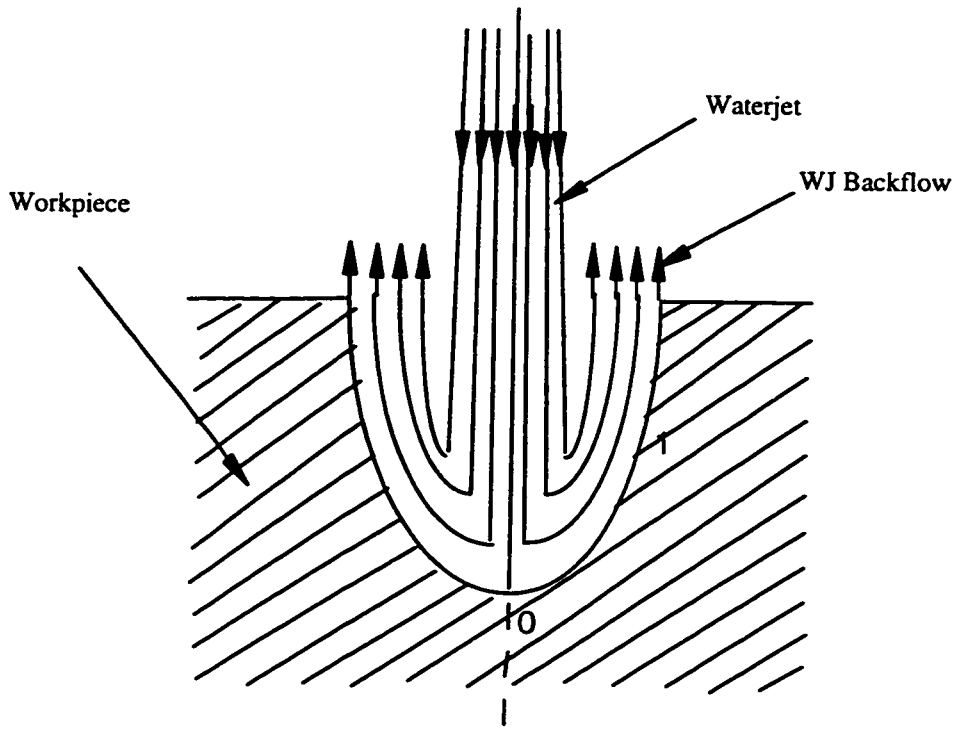

Figure 3.5 A schematic of AWJ Drilling [68]

4. Secondary erosion
5 Melting and splatting
6. Embedding
7. Ripple formation and macro-flaking

When cutting with an erodent with sharp edges and relatively small impact angles, the impacting particle displaces, along its trajectory, a portion of target material into a chip by shearing. An extrusion mechanism is normally induced, where the target material is displaced to form a lip (or ridge) under the impact of an erodent with round edges or large edge angles. These lips (or ridges) remain attached to the target surface until subsequent impacts knock them off. However, there are no clear indications where a

single mechanism is involved in a machining process. Sometimes even sharp erodents impacting at small angles may result in ridges instead of chips due to the particle orientation, as suggested by Tilly [70]. Micro-flaking or deformation wear occurs in the event of multi-particle erosion, especially with large impact angles. In this process, when a critical strain is reached[71], the overlapped impacts produce highly strained regions where thin platelets spall off from the target material. In contrast to the lips formed by oblique impacts, which generally are quite bulky and project above the surface level, these platelets tend to be thinner, and, in many cases, lie almost parallel to the surface. Further impacts increase the number of these platelets and increase the extent of material removal.

Secondary erosion, melting and splattering, and particle embedment are less significant material removal mechanisms. Secondary erosion is due to the secondary impacts of particle fragments[72]. Ductile erosion is a two - stage process. The impacting particle strikes the surface and produces an indentation, or possibly removes a chip of metal. In the secondary stage the particle breaks up, and the fragments are projected radially from the primary impact site. These fragments produce secondary damage. A melting and splattering mechanism is caused by the local high temperature in the immediate impact zone, where target and/or the particle material is molten, and molten debris is ejected [73]. Particle embedment produces material removal only when the embedded particle is subsequently detached so that some bonded material is removed, or when the brittle surface layer by the particle embedment is eventually fractured away [74]. A typical material removal mechanism in a ripple formation process is the formation and detachment of macro-flakes at the ripple crests. Formation of these macro-flakes is usually attributed to surface plastic flow [75]. Ripple formation often occurs when the erosion conditions include either a soft target material [76] with a small impact angle [77], or a

large stream impact angle with tangential flow component. These were also observed in Zeng's[69] study

Erosion processes for brittle materials are more complex than those of ductile materials. The mechanisms for brittle materials can also be classified into seven categories [30]:

(1) Conical, radial, and lateral crack system
(2) Ring fracture
(3) Micro-crack nucleation and microchipping
(4) Plastic deformation and melting
(5) Ripple formation
(6) Mixed mode damage

The formation of conical, radial, and lateral crack systems is the most commonly observed impact damage on the brittle materials. The detail is shown in section A.3 of Appendix A. The general appearance consists of a central plastic impression and surrounding conical, radial and lateral cracks. However, some of these damages may be missed sometimes. Chaudri and Walley [78] revealed that the conical and radial cracks form during the loading period of the particle/target interaction, while the lateral cracks form during the unloading period. Material removal is usually due to the lateral cracks that are formed, which grow out to reach the surface. Ring fracture damage includes a main ring crack and many short circumferential fractures [79]. Such damages have been primarily observed for normal (90°) impacts.

Ramulu[17] reported evidence involving micro-crack nucleation and microchipping in an annealed polycarbonate specimen under high-pressure waterjet and abrasive waterjet piercing. Typical scanning electron microscopy (SEM) micrographs of the cross section of a pierced hole is shown in Figure 3.6. In the machining process, interaction

between abrasive particles compounded by the turbulent water flow caused the particles to collide, fragment, and rotate. The return flow of the jet after impact created a micro-irregularity on the shape of the hole. The micrographs exposed numerous microcracks at the bottom of the holes. Material removal in drilling was a result of the continual bombardment and invasive penetration of the abrasive particles on the material surface, which created microcracks. Pressurized water entering the cracks caused hydrowedging. The incoming abrasive particles shattered the crack-weakened surfaces. Material was thus removed and the process repeated itself.

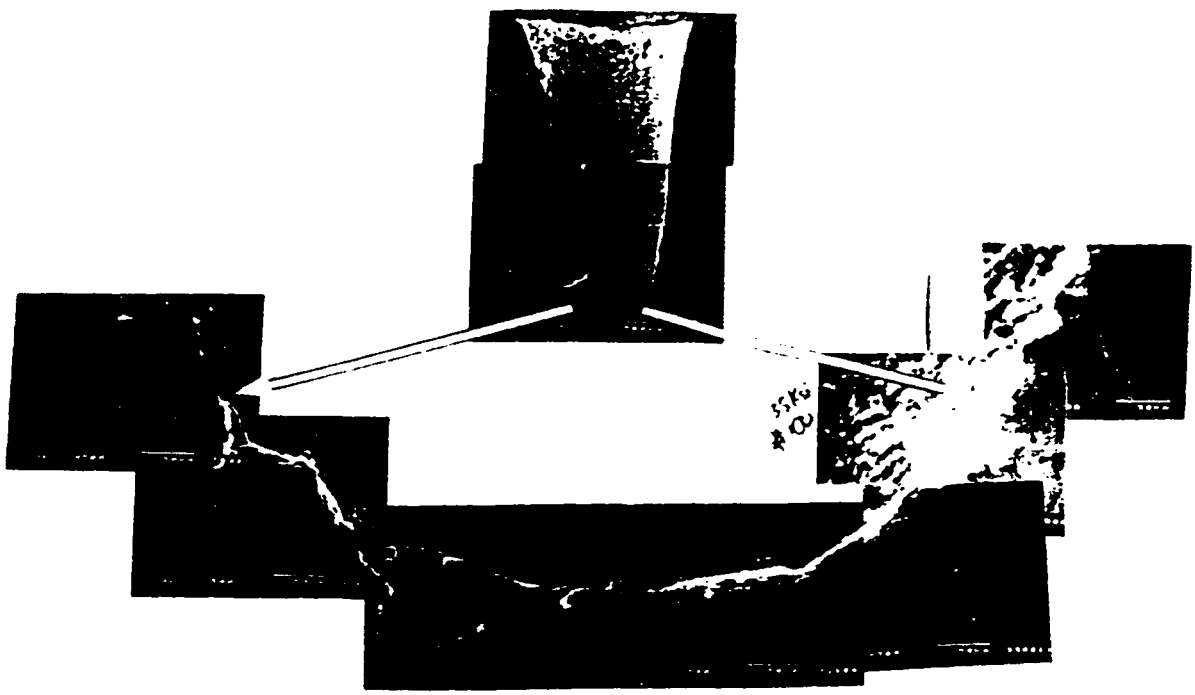

Figure 3.6 Typical SEM Micrograph of a Sectioned Hole in AWJ Machined Polycarbonate Material [17]

Plastic deformation has also been observed in many impact events of brittle materials involving angular and rounded erodents. Erosion by virtue of ripple formation was absent in most erosion tests of brittle materials, but an exception was found on a silica glass specimen observed by Sheldon and Finnie (1966)[80]. Erosion of brittle material, especially polycrystalline ceramics, is due to a combination of plastic flow and network cracking[69]. The cause of network cracking has been attributed to stress wave induced fractures.

Investigators have rendered many mathematical models on material removal. These models can be classified into two categories: 1) cutting model and 2) deformation wear model. It seems that all the cutting models have originated from, or are similar to, Finnie's model [81]. The concept of deformation wear was first used by Bitter (1963)[67]. Generally the cutting models are associated with small impact angles, while the deformation wear models are associated with large impact angles (most of them with 90°).

Finnie[82] investigated the erosion phenomenon caused by solid particles entrained in fluid stream. He concluded that erosion is dependent on the flow condition and material removal mechanisms. Furthermore, the fluid turbulence at the impact zone may increase the material removal rate when a solid surface is roughened by erosive action of solid particles. Sheldon and Finnie investigated the erosive wear using solid particle stream impact on the brittle material[80]. They also set up an analytical model which establishes the relationship of the volume of material removed as a function of the number of impact particles.

$$W = kr^{f_1(m)}U^{f_2(m)} \tag{3.3}$$

Where K is the quantity involving material constant, r is average radius, and U is the impacting velocity of particles. The exponents $f_1(m)$ and $f_2(m)$ are the prescribed

functions of m, which is the flaw parameter of the Weibull fracture strength distribution. Another study by the same authors evidenced the ductile behavior of normally brittle materials during erosive wear[80]. It was indicated that the erosive mechanisms of brittle materials are dependent on particle size. For example, when impacted by smaller particles, ductile behavior may appear on brittle materials.

Erosion is composed of deformation wear and cutting wear[67]. Specifically, deformation wear is caused by repeated deformation during particle collision on the target material in a shallow angle, which eventually results in material breakage and chipping into pieces. The material removal is highly dependent on the impingement particle velocity, as well as the angle of the particle attacking the surface. The material volume lost in deformation wear type of erosion is written as

$$W_D = \frac{1}{2}\frac{M(V\sin\alpha - K)^2}{\varepsilon} \tag{3.4}$$

Where M and V represent the total mass and velocity of the impinging particles respectively, α is the impact angle, K is the maximum threshold particle velocity at which the collision is still elastic, and ε is the energy required to remove unit material.

In contrast, cutting wear is caused by cutting actions of particles bombarding the workpiece in a sharp angle. After the impingement, particles either keep their horizontal velocity and create more damage, or lose all their velocity and stand still. An analytical model describing the material removal volumes is shown below.

$$W_c = 2M\frac{C(V\sin\alpha - K)^2}{\sqrt{V\sin\alpha}}[V\cos\alpha - \frac{C(V\sin\alpha - K)^2}{\sqrt{V\sin\alpha}}]\xi \tag{3.5}$$

and $$W_C = \frac{1}{2} M \frac{[V^2 \cos^2 \alpha - K_1 (V \sin \alpha - k)^{1.5}]}{\xi} \qquad (3.6)$$

where ξ is the cutting wear factor. It was reported that the experimental data agrees quite well with what was predicted by these equations.

Evans and Hockey, et al.[83,84] described the erosion of brittle material by angular particle impact in terms of elastic-plastic deformation. A mathematical model of material removal rate was established in terms of the penetration depth of the impact and the size of the lateral cracks. The material removal rate for a single impact can be written as:

$$W \sim V_0^{2.5} R_p^{\frac{1}{4}} \rho_p^{0.3} H^{-0.3} K_c^{-1.5} \qquad (3.7)$$

where H is the material hardness, Kc is the critical stress intensity factor, V_0 is the impact velocity; R_p is the particle radius; and ρ_p is the particle density. The exponent of impact velocity is 3.5, which is determined by considering the extent of damage observed in experiments and by mathematical analysis. For multi-particle impact, as long as each impact is similar, the material removal $\dot{W}$ rate can be described as

$$\dot{W} \sim \dot{m} V_0^{2.5} R_p^{\frac{1}{4}} \rho_p^{-0.7} H^{-0.3} K_c^{-1.5} \qquad (3.8)$$

where $\dot{W}$ is the material removal rate and $\dot{m}$ is the abrasive flow rate.

Analytical models for the total depth of cut in the abrasive waterjet machining of polycrystalline brittle material and ductile material were established by Paul, et al[85]. The models assume that material removal takes place in abrasive waterjet machining in two zones: 1) the micro-cutting and fracture that is due to shallow angle impact by the abrasive particles, and 2) the plastic deformation and fracture that is due to orthogonal impact of the abrasive particles. Using the concept of specific energy an analytical model

was also developed for ductile materials[86]. Good correlation with the experimental results was obtained.

Arola and Ramulu[87] compared the abrasive waterjet machining mechanism between G/E laminate and aluminum materials. They found that in composite material, abrasive shearing and brittle fracture mechanisms predominated, with limited post-processed constituent disruption and high interstitial integrity. For aluminum, the mechanism of material removal was a combination of ductile shear induced by scooping and plowing actions of the abrasive particles. Momber and Kovacevic[88] studied a multiphase concrete machined by abrasive waterjet, and found that the cutting of pre-cracked multiphase materials with high-pressure waterjet was highly localized. The width of the generated fracture in the processed specimens was proportional to the local fracture probability, which depended on the applied stress (pump pressure), the local fracture toughness, and the local microcrack distribution.

3.4.3 Machining Mechanism of Abrasive Waterjet on Ceramics

During the AWJ cutting process, the cutting wear mode occurs at the top of the kerf due to shallow angles of impact[89]. The deformation wear mode occurs below the cutting wear mode due to large angles of impact. Momber[90] investigated abrasive waterjet machining on refractory ceramics, such as bauxite and magnesia chromate, and found that the machining mechanism changed with the depth of cut. In the upper region of the cut, the main material removal mechanism was a simultaneous cutting of matrix and inclusion grains (transgranular). In the lower region, the removal process was characterized by the removal of the binding matrix, followed by washing of the inclusion grains (intergranular), Zeng and Kim[91] developed an equation for the prediction of the depth of cut, which was based on an erosion model semi-empirical equation by regression of a large number of experimental data. The "machineability number" representing the

unique property of a material under the condition of abrasive waterjet machining could be determined from AWJ cutting experiments.

Aluminum based ceramic materials were studied based on a statistical experimental design principle[92]. The experimental data showed that the AWJ technology is effective for machining brittle materials such as ceramics. The machined kerf consists of three zones, including upper, middle, and lower zones. Zeng [18] studied the erosion phenomenon associated with abrasive waterjet cutting of polycrystalline ceramics. The erosion mechanisms were found to include intergranular network cracking and plastic flow. The cause for the network cracking was fracture, which was induced by stress wave from impact. The erosion rate was strongly correlated with the grain size and fracture energy of target materials.

Abrasive waterjet machining has been used for machining unidirectional graphite/epoxy composite. The abrasive waterjet machining mechanisms of the unidirectional graphite/epoxy composite was studied by Ramulu and Arola[93]. The secondary processing effects and damage mechanisms for abrasive waterjet machining of CFCC composites were investigated by Ramulu, et al[94, 95]. They found that AWJ is a feasible machining process that generates reasonable quality surface due to its material removal mechanisms, including bending, shearing, micro-machining, and erosion.

3.5 OPTICAL EXPERIMENTAL STUDIES ON AWJ MACHINING

The mechanisms of material erosion in ductile and brittle materials under the impingement of high pressure waterjet have been found to be due to a combination of factors: microfracture, erosion, compressive shearing, and melting, as described in the previous sections. However, experimental investigation of the interaction between AWJ

and the workpiece is very rare. Most experimental works concerning AWJ are parametric studies.

Photoelasticity was first used as a tool to investigate the jet/workpiece interactions and machining mechanism in the early 1970s. Daniel, et al[96] and Daniel[97] studied the phenomena of deformation and fracture of brittle solids under waterjet impact, using dynamic photoelasticity and high speed photography. The experimental evidence showed that brittle-material failure under waterjet impact was related to stress wave induced fracture, transient state of stress, and material properties. Dense fringes from a CR-39 Columbia Resin under impingement of waterjet were photographed. A sequence of phenomena in the material damage consisted of 1) initial jet penetration with cratering enhanced by the shear waves, 2) wave propagation with the pronounced attenuation of dilatational wave, 3) quasi - static crater pressurization, 4) cracking and pressure relief, and 5) further pressurization and cracking. There was no evidence of very high pressure buildup, as would be predicted by hydrodynamic theory.

Photoelasticity technique was also applied to the field of abrasive waterjet machining by Ramulu[17]. A two-dimensional dynamic photoelasticity experiment was conducted to study the mechanics of material removal in the AWJ piercing process in a bi-refringent polymer material. A typical dynamic photoelastic fringe pattern associated with the abrasive waterjet penetration process is shown in Figure 3.7. It was concluded that the stresses involved in the machining process were highly localized. It was demonstrated that abrasive waterjet was more efficient because pure waterjet exhibit larger cracks, and the cutting action was uneven compared with the abrasive waterjet. Microcracks were observed in the bottom of the hole, indicating that the incessant bombardment of an AWJ created crack-nucleation sites with crack growth that was abetted by the hydrowedging action of the incoming jet.

Figure 3.7 Dynamic Photoelastic Fringe Patterns in an AWJ Penetration Process [17]

Supply pressure: 110 MPa, Standoff distance: 8 mm;
Abrasive: Garnet, 100 mesh; Abrasive flow rate: 11.2 g/s;
Jet exposure time: 2 second

As can be seen in this review, investigations of abrasive waterjet machining using optical technique is very limited in the open literature available to date. Even in the limited research conducted thus far, the techniques that were used generally yielded two dimensional state of stress fields, which provided very limited observation of the stress and strain fields. In order to better understand the mechanisms of abrasive waterjet machining, numerical modeling is essential to supplement the experimental work.

3.6 NUMERICAL MODELING

With the development of large-scale computational capability in structural and fluid dynamic analysis, finite element analysis (FEA) has begun to be applied in the field of waterjet cutting. A few researchers have also studied contact-impact problems with FEA modeling. Przylenk and Schlatter [98] simulated the waterjet cutting process with the finite element method. The waterjet impact loading was applied numerically to the workpiece in the form of both point force and area load. In this case of reciprocation between waterjet and a solid body, the modeling was based on treating the continuous jet as "successive rounds of high speed jet impacts". After the workpiece surface is hit by the first round of jet, it deforms. Another round of impact adds one more layer of deformation to the already deformed surface. This process continues. Since the numerical modeling could not take material stock removal into consideration, it was assumed that the volume of the material removed, when the real jets hit the workpiece, was the same as the volume of the calculated deformation. In other words, the new workpiece surface was the same as the deformed surface. Thus the cutting processes were simulated by multiple runs of the FEM program. The machining time, which was not considered in this model, was compensated for by running the program many times.

A program, ASKA, coded in FORTRAN 77, was used to separately analyze, in sequence, the fluid flow and the liquid - workpiece impact within the waterjet system. The following Figure 3.8 is a comparison of an experimentally obtained kerf machined by waterjet, and the FEM calculated kerf on an AlSi 12 solid body. Both kerf curves are superimposed in a single frame. The computed cutting kerf was obtained after 200 runs of the finite element program. Even though they show similar contours of the machined kerfs, there is much room for improvement.

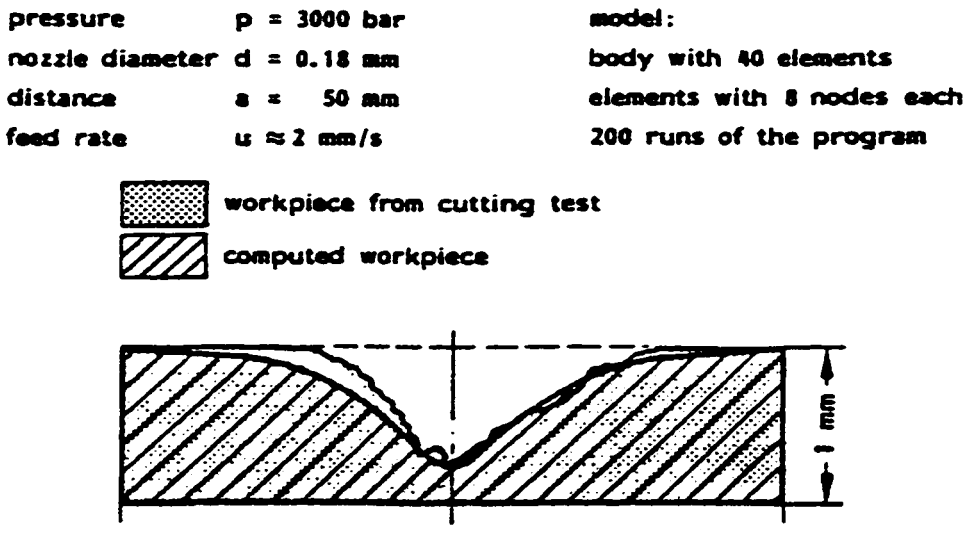

Figure 3.8 Comparison of a Waterjet Machined Kerf on AlSi 12 [98]

(FEM vs. Experimental)

Another study involving micro-physical phenomena was conducted by Rosenblatt, et al [99]. They investigated the effects of surface flaws on ceramic target damage from subsonic water drop impacts. Simulations using a numerical code *WAVE-L*, which is based on fundamental wave propagation and fracture mechanics concepts, were implemented. The code was based on HEMP scheme, which integrates the governing partial differential equations of motion for arbitrary dynamic problems in solid and fluid dynamics. Figure 3.9 is an initial computational grid of the target material *ZnSe*, using 80 cell per drop diameter. The surface flaw is modeled as a crack across a computational cell near the surface. The activation of a crack is defined by the condition where $K_I \geq K_c$, where K_I is the stress intensity factor. The researchers concluded that the surface crack activation under water drop impact is dependent on the depth of surface flaws. A relatively large surface flaw can perturb the stress field so that crack activation in its vicinity is suppressed.

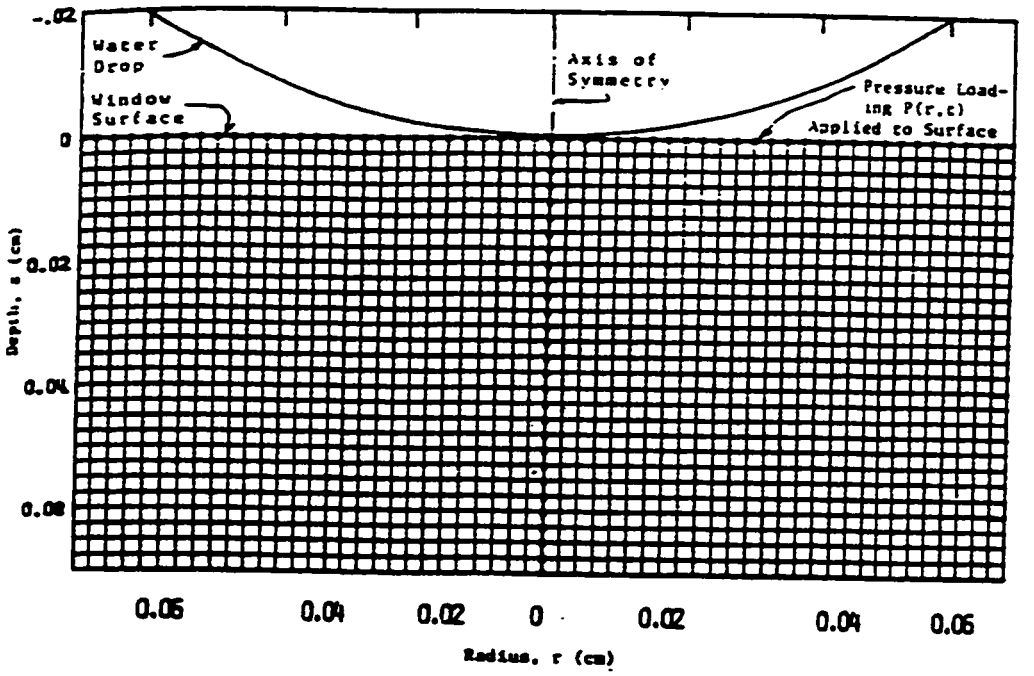

Figure 3.9 A Solid Target FEM Model Mesh [99]

A numerical computation[100] of the striation of the abrasive waterjet cut surface was performed based on the following equation proposed by Bitter,

$$W = \frac{Mv_a^2 \cos^2 a}{2\beta} + \frac{Mv_a^2 \sin^2 a}{2\varepsilon} \qquad (3.11)$$

where M denotes the mass of the abrasive particle, v_a particle velocity, α collision angle, β cutting wear constant, and ε deformation wear constant (β/ε =150). The results from the 2-dimensional computation revealed that the random distribution of abrasive particles was essential for the striations on the machined surface. In this simulation the effect of water and the oscillation of the jet perpendicular to the traversing direction was not included, and thus the results were different than those found from the experiments. In this report no detailed simulation method was given.

The effects of ceramic material under static and dynamic loading have been studied extensively with a hybrid experimental-numerical approach. Liaw, et al[101] investigated the dynamic fracture response of reaction bonded silicon nitride under wedge-loaded impact loading. In this research, the experimentally determined crack extension history drove a finite element code in its generation mode. The dynamic finite element analysis, in turn, numerically yielded the dynamic stress intensity factor and energy partitions during crack propagation. Mark and Jenkins[102] implemented an FEA work to predict the mechanical response in the non - uniform stress state of flexure for a continuous fiber ceramic composite. A single plane of nodes was used to define the shape of the model with two coincident sets of elements to model the matrix and fiber meshes. The element meshed is illustrated in Figure 3.10. Some unique commands, such as the "kill" command, were used to modify the stiffness of elements for which the stress exceeded their respective strength. The FEA results were found to be very close to those of the experimental test results.

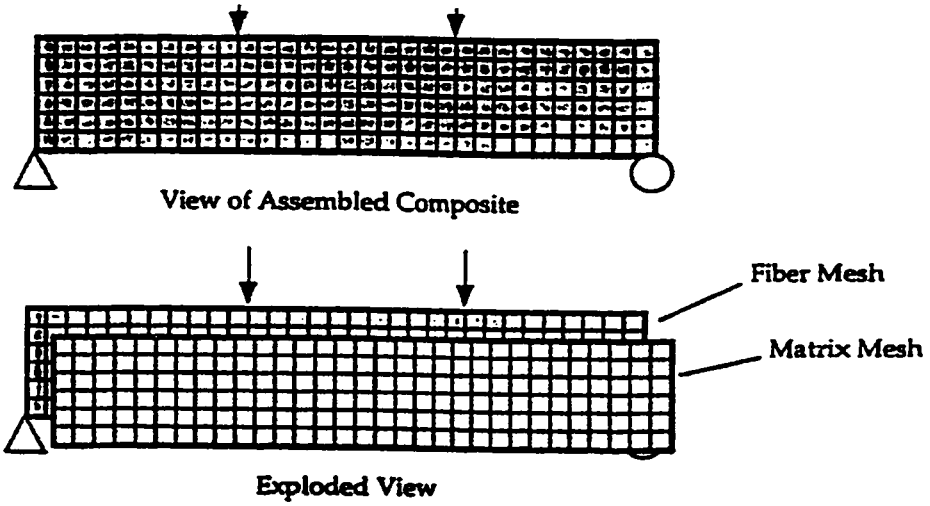

Figure 3.10 Single set of nodes and coincident matrix and fiber element meshes [102]

3.7 SUMMARY

Ceramics have great potential to be used in a larger number of applications where resistance to temperature, stress, and environment is required. However, manufacturing and machining of ceramics have always created serious bottlenecks when exploring their applications. In order to expand the possible applications of ceramic material, suitable machining methods need to be developed to allow for successful fabrication of component parts.

Of all the machining processes discussed in Appendix A, abrasive waterjet machining, indeed, is among the most economical and efficient non-traditional machining technique for the advanced ceramics. It is a nonthermal, nonchemical, and nonelectrical process that creates no change in the metallurgical, chemical, or physical properties of the workpiece. It is also suitable for many operations such a turning, milling, and drilling with reasonably large material removal rates, and with no dulling of "tools". Abrasive waterjet machining is ideal for automation, robotics, and remote control. It appears that AWJ processes provide greater benefits for a wide range of machining operations.

Abrasive waterjet machining is a relatively new industrial manufacturing process, especially in the machining of advanced ceramics, and it is insufficiently studied. Many of the principle problems related to this process are not yet clearly understood. These include 1) basic cutting processes, 2) design and development of high-speed waterjet systems, 3) development of hydrocutting machines, and 4) improvements in material AWJ cutting efficiency [65]. Furthermore, the successful technological development of abrasive waterjet machining of advanced ceramic materials requires an in-depth knowledge of the machining process micro-mechanisms in order to improve the quality, efficiency, and design of a highly efficient abrasive nozzle. This current review of the open literature on the abrasive waterjet machining of brittle materials, indicates that most of the research efforts have concentrated on parametric experimental study, and on the

material erosion phenomenon during waterjet (drop) impact with a solid. The parametric studies only concern the dimensional quality characteristics of the cutting process and the material removal rate. The few theoretical erosion theories reported refer to mechanisms of erosion that are due to single abrasive particles, or to a multitude of particles. Investigations of the mechanisms of abrasive waterjet machining of hard and brittle ceramics have been very limited. It is important that new experimental and numerical research be developed in order to study the mechanisms of abrasive waterjet machining of advanced ceramic materials. The proposed research will focus on the mechanics of abrasive waterjet impact on machined ceramic materials.

CHAPTER 4

MACHINEABILITY OF BRITTLE MATERIALS

4.1 INTRODUCTION

Ceramic materials have the potential to offer superior performance when compared to base ceramics and metals. Continuous fiber-reinforced ceramic composite (CFCC) materials offer not only high strength-to-weight and stiffness-to-weight ratios, but also possess increased "toughness," and are therefore better than their monolithic counterpart. In addition, they also have the extremely good high-temperature properties of monolithic advanced ceramics. These materials are envisaged to be competitive for an impressive array of industrial applications, ranging from piping and chemical reactors to combusters and tubes in heat-recovery systems[103,104,105]. Widespread industrial use of these advanced ceramics has required the development of secondary processing, such as net-trimming or edge finishing, to meet such engineering specifications as tight tolerances, as well as production of hole for fasteners which are necessary to facilitate assembly [103,104,105,106].

In order to expand the possible applications of these materials, machining methods must be developed to allow for successful fabrication of components. However, conventional methods of machining often induce critical flaws to the component parts when employed for finish operations, owing to the non-homogeneity and anisotropy of composites[107 108 109 110]. They are also not very efficient in stock material removal due to the extremely long machining times required. Of the various methods of unconventional technology, abrasive waterjet cutting appears to be the most suitable, based on its ability to produce reasonable quality surfaces at high production rates. For these reasons, the

AWJ is currently being investigated for industrial composite trimming applications[111 112 113]. Since high-temperature composites in general, and CFCCs in particular, are relatively new material systems, their machineability has not been studied, except in recent work by Gonczy, et al [114], and in the preliminary work by Ramulu, et al[94].

In this chapter, the machining characteristics of ceramic and CFCC composite material by an abrasive waterjet are reported. Machining results of the application of abrasive waterjet to slot cutting of ceramic and composite materials are evaluated. Optical and scanning electron microscopes were used to determine if abrasive waterjet machining caused distinguishable surface features or microcracks in the composites. The surface roughness of the machined surface was determined as a function of machining conditions.

4.2 AWJ MACHINING SYSTEM

The abrasive waterjet machining system in the Abrasive Waterjet Machining Laboratory at the University of Washington, as shown in Figure 4.1, is a POWERJET 20-35 abrasive waterjet system. It has been used extensively in this research. The abrasive waterjet system consists of a waterjet pump connected to an AWJ nozzle, a commercial milling table, and an abrasive delivery system. The pump is a 15 KW single intensifier waterjet pump, capable of delivering water at pressure up to 241 MPa.

The first stage of the pump is a 20 horsepower motor, driving a hydraulic pump that outputs high pressure hydraulic oil. The high pressure oil then pushes an intensifier pump (see Figure 3.5). Thus output water can be pressurized to as high as 241 MPa. The maximum water flow rate is approximately 25 liter per minute. Inside the AWJ nozzle there is a waterjet orifice of size 0.30 mm in diameter and a tungsten carbide focusing tube of size 0.812 mm. The abrasive waterjet nozzle, illustrated in Figure 4.2, incorporates a unique design feature that adjusts the position of the tungsten carbide abrasive waterjet insert. The adjustment allows for fine tuning of the abrasive waterjet,

insuring that the resulting waterjet at the nozzle exit is collimated. This fine tuning allows for optimal performance of the abrasive waterjet. The abrasive delivery system is a simple gravity-fed hopper. The abrasive flow rate is controlled by varying the size of an orifice located on the supply valve of the abrasive delivery system.

The abrasive waterjet system was used in conjunction with a modified milling machine to provide the necessary motion required for slot cutting. The abrasive waterjet milling table provides two-dimensional cutting capacity through the use of a manually operated translational table. The AWJ nozzle remains in a fixed position and a tube type jet catcher is employed. However, since a manual feed table can not provide the necessary accuracy and repeatability required for the slot cutting experiments, a milling machine was modified for this task.

Since the translational table was the only necessary component of the milling machine, the conventional milling head and power supply were removed. A DC motor and motor controller were then installed to provide the necessary power to move the table. A cutting table suitable for the AWJ process was designed and built such that it could be directly attached to the milling table. For abrasive waterjet machining, this table required a drain hole and high side wall to contain the excess abrasive and water. Finally, simple clamp type fixtures were designed and built to rigidly hold the workpiece material in place, allowing for both piercing and slot cutting.

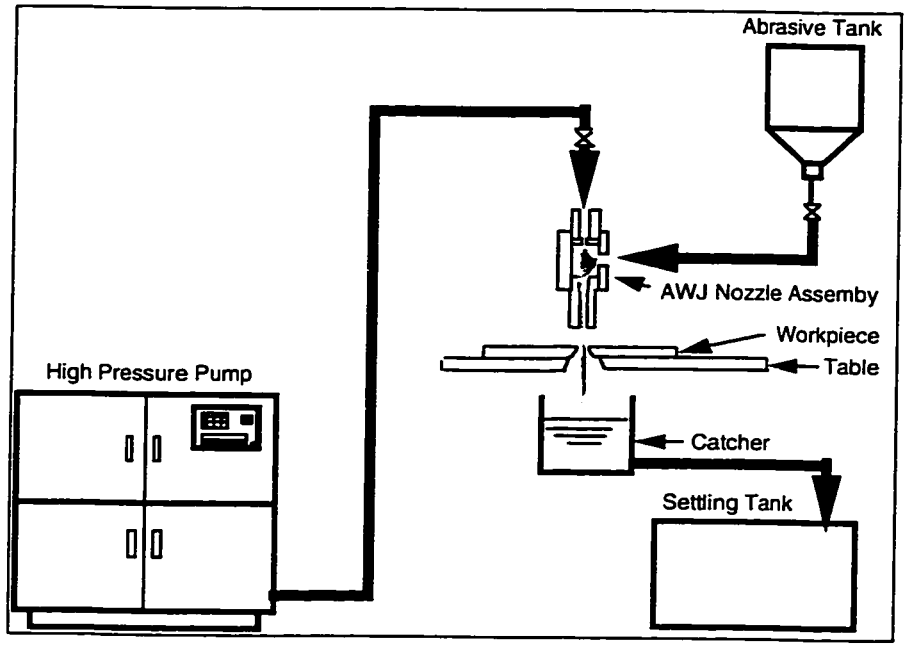

Fig. 4.1 Schematic Diagram of an Abrasive Water Jet System

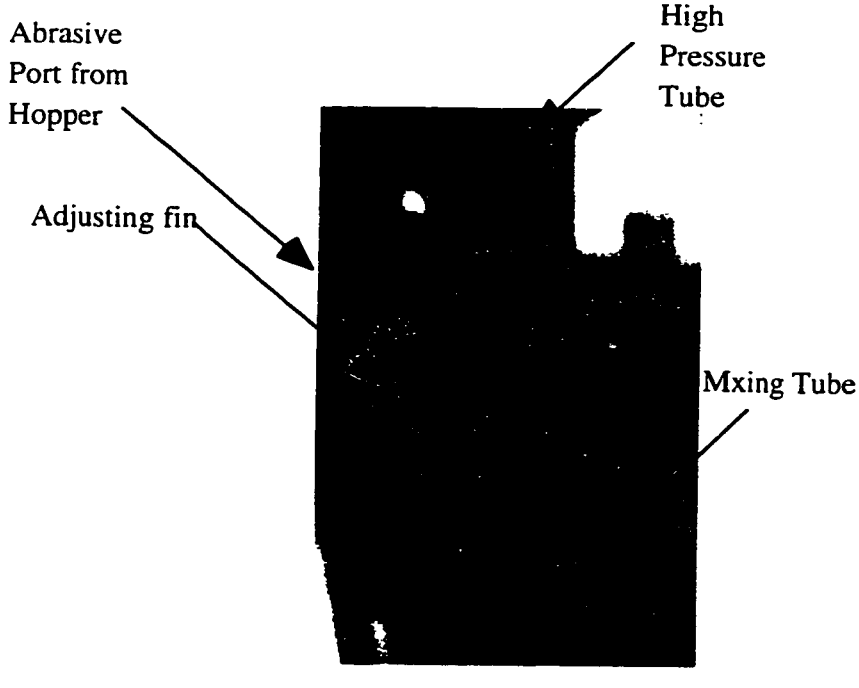

Fig. 4.2 AWJ Nozzle Assembly

4.3 TEST SPECIMEN MATERIALS

Ceramic materials machined in this study were an alumina (Al_2O_3), a titanium diboride (TiB_2), a silicon carbide (SiC), and a silicon nitride (Si_3N_4). Since advanced ceramics possess high stiffness and strength they can be used as structural materials[115]. All these materials were commercially acquired in plate form with a thickness of 6.35 mm. The material properties are listed in Table 1.1.

The CFCC specimen used was in a plate form of dimensions 200 x 10 x 3.7 mm. The reinforcing fiber was a ceramic grade (Nicalon™) Si-C-O fiber produced by pyrolysis of a spun polymer-derived ceramic precursor. A two-dimensional reinforced, plain woven cloth was fabricated using ~1800 denier fiber bundles (~500 fibers/bundle) by the fiber producer. The fiber was fabricated by layering twelve plies of cloth, with the warp of the fibers aligned in the longitudinal direction. The interphase (i.e. material at the fiber/matrix interface used to promote fiber debonding and pullout) was produced by depositing a ~0.3 mm interfacial layer of pyrolytic carbon through chemical vapor infiltration onto the fiber. The material was formed by decomposition of methyltrichlorosilane and the infiltration of the preforms by CVI until all the surface micro-porosity was filled. The matrix was thus in the form of a crystalline β-SiC [116,117]. The thickness of all the cutting and piercing specimens was about 3.7 mm. Garnet abrasive of different mesh sizes (#50, #80 and #150) was chosen for economy, longer nozzle life, and its proven performance with regard to metal cutting[55,118]. The properties of the typical abrasives are reported in Table 4.1

Table 4.1 Properties of Abrasives used in the AWJ Machining[119]

Abrasive Material	Mesh No.	Average size (micron)	Specific Gravity	Knoop Hardness
Garnet	#50	350	3.4 to 4.3	1350
Garnet	#80	180	3.4 to 4.3	1350
Garnet	#100	130	3.4 to 4.3	1350
Garnet	#150	100	3.4 to 4.3	1350

4.4 EXPERIMENTAL PROCEDURE

4.4.1 Machining Tests

Two different abrasive waterjet machining operations were undertaken in the present study: piercing and slot cutting. Since both abrasive waterjet piercing and slot cutting are dependent on several process parameters, it was important to carefully choose and systematically vary the parameters of interest. For the slot-cutting experiments in ceramics, AWJ pressure, stand-off distance, abrasive flow rate, and cutting speed were varied and detailed in Table 4.2. The slot-cutting experiments were conducted to study the machineability. Table 4.3 lists the AWJ conditions used for drillings tests and the machining forces that were recorded during these drilling experiments.

Table 4.2 Abrasive Waterjet Cutting Conditions

Parameters	Ranges
Work Materials	Al_2O_3, TiB_2, SiC, Si_3N_4, TiB_2/SiC
Supply Pressure (MPa)	85, 140, 190, 210, 225
Abrasive Flow Rate (g/s)	4.5, 7, 17
Traverse Speed	50, 100, 150, 200, 250, 300
Standoff Distance (mm)	1, 2, 3
Abrasive Grain Size (#)	50, 80, 150
Passes	1, 2, 3, 4, 5, 6, 7, 8, 9, 10
Abrasive Type	garnet

Table 4.3. Test Matrix for AWJ Drilling

Material	Supply Pressure (MPa)	Standoff Distance (mm)	Abrasive Grain Size (#)	Abrasive Type
Al2O3	138	2	80	Garnet
TiB2	180			
SiC	208			
Si3N4				

Test matrix and test parameters of WJ/AWJ cutting of CFCC materials are in Table 4.4. All specimens were machined over a length of 25 mm or more to ensure a constant cutting condition. CFCC materials were also machined with a diamond-grit saw to compare the surface finishes produced by AWJ and diamond-grit saw cutting. A commercial slot machine configured with computerized motion control was used for sawing the CFCCs. A 102 mm-diameter saw blade of width 0.254 mm and #100 diamond grit was used for all slotting. The slotting parameters include a traverse speed of 3.15 m/min, a feed index of 76.2 μm for each pass. The spindle speed was 6000 rpm. After each slot was completed, the diamond wheel was dressed to the aforementioned parameters.

Table 4.4 AWJ Experimental Cutting Test Matrix (CFCC)

Specimen No.	Pressure, MPa	Abrasive Flow Rate, g/s
12	240	12
9	210	12
6	172	12
1	127	12
3	82	12
13	240	7
10	210	7
7	172	7
2	127	7
4	82	7
11	240	16
8	210	16
5	172	16

Note: Abrasive waterjet cutting conditions:
Stand-off distance10 mm;
traverse rate 200 mm/min;
garnet abrasive mesh #100

The actual abrasive waterjet machining was performed by first mounting the appropriate specimen in the fixture attached to the abrasive waterjet cutting table. The specimen was then properly positioned for either AWJ slot cutting or piercing. The pump was started and the abrasive delivery hose was connected to the abrasive waterjet nozzle. The on/off valve was opened, and for slot cutting, the translational table was placed to motion. The part was then machined. Cutting experiments were conducted with varying water pressures, grit sizes, traverse speeds, and standoff distances.

4.4.2 Surface Characteristics

The drilled ceramic specimens were further studied using the Scanning Electron Microscopy (SEM) for evaluating the surface topography and material removal mechanisms. An optical microscope was used to determine the degree of taper for both the slot cuts and pierced holes. A schematic representation of the cutting state is presented in Figure 4.3, with a sectioned view showing the tapered kerfs. The degree of taper is reported as a ratio between the upper surface kerf (W_{top}) and the lower surface kerf (W_{bottom}). The surface damage after machining was evaluated qualitatively by an optical and scanning electron microscope. A stylus surface profilometer was employed to measure the surface finish of the machined surface. The depth of cut was measured with a stylus of fine point in conjunction with a digital height gage. The surface roughness for AWJ cut and diamond-grit saw machined specimens was measured using a commercial diamond stylus profilometer. This system is capable of producing an absolute profile of a surface, as well as evaluating the associated parameters. The surface roughness parameters were evaluated according to Surface Texture, Surface Roughness, Waviness and Lay (ANSI B46.1-1978)[120]. A commercial SEM and optical microscopy were used to study the microstructural integrity of the machined specimens.

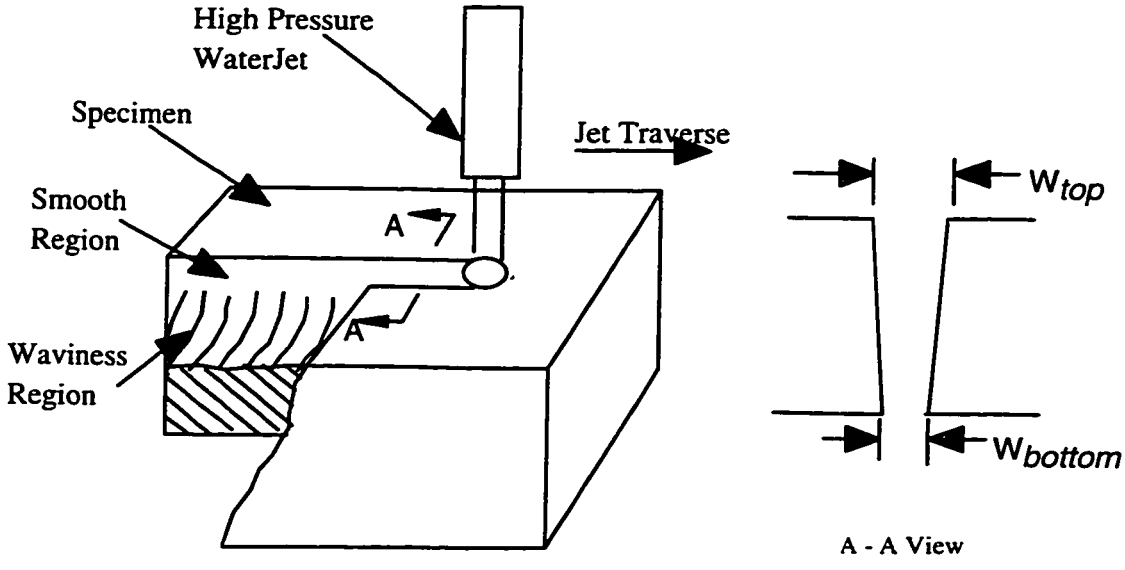

Figure 4.3 Schematic of the AWJ Cutting State

4.4.3 Machining Force Measurement System

The machining force measurement system is shown schematically in Figure 4.4. It consists of a dynamometer, a signal conditioner, a multimeter, an A/D converter, and an IBM computer to record the cutting forces. The specimen was fixed to the top of the dynamometer fixture, which was connected to a computer data acquisition system.

During abrasive waterjet machining, the waterjet impinging force on the material was transferred to the dynamometer and registered by the computer. The machining forces that were exerted on the material under different drilling conditions were measured and recorded. The typical duration of the forces recorded was 3 or 5 seconds, and the sampling frequency for the dynamic force was 200 Hz. Each specimen was drilled with both waterjet and abrasive waterjet. The drilled specimens were further studied using the SEM for evaluating the surface topography and material removal mechanisms.

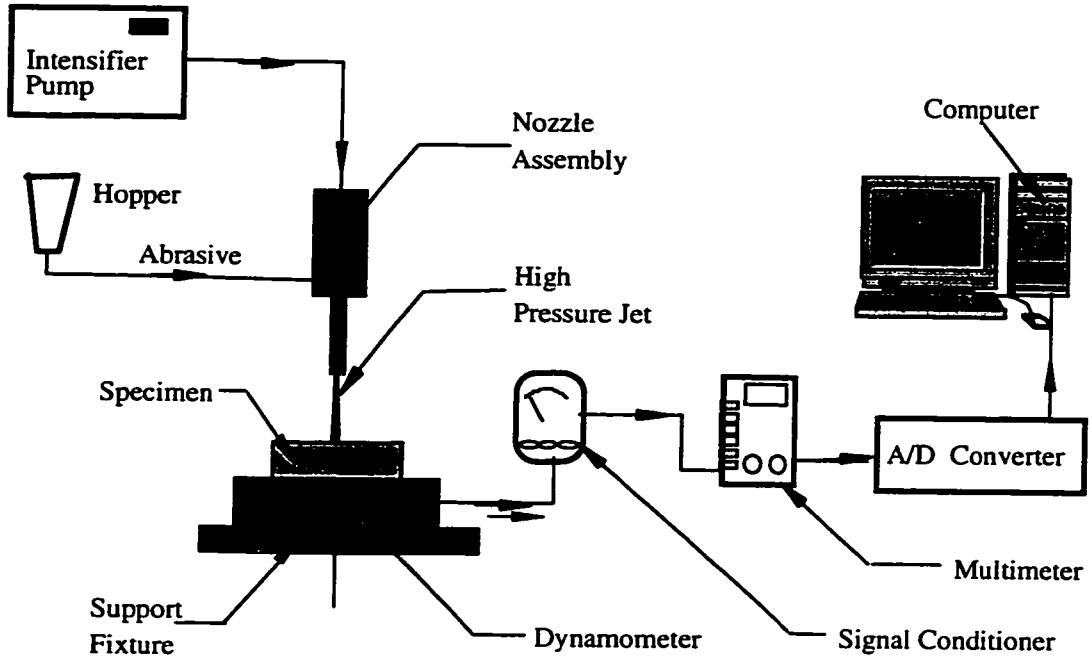

Figure 4.4 Schematic of machining force measurement data acquisition system

4.5 MACHINEABILITY RESULTS FOR CERAMICS

4.5.1 Depth of Cut vs. Mesh Size

Garnet abrasives, including three mesh sizes, were used for machining Si_3N_4 in this experiment. The abrasive mesh numbers were #80, #100, and #150. Figure 4.5 is a typical graph of the test results, depicting the relationship between the depth of cut and the grain sizes of the abrasives used. The supply pressure in this test was 220 MPa, and abrasive flow rate was 17g/s. The workpiece traverse speed was 20 mm/min. It appears that the depth of cut is not linearly related to the mesh sizes of the abrasives. The larger

grain size removes more materials and vise versa. Apparently in a high pressure and high speed waterjet flow, abrasives with large mass carry more kinetic energy needed for the machining process. Thus, increasing the size of abrasives also increases the capability of material removal. If the grain size is too large, fewer particles may be able to get into the main jet flow in a unit time, thus the material removal rate decreases. If the grain size is too small, the kinetic energy that each particle carries is also limited, even though more particles may be laden in the jet stream for impingement.

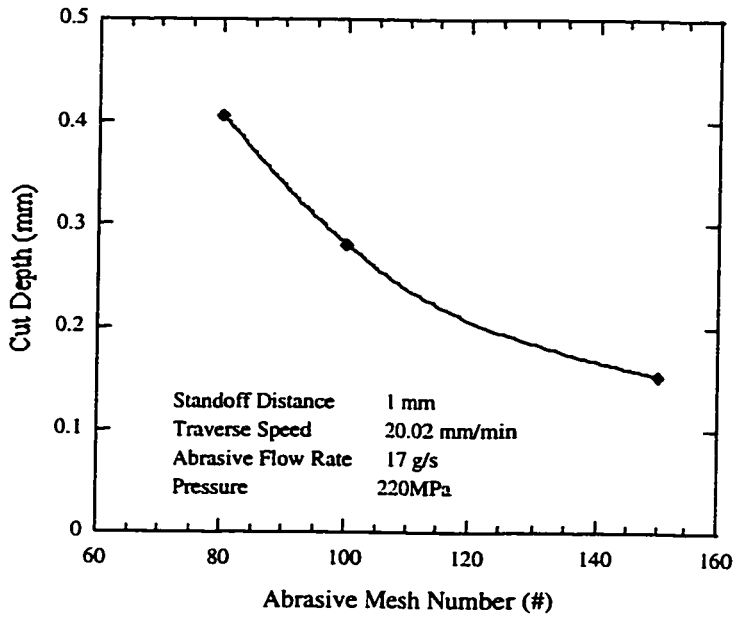

Figure 4.5 The effect of abrasive mesh size on the depth of cut (Si_3N_4)

4.5.2 Depth of Cut vs. Abrasive Flow Rate

Abrasive flow rate is one of the most important parameters determining the material removal rate. Figure 4.6 shows the depth of cut as a function of abrasive flow rate for TiB_2. The supply pressure and the traverse speed were 166 MPa and 75 mm/min, respectively. The standoff distance was 2 mm and the abrasive was #80 garnet. The material removal rate increases as the abrasive flow rate increases. The more that the abrasives are entrained in the waterjet, the more kinetic energy is stored in the jet flow. Thus, more materials can be machined by the more energized waterjet. At low abrasive flow rates, the material removal rate should be minimal. However, a change in the abrasive flow rate in the range of 0 to 6 g/s resulted in insignificant changes in the material machined. When an abrasive flow rate was increased to 8.5 g/s, the depth of cut increased by 3%. For an abrasive flow rate of 13 g/s the depth of cut was 0.97 mm, a change of 15%. This suggests the existence of a critical abrasive flow rate that varies with the workpiece material.

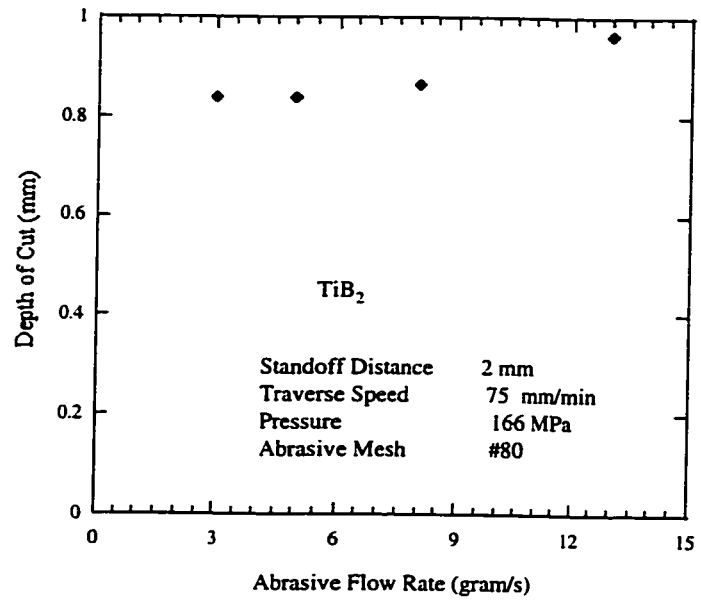

Figure 4.6 Depth of cut and Abrasive Flow Rate for TiB_2

4.5.3 Traverse Speed

Contrary to the effect of abrasive flow rate on the material removal rate, an increase of the traverse speed reduces the material removal rate, and vise versa. The results indicate that higher traverse speed yields a smaller depth of cut, and vise versa. However, the depth of cut is not inversely proportional to the traverse speed. At the lower end of the traverse speed, an incremental change in speed produces a deeper cut than the same increment produces at the high end of the traverse speed. Shown in Figure 4.7 (a) is a typical abrasive waterjet machining result for Al_2O_3 at flow rates of 3 g/s, 4 g/s and 8 g/s, and supply pressure of 138 MPa. As the traverse speed increases beyond 70 mm/min, the depth of cut reaches its minimum. With further increases beyond this traverse speed, or the critical traverse speed, the depth of cut does not produce much change. Similarly, for Si_3N_4 the depth of cut decreases as the traverse speed increases, as is shown in Figure 4.7 (b), at the supply pressure of 224 MPa and abrasive flow rate of 17g/s. The critical traverse speed is about 70 mm/min for these cutting conditions and is a function of the abrasive waterjet cutting parameters, such as workpiece materials, supply pressure, abrasive flow rate, etc. The test results also suggest that increasing the abrasive flow rate, while at traverse speeds less than the critical traverse speed, is the most effective way to increase the material removal rate. The same phenomenon is shown for SiC in Figure 4.7 (c) with a supply pressure of 224 MPa. At high traverse speeds, varying the abrasive flow rate did not produce significant increases or decreases in depth of cut. It is noted that this applies to the cutting experiment conducted for the three flow rates used: 7 g/s, 4.5 g/s, and 17 g/s.

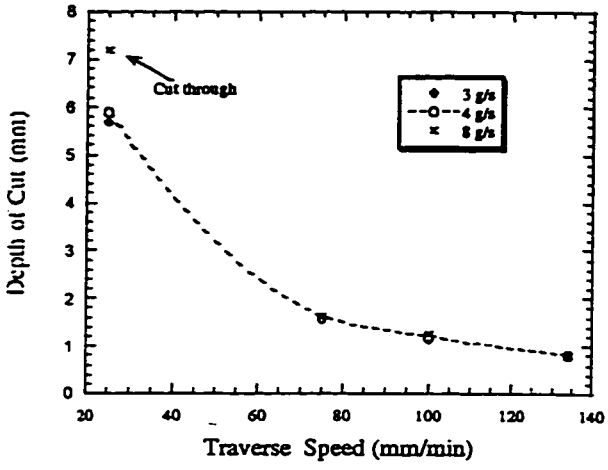

(a) Al_2O_3, supply pressure 138 MPa;

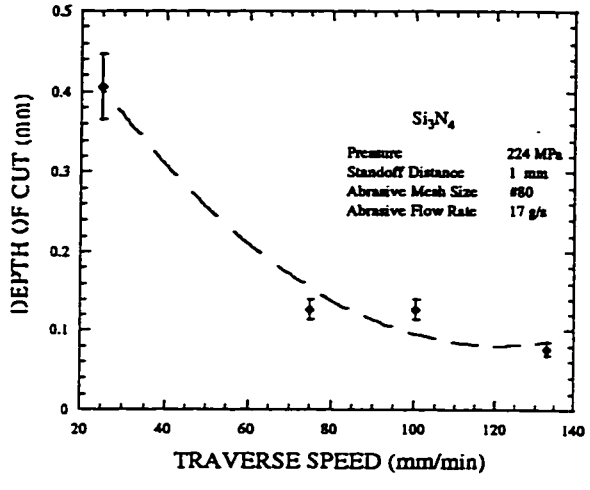

(b) Si_3N_4, supply pressure 224 MPa

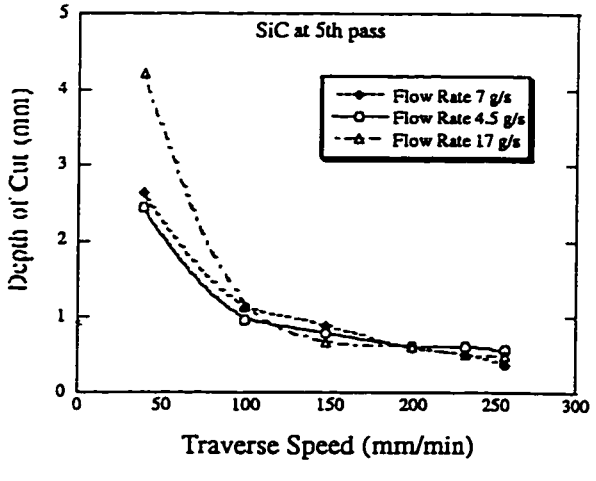

(c) SiC, supply pressure 224 MPa

Figure 4.7 Depth of cut vs. traverse speed

4.5.4 Depth of Cut vs. Supply Pressure

Supply pressure is the most important parameter in determining the material removal rate. Figures 4.8(a) and (b) depict the depth of cut as a function of the supply pressure for Al_2O_3 and Si_3N_4, respectively. Higher supply pressure produces deeper cuts, and vise versa. This material removal rate is predicted by Evans and Hockey's [83] analytical model, in which the material removal rate is proportional to the particle speed to the power of 2.5. This is because the kinetic energy needed for the abrasive waterjet machining process is determined by the waterjet velocity, which in turn is dependent on the supply pressure. Thus, higher supply pressure produces much greater depth of cut. Further, material removal occurs more effectively at higher waterjet pressure due to the nonlinear relation between the depth of cut and the supply pressure. It appears that a threshold cutting pressure exists for each material under certain conditions, such as traverse speed, abrasive flow rate, etc. If the supply pressure is less than the threshold pressure, the material removal rate will be minimal. This result agrees with the findings in Hashishi' work[43]. The threshold pressure can be determined by expending the curve in the figure until it intersects the pressure axis. In addition to the material properties themselves, other abrasive waterjet machining parameters also determine the threshold pressure, such as abrasive flow rate, traverse speed, etc. In the present experimental works, the threshold pressure for Al_2O_3 is about 90 MPa for traverse speed of 133 mm/min, abrasive flow rate of 3 g/s, standoff distance of 2 mm, and with #80 mesh size for the abrasive garnet. Similarly, the threshold pressure for Si_3N_4 is about 105 MPa for standoff distance of 1 mm, abrasive flow rate of 17 g/s, traverse speed of 25 mm/min, and with #80 mesh size for garnet. It is noted from these graphs that the relationship between the depth of cut and the pressure is approximately linear in the range of the experimental supply pressure.

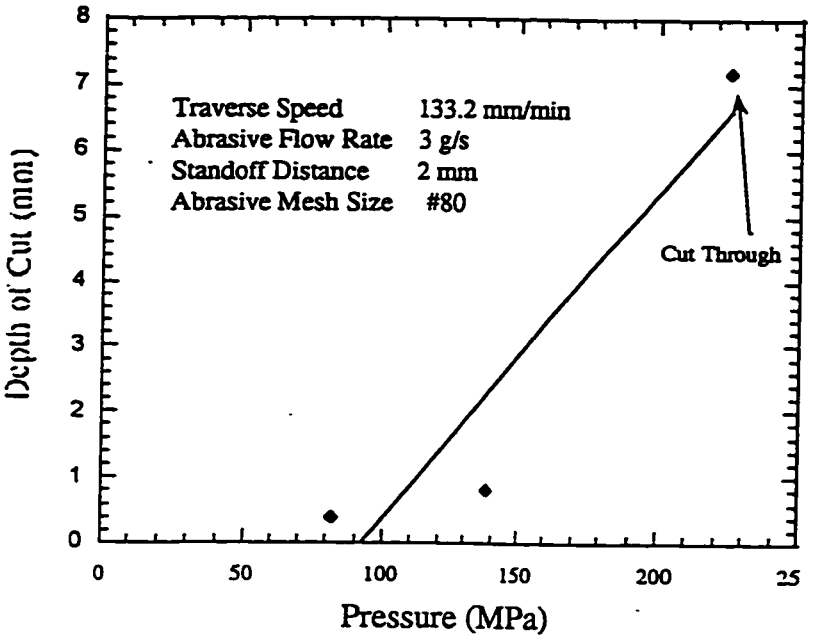

(a) Al_2O_3

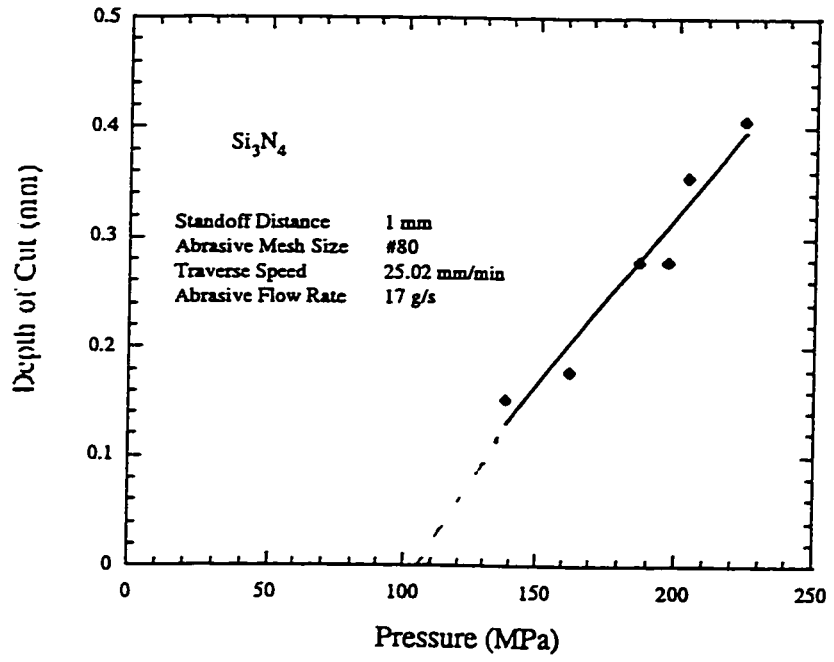

(b) Si_3N_4

Figure 4.8 Depth of cut vs. supply pressure

4.5.5 Depth of Cut vs. AWJ Machining Passes

For thick workpieces it may take several abrasive waterjet cutting passes to machine through the whole thickness of a specimen. At each cutting pass, the abrasive waterjet removes some material, and produces a deeper kerf. Figures 4.9 (a-c) show the depth of cut as a function of the cutting passes for SiC at abrasive flow rate of 4.5 g/s, 7 g/s, and 17 g/s, respectively. The initial standoff distance was 2 mm and the supply pressure was 224 MPa. The traverse speed of the workpiece was varied to further study the effect of the traverse speed on the material removal rate. The materials were cut using traverse speeds of 38, 99,147, 198,231, and 255 mm/min. It was observed that the depth of cut was almost linearly proportional to the cutting passes at any parameter setting, even though the change was not very obvious due to the relatively small cutting depths. It was also observed that at low traverse speeds, the cut depth was much greater than those at higher speeds. The linearity between the number of passes and the depth of cut was also exhibited in TiB_2 material, as shown in Figures 4.9 (d-f). From Figures 4.9 (a)-(f), note that the material removal rate decreases as the traverse speed increases.

4.5.6 Kerf Width vs. Traverse Speed

The kerf width is defined as the width of a kerf at the abrasive waterjet cut entry. The cut kerf is typically tapered with a wider entrance on the top and a smaller exit on the bottom. Figure 4.10 is a comparison of the kerf width as a function of the traverse speed for TiB_2 materials at an abrasive flow rate of 17 g/s and supply pressure of 165 MPa. It is obvious that the traverse speed influenced the kerf width, and the width of kerf is inversely proportional to the traverse speed. This observation agrees with Hochang's[26] experimental result. When the traverse speed was lower, the kerf width was wider. When the traverse speed was higher, the kerf width became narrower. For example, at

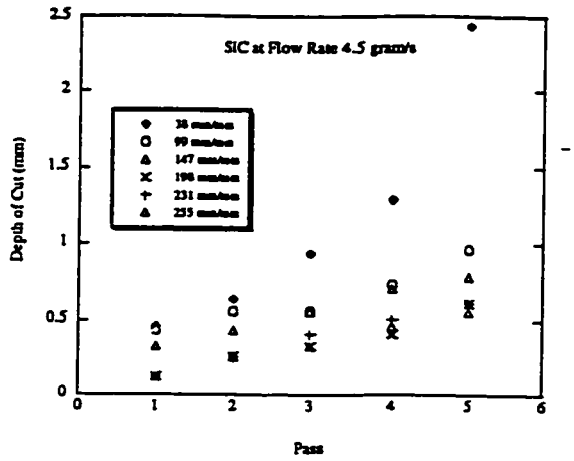

(a) SiC, afr=4.5 gram/s

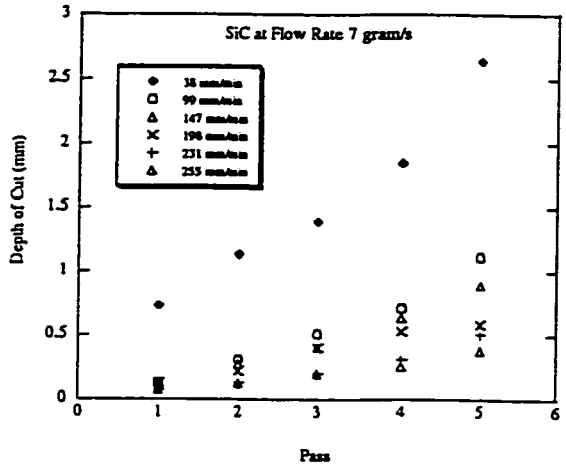

(b) SiC, afr=7.0 gram/s

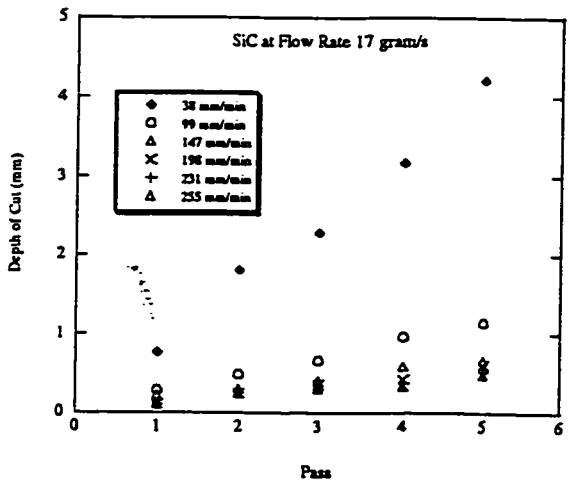

(c) SiC, afr=17 gram/s

Figure 4.9 (a,b,c) Depth of cut vs. cutting passes for SiC

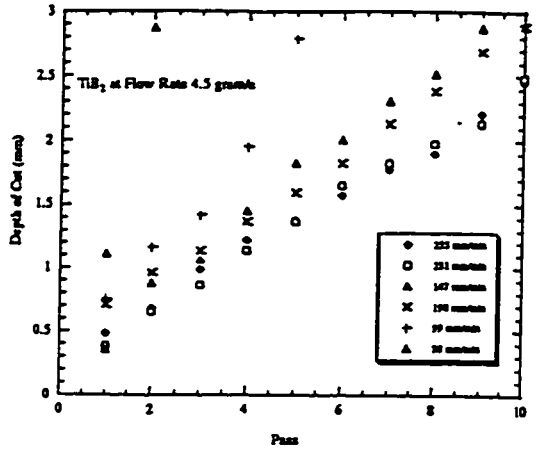

(d) TiB_2, afr=4.5, 7, 17 gram/s

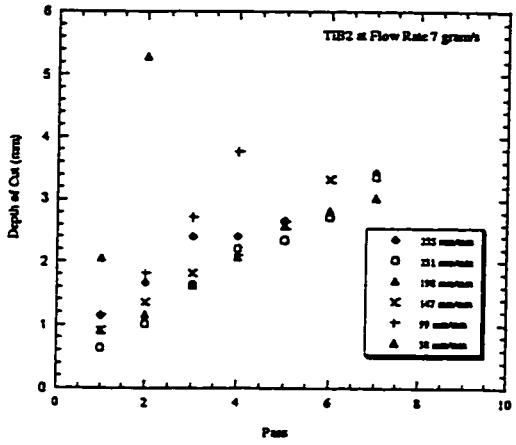

(e) TiB_2 afr=7 gram/s

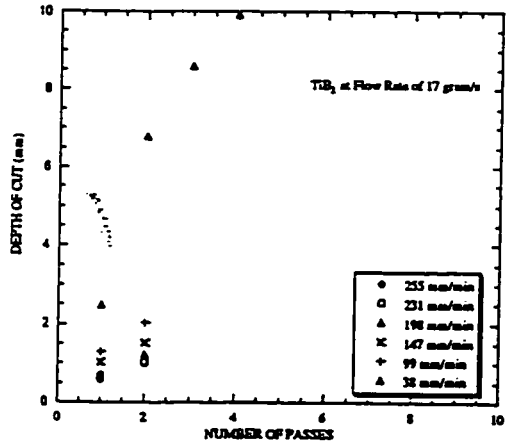

(f) TiB_2 AFR= 17 gram/s

Figure 4.9(d,e,f) Depth of cut vs. cutting passes for TiB_2

increased to over 150 mm/min the kerf width was reduced to 1.6 mm. When the supply pressure and abrasive flow rate are the same, lower traverse speed allows more abrasive particles to bombard the workpiece in a unit time. Thus, more material was removed through erosion by the abrasive waterjet, and a wider kerf was generated. On the other hand, when the traverse speed increased, the kerf width became smaller, because fewer particles were involved in the material erosion within a unit time. Similarly, the kerf width was also related to the supply pressure and the abrasive flow rate of the abrasive waterjet. Higher supply pressure and the abrasive flow rate produced wider kerfs, and vice versa.

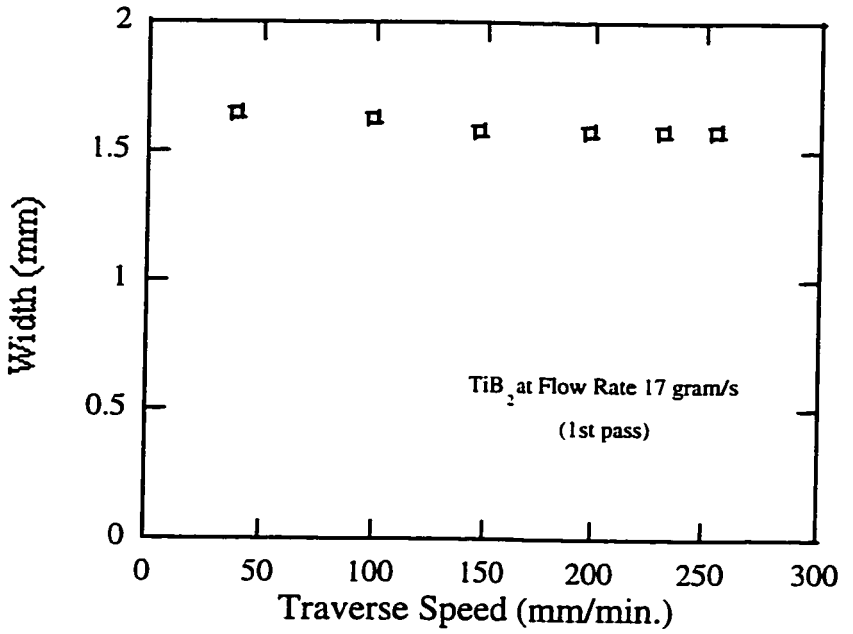

Figure 4.10 Comparison of kerf width vs. traverse speed for TiB_2

4.5.7 Depth of Cut vs. Workpiece Materials

In this study, several types of ceramic materials were cut by abrasive waterjet. The material removal rate was compared among these ceramic materials under the same abrasive waterjet machining conditions. Figure 4.11 (a) compares the depth of cut for TiB_2 , TiB_2/SiC, and SiC with abrasive flow rate of 13 g/s. At slow traverse speeds (~50 mm/min) the differences in material machined by the abrasive waterjet were much greater. The TiB_2 material had the most material removed, and SiC the least. It appears that there is a correlation between the depth of cut and the hardness of the workpiece material. The harder the workpiece material, the less the material removal rate, since it becomes increasingly difficult to machine the harder materials with waterjet. Figures 4.11 (b) and (c) show more experimental data comparing the depth of cut in Al_2O_3, TiB_2, SiC, and Si_3N_4 as a function of supply pressures under both pure waterjet and abrasive waterjet. In pure waterjet piercing of Al_2O_3 most of the material was removed. For TiB_2 only half as much material as for Al_2O_3 material was removed. In SiC and Si_3N_4 the removed material by pure waterjet was unnoticeable because the supply pressure was below their threshold pressures.

In abrasive waterjet machining, the abrasives used in the abrasive waterjet piercing were #80 garnet. The amount of material removed by AWJ is in the order, from the most to the least, Al_2O_3, TiB_2, SiC, and Si_3N_4. This is also the order for the hardness of the test materials. Thus, the hardness of the workpiece material played a very important role in determining the material removal rate. The hardness was inversely proportional to the material removed.

Experimental data from this parametric study indicated that the effect of varying the standoff distance in the range of 1 mm to 3 mm does not seem to be very significant on the material removal rate. A temperature rise in the cutting region was observed. This

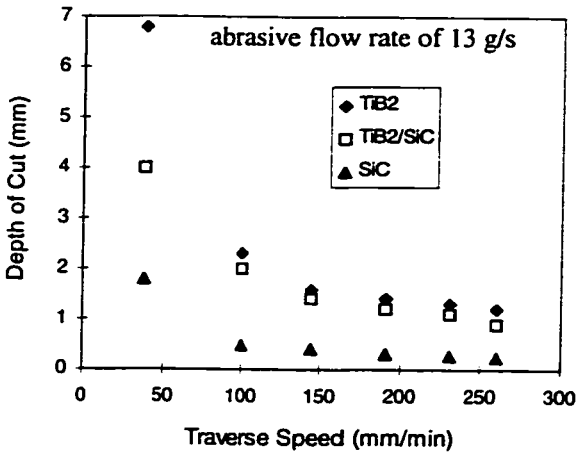

(a) Depth of cut for TiB_2 , TiB_2/SiC and SiC vs. traverse rate

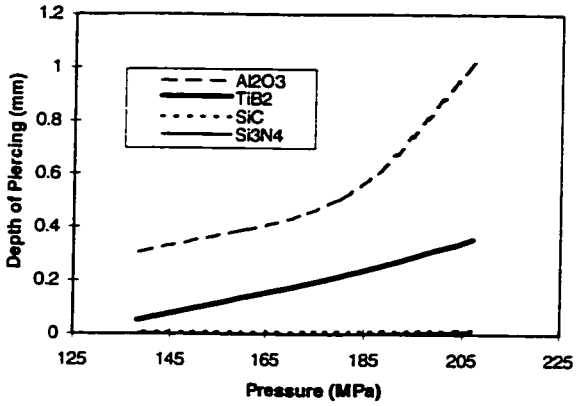

(b) Pure waterjet for Al_2O_3, TiB_2, SiC and Si_3N

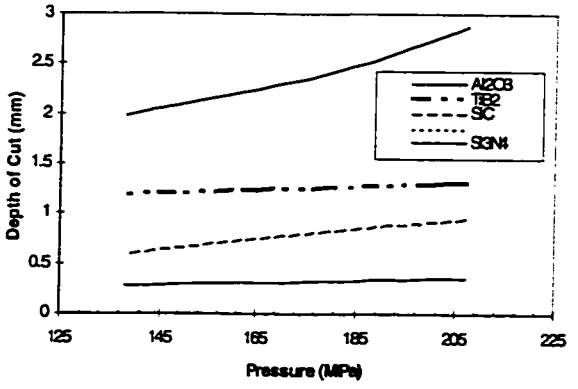

(c) abrasive waterjet for Al_2O_3, TiB_2, SiC and Si_3N

Figure 4.11 Correlation between the depth of cut and supply pressures

temperature rise was much smaller than that measured in traditional machining. This agrees with the experimental finding by Arola and Ramulu[48].

4.6 WJ AND AWJ MACHINING FORCES ON CERAMICS

4.6.1 WJ/AWJ Impact Forces Analysis

The forces exerted on the workpiece specimens by pure waterjet and abrasive waterjet during piercing were measured. In addition to the ceramic materials tested, non-ceramic materials were also tested, and the machining forces were recorded. These non-ceramic materials included polycarbonate, steel, and aluminum. All these materials were in plate form with a thickness of 6.25 mm. The recorded machining forces are graphed in two groups. The first group includes four ceramic materials, Al_2O_3, TiB_2, SiC, and Si_3N_4, for pure waterjet and AWJ. Figures 4.12(a) is a typical impacting force recorded for Al_2O_3 by both waterjet and abrasive waterjet under pressures of 138 MPa, 180 MPa, and 207 MPa. Figures 4.12(b)-(d) are the force measurement results for TiB_2, SiC, and Si_3N_4, respectively. The measured forces are presented in Figures 4.12(e)-(g) for polycarbonate, steel, and aluminum (*Al*). The average jet exposure time for each piercing run at each pressure for all the materials tested was 4 to 5 seconds.

The machining forces for different material, but under a certain supply pressure, are compared. Figures 4.13(a)-(f) are the machining forces of ceramic materials for supply pressure of 138 MPa, 180 MPa, and 207 MPa, respectively . The second group compares the three non-ceramic materials and two ceramics, Si_3N_4, and Al_2O_3. Figures 4.13(g) - (*l*) are for supply pressure of 138 MPa, 180 MPa, and 207 MPa, respectively. The average machining forces for all these materials are collected in Table 4.5.

Figures 4.12 (a)-(g) show that the impacting forces varied with the supply pressure. Higher supply pressures generated higher machining forces. Lower pressures had lower machining forces.

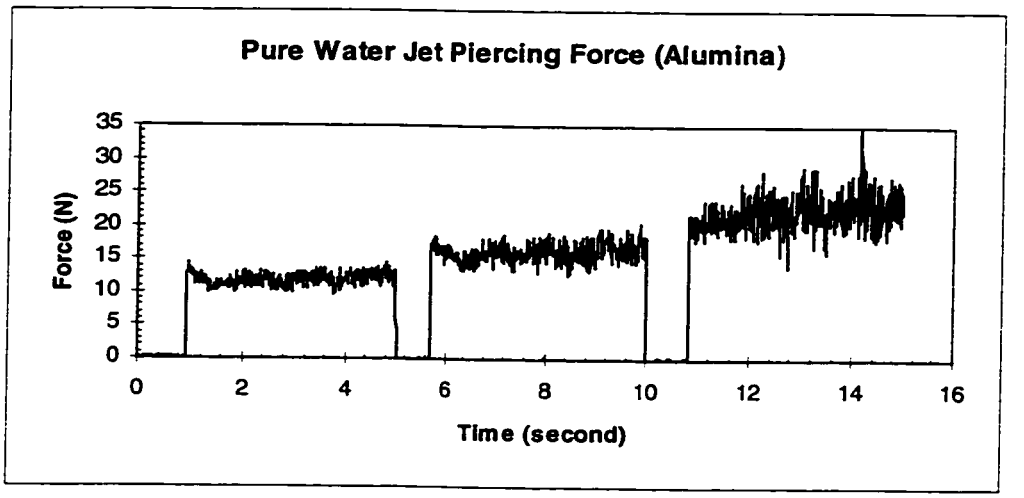

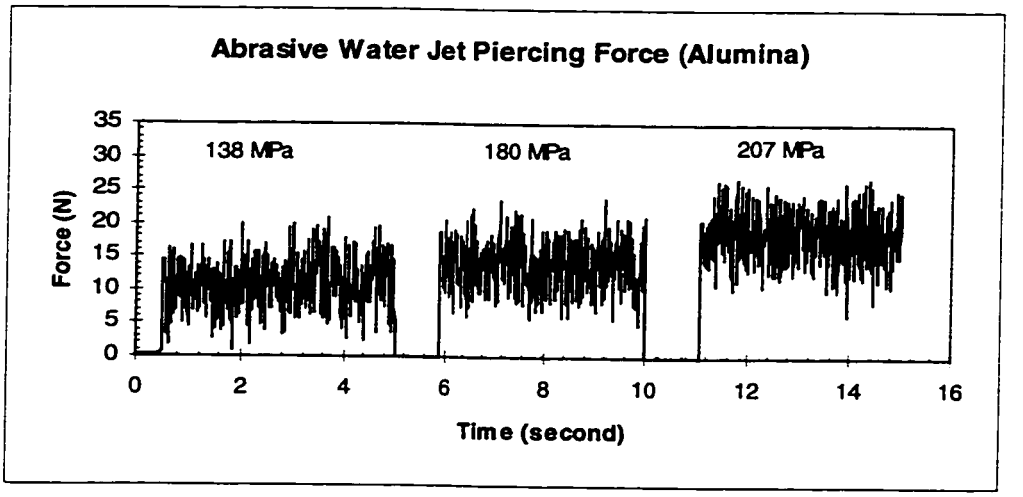

Figure 4.12 (a) WJ/AWJ Impact Forces of Various Supply Pressure on Alumina

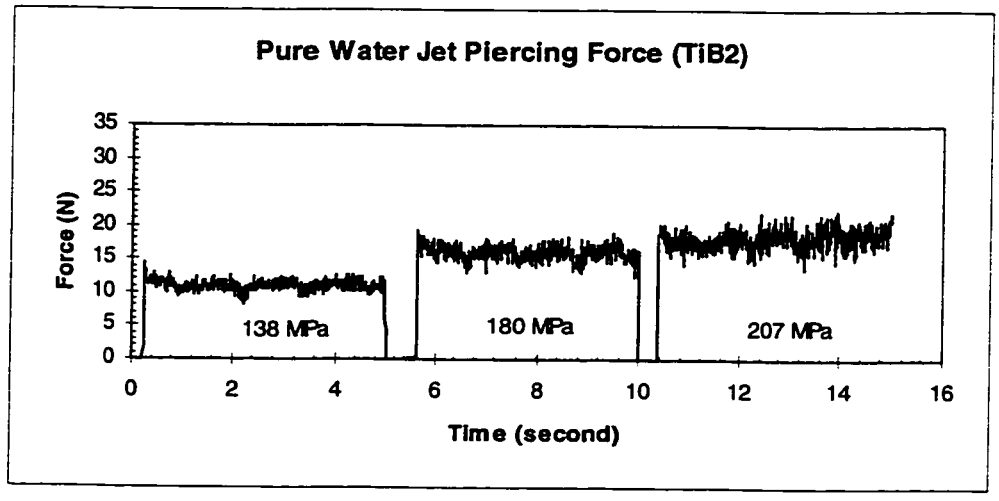

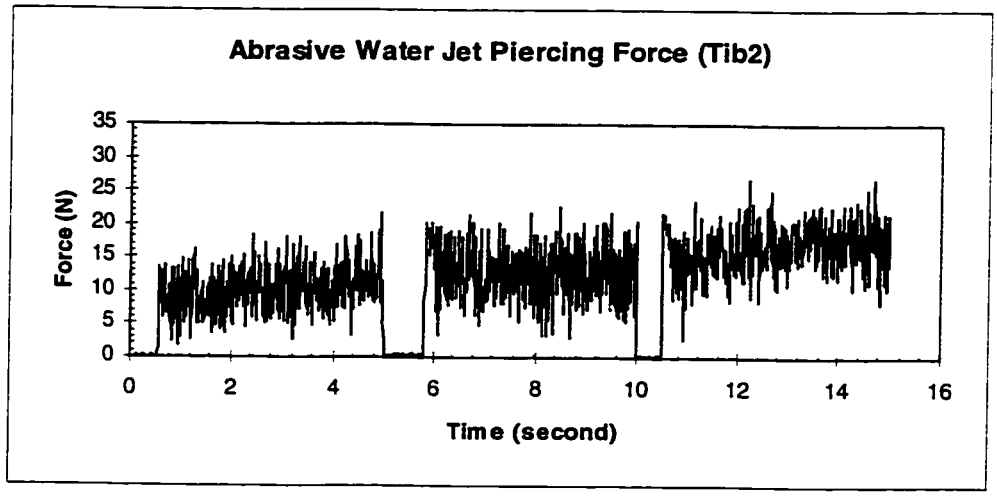

Figure 4.12 (b) WJ/AWJ Impact Forces of Various Supply Pressure on Titanium Diboride

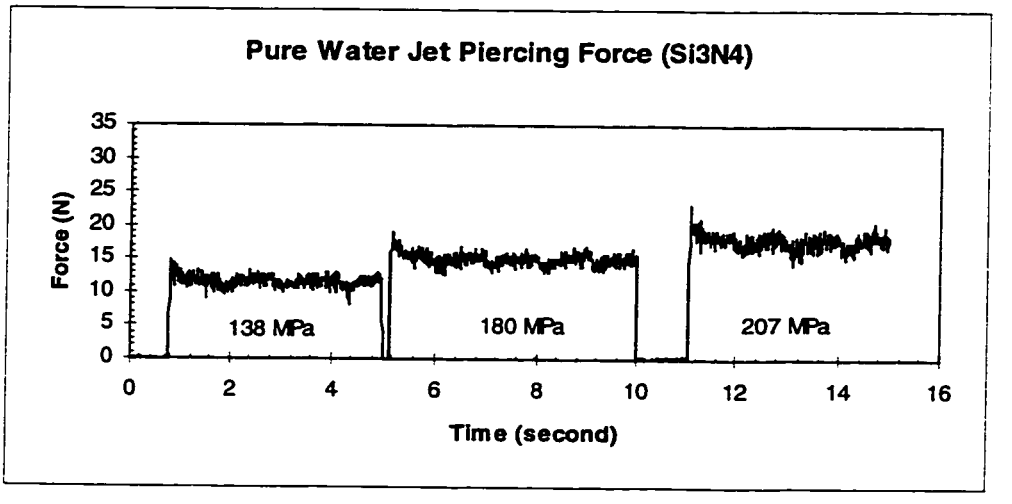

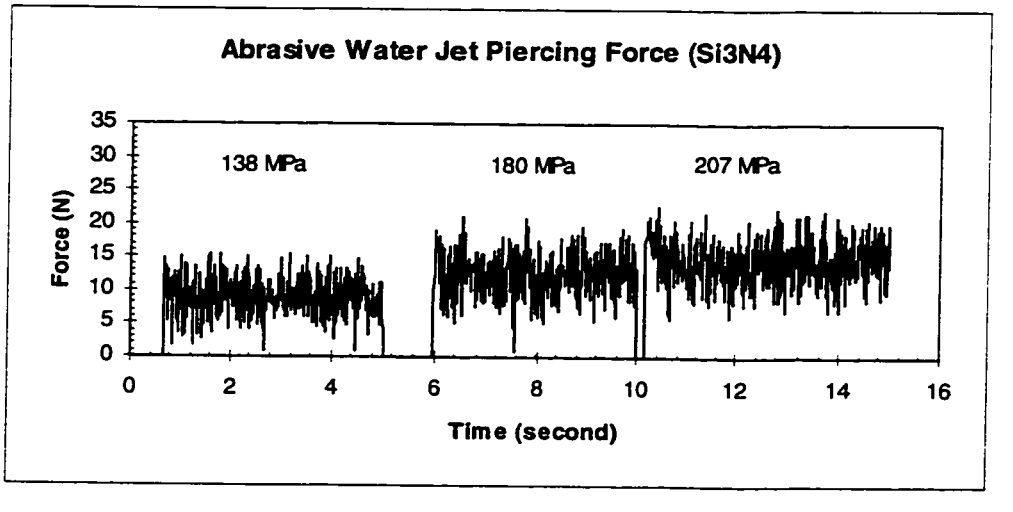

Figure 4.12 (c) WJ/AWJ Impact Forces of Various Supply Pressure on Silicon Nitride

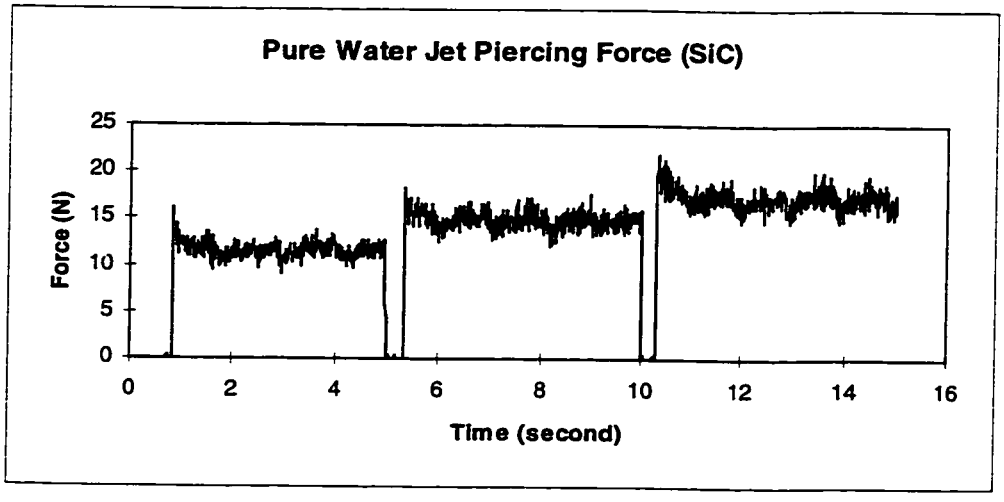

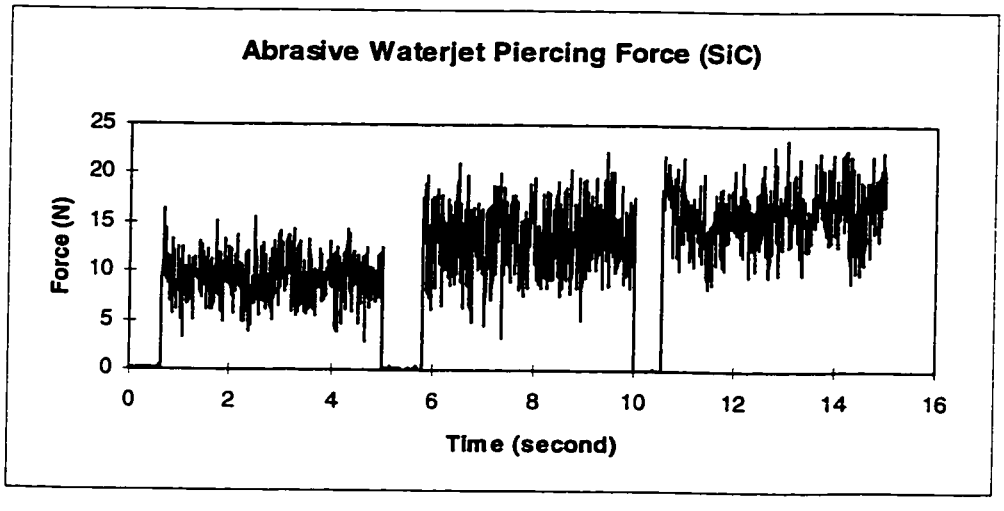

Figure 4.12 (d) WJ/AWJ Impact Forces of Various Supply Pressure on Silicon Carbide

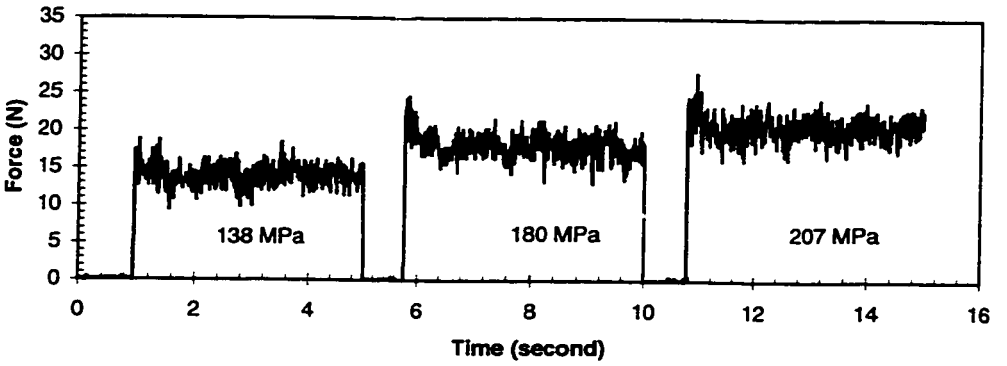

Pure Waterjet

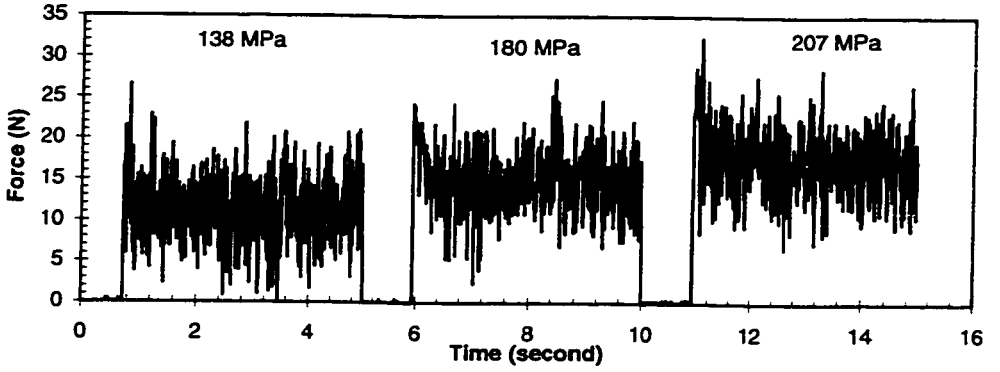

Abrasive Waterjet

Figure 4.12 (e) WJ/AWJ Impact Forces of Various Supply Pressure on Polycarbonate

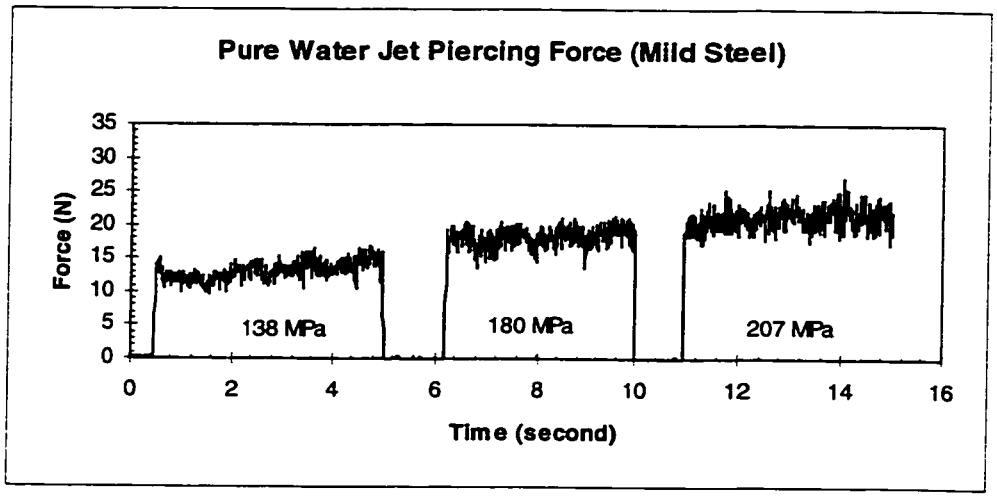

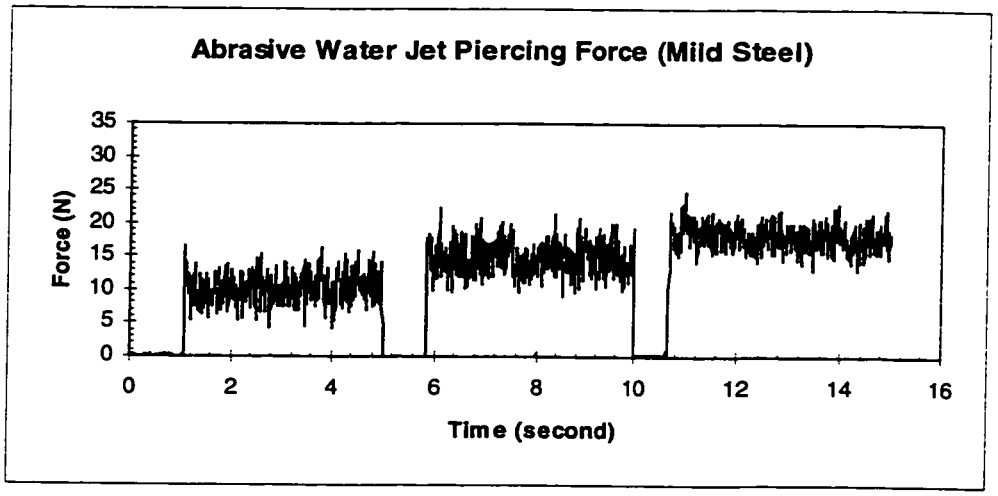

Figure 4.12 (f) WJ/AWJ Impact Forces of Various Supply Pressure on Silicon Carbide

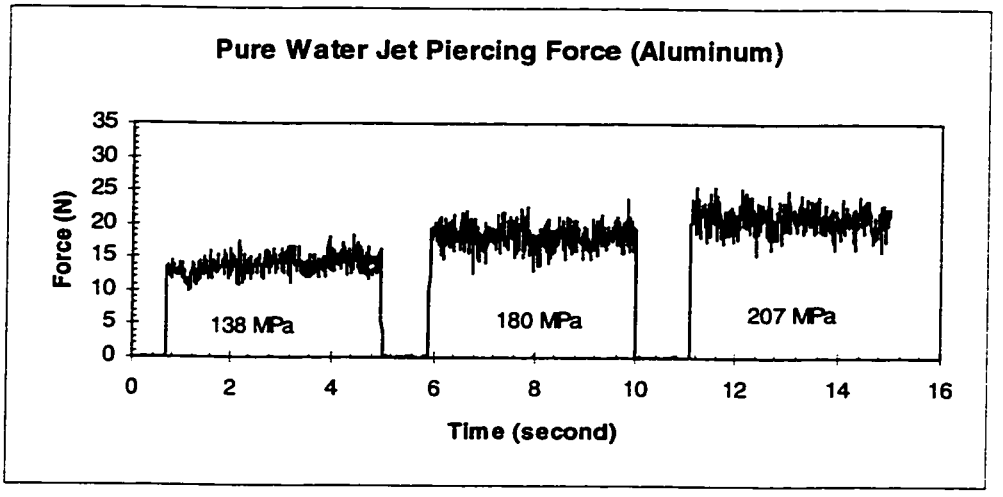

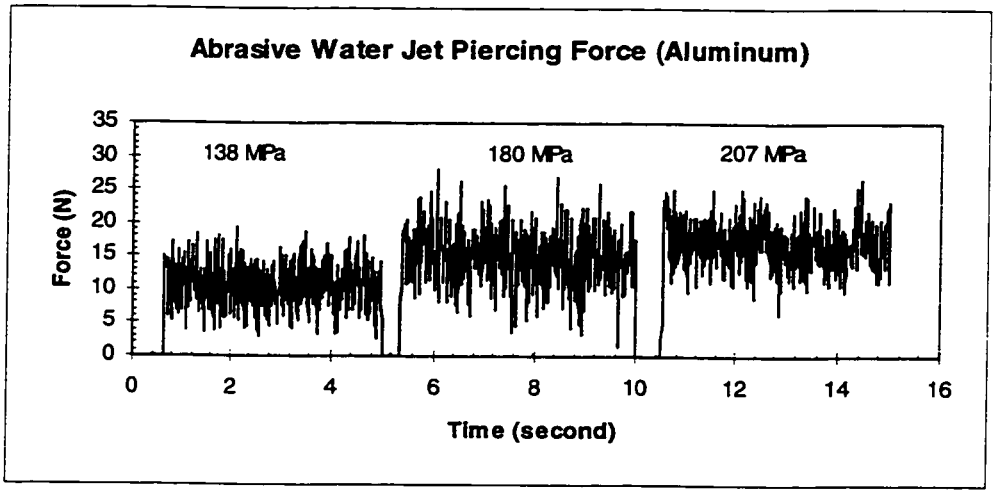

Figure 4.12 (g) WJ/AWJ Impact Forces of Various Supply Pressure on Aluminum

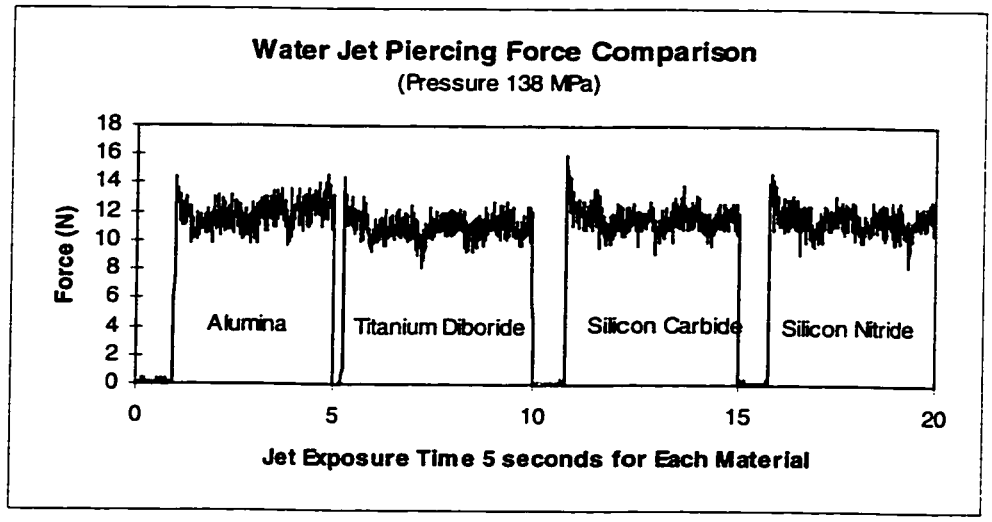

(a) Pure Waterjet with Supply Pressure of 138 MPa

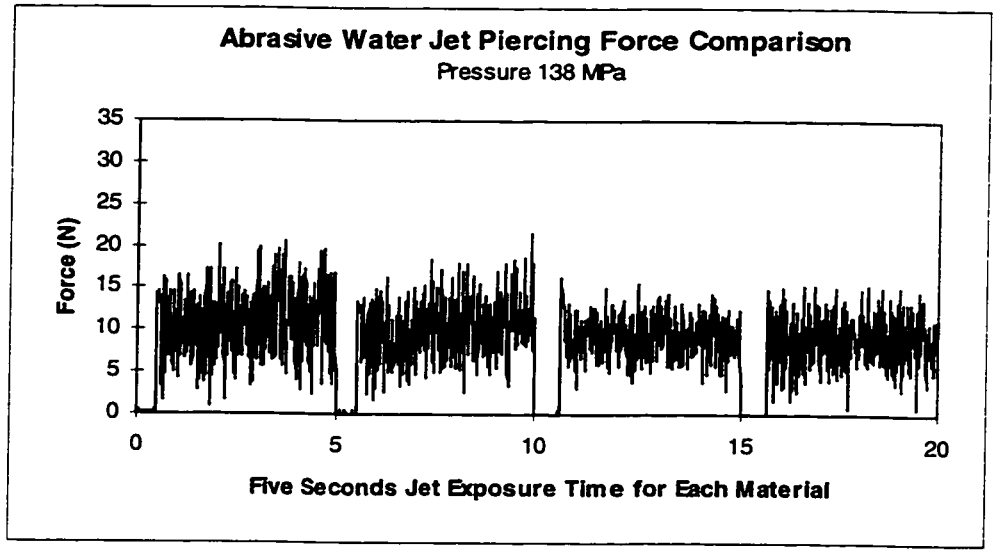

(b) Abrasive Waterjet with Supply Pressure of 138 MPa

Figure 4.13 (a), (b) Comparison of WJ/AWJ Piercing Forces of Different Materials

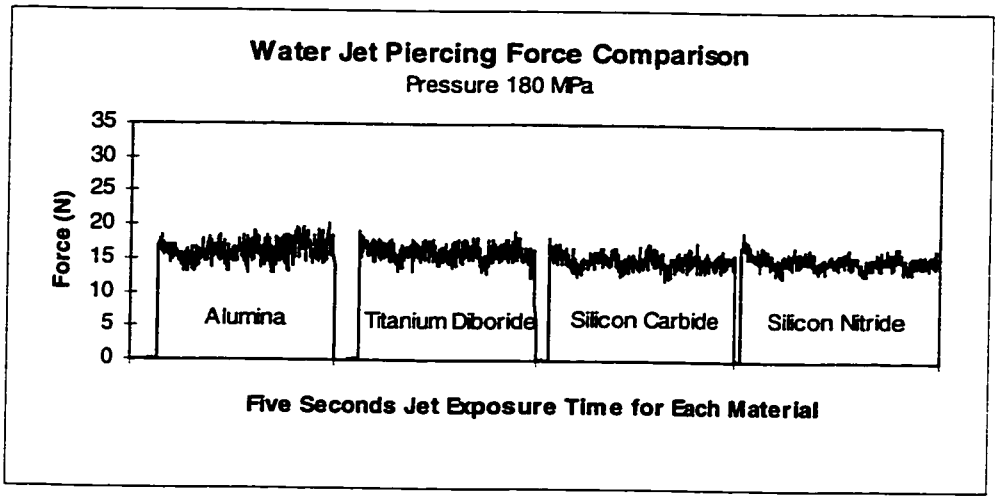

(c) Pure Waterjet with Supply Pressure of 180 MPa

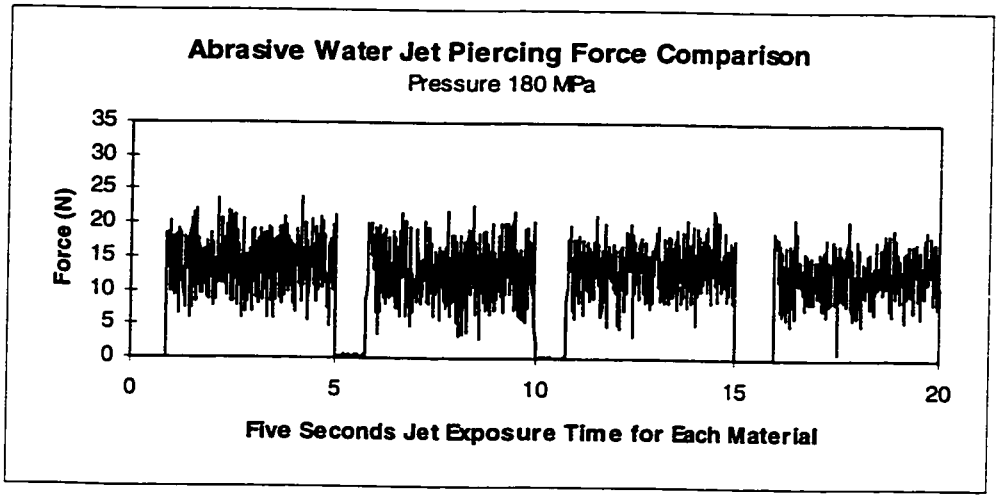

(d) Abrasive Waterjet with Supply Pressure of 180 MPa

Figure 4.13 (c), (d) Comparison of WJ/AWJ Piercing Forces of Different Materials

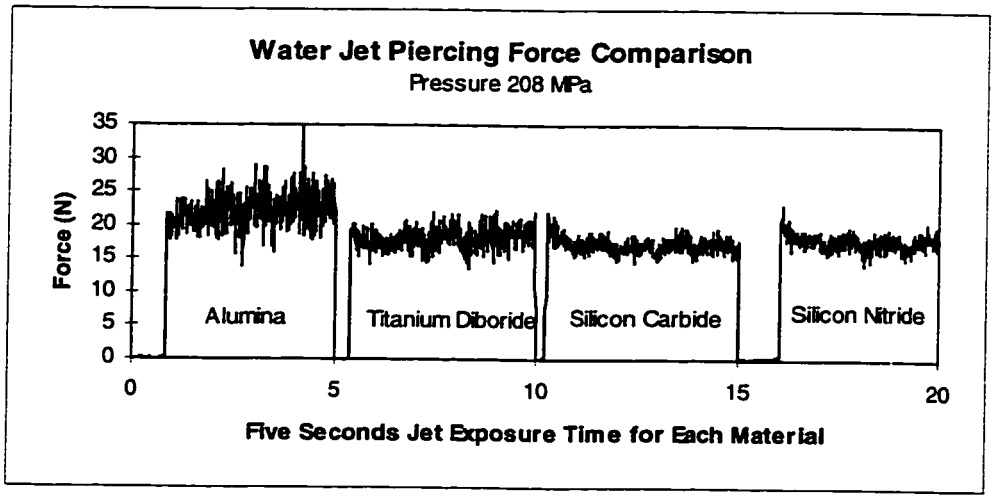

(e) Pure Waterjet with Supply Pressure of 207 MPa

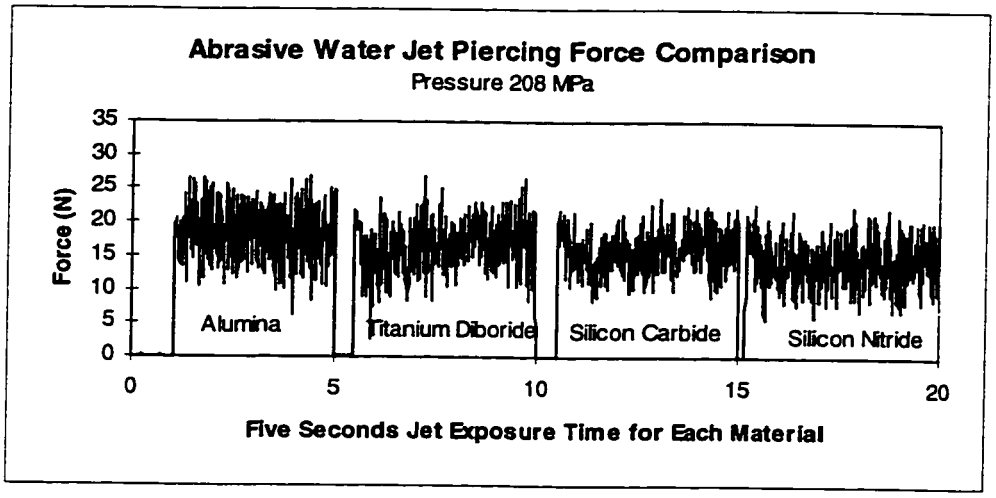

(f) Abrasive Waterjet with Supply Pressure of 207 MPa

Figure 4.13 (e), (f) Comparison of WJ/AWJ Piercing Forces of Different Materials

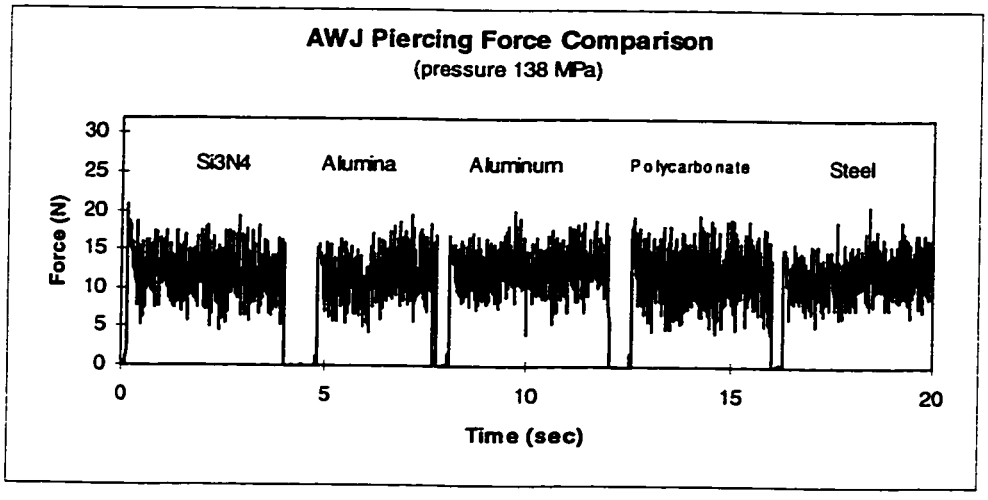

(g) Pure Waterjet with Supply Pressure of 138 MPa

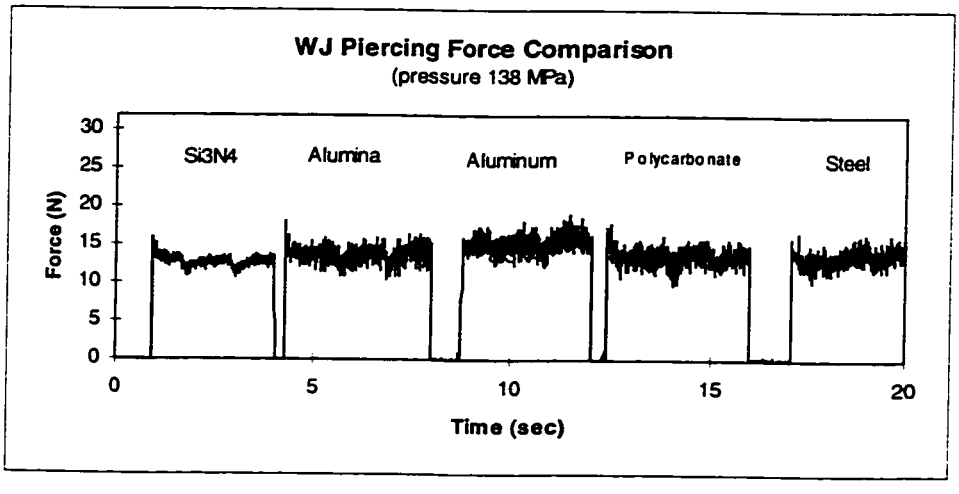

(h) Abrasive Waterjet with Supply Pressure of 138 MPa

Figure 4.13 (g), (h) Comparison of WJ/AWJ Piercing Forces including non-ceramics

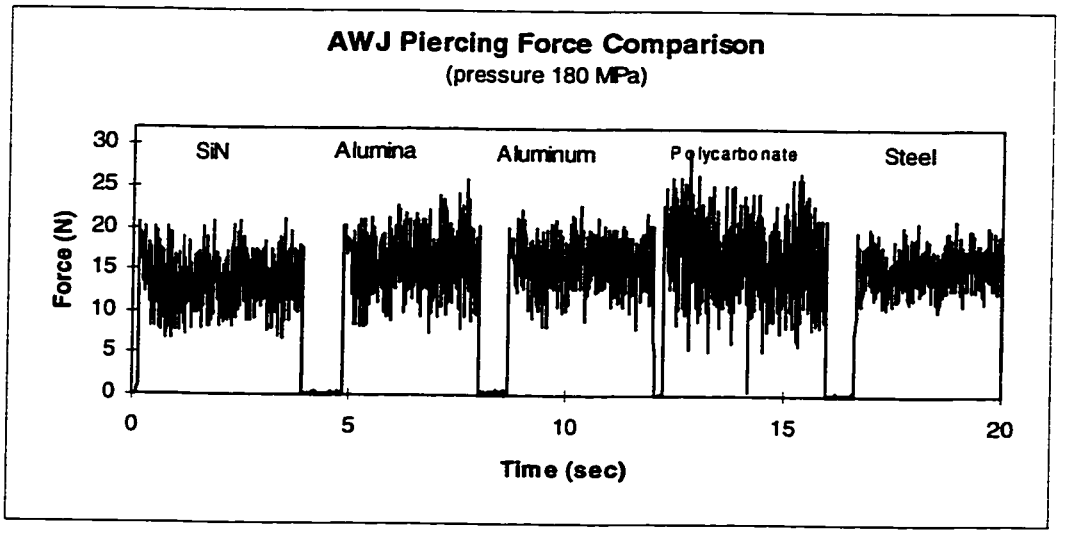

(e) Pure Waterjet with Supply Pressure of 180 MPa

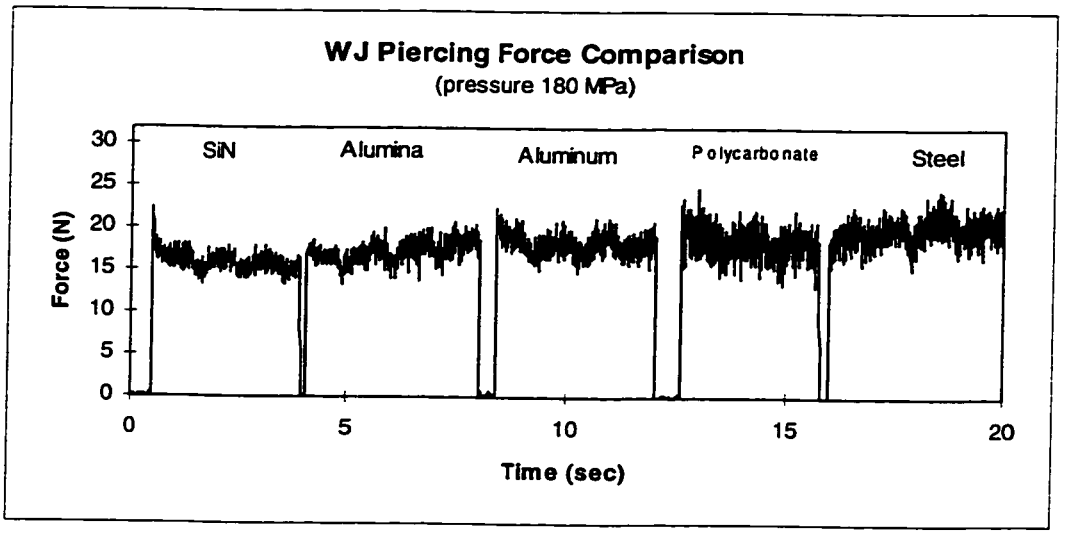

(f) Abrasive Waterjet with Supply Pressure of 180 MPa

Figure 4.13 (i), (j) Comparison of WJ/AWJ Piercing Forces including non-ceramics

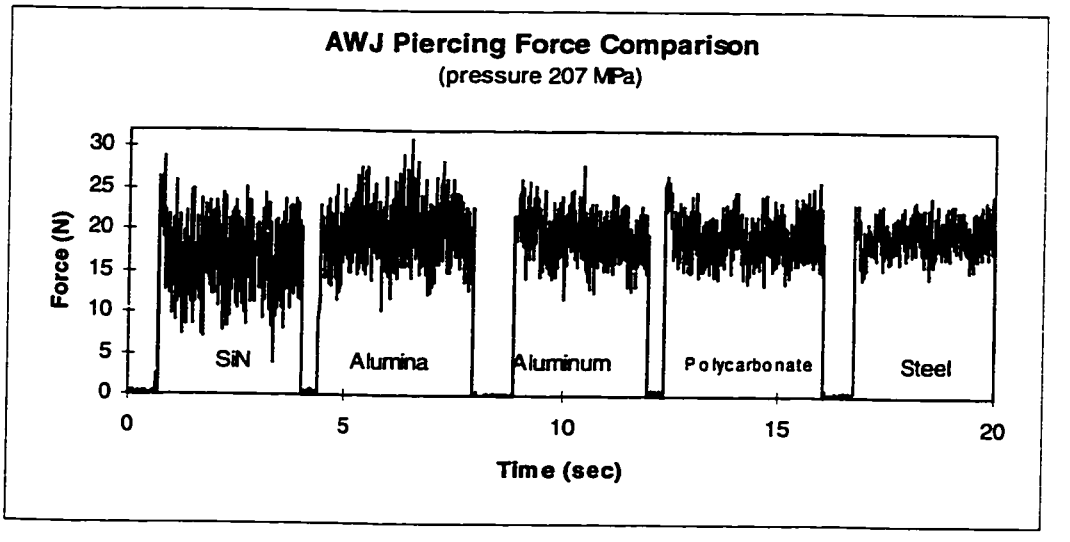

(e) Pure Waterjet with Supply Pressure of 207 MPa

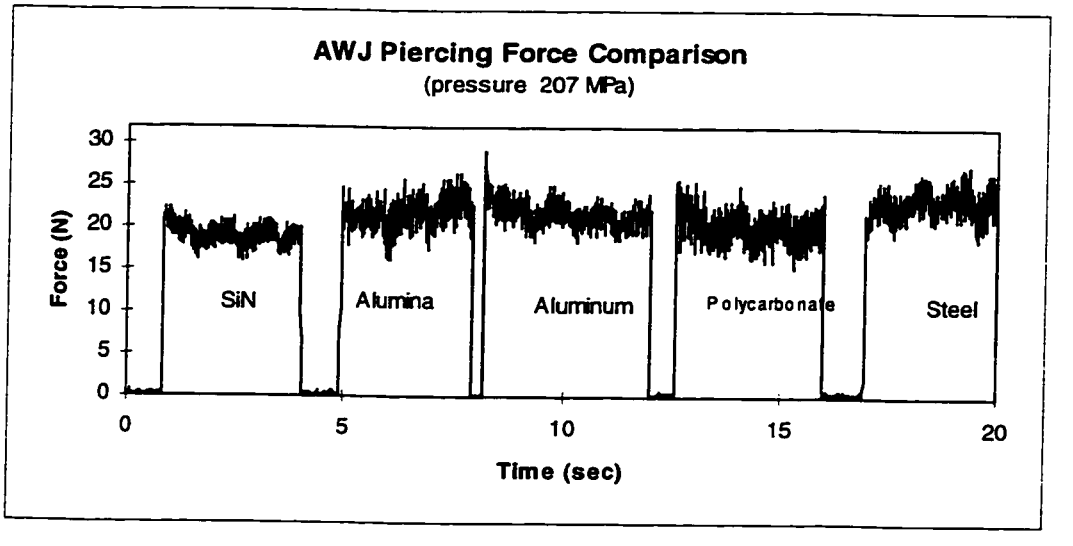

(f) Abrasive Waterjet with Supply Pressure of 207 MPa

Figure 4.13 (k), (l) Comparison of WJ/AWJ Piercing Forces including non-ceramics

Table 4.5 WJ/AWJ machining forces (average) for all tested materials

	Pure Waterjet			Abrasive Waterjet		
Supply Pressure (MPa)	138	180	207	138	180	207
Silicon Carbide (SiC)	11.5	15.3	17.0	10.0	14.0	16.5
Silicon Nitride (Si_3N_4)	11.5	15.1	18.0	10.0	13.5	16.0
Titanium Diboride(TiB_2)	11.0	16.0	18.0	10.0	13.0	17.0
Alumina (Al_2O_3)	12.0	16.2	22.5	10.5	14.5	18.0
Steel	12.0	18.2	22.0	13.0	15.0	19.5
Aluminum (Al)	12.8	18.0	22.0	15.0	14.6	19.0
Polycarbonate	12.4	19.5.	20.7	13.0	16.0	19.00

For Al_2O_3 the average machining force in pure waterjet drilling was about 12 N at a supply pressure of 138 MPa. The average machining forces for the Al_2O_3 were 16 N and 22 N for pure waterjet at supply pressures 180 MPa and 207 MPa, respectively, as shown in Figure 4.12 (a). In abrasive waterjet machining, the machining forces recorded were smaller than those in pure waterjet machining. The corresponding average forces in AWJ machining were 11 N, 14 N, and 18 N for supply pressures of 138 MPa, 180 MPa, and 207 MPa. This trend also applies to other ceramic and non-ceramic materials at other supply pressures shown in Figures 4.12(b)-(g). The reduction in machining force is a result of mixing abrasive particles with the pure waterjet. When abrasives are added to the high speed waterjet stream, the average velocity of the mixed jet flow decreased with respect to the pure waterjet flow, and kinetic energy dissipated due to inefficient momentum transfer that caused the machining forces to drop. This can be explained with the following equations.

When high pressure pure water exits the orifice, the jet stream speed is accelerated to V_j. The velocity of waterjet V_j can be calculated by applying Bernoulli's law of pressure constancy:

$$V_j = \sqrt{\frac{2P}{\rho_w}} \tag{4.1}$$

where V_j is the velocity of the jet exiting the waterjet orifice, P is the applied water pressure, and ρ_w is the density of water on exit.

During the mixing process between the waterjet and abrasives, momentum transfer occurs. Apply the momentum transfer principle, the abrasive waterjet velocity V_a after the mixing of water and abrasives can be expressed as:

$$V_a = \eta \frac{V_j}{1+(m_a / m_w)} \tag{4.2}$$

where V_a is the abrasive waterjet velocity after mixing, and η is the mixing efficiency or the momentum transfer efficiency, which is typically around 80%[50]. m_a and m_w are the masses of the abrasive and water respectively. Apparently V_a is much less than the jet velocity V_j. According to Neusen, et al.[121], the velocity of an abrasive waterjet can be as low as 30% to 60% of the pure waterjet.

The measured machining forces between the pure waterjet and abrasive waterjet are compared in Figure 4.14. The differences in machining forces with waterjet and abrasive waterjet are about 20%, as can be observed from the two curves of dashed lines in Figure 4.14. The difference in WJ/AWJ forces is mainly due to the dissipation of pure waterjet input energy during the formation of the abrasive waterjet. These results are in agreement with those reported by Momber, et al[122].

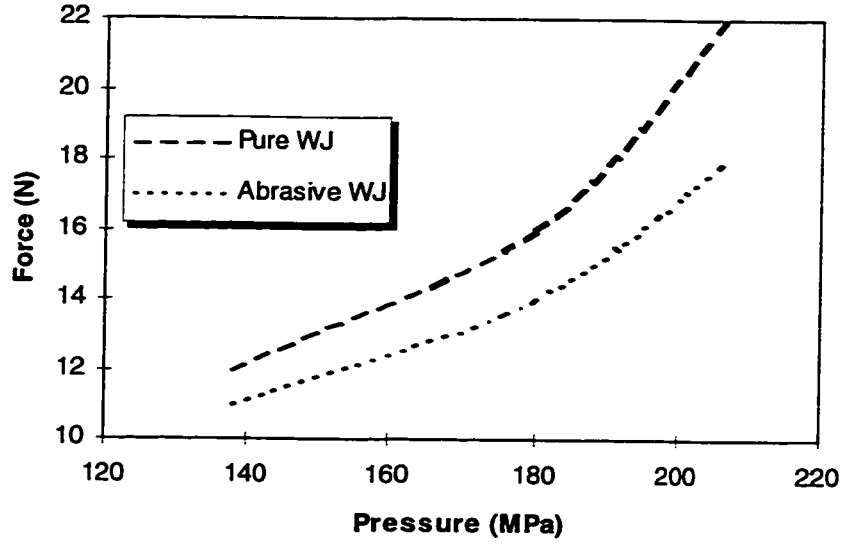

Figure 4.14 WJ/AWJ Impact Force Comparison

4.6.2 Material Hardness and Impact Forces

In this section the machining forces of WJ/AWJ exerted on different workpiece materials were compared. In the above graphs, it is noted that the differences in average machining forces for different workpiece materials are very small within each of the two groups.

From the average force data presented in Table 4.5, there is a correlation between the average machining forces and the hardness of the specimen materials. It appears that the greater the material hardness, the smaller the average machining force. Considering the difference of average machining forces between the hardest material and the softest material listed in the table, for both WJ and AWJ machining, the difference is greater under higher supply pressure than under lower supply pressure. The machining forces with pure waterjet are greater than with abrasive waterjet. During the WJ/AWJ

machining process, softer material can be penetrated more easily than the harder material, and hence has a deeper hole for a certain jet exposure time. The WJ/AWJ energy is used more efficiently in the softer material than in the harder material. This is because the WJ or AWJ bounces from the work surface more from a harder material than from a softer material. This is also evidenced by Momber [50], where the energy absorption depends on the depth of cut following a second order equation. Therefore, in softer material the reactive forces are higher than in harder materials.

Examining the machining force graphs for the seven materials discussed here, it appears that there is a slight increase in machining forces as the jet exposure time increases during both AWJ and WJ impact. Furthermore, the trend of increasing is more detectable in the softer materials than in the harder materials. This suggests that the machining forces increase slightly as the depth of hole increases.

4.6.3 Fluctuation of the WJ/AWJ Impact Forces

From Figures 4.12 (a)-(g) and Figures 4.13(a)-(l) the impacting forces on the workpiece ceramic materials by the waterjet and abrasive waterjet are seen to fluctuate. It appears there is a basic cyclic frequency associated with the fluctuations. The recorded force measurement data were analyzed by using a spectrum analyzer program. The analyzed data is plotted in frequency domain and is shown in Figure 4.15. The force data spectra are very similar in the frequency domain for both AWJ and pure WJ drilling. In the time domain, they are quite different. The force magnitude in pure WJ is greater than that in the AWJ case. From the spectrum-analyzed data, it appears that there is one dominant frequency in both AWJ and WJ drilling. This basic cyclic frequency in the measured force spectrum is most probably determined by the cyclic water pressure from the waterjet intensifier pump, even with a water pressure attenuator or accumulator installed in the pump system. The period of the fluctuation is approximately 1.1 second.

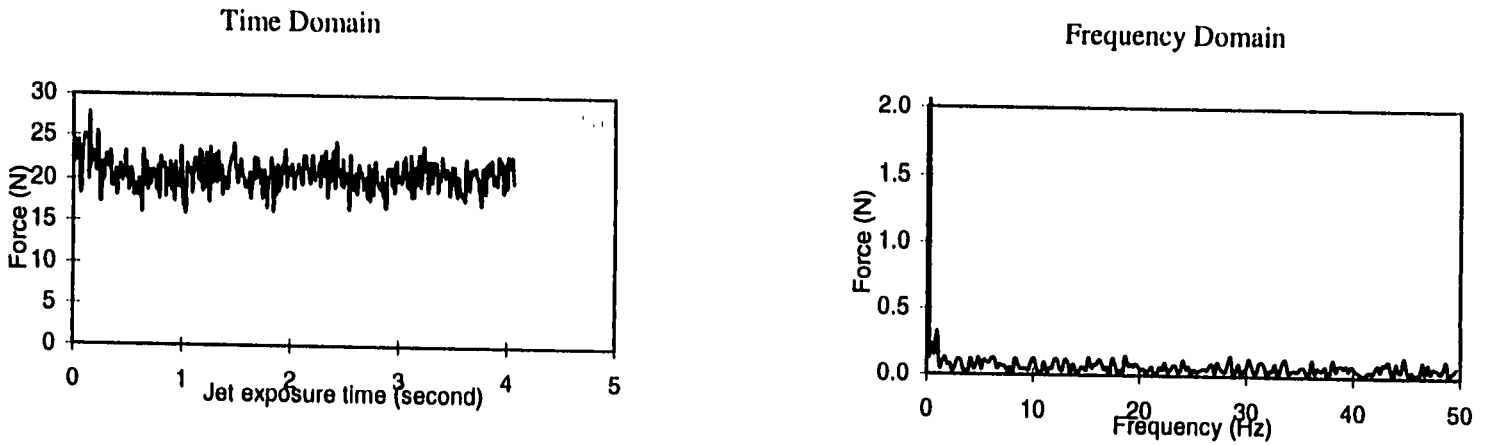

(a) Pure Waterjet (supply pressure 207 MPa, SOD 2 mm)

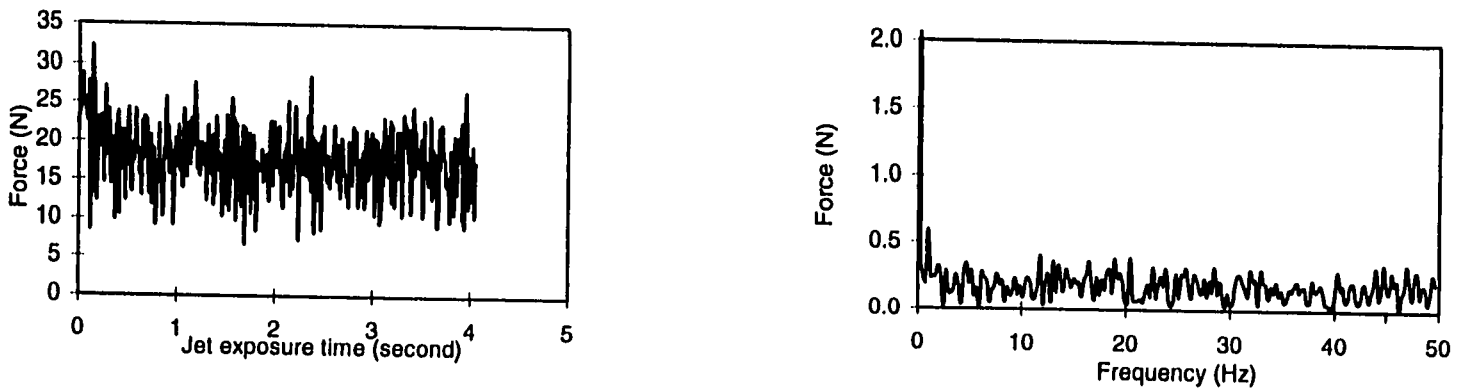

(b) AWJ (supply pressure 207 MPa; garnet mesh 80, SOD 2mm)

Figure 4.15 Spectrum analysis of WJ/AWJ drilling force on polycarbonate

Within each basic fluctuation cycle, the measured machining forces have random fluctuations. This is indicated by the small signal in the frequency chart. Many parameters are responsible for the random fluctuation in machining forces, for example, the vibration of the abrasive waterjet pump system, and the non-homogeneity of the ceramic materials. The irregular interactions between the return flow of water, abrasives, and cutting debris with the incoming jet also contribute to the fluctuation in the impact forces. The magnitude of the random fluctuation in abrasive waterjet machining process is much greater than that in that the pure waterjet machining process. When the same specimen material is drilled by pure waterjet, the magnitude of fluctuation is higher at high supply pressure and vise versa. In this case, the peak - valley difference of fluctuation can be up to 25% of the average drilling forces. When the same specimen material is drilled by abrasive waterjet, the peak-valley value of fluctuation can be 50% of the average drilling forces. The large peak-valley fluctuation in AWJ machining is due to the random impingement of the abrasive particles.

The abrasive waterjet piercing process can be considered as many micro "crack initiation and erosion" cycles. The high speed and high pressure WJ/AWJ initially impacts the workpiece material and creates some cracks. The hydraulic wedging action of the WJ/AWJ opens the cracks and propagates the cracks. The scouring action of the WJ/AWJ tends to remove the debris from the damaged zone. The process repeats itself. The machining force increases in the "crack initiation" stage when water impinges the workpiece and microcracks are created, and machining force decreases in the "erosion" stage when water flow reverses and cracked material is removed by the powerful water flow. These random machining cycles are influenced by the characteristics of the workpiece material, the waterjet parameters, and the abrasive waterjet machining system. It appears there is a correlation between the erosion rate and the fluctuation amplitude in machining force. Greater erosion rate causes larger fluctuation as material non-homogeneity is more pronounced.

4.7 AWJ MACHINED SURFACES AND TOPOGRAPHY

Figure 4.16(a) is a micrograph of a typical kerf profile, and figure 4.16(b) is a micrograph of the surface of an Al_2O_3 specimen cut by abrasive waterjet. On an abrasive waterjet machined kerf, the ratio of the depth of the smooth surface region in the top half, and the depth of the grooved surface region in the bottom half, is a function of effective abrasive waterjet machining capability. This is related to the supply pressure, the traverse speed, and the abrasive flow rate. etc. When the supply pressure is high, the kerf surface is more uniform, due to kinetic energy that is sufficient to machine the whole material all the way through, as depicted in Figure 4.17 (a). For lower supply pressure, the kerf profile may not be uniform because of the reduced kinetic energy. The grooved region may occupy the majority of the total kerf surface. Figure 4.17 (b) depicts an enlarged view of the grooved region of the kerf surface in Al_2O_3. The surface characteristics of the upper surface indicate that the material is being removed by a micro-cutting action. On the lower part of the machined surface, the orientation of the grooves is away from the traverse direction, suggesting that the flow of the abrasive waterjet is removing material by erosion in this surface region. This erosion phenomenon explains the formation of the curved grooves observed in the unsteady and grooved region of the cut surface.

The abrasive waterjet machined kerf can be characterized by four surface regions: a top surface damage region, a smooth surface region, a grooving region, and a fracture region. Figure 4.18(a) shows the damaged top surface of an abrasive waterjet machined surface. The damage on the top surface resulted from the bombardment by the stray abrasive particles. Due to a continuous abrasive waterjet flow a smooth edge on the top surface was machined, as seen in the magnified kerf profile shown in Figure 4.17(a). The next region on the machined surface is the smooth surface region, as in Figure 4.17 (b). The leading edge of the waterjet impacted the surface of the workpiece at a shallow

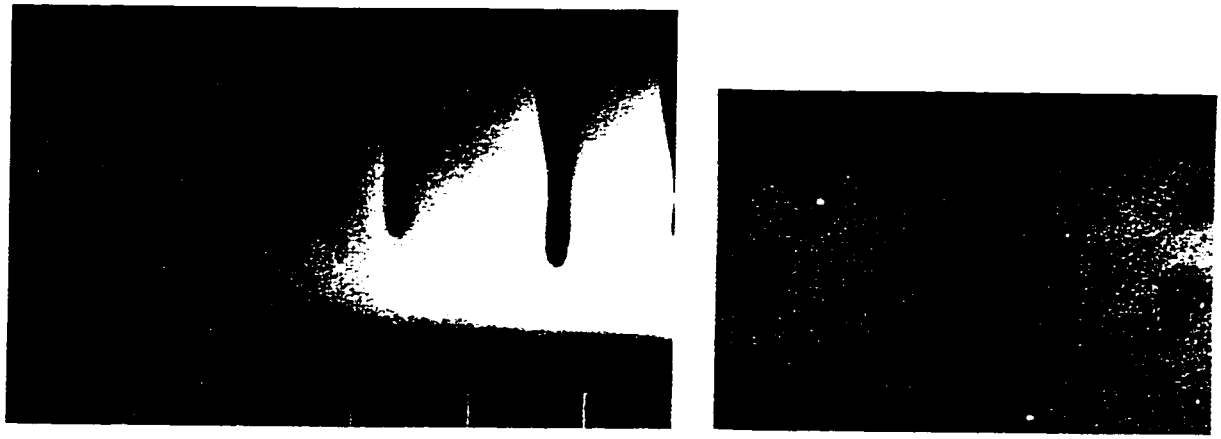

(a) Graduated cutting profiles (b) Magnified view

Figure 4.16 Micrographs of AWJ Cut Alumina

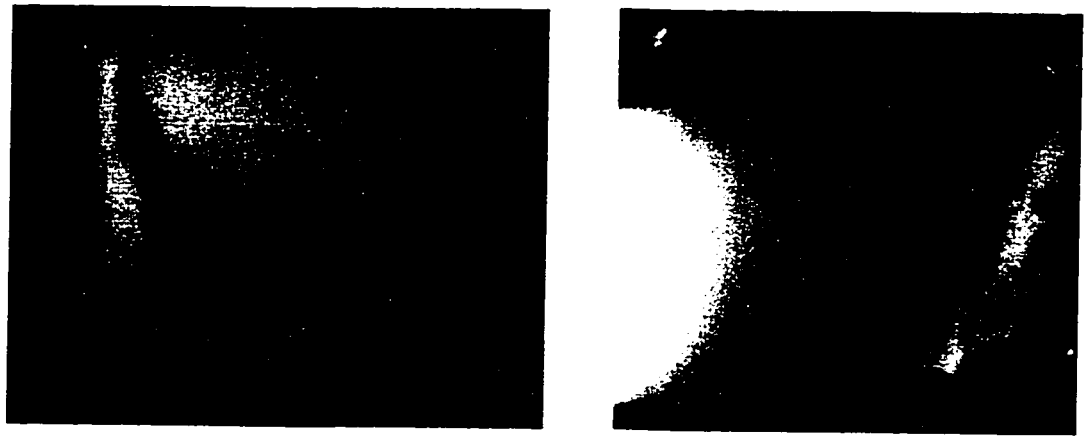

(a) Smooth cutting surface (b) Cutting surface with grooves

Figure 4.17 Micrographs of AWJ Cut Surfaces of Alumina

Figure 4.18(a) Micrograph of the Entry of an AWJ Pierced Alumina

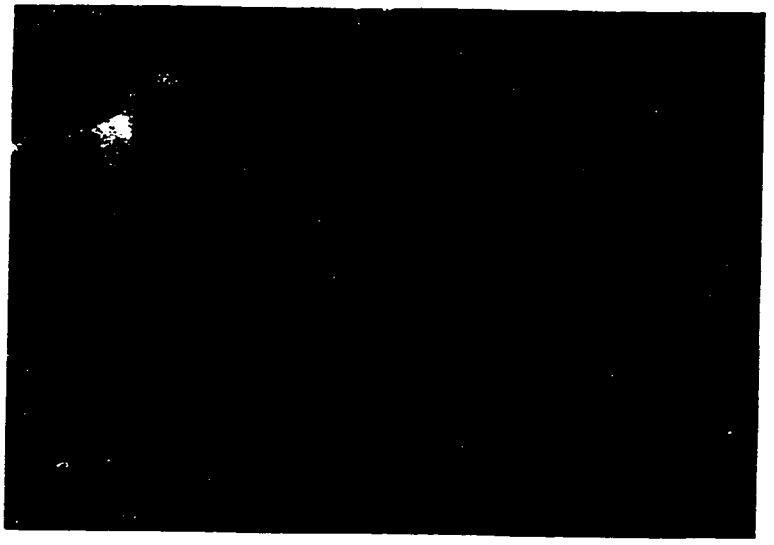

Figure 4.18(b) Micrograph of the Bottom Surface on TiB_2 Generated by AWJ

angle, resulting in a smoother surface. The mode of material removal is governed by cutting wear. The kinetic energy of the abrasive waterjet decreased after the material in the smooth surface region was removed. The jet was deflected away from its original direction and a region of grooved surface was then formed. The grooving direction was always curved away from the traverse direction, as demonstrated in Figure 4.17 (b).

At the grooving region, the mode of material removal was a deformation cutting mechanism. The fractured surface was always in the shape of a triangle. Right before the material was completely cut through, the remaining area could not take the load from the abrasive waterjet impingement, and the ceramic material fractured due to its brittleness.

The kerf surface characteristics not only depend on the supply pressure and traverse speed, but also on the thickness and material properties. A faster traverse speed seems to produce deeper and more closely spaced grooves. Figure 4.18(b) is a micrograph of the bottom surface of a TiB_2 ceramic specimen, directly impinged by the abrasive waterjet. On the bottom surface, a rough area with periodic peaks and valleys was produced. This is an indication of a harder work material and an abrasive waterjet with insufficient kinetic energy. The lower the supply pressure, the higher the peak to valley height, resulting in a rougher machined surface. The roughness of the abrasive waterjet machined surface is related to the machining energy of the abrasive waterjet. Higher energy produces smoother surfaces and vice versa.

4.8 CFCC EXPERIMENTAL RESULTS

4.8.1 AWJ Machining Forces

The AWJ cutting on a CFCC specimen is illustrated in Figure 4.19. Using the same machining force measurement system as depicted in Figure 4.4, the jet impact forces exerted on the CFCC specimen by the AWJ and pure WJ during piercing were

recorded. Figures 4.20(a)- (b) are typical recorded impacting forces on CFCCs by the waterjet and abrasive waterjet, for supply pressure of 138 MPa, 180 MPa, and 207 MPa. The time durations for each piercing run of various jet pressures were between 1- 2 seconds, which were nearly the same as the specimen drill-through time. A list of the piercing runs is shown in Table 4.6. Specimens #32, #34, and #36 were penetrated with pure waterjet. The average machining force is about 15 N in the case of pure waterjet drilling at a supply pressure of 138 MPa, and the average force is about 12 N for abrasive waterjet. It is obvious from Figures 4.20(a) and (b) that the machining force decreases as abrasive particles are added in the pure waterjet. The reduction in machining force is because of average velocity of the mixed abrasive and waterjet flow with respect to the pure waterjet flow. The measured AWJ and the pure WJ machining forces are compared in Figure 4.20(c). The differences in machining forces with waterjet and abrasive waterjet are about 20%. These results are in agreement with those reported by Momber, et al [122].

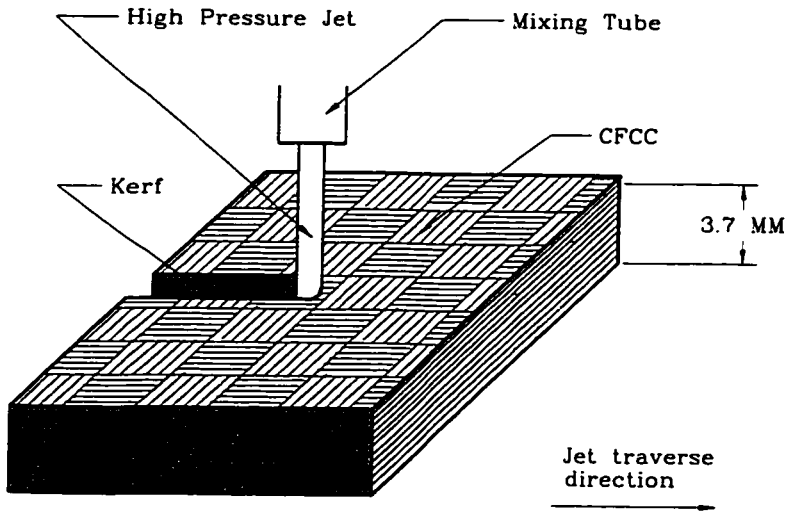

Figure 4.19 Illustration of AWJ cutting on CFCC Specimen

Table 4.6 AWJ Experimental Piercing Conditions (CFCC)

Specimen ID	Pressure,	Mesh #	SOD	Abrasive Flow Rate,
21	127	100	5	7
22	127	100	10	7
23	127	100	15	7
24	127	100	20	7
31	138	80	2	13
32*	138	N/A	2	N/A
33	180	80	2	16
34*	180	N/A	2	N/A
35	207	80	2	17
36*	207	N/A	2	N/A

*Pure waterjet

Comparing the impact forces on the CFCC materials and with those on the monolithic ceramics, the reaction forces on the CFCC materials are greater than those on the monolithic ceramics in both WJ and AWJ cases.

It should be noted that the recorded dynamic piercing forces on CFCC materials behave very similarly to monolithic ceramic materials that were discussed in the previous section. One of the similarities is that the WJ/AWJ impact forces also fluctuate. The sources responsible for the force fluctuation include the cyclic water pressure from the waterjet pump, vibration of the abrasive waterjet machining system, and the non-homogeneity of the CFCC materials. It appears that a basic cyclic frequency associated with the fluctuations also exists. However, the force randomly fluctuates within each basic cycle. The abrasive waterjet machining process can also be considered as many micro "crack initiation and erosion" cycles. The machining force increases in the "crack initiation" stage when water impinges the workpiece and microcracks are created in the

workpiece. Machining force decreases in the "erosion" stage when water flow reverses and cracked material is removed. The micro machining cycle continues until a hole is created. The basic cyclic phenomenon was strongly influenced by the WJ pump system. The random forces during each basic cycle machining cycles are affected by the characteristics of the workpiece material, the waterjet cutting parameters, and the abrasive waterjet machining system. The correlation between the erosion rate and the fluctuation amplitude in machining force is the same for the monolithic ceramic materials discussed previously.

From Figures 4.20(a) and (b), it is noted that the process of penetrating through a CFCC specimen by WJ or AWJ consists of two parts. The first part is relatively consistent. The second part begins right before the specimen is drilled through by WJ/AWJ. Within each part, the average impact forces are relatively "stable". However, the impact forces change when the first part ends and the second part begins. A reduction in jet machining forces occurs at that moment of change. This phenomenon was observed in CFCC materials only for both pure waterjet and AWJ machining. At low supply pressure, for example, 138 MPa, this phenomenon is not very obvious. The average machining forces before and after the changes are reported Table 4.7.

The timing of the force reduction occurring is dependent on the CFCC material quality and the AWJ machining parameters, such as traverse rate, abrasive flow rate, supply pressure, etc. In a CFCC material of reasonable thickness, right before the jet penetrate through the whole thickness, the WJ or AWJ partially damages the matrix material and the continuous fiber in the CFCC. This damage may include fiber roll out, delamination, or fractured fibers. When this occurs, the machining forces decrease. The forces are reduced to zero when the material is drilled through.

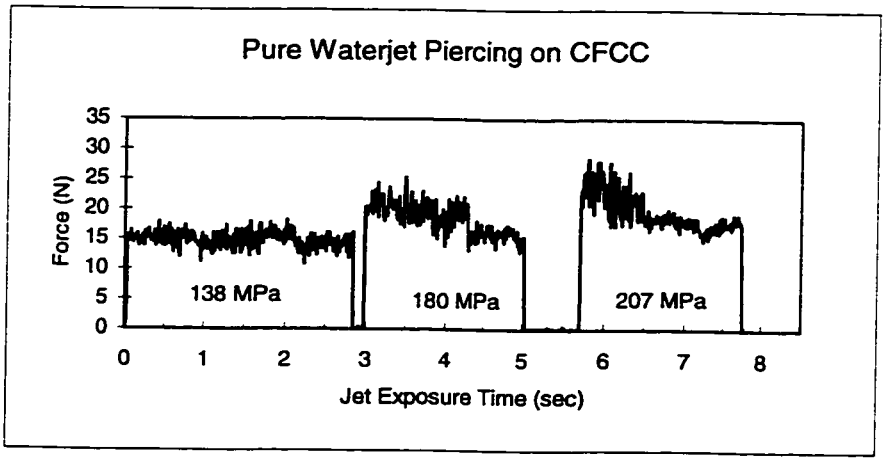

(a) Pure waterjet piercing

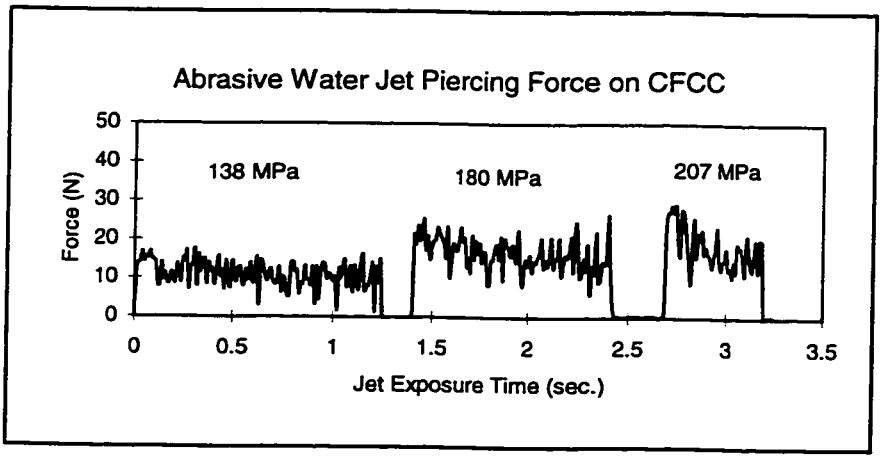

(b) Abrasive waterjet piercing

Figure 4.20(a) (b) Typical pure waterjet and AWJ machining forces on CFCC

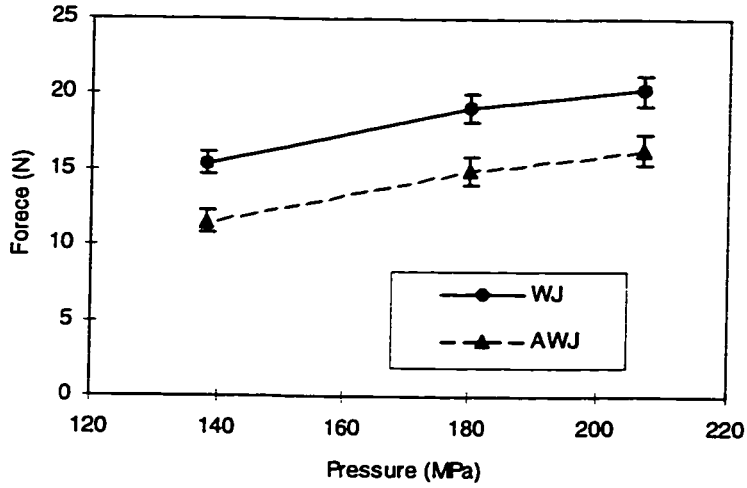

Figure 4.20 (c) Comparison of machining forces on CFCC

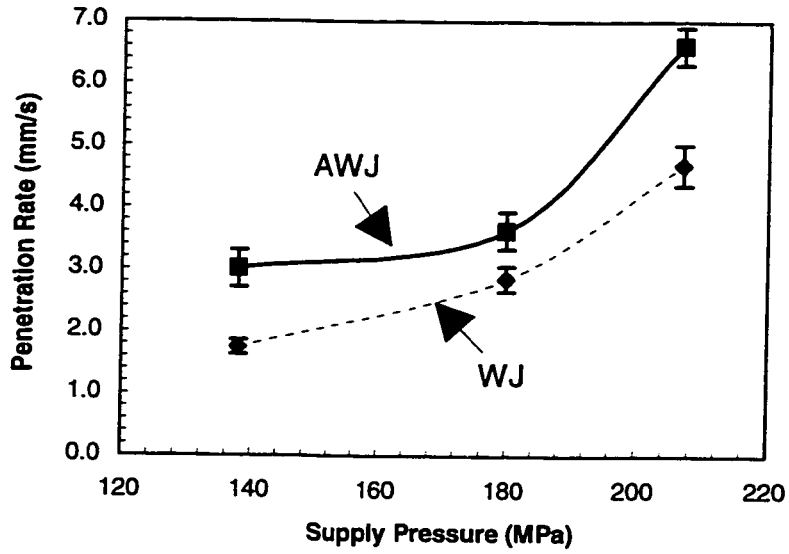

Figure 4.21 AWJ Material Removal Rate vs. Supply Pressure in CFCC (mm/s)
(Abrasive e: garnet; Mesh size: #80; SOD 1mm)

Table 4.7 WJ/AWJ machining forces reductions for CFCC material

	Waterjet		Abrasive Waterjet	
Supply Pressure	First Part	Second Part	First Part	Second Part
138 MPa	15.0	15.0	11.0	11.0
180 MPa	20.0	16.0	17.5	14.5
207 MPa	23.0	18.0	20.0	16.0

The AWJ and pure waterjet penetration rates before the CFCC specimen was drilled through, were recorded and graphed in Figure 4.21. The machining conditions include supply pressures of 138 MPa, 180 MPa, and 207 MPa, standoff distance of 1 mm, and mesh size #80. For both pure waterjet and abrasive waterjet machining, the penetration rates follow the same trend: The penetration rate is higher at higher pressures, and vise versa.

4.8.2 Surface Roughness

The surface roughness for both the diamond saw machined and the AWJ machined CFCC surfaces were compared. Table 4.4 is a test matrix of AWJ cutting. The influences of jet entry and exit were avoided by taking the roughness measurements in the mid section. Surface profiles were measured for traverse lengths of 3.25 mm with a 0.8 mm cut-off length. For specimens machined with both AWJ and diamond saw, surface profiles for longitudinal measurements on the cut edges are shown in Figure 4.22. Note the large, jagged excursions from the mean for the AWJ cut surface, as shown in Figure 4.22(a), compared to the more consistent roughness of the diamond-grit ground surface,

as shown in Figure 4.22(b). The mean average surface roughness, R_a, of the cut surfaces in the longitudinal direction, was 0.91 μm and 6.04 μm for the diamond-grit ground and AWJ cut surface, respectively. This suggests that the diamond grit grinding creates a much smoother surface than the AWJ method, which is consistent with the previous results.

All surface profiles machined by AWJ exhibited irregularly spaced and non-uniform peaks and valleys. The surface profiles created by the diamond saw were much more uniform, and the variance in peak-to-valley height was smaller when compared with the AWJ cut surface profiles, regardless of the fiber orientation relative to the cutting direction. In both cutting processes, the profiles generally were found to be random in nature [94].

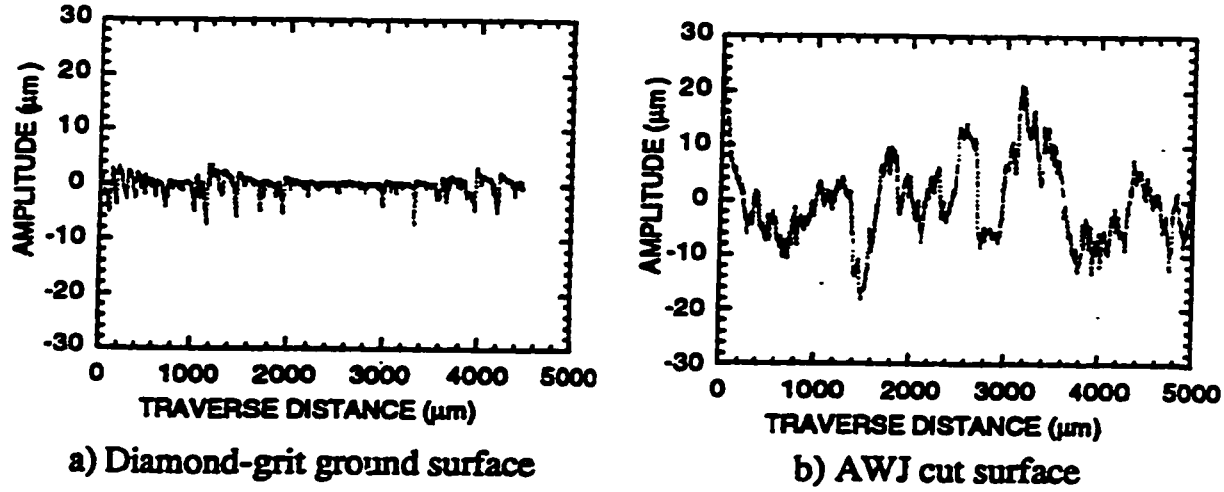

Figure 4.22 (a, b) Surface profiles of cut edges in the longitudinal direction of a CFCC

(CFCC: plain weave, Nicalon-reinforced, melt-infiltrated aluminum oxide matrix)

4.8.3 Microscopy

The abrasive waterjet machined surfaces for both AWJ cutting and piercing processes were evaluated using SEM. Figure 4.23 is a typical SEM micrograph showing the hole drilled with AWJ at a stand-off distance (SOD) of 15 mm. The surface area around the entrance of the hole appears jagged and rough. The damage on the top surface is due to the erosion by the random bombardment of high speed abrasive waterjet droplets and particles, which wash away the matrix and fractured fibers. Figures 4.24(a)-(d) are typical SEM photographs showing the topography of the hole surface. From Figures 4.24(a)-(c) pitting can be observed, and bare woven fibers and fiber bundles are clearly visible. The filler material (matrix) in between the woven fibers is also washed away. The ragged surface with fractured fibers protruding from the supporting matrix is clear from the higher magnification micrograph shown in Figure 4.24(d). When compared to the exit side of the hole, the severity of damage is greater near the top surface. At the jet exit, most of the matrix material was washed out, as seen in Figure 4.24(e). The outer ply at the jet exit shows delamination and severe damage, as shown in Figure 4.24(f). From observation of the delamination height regularity, it appears that delamination occurred due to the lack of support of the exterior fibers.

For various standoff distances, the hole tapers were measured with optical microscopy. The degree of taper was calculated as a ratio between the upper surface hole diameter and the lower hole diameter. The representative and limited taper results are shown in Table 4.8. The drilled holes were generated using a supply pressure of 172 MPa with #100-mesh garnet at an abrasive flow rate of 3.3 g/s. It appears that a linear relationship exists between standoff distance and hole taper within the experimental conditions.

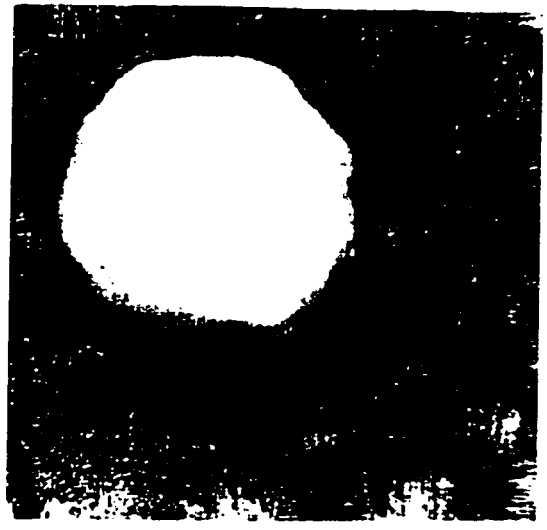

Figure 4.23 SEM micrograph at the entry of an AWJ pierced hole in CFCC

Table 4.8 Taper Ratio of the Drilled Hole (CFCC)

Specimen ID	Stand-off Distance, mm	Hole Taper Ratio
21	5	1.1
22	10	1.4
23	15	1.6
24	20	1.8

Microscopically, three cutting regions can be identified from the kerf profile and kerf face. They include an initial damage region at jet entry, a smooth cutting zone, and a waviness region near the jet exit. Figure 4.25(a) is a micrograph depicting the three machining regions. The initial damage region extends from the jet entrance. The damage on the top surface and the surrounding of the entrance kerf are dependent on the grit size and standoff distance. Shallow abrasive wear tracks can be distinguished perpendicular to the fiber axis. These are caused by stray abrasive particles at the outer portion of the penetrating jet. This phenomenon is most predominant near the jet entrance region. Between the initial damage zone and the beginning of the waviness patterns at greater cutting depth can be characterized as cutting wear zone, as in Figure 4.25(b). This region exhibits a smooth surface texture. The limited surface variations within this domain result from a combination of optimum coherency of the abrasive slurry with low exterior abrasive particle energy, and minimal jet deflection. Below the cutting wear zone and extending to the jet exit edge on the kerf surface is the roughness region, as indicated in Figure 4.25(c). Contrary to the jet entry and the cutting zone surface, the jet exit surface damage is associated with fiber pull-out, bending fracture, delamination. Some of the matrix was washed away, resulting in pitting in the region.

Figure 4.25(d)-(f) shows the SEM micrographs of the typical abrasive waterjet generated surface in the cutting zone at a supply pressure of 240 MPa. When fibers are oriented 90° to the cutting direction as shown in Figure 4.25(d), the kerf walls are relatively smooth with very little irregularity in texture throughout the specimen depth. Minor delamination and cracking of the fibers were observed near the jet exit. The fractured surface of the fibers and the surrounding matrix appear to be machined. This is different from those macro-fracture induced by bending from sustained loading forces that are typical of conventional processes [94]. As shown in Figure 4.25(d), nearly all matrix adjacent to the fibers remains intact in its supportive position after abrasive waterjet machining. Fiber pullout and fiber-matrix delamination are also very limited.

This may be due to a strong interfacial bond between the fiber and the matrix, coupled with localized cutting forces of the AWJ. The action of the added abrasives in the slurry is mainly responsible for this machining phenomenon.

Obviously, brittle fracture, including shearing and abrasive micro-fracturing, is the material removal mechanisms for the 90° plies fiber bundles. For fiber bundles oriented in the 0° direction, wear tracks are an important characteristic present on the machined surface. These wear tracks are parallel to the jet path, and are caused by stray abrasive particles in the exterior of the coherent jet, as can be seen in Figure 4.25(e). The particles create wear tracks along the kerf until they reach their minimum threshold for machining. Due to an increase in jet deflection with penetration depth, the wear track angle increases with cutting depth. However, the severity and depth of wear track penetration decrease with observation depth as a result of the reduction in abrasive kinetic energy. In this CFCC, some of the woven fibers were about 45° with respect to the incident waterjet. The machined surface exhibited material removal characteristics quite similar to those of the 90° surfaces. Figure 4.25(f) is a micrograph with high magnification, showing the effects of shearing, micro-machining, and erosion mechanisms associated with AWJ. The fibers in this orientation suggest that both microcutting and brittle fracture are dominant modes of material removal. Fiber roll-out on the AWJ machined specimens is observed near the jet exit due to the absence of supporting material in this region. Although the surface of some exposed fibers are fractured, the matrix remains intact on the machined surface. The machined surface suggests that abrasive shearing and brittle fracture account for the dominant portions of material removal.

SEM investigations of AWJ cut surfaces have shown that the micro-mechanisms of the material removal process change across the cut section from the jet entrance region to the jet exit region. Specifically, at the jet entrance, the high kinetic energy of the

abrasive produces relatively clean, independent fracture of the fibers and matrix. The matrix material adjacent to fibers remains intact. Limited fiber pull-out and almost no fiber/matrix delamination occur. However, at the jet exit, the reduced kinetic energy of the abrasive jet produces bending fractures of the fiber, and washes out the matrix from between the fibers. Fiber/matrix delamination is more apparent.

For comparison of the different machining methods on CFCC materials, a diamond-grit saw was used. On a surface machined with a diamond-grit saw, as shown in Figure 4.26, there is a low degree of damage to the constituent materials. The fiber and matrix have both been machined, and the matrix is intact along with the fibers. In general, fibers appear undisturbed on the kerf wall, with minimal evidence of fiber pullout. The results are consistent with those of Gonczy, et al [114]. Interstitial matrix between adjacent fibers remains in its supportive position, with only limited signs of matrix smearing. There is no evidence of thermal degradation. Both parallel and perpendicular fibers remain intact on the kerf without indication of shear induced material removal. This suggests that the material removal occurs at low magnitudes of cutting force.

(a) eroded surface

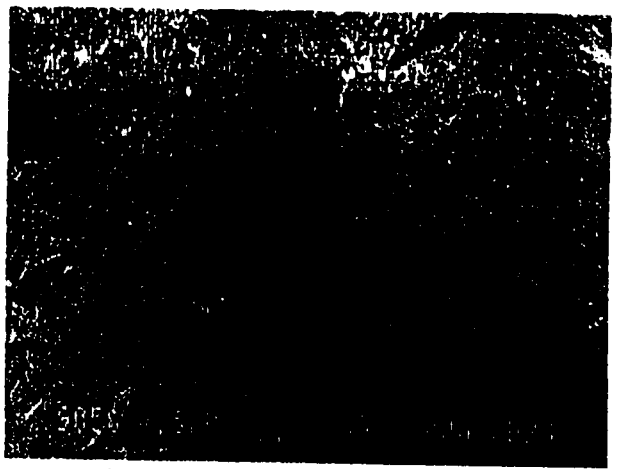

(b) erosion and fracture of fibers

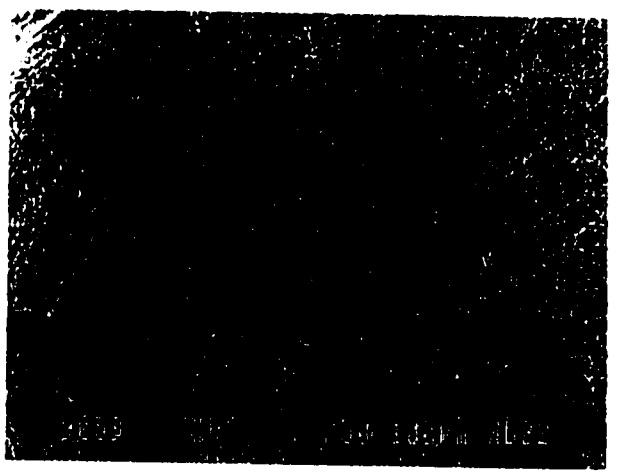

(c) interface

(d) fracture and erosion

Figure 4.24(a-d) Typical SEM micrographs of hole surface features a the jet entry, mid-section

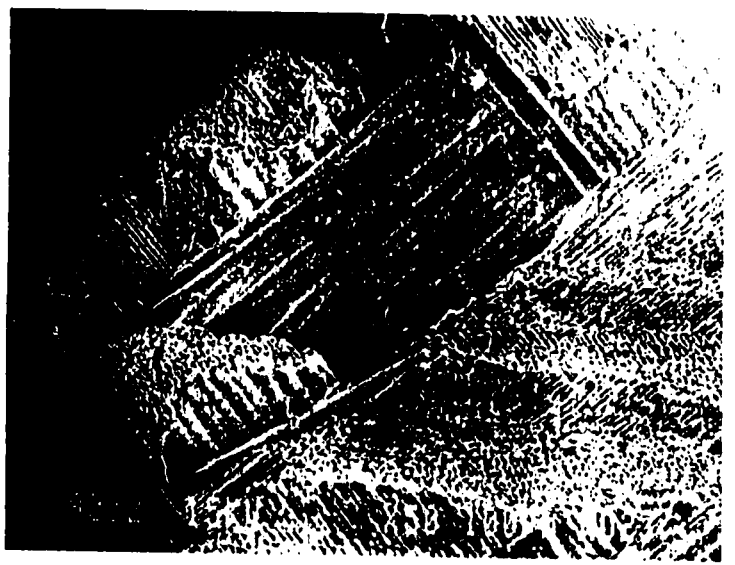

(e) typical jet exit zone

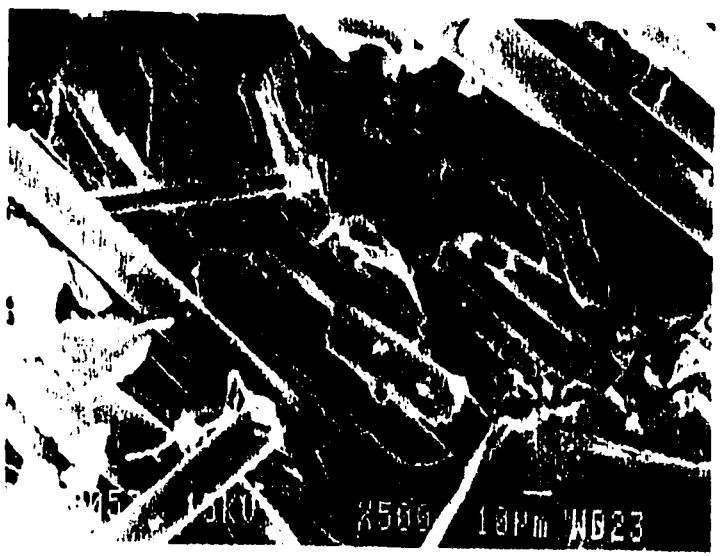

(f) magnified image of the damaged zone at the jet exit

Figure 4.24(e-f) Typical SEM micrographs of hole surface features a the jet exit

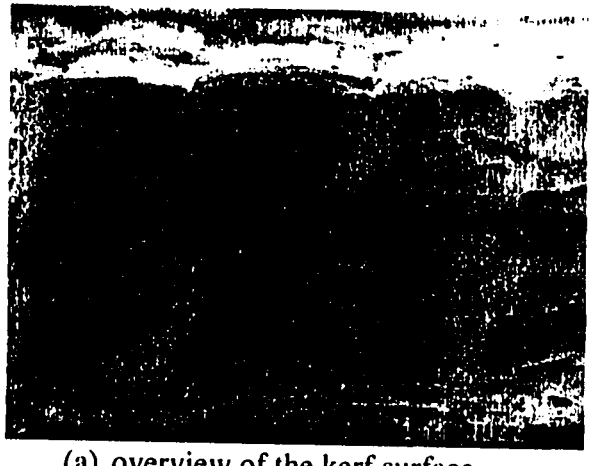

(a) overview of the kerf surface

(b) abrasive waterjet cutting region

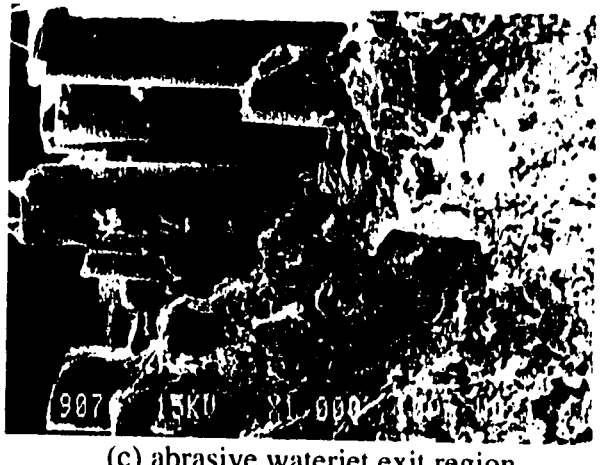

(c) abrasive waterjet exit region

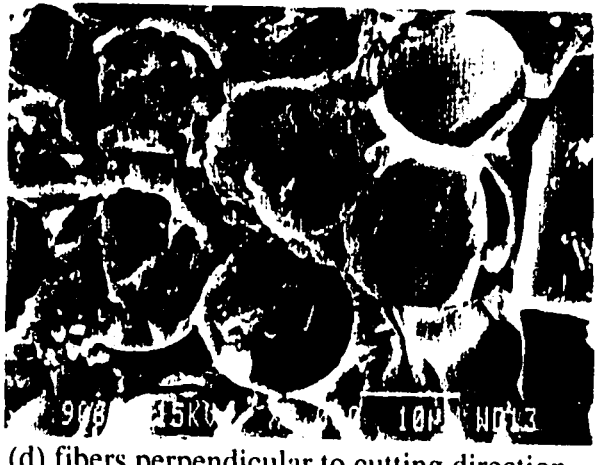

(d) fibers perpendicular to cutting direction

Figure 4.25(a-d) Typical SEM micrographs of the surface morphology of AWJ machined surfaces

(e) fiber para;;el to cutting direction

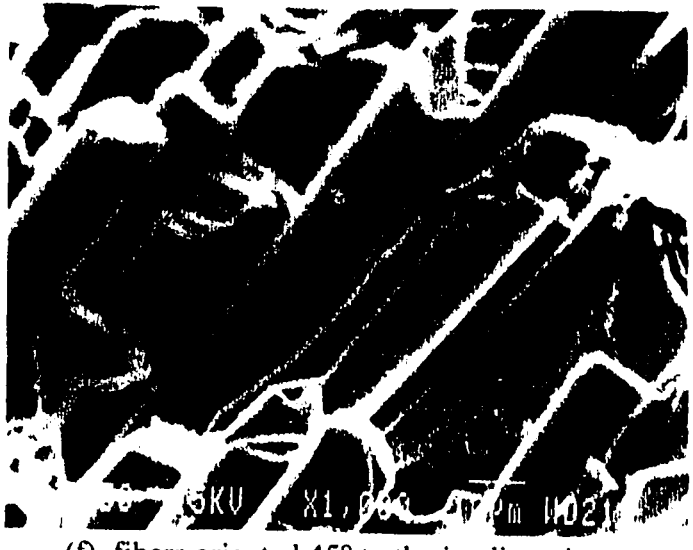

(f) fibers oriented 45° to the jet direc tion

Figure 4.25(e,f) Typical SEM micrographs of the surface morphology of AWJ machined surfaces

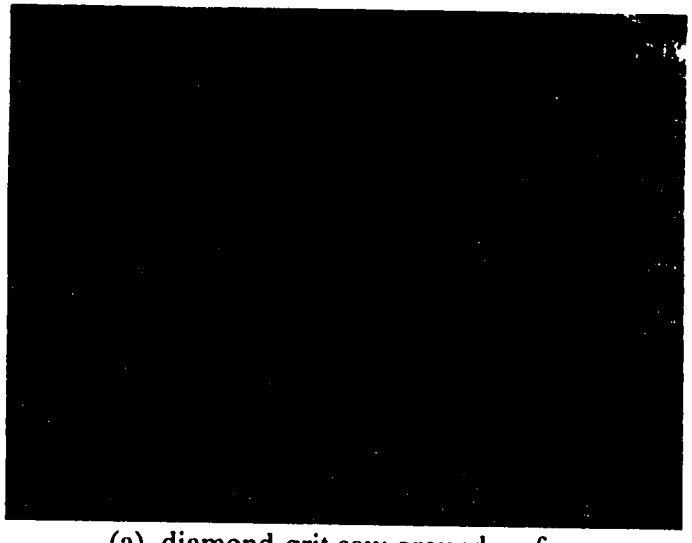

(a) diamond-grit saw ground surface

(b) 90 fiber surface

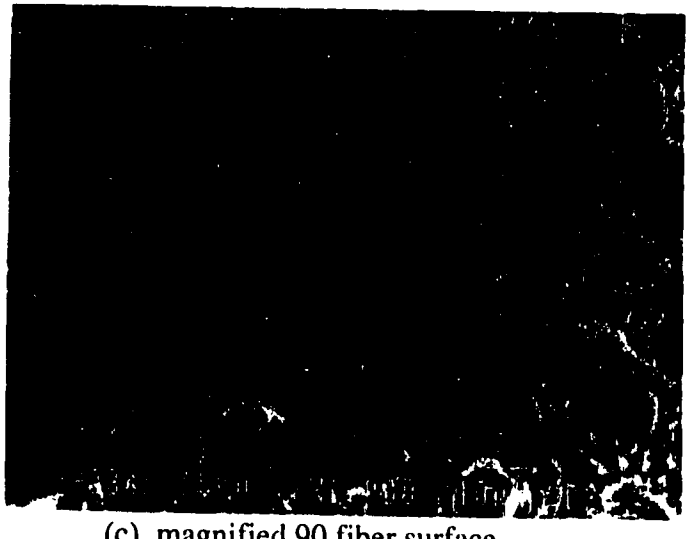

(c) magnified 90 fiber surface

(d) magnified 0 fiber surface

Figure 4.26 Typical SEM micrographs of the diamond-grit saw cut surface

4.9 DISCUSSION AND SUMMARY

In the current research, the phenomena of abrasive waterjet machining on ceramic and ceramic composites have been investigated through a rigorous parametric study. This parametric study of abrasive waterjet machining helps in the understanding of the effect, during the abrasive waterjet machining process, of each machining parameter on polycarbonate, monolithic ceramic, and ceramic composite materials, including fiber reinforced ceramic composite. The test results show a good correlation between the mesh size of the abrasive waterjet and the depth of cut, with other parameters remaining constant. Increasing the size of abrasive increases the capability of material removal. This is because abrasives with large mass carry higher kinetic energy that is needed for the machining action. Due to the special construction of the nozzle assembly, particle size above a threshold can adversely affect the smooth flow of the particle into the jet stream, and thus reduce the net machining energy. The energy theory can also explain the effect of the abrasive flow rate on the material removal rate. As more abrasives are entrained in the waterjet stream, more kinetic energy is stored in the jet flow, resulting in more material that can be removed. In general, traverse speed of the workpiece affect the material removal rate differently from the abrasive flow rate. Higher traverse speed reduces the material removal rate. The other most important parameter is the applied pressure. Obviously, higher pressure removes more material from the workpiece. However, there exists a threshold pressure for a specific workpiece material under certain conditions. For supply pressure less than the threshold pressure, the material removal rate will be minimal. This is because that the kinetic energy for material cutting is determined by the waterjet velocity, which is in turn dependent on the supply pressure. A minimum energy level is needed to initiate material erosion. The hardness of the workpiece material also plays a very important role in determining the material removal rate. Harder material requires higher AWJ machining energy. The harder the material is, the smaller the material removal rate.

One advantage of abrasive waterjet machining is its very small machining force in comparison with traditional machining techniques. For example, the measured machining forces are 22 N and 18 N for pure waterjet and abrasive waterjet under supplied pressure of 207 MPa for alumina. The reduction in the machining force is a result of mixing abrasive particles with the pure waterjet stream. Due to the inefficient momentum transfer, the kinetic energy is dissipated during the mixing of abrasive and waterjet stream. It was estimated that about 20% of the pure waterjet input energy is dissipated at lower supply pressure during the formation of the abrasive waterjet.

The fluctuation in abrasive waterjet is mainly due to the cyclic water pressure from the waterjet pump, which has a cyclic period of 1.1 second. The other external factors include vibration of the abrasive waterjet pump system and the non-homogeneity of the machined materials. The abrasive waterjet drilling process is considered as many micro "crack initiation and erosion" cycles. This can be treated as a loading and unloading process. In the crack initiation stage the machining forces increase as the abrasive waterjet impinges the workpiece and creates cracks in the workpiece. In the erosion state, the powerful return flow removes the cracked material. Due to the relative consistency in the machining forces, the abrasive waterjet machining processes can be treated as a quasi-static state, which is the basis for the finite element analysis of the machining process.

The machining forces is linearly proportional to the supply pressure. This can be demonstrated from the following derivation. The hydraulic power of the abrasive waterjet pump system, P, can be expressed as:

$$P = p.\dot{Q} \tag{1}$$

where p is the supply pressure of the waterjet system; $\dot{Q}$ is the waterjet flow rate, which is

$$\dot{Q} = A_j V_j \tag{2}$$

where A_j is the area of the jewel sapphire; V_j is the waterjet velocity exiting the sapphire.

According to Bernoulli's equation,

$$p = \frac{1}{2}\alpha\rho V_j^2 \tag{3}$$

$$V_j = \sqrt{\frac{2p}{\alpha\rho}} \tag{4}$$

where α is the waterjet energy loss in the jewel sapphire; ρ is the density of the water.

Following the mass conservation, we have

$$\rho V_j A_j = \rho V_{im} A_{im} \tag{5}$$

where A_{im} is the waterjet impact area; V_{im} is the waterjet impact velocity.

Assuming that

$$A_{im} = \beta A_j \qquad (\beta \text{ is a constant}) \tag{6}$$

thus $$V_j = \beta V_{im} \tag{7}$$

At jet impact, the impulse of the waterjet can be written as:

$$\dot{I}_{im} = F_{im} = \dot{m}_j (V_{im}\varphi) \tag{8}$$

where φ is the correction factor considering the velocity of the returning flow.

Hence, $F_{im} = \rho \dot{Q} V_{im} \varphi = \varphi \rho A_j V_j V_{im} = \varphi \rho A_j \frac{1}{\beta} V_j^{\,2} = \frac{\varphi}{\beta} \rho A_j \frac{2p}{\alpha \rho} = \frac{\varphi}{\alpha \beta} A_j p$

Or $F_{im} = \frac{\varphi}{\alpha \beta} A_j p$ (9)

If α, β, φ are all constant, the impact force of the waterjet is linearly proportional to the supply pressure of the water. The experimentally measured WJ drilling forces in Table 4.5 is plotted in Figure 4.27. It is apparent that the WJ drilling forces are a linear function of the supply pressure of the waterjet.

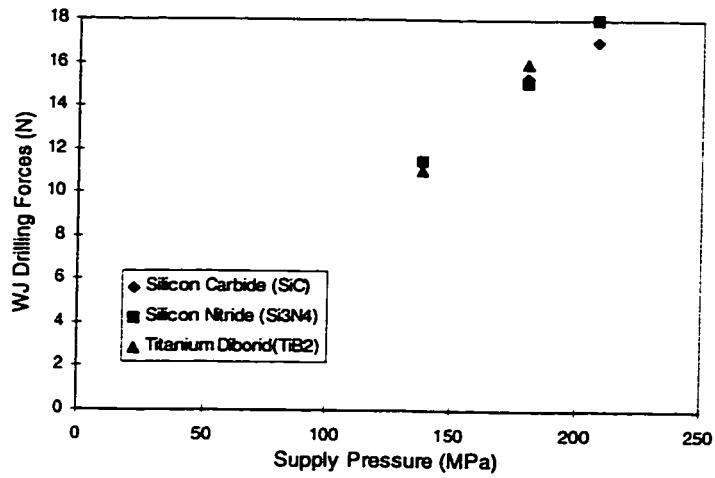

Figure 4.27 Experimental measured WJ drilling forces vs. supply pressure

If the WJ drilling forces is normalized by the hydraulic power, a correlation between the normalized force and the supply pressure can be found. From equation (8),

$$F_{im} = \rho \dot{Q} V_{im} \varphi = \rho (\dot{Q} p) \frac{1}{p} V_{im} \varphi = \frac{\rho}{p} P V_{im} \varphi = \varphi P \frac{\rho}{p} \frac{1}{\beta} V_j = \frac{\varphi}{\beta} \frac{\rho}{p} P \sqrt{\frac{2p}{\rho}} \qquad (10)$$

Finally: $$\frac{F_{im}}{P} = \frac{\varphi}{\beta}\sqrt{\frac{2\rho}{p}} \qquad (11)$$

Therefore, the drilling forces normalized by the hydraulic power is inversely proportional to the square root of supply pressure of the waterjet. If $\phi/\beta=1$, a theoretical trend of the normalized drilling force by the hydraulic power can be shown in Figure 4.28.

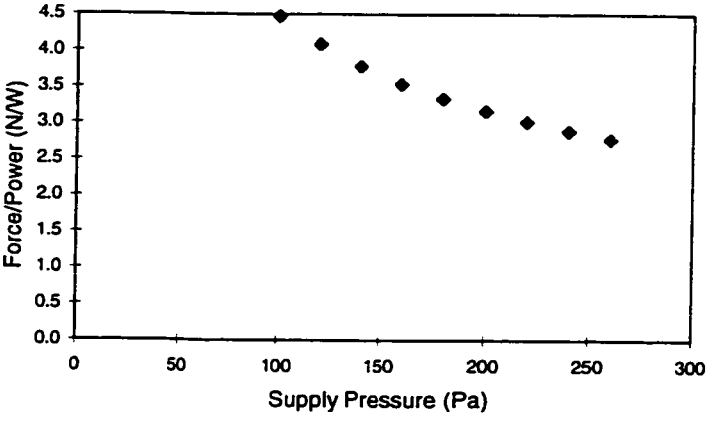

Figure 4.28 Normalized WJ drilling forces vs. supply pressure ($\phi/\beta=1$)

The experimental results on CFCCs have demonstrated that abrasive waterjet machining is a feasible rough and medium machining process. The limited machining forces on the CFCC also demonstrated the abrasive waterjet machining is a viable means for CFCC, since it causes limited damage to the material. The abrasive waterjet machined surfaces can be characterized by three damage regions. They are the initial damage region, the smooth cut region, and the exit roughness region. In an AWJ drilled hole in a CFCC material, the surface damage includes micro-fracture of fibers and matrix, and delamination. There exists a linear relationship between the standoff distance and the

hole taper within the experimental conditions. This relation suggests that reducing the standoff distance between the jet exit and the workpiece reduces the taper ratio of the hole. From surface roughness comparison, it is obvious that the diamond-grit saw creates a smoother surface than the AWJ.

Micro-cutting, shearing, and erosion modes are the dominant mechanisms of material removal during AWJ cutting, which causes minimum material damage to both the fiber and matrix. Due to the brittle nature of the fibers in the CFCC, the pull out of the fibers is generally very short when compared with the abrasive waterjet machining of fiber reinforced plastic, as reported by Chelikani and Kalpakjian [123]. Brittle fracture through abrasive-induced shear loading occurs in both 0° and 90° fiber bundles. In the 0° fiber direction, bundle roll-out seldom exists, which is an indication of a small machining force on the kerf. This is consistent with the machining forces recorded in this study.

The micro-mechanisms associated with AWJ hole drilling include microfracture of fibers and matrix, and delamination and fragmentation of fiber bundles. The micromechanisms of the material removal process change across the cut section from the jet entrance region to the jet exit region. At the jet entrance, the high kinetic energy of the abrasive jet produces relatively clean, independent fracture of the fibers and matrix. The matrix material adjacent to fibers remains intact. Limited fiber pullout and almost no fiber/matrix delamination occurs. However, at the jet exit, the reduced kinetic energy of the abrasive jet produces bending fractures of the fibers, and washing out of the matrix from between the fibers. Fiber/matrix delamination is more apparent. The greater micro damage introduced by the AWJ is apparent in the surface profile. A comparison of the material removal characteristic between the pure waterjet, AWJ, and diamond - grit saw machining on CFCC suggests that AWJ is the most efficient method for rough machining. The machining force with AWJ is the least, and the material removal rate is the greatest. Most importantly, AWJ machined surfaces do not impair the material properties.

SEM investigations of AWJ cut surfaces have also shown that the micromechanisms of the material removal process change across the cut section from the jet entrance region to the jet exit region. Specifically, at the jet entrance, the high kinetic energy of the abrasive jet produces relatively clean, independent fracture of the fibers and matrix. The matrix material adjacent to fibers remains intact. Limited fiber pullout and almost no fiber/matrix delamination occur. However, at the jet exit, the reduced kinetic energy of the abrasive jet produces bending fractures of the fibers, and washing out of the matrix from between the fibers. Fiber/matrix delamination is more apparent. The greater micro-damage introduced by the AWJ is apparent in the surface profile. Therefore, the micromechanisms associated with AWJ hole drilling are: microfracture of fibers and matrix, and delamination and fragmentation of fiber bundles, which are illustrated in Figure 4.29.

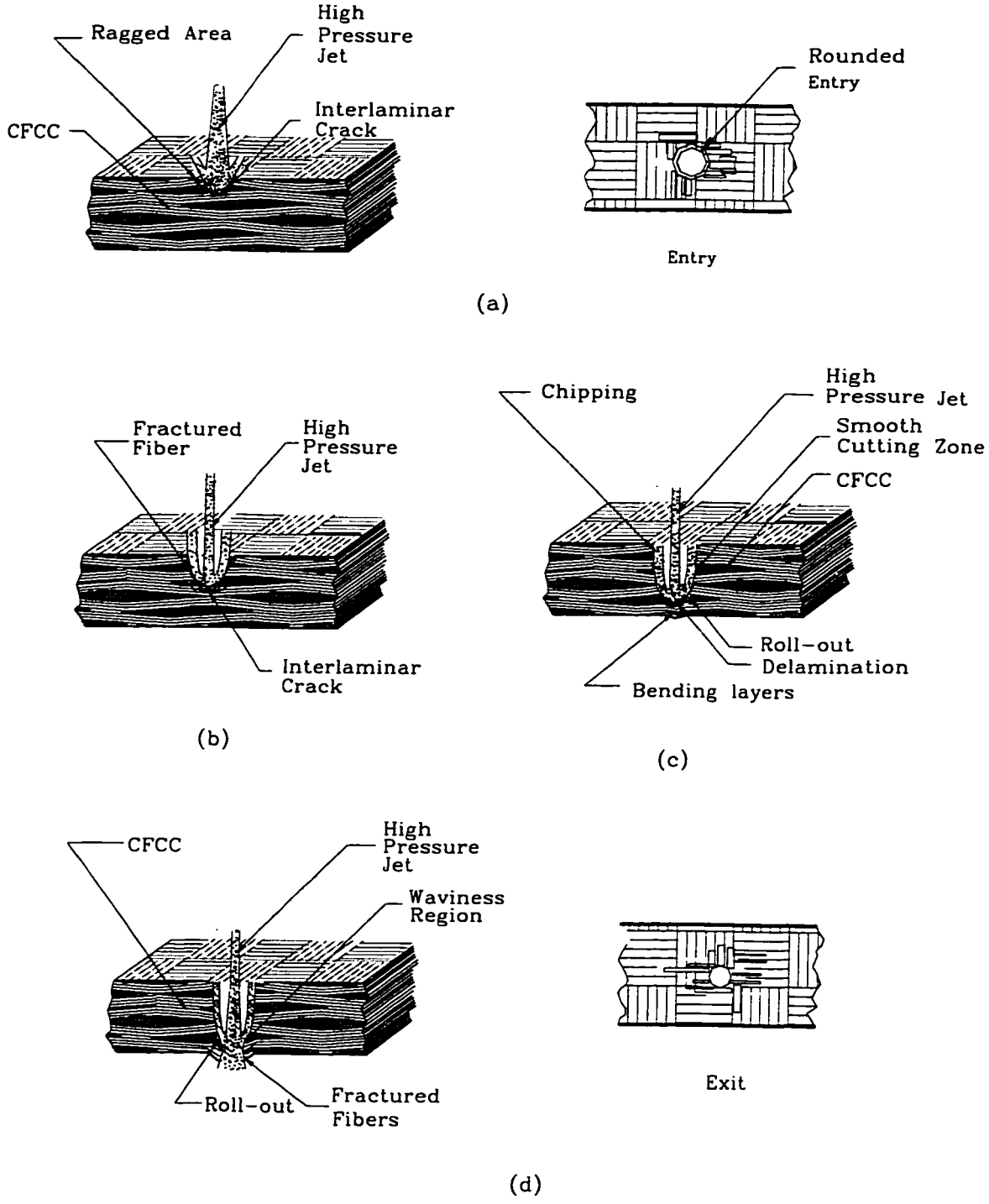

Figure 4.29 AWJ Machining Mechanisms on CFCC Material/

CHAPTER 5

OPTICAL EXPERIMENTS AND NUMERICAL MODELING

5.1 BACKGROUND

A hybrid experimental - numerical analysis approach advanced by Kobayashi [16] was used to study the displacement and the stress state of material while pierced by AWJ. In practice, when using the hybrid experimental-numerical stress analysis technique, the experimental data are interpreted through a physical model of the real event. This real event can equally be interpreted through mathematical and physical models[124]. A combination of mathematical and physical models, which augment each other, provides a better knowledge of the structure and process, as well as the most reliable results in stress analysis. This is because it is often impossible or too costly to find the complete state of stress and strain through experimental means in manufacturing processing. However, with the help of modern computing technology, numerical modeling experiments can be used to calculate the stresses and strains. For the given initial and boundary conditions from experiments, the stress state of a structure can be found by finite element analysis (FEA). In the current study, experimental measurements and numerical procedure have generated the data that were synthesized to understand the material removal mechanisms for polycarbonate and alumina during abrasive waterjet machining. Using the hybrid experimental-numerical stress analysis approach, the transient state of stress or strain associated with the notch crest of the jet induced hole at the impingement zone of the target material during the abrasive waterjet piercing can be numerically modeled.

5.2. OPTICAL EXPERIMENTS

5.2.1 Introduction

The optical experimental technique, moiré interferometry, was utilized to investigate the stress and strain state in brittle polycarbonate and ceramic material during AWJ piercing. The first step was to measure the surface displacement field in a test material, by using the moiré interferometry technique, while the specimen was being pierced by high pressure abrasive waterjet. The force exerted on the specimen by the abrasive waterjet was also measured by using a specially designed force dynamometer. Finally the state of stresses in the machined specimen was numerically analyzed by using a commercial finite element analysis (FEA) code. Through a trial and error process by FEA modeling, the data obtained from the experiments was used to find the loads that caused the displacement as recorded in the form of moiré fringes. In addition, the boundary conditions in the FEA model must conform to those in the experimental situation.

5.2.2 Moiré Interferometry Testing System and Setup

The moiré interferometry experimental system is composed of several mechanical, optical, and electronic equipment configured together to capture the dynamic moiré fringes. Figure 5.1 shows the experimental setup of the optical system and AWJ machining system. The AWJ machining system consists of a waterjet pump and nozzle assembly, which provide high pressure abrasive waterjet for specimen drilling. A specimen fixture includes an abrasive water specimen shield and a specimen holder. A moiré interferometry optical system was set up for measuring the surface displacement of a specimen. Two optical tables were used to arrange the optical apparatus. One of the optical tables was aligned with the abrasive waterjet and the specimen. The other table

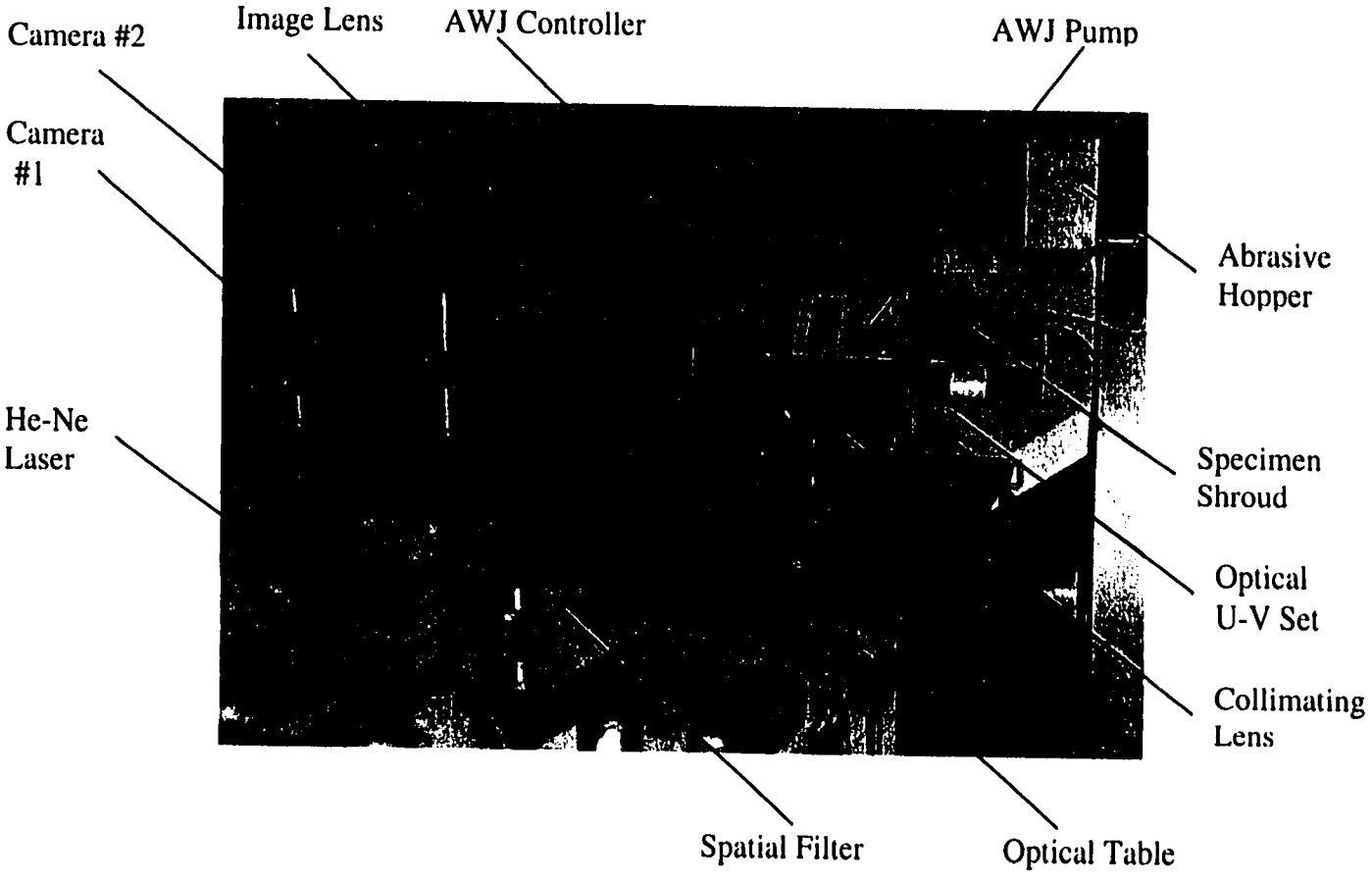

Figure 5.1 Photograph of the Optical Experimental Setup

was used for optical moiré fringe image recording using two cameras. An electronic control box was utilized for linking and synchronizing devices, such as the AWJ pump system and cameras.

5.2.2.1 Test Specimen and Its Preparation

Polycarbonate and ceramic specimens used in the waterjet optical experiments were in thin plate form with dimensions of 25.4 mm x 19.1 mm x 6.25 mm and fabricated by slicing with a diamond saw from a plate of 76 mm x 19.1 mm x 6.25 mm. The surfaces facing the optical setup were ground using a diamond grinding wheel, and were carefully polished before specimen grating was transferred to the polished surface.

The polished specimen was first placed in the specimen holder, which is shown in Figure 5.2. The top surface of the specimen and its contact surface area on the water splash shield were thoroughly cleaned using both acidic cleaning fluid and conditioner. The aforementioned contact area was sealed with epoxy adhesive. The adhesive was cured for approximately 24 hours.

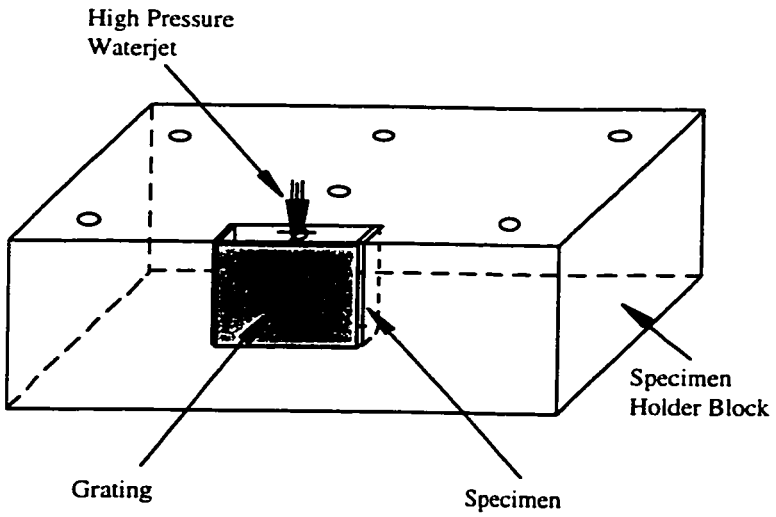

Figure 5.2 Specimen and Specimen Holder

The next step was specimen grating transfer. The grating transfer process is described here following a concise description of the fabrication process of the moiré gratings. The moiré gratings used in the current experiments were produced on a glass photographic plate by using an optical arrangement similar to that described in Figure 5.6. A master grating was necessary and used for calibration purpose. After the photographic glass plate was exposed to the virtual grating created from the above optical system, and after the photographic emulsion was developed, the alternating bands of exposed and unexposed silver halide produced a wave pattern. The waved surface of the photographic plate was coated with a very thin coating of aluminum, using a high vacuum deposition process in the Deposition Laboratory at the Mechanical Engineering Department.

The moiré grating transfer to the specimen surface is one of the most important steps in specimen preparation, which is critical to the success of the whole experiment. The specimen grating transfer process is a replication process, in which the aluminum coated photographic plate serves as a mold. A small quantity of adhesive (epoxy) was applied between the mold and the specimen. Excessive adhesive was squeezed out by slightly applying pressure on the specimen. A two-part adhesive PC-10[125] epoxy was used for the specimen grating transfer, which had a curing time of approximately 24 hours. After the adhesive was cured, the grating mold was stripped off the specimen surface and left a reflective diffraction grating bonded to the surface of the specimen[126]. Before the mounted specimen was put to use, a gauging mark was inscribed around the edge of the specimen grating surface as a scale reference for analysis.

5.2.2.2 Specimen Holder and Splash Shroud

Due to the nature of abrasive waterjet machining, the testing lab can be very dusty and humid. Therefore, adequate protection for the optical setup was a key to the success of this study. The specimen holder was machined from a metal block of 100 mm x 100 mm x 25.4mm, and the optical specimen gratings that adhered to the specimen were

completely shielded from the contaminants by installing a water splash shroud. Figure 5.3 illustrates a specially designed abrasive water shield that was installed to the specimen holder block. The interface between the specimen and the abrasive water shield was sealed with an adhesive. Figure 5.4 is a photograph showing the abrasive waterjet system with the specimen mounted.

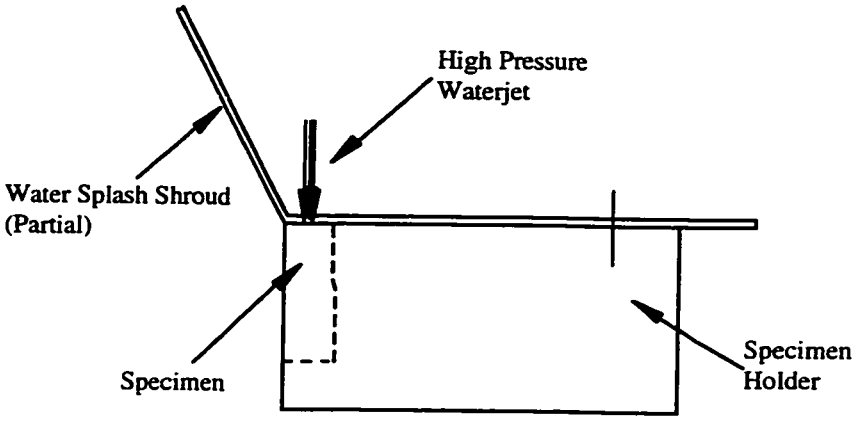

Figure 5.3 Specimen Holder and Splash Shroud Assembly

5.2.2.3 Dynamometer for the Abrasive Waterjet Machining

A dynamometer was designed and fabricated for measuring the real time machining forces exerted by the abrasive waterjet on the workpiece. The dynamometer consisted of a specimen holder, abrasive jet protector, and a dynamic load cell connected to a data acquisition system using a personal computer. A schematic of the force dynamometer is shown in Figure 5.5. The dynamometer system is very sensitive and also very susceptible to environmental temperature change. To minimize the potential temperature effect, the dynamic load cell was very well insulated and protected.

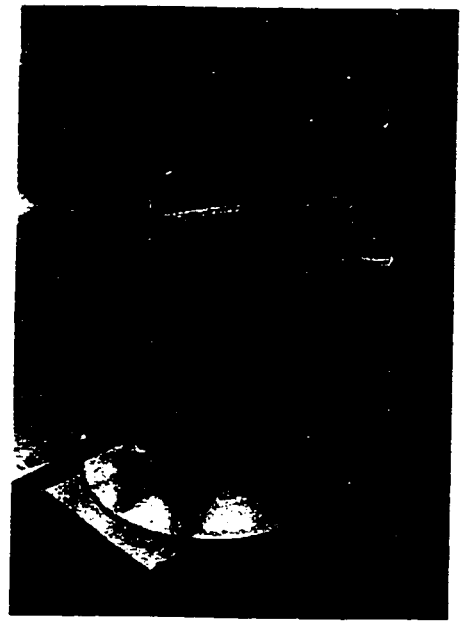

Figure 5.4 Photograph of AWJ System with Specimen

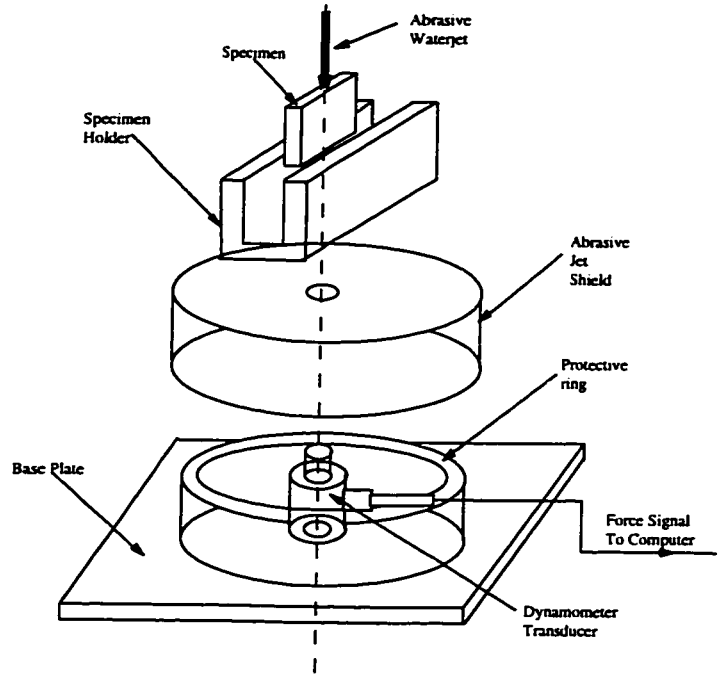

Figure 5.5 Schematic of AWJ Machining Force Dynamometer

5.2.3 Moiré Interferometry Technique

5.2.3.1 Introduction

The moiré phenomenon is a case of optical interference[127]. It occurs whenever two similar, but not quite identical, arrays of equally spaced lines or dots are arranged so that one array can be viewed through the other [128]. However, with high quality arrays of lines with spacing of 1200 lines/mm, moiré interferometry method provides a unique combination of high sensitivity, excellent contrast, range, and spatial resolutions [126]. The advantage of moiré interferometry is that it offers whole-field, in-plane displacement measurements. Thus it has been widely used in the field of experimental stress analysis. The fundamentals of moiré interferometry are given in Appendix C. Moiré fringes represent in-plane displacements of every point on a specimen surface as contour maps of equal-displacement. Quantitatively, for each point in the fringe pattern,

$$u = \frac{N_x}{f} \tag{5.1}$$

$$v = \frac{N_y}{f} \tag{5.2}$$

where u and v are components of displacements in the x and y directions, respectively. N_x and N_y are fringe orders in the u- and v-displacement fields, respectively.

5.2.3.2 Optical Setup and Test Procedure for AWJ Piercing

A four-beam moiré interferometry was used in the dynamic analysis of the jet penetration in the brittle material system. The workpiece, or the test specimen, under high pressure waterjet piercing was held in the specimen holder fixture. The density of the specimen gratings for the moiré interferometry experiments on the polycarbonate and ceramic specimen was 1200 lines/mm. These arrangements provided a moderate sensitivity for measuring the in-plane displacement. Figure 5.6 is a sketch of the optical arrangement for the abrasive waterjet optical setup. It was designed to measure the in-

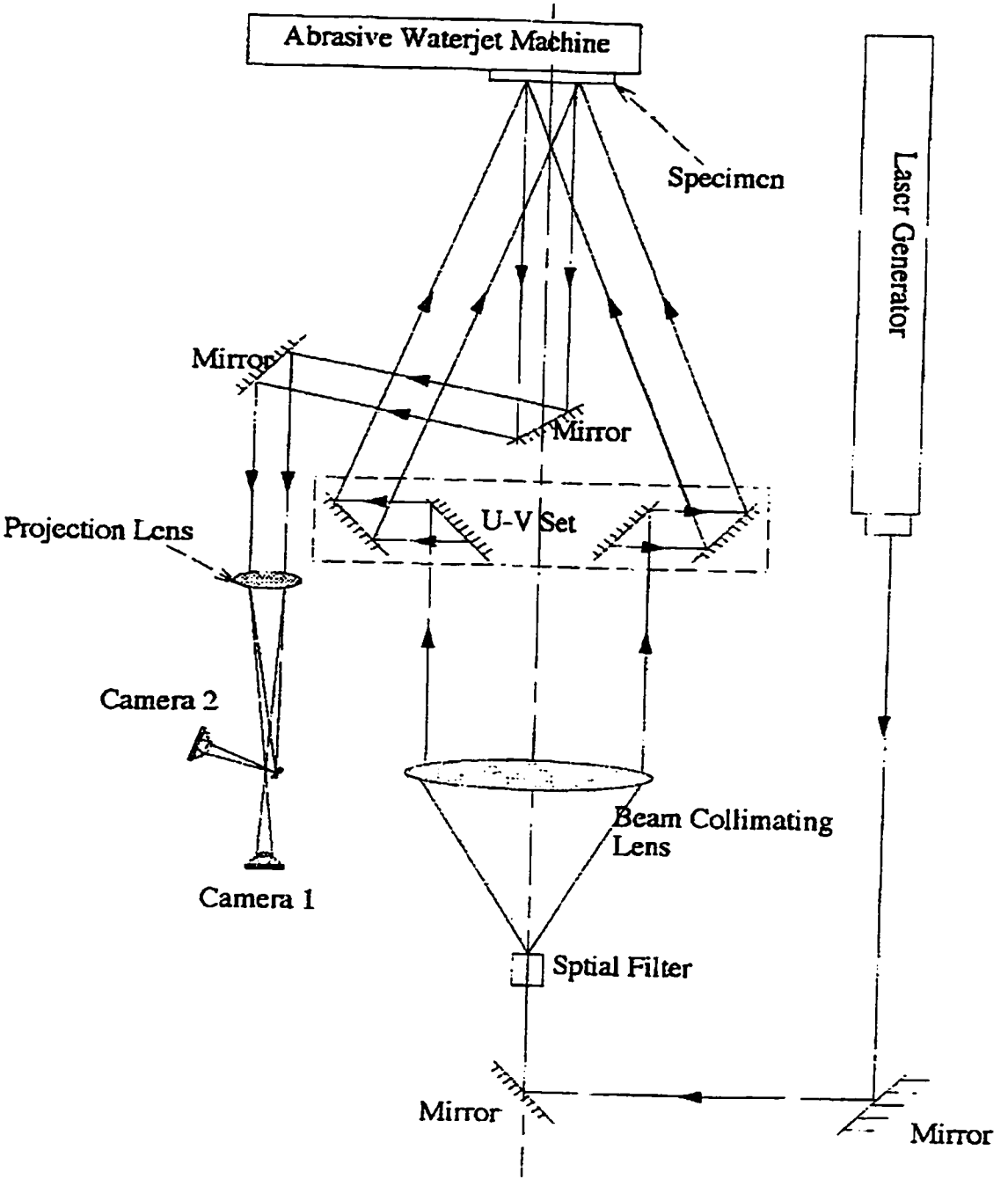

Figure 5.6 AWJ Optical Setup Sketch

plane surface displacements in both u- and v- fields while the workpiece was pierced by high pressure abrasive waterjet. Due to the sensitivity of the optical experiment, the dynamometer was not used during the fringe recording sessions. However, the machining forces were measured separately instead. The WJ/AWJ machining force acquisition system was described in the previous chapter.

The light source used in the optical experiment was a 20 mW polarized He-Ne laser generator (wavelength 632.8 nm). A spatial filter that also filters the noises of the laser beam was used to expand the laser beam. The expanded light was collimated by a large collimating lens shown in Figure 5.1. A custom designed u-v mirror set was designed and fabricated for the moiré experimentation. The two moiré patterns in the orthogonal displacement field, u- and v, were recorded simultaneously with this special arrangement of the u-v set. The u-v fields can be recorded on a single frame of negative film as discussed in Appendix D. In the early phase of the study, two commercial 35 mm cameras with motor drives (maximum speed of 5 frames per second) were used to record the moiré fringe patterns of both displacement fields simultaneously, but separately. A control box designed to synchronize the timing of the abrasive waterjet system and moiré fringe recording system was also utilized. The control box triggers the abrasive waterjet system and the two cameras simultaneously, leading to real time recording of the displacement fringe patterns. A simplified control diagram is shown in Figure 5.7. These cameras were triggered at a selected delay time from the control box. Five frames of transient moiré fringe patterns were recorded per second normally for u and v fields, respectively. In the second phase of the experiments, two commercial high speed CCD (coupled charge diodes) video cameras replaced the single reflective lens (SRL) cameras, and the moiré fringe patterns of both fields were recorded on Hi8 tapes during the abrasive waterjet machining process. These fringes were the real time response of displacement on the workpiece.

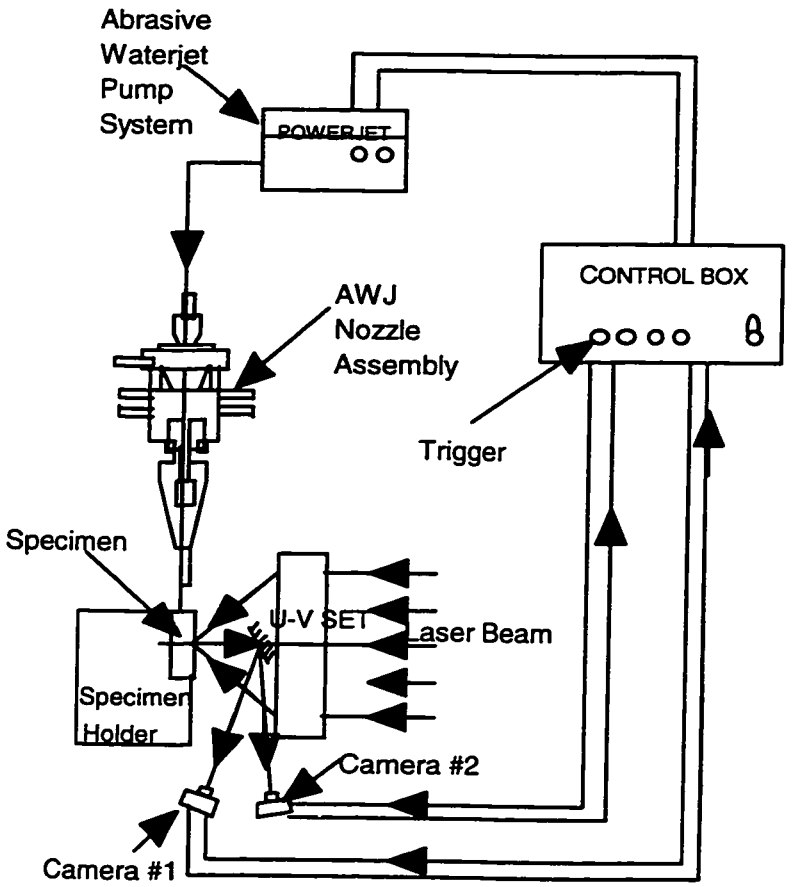

Figure 5.7 Diagram of AWJ Machining Control System

In the first phase of the optical experiments, the workpiece specimen was polycarbonate. Thus the reproducibility and deformation fields can be verified with photoelastic results. After the field surface displacement was obtained through this optical experiment, the field stresses and strains were calculated by using the finite element method that is discussed in next section. Typical moiré fringe patterns for both u and v fields recorded 2.4 seconds after jet exposure are shown in Figure 5.8.

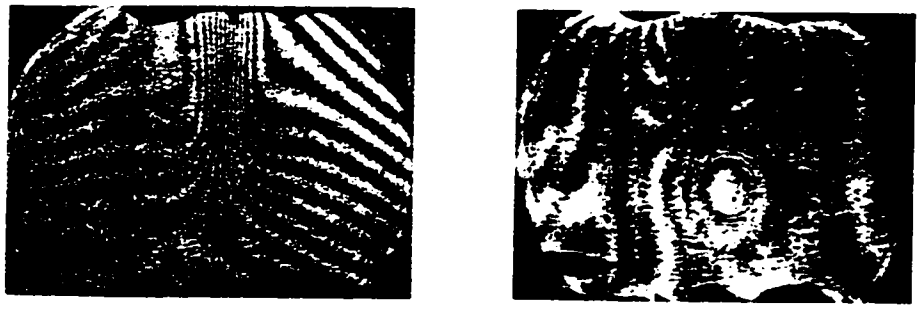

(a) *u* field (b) *v* field

Figure 5.8 Typical Moiré Fringe Patterns

(supply pressure 207 MPa; SOD 1mm; garnet mesh #50; jet exposure time 2.4 seconds)

5.2.4 AWJ Parameters for the Optical Experiments

The AWJ drilling experimental conditions for polycarbonate specimens are given in Table 5.1. In addition to polycarbonate, advanced structural ceramics were of major interest in this research work. However, the moiré interferometry system did not seem to be sensitive enough for Si_3N_4 and SiC materials, due to their high stiffness and hardness. Therefore, the moiré interferometry experiments for ceramics were focused on the alumina AD90 (Al_2O_3) specimens. A wide range of the abrasive waterjet variables was applied to the specimen. The AWJ drilling experimental conditions are tabulated in Table 5.2.

Table 5.1 AWJ Drilling Conditions for the Polycarbonate Specimens

Typical AWJ Parameters	Polycarbonate
Supply Pressure	207 MPa
Standoff Distance	1 mm
Abrasive Particles	Garnet, Mesh # 50
Abrasive Flow Rate	30 g/s
Jet Exposure Time	3 seconds
Orifice Diameter (mm)	0.88
Carbide Tube Diameter	1

Table 5.2 AWJ Drilling Conditions for Alumina Specimens

Typical AWJ Parameters	Alumina		
Supply Pressure (MPa)	125	167	207
Standoff Distance (mm)	1	1	1
Abrasive Particles	Garnet, Mesh # 80		
Abrasive Flow Rate (g/s)	13	14	17.5
Jet Exposure Time (second)	30	30	30
Orifice Diameter (mm)	0.88		
Carbide Tube Diameter (mm)	1		

5.3 NUMERICAL MODELING

5.3.1 Introduction

The finite element code used in this study was a commercial code, ANSYS, of the ANSYS Corporation[129]. This is a large-scale general purpose finite element for various engineering disciplines, such as static and dynamic structural analyses, heat transfer problems, magnetic analysis, fluid analysis, etc. The ANSYS program has been used extensively in various industries, as well as in educational institutions.

High pressure waterjet piercing of a polycarbonate or ceramic specimen was numerically modeled using this finite element code. To implement the FEA, the input data needed for numerical modeling was extracted from optical experiments discussed earlier. The abrasive waterjet drilling on both ceramic and polycarbonate material was treated as a 3-D problem. Similar boundary conditions to those used in the experimental tests were input to the FEA model. The approach to the current FEA analysis was a trial and error process for load matching. Since the current analysis is an inverse problem, the loads and loading combinations applied to the specimen were varied and tested until the surface displacement solutions from the modeling closely matched the experimental moiré fringe patterns. The solution matching process was lengthy because of many variables, such as jet pressure, normal pressure, and shear on a kerf surface for different hole depths. Therefore, a parametric numerical study was conducted first, and will be described in the next chapter. After the optimum loads were found out, the displacement and stress distributions, both beneath the pierced hole and on the surface of the specimen model could be easily extracted from the FEA solutions. In general, this approach yields a much better understanding of the abrasive waterjet machining process.

Solid element, SOLID45, was utilized in this numerical modeling, since this element provides very high accuracy and reliability. The element is defined by eight nodes having three degrees of freedom at each node, as shown in Figure 5.9, where u, v,

and w are the translations in the nodal x, y, and z direction. The shape functions used in this solid element were:

$$u=\frac{1}{8}\{u_I(1-s)(1-t)(1-r)+u_J(1+s)(1-t)(1-r)+u_K(1+s)(1+t)(1-r)+u_L(1-s)(1+t)(1-r)$$
$$+u_M(1-s)(1-t)(1+r)+u_N(1+s)(1-t)(1+r)+u_O(1+s)(1+t)(1+r)+u_P(1-s)(1+t)(1+r)\} \quad (5.3)$$

$$v=\frac{1}{8}\{v_I(1-s)(1-t)(1-r)+v_J(1+s)(1-t)(1-r)+v_K(1+s)(1+t)(1-r)+v_L(1-s)(1+t)(1-r)$$
$$+v_M(1-s)(1-t)(1+r)+v_N(1+s)(1-t)(1+r)+v_O(1+s)(1+t)(1+r)+v_P(1-s)(1+t)(1+r)\} \quad (5.4)$$

$$w=\frac{1}{8}\{w_I(1-s)(1-t)(1-r)+w_J(1+s)(1-t)(1-r)+w_K(1+s)(1+t)(1-r)+w_L(1-s)(1+t)(1-r)$$
$$+w_M(1-s)(1-t)(1+r)+w_N(1+s)(1-t)(1+r)+w_O(1+s)(1+t)(1+r)+w_P(1-s)(1+t)(1+r)\} \quad (5.5)$$

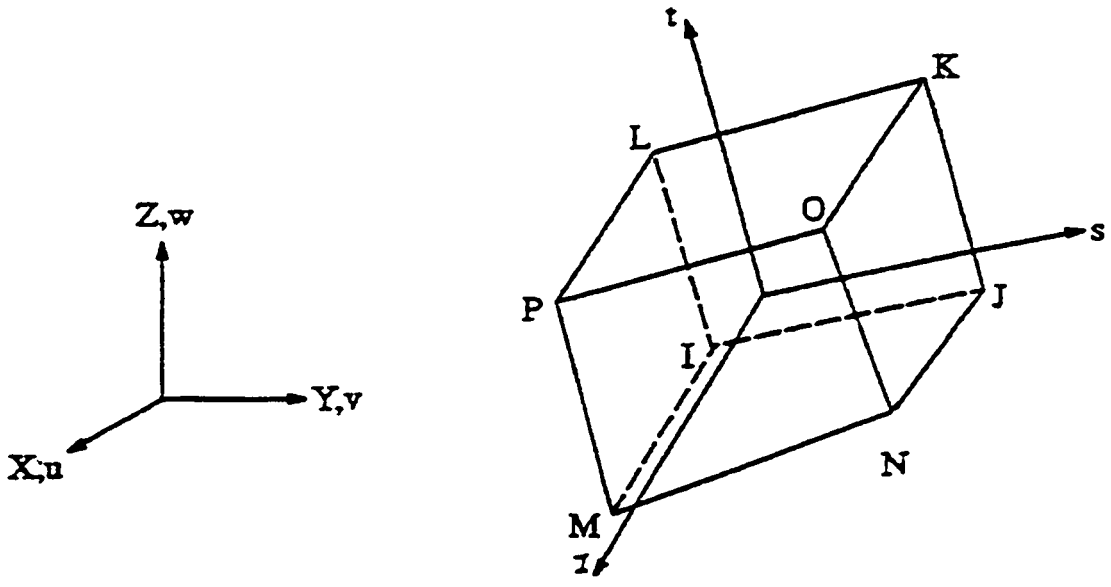

Figure 5.9 Schematic of the solid element used in the FEA modeling

A surface effect element, SURF22, was used for surface pressure application. This 4-node element, as shown in Figure 5.10, was overlaid onto an area face of the 3-D elements. Both in-plane and out-of-plane pressure loads could be specified in this element. The in-plane load refers to the shear on the surface of a 2-D element, and the out of plane loads can be a pressure applied to the element surface in the normal direction or any arbitrary angles.

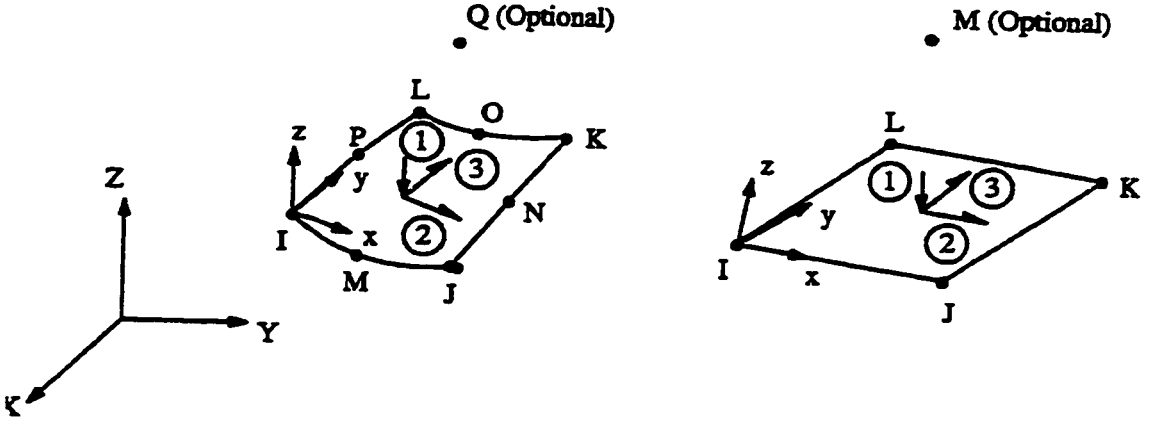

Figure 5.10 Schematic of the 3-D surface effect element

The overall equilibrium equations for linear structural static analysis are:

$$[K]\{u\}=\{F^a\}+\{F^r\} \tag{5.6}$$

where

$[K]$ = total stiffness matrix $= \sum_{m=1}^{N}[K_e]$

$\{u\}$ = nodal displacement vector

N = number of element

K_e = element stiffness matrix

$\{F^a\}$ = the total applied load vector

$\{F^r\}$ = rection load vector

When computing the solution in the finite element code ANSYS, wavefront or frontal solution procedure was used. Wavefront is the number of active equations after any element has been processed during the solution procedure. The ANSYS solver tries to minimize the size of the wavefront by processing the element in an optimized sequence so that the solving time can be minimized. In the case of geometric non-linearity, such as large deformation, Newton-Raphson iteration was utilized to obtain a converged solution.

Small models of simple geometry were created and analyzed using both SOLID45 and SURF22 elements. Various loads were also applied to the small models. The results were verified by comparing them with closed form solutions. The verification study confirmed the accuracy of the elements and the model, and the correct application of the various loads.

5.3.2 Numerical Modeling of Waterjet Penetration Process

Figure 5.11 is a full model of a specimen with a hole in its center. Induced by the abrasive waterjet, the hole approximated a parabolic curvature. The geometry of an AWJ machined hole was measured and drawn in Figure 5.12. This curvature was compared with a standard parabolic curvature used in the FEA in the same graph. It can be noted that the two curves are very comparable. The full model has approximately 15,000 nodes and 13,248 elements.

Since the model geometry was symmetric with respect to the x, y, and z axes, a half model was created for reasons of simplicity and clarity. Figure 5.13 is a typical model mesh of the 3-D geometry for a ceramic plate under high pressure waterjet piercing. The model was generated in ANSYS, using the bottom-up approach, with an eight-node solid element SOLID45 and surface effect element SURF22. In this half model there are 7815 nodes, and 6624 elements were defined. The physical properties for polycarbonate material used in the finite element analysis are listed in Table 5.3.

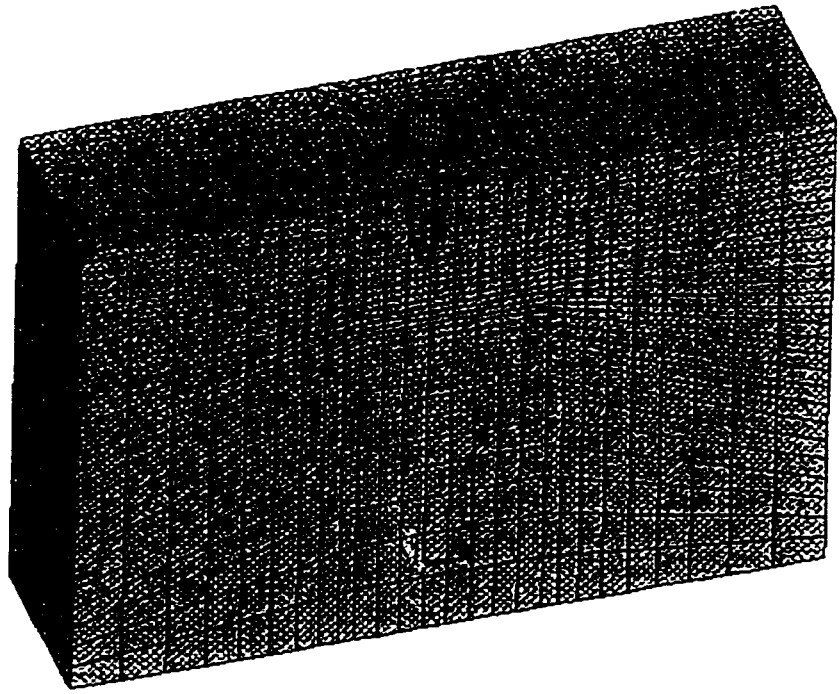

Figure 5.11 A FEA mesh for a full model of a specimen with a AWJ drilled hole

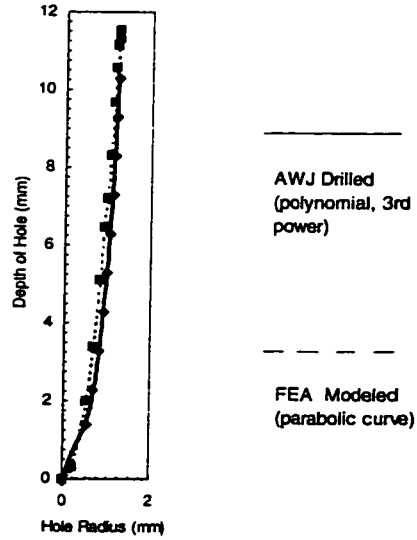

Figure 5.12 Comparison of Profiles of a Hole in Polycarbonate Material
(AWJ Drilled Hole vs. FEA Modeled Hole)

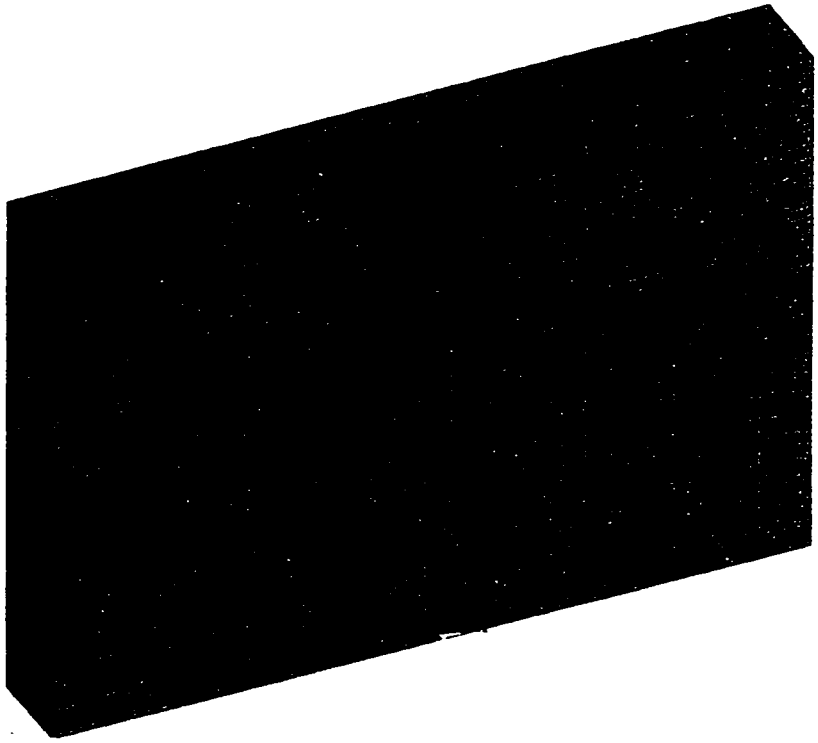

Figure 5.13 Typical Meshed Model for the 3-D Ceramic Plate under AWJ Piercing

Table 5.3 Polycarbonate Material Properties for FEA Use

Polycarbonate Property	Symbol	IS
Poisson Ratio		0.36
Static Young's Modulus	E_s	2.38 GPa
Dynamic Young's Modulus	E_d	2.72 GPa
Shear Yield Strength	τ_s	60 MPa
Tensile Yield Strength	σ_s	64 MPa
Density	ρ	1200 kg/m^3
Stress Intensity Factor	K_{Ic}	3430 KPa*m$^{-1/2}$
Initial Stress Intensity Factor	K_{ic}	2.24 MPa* m$^{-1/2}$

As indicated by the real time machining force data measured during AWJ piercing, the machining process can be treated as a quasi-static process. The high pressure and high speed abrasive waterjet impingement to the specimen was modeled at the center of the alumina or polycarbonate piece. The kerf of the hole created by the abrasive waterjet was modeled as a parabolic curve. According to Tikhomirov [65], there are three types of jet action on the machined material as discussed in Chapter 2. They are impact jet, slipping jets, and slanting jets. Similarly, three loads were also applied to the model, including the jet pressure, the quasi-hydrostatic normal pressure, and the shear on the kerf surface due to reversal flow. The loads recorded by a load cell during an AWJ drilling process was used as a baseline for estimating the pressure loads applied to the kerf surface by the abrasive waterjet. According to the symmetry of the workpiece geometry and the applied load, half of the specimen was modeled and meshed in the finite element analysis. This model was symmetric with respect to the x, y, and z axes. The origin of the coordinate system for the model was chosen at the bottom of the kerf surface, which was fixed in all degrees of freedom.

Continuous waterjet piercing on the workpiece can produce a through hole along the jet path. However, computer modeling cannot take into account of automatic material removal because of its complex machining process. A material removal mechanism has to be supplemented with the code. The challenge is to find a reasonable material removal criterion that best describes the machining process. The damage to a target material caused by the high pressure abrasive waterjet can be from the tensile stresses generated by the impact. A criterion based on crack nucleation and the stress intensity of fracture mechanics will be hypothesized. The approach of numerical data deduction process is shown in Figure 5.14.

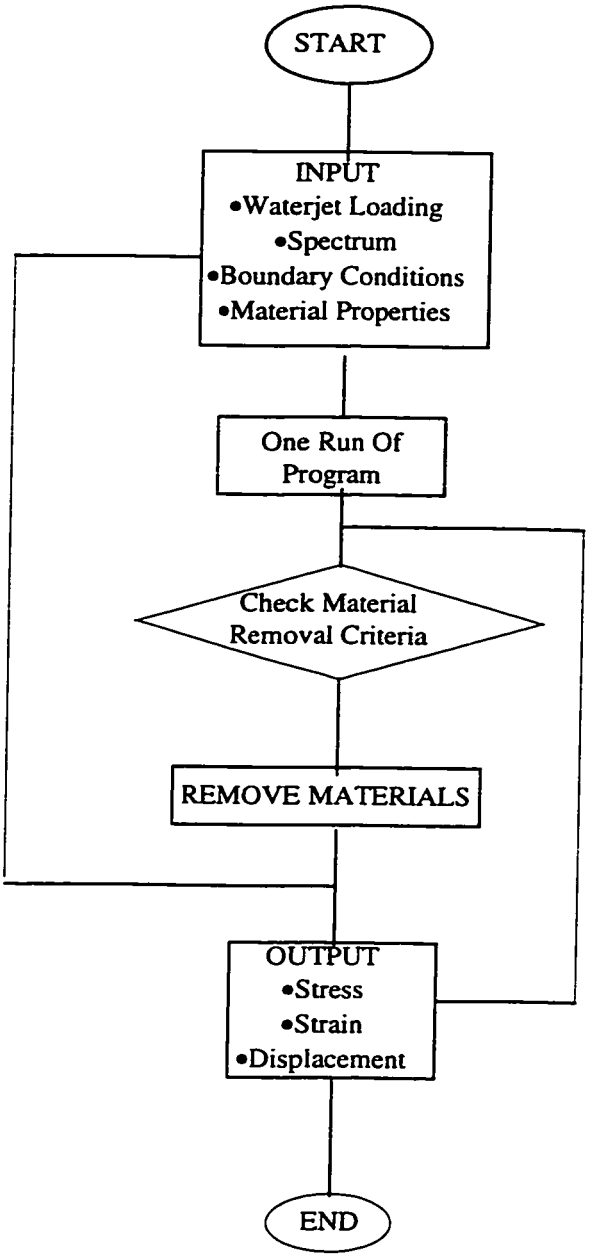

Figure 5.13 A Flow Chart for FEA Modeling of AWJ Machining

One approach to accomplishing the material removal using the FEA model is to utilize an "element death" option within the ANSYS code. Any element with stress intensity that equals or exceeds the predetermined critical value will be deactivated. To achieve the "element death" effect, the ANSYS program does not actually remove the "killed" elements. Instead, it deactivates them by multiplying their stiffness by a severe reduction factor, which can either be the default value 1.0E-6 or a given value. This process was simplified through a macro program in the ANSYS code, but was time consuming.

In order to simplify the modeling process, a different approach was utilized. Instead of using a semi-automatic material removal method, each model was built at a predetermined hole depth simulated using a different meshed model. The boundary conditions used in the simulation were similar to those used in the optical experiments. The loads applied to the model should simulate the AWJ interaction with the workpiece. It was assumed that a combination of pressure load was exerted in the cavity pierced by the AWJ. These AWJ pressures were inversely obtained through surface displacement matching.

The load finding process was by trial and error. For a certain assumed AWJ pressure load, a displacement contour could be obtained using the similar boundary conditions as observed in an optical experiment. The surface displacement contours from the optical experiments were compared with the surface displacement distribution from each FEA run of an assumed AWJ loading. After the AWJ loads for each depth of drilled cavity were found out, the displacement distribution on the outer surface for each depth could be calculated. Therefore, the stress and strain state of the 3-D body workpiece under AWJ piercing could be obtained. In Chapter 6, more details on FEA modeling of the AWJ drilling will be provided.

CHAPTER 6

NUMERICAL EXPERIMENTS AND SIMULATION

6.1 INTRODUCTION

The material removal in the abrasive waterjet machining process is a very complex process of microcrack initiation, micromachining and erosion [16]. Therefore, the process can be modeled with finite element method under certain assumed loading conditions in order to obtain the associated stress and strain distributions. As discussed in AWJ experiments, the reaction forces during AWJ drilling were measured, but the interaction between the AWJ and the specimen, or the impact load distribution within the cavity produced by the abrasive waterjet drilling, is unknown. In this chapter a FEA study is aimed at finding the unknown pressure loads, as well as understanding the relationship among the different loads and their magnitude. Three pressure loads were assumed during the AWJ drilling process. A numerical experiment was executed to study the effects of these loads on the displacement distribution as a function of the depth of hole. The finite element model is verified by comparing moiré interferometry experimental results with numerical results that use this FEA model of specimen under static loading. Both polycarbonate material and alumina material were experimentally tested and numerically analyzed.

6.2 NUMERICAL EXPERIMENTS

As discussed in chapter 3, three types of jet actions are involved during the waterjet penetration process. They are called impact jet, slipping jet, and slanting jet [65]. In order to account for these jets, the AWJ machining action was characterized by three

types of loads. They are: 1)impact *jet pressure* exerted in a small impingement area in the bottom of the hole generated by the AWJ in the case of progressing hole, which is shown schematically in Figure 6.1(a); 2) *shear* that is caused by the reverse flow of the abrasive waterjet, as illustrated in Figure 6.1(b); and 3) *normal pressure* acted on the kerf of the hole shown in Figure 6.1(c). The combined pressure loading from the AWJ impact is depicted in Figure 6.2. The three loads varied in both magnitude and direction at different locations along the kerf of the hole. The *jet pressure* represents the direct impact of the waterjet at the stagnation area. The direction of the jet pressure is the same as the jet direction. The normal pressure simulates the quasi-hydrostatic loading in the machined hole due to the high pressure of the waterjet. The *normal pressure* is applied in the direction normal to the kerf surface, as shown in detail in Figure 6.1(c). The *shear* is caused by the return flow of the abrasive waterjet on the kerf surface, which is applied to the kerf surface in the direction tangent to the kerf. The whole kerf surface is affected by the shear force. The effect of the three pressure loads on the surface displacements distribution was studied by varying the three loads. In each of the FEA loading cases, two parameters were fixed while the third one was varied.

The finite element model described as shown in Figure 5.12 was used for all the modeling with modifications to the depth of holes. The interaction between the AWJ and the solid model with a hole of four selected depths was modeled numerically to mimic the continuous machining process. The hole depths for the solid model with a similar size of the test specimen include 2mm, 4 mm, 6 mm, and 8mm. In the numerical experiments, the jet and normal pressures varied from 0, 1, 2, 3, to 5. The experimental shear included 0, 0.025, 0.15, 0.25, and 0.5. The displacement distribution on the frontal surface under each loading condition at each depth was examined. The modeled surface distributions were compared with the experimentally obtained displacement contours, or the moiré fringe patterns. Both u-field and v-field displacements were compared.

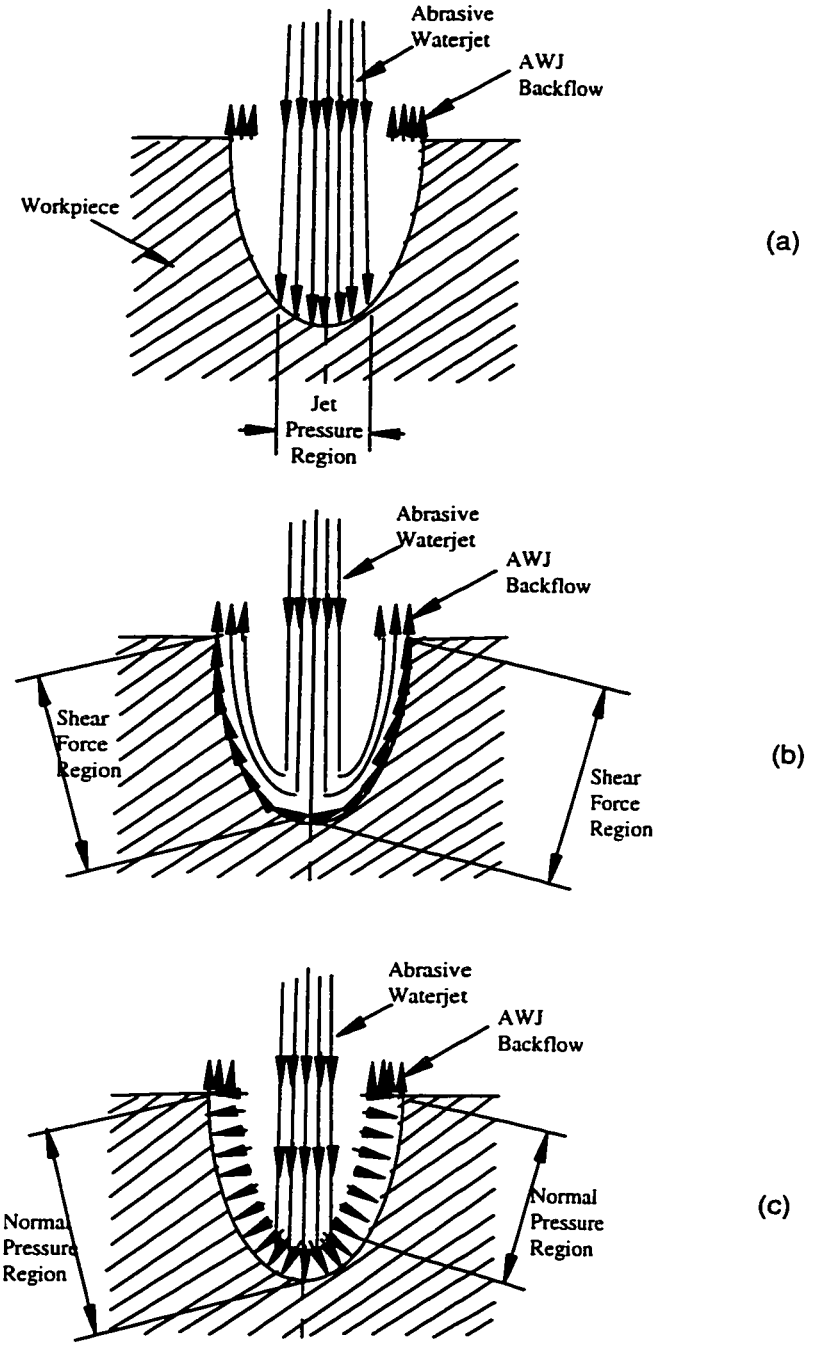

Figure 6.1 Schematic of the AWJ Pressure Loading Components for

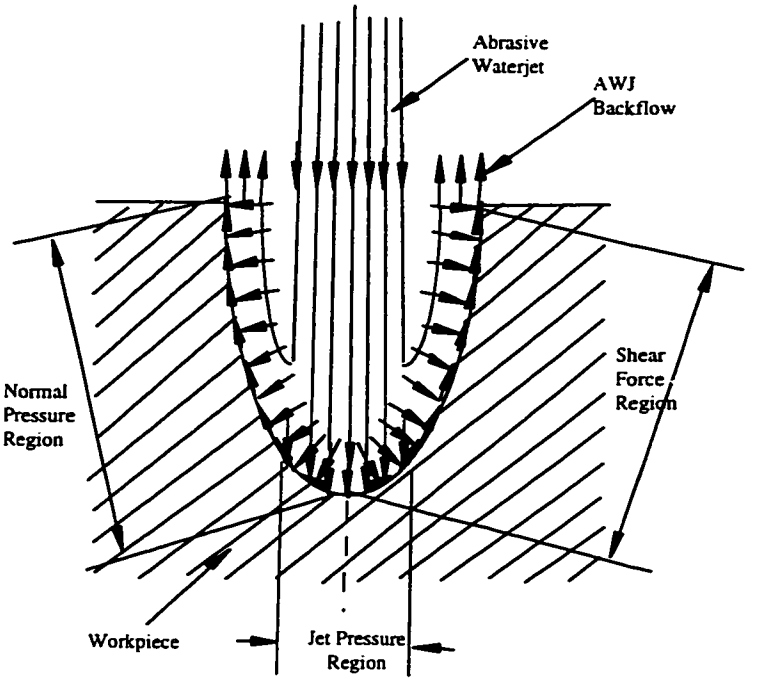

Figure 6.2 Schematic of the combined AWJ Pressure Loading for

6.3 SIMULATION RESULTS

Figures 6.3 (a) and (b) are typical surface displacement distribution contours calculated with the ANSYS FEA program in the *u*-field and *v*-fields for a hole depth of 8 mm with a normal pressure of 5, a shear of 0.2 and a jet of 0. The normal pressure was applied to the kerf, starting from the mid-height to the top of the hole. As shown in Figure 6.3(a), the *u*-field displacements are symmetric with respect to the x=0 plane. The displacements in the area of x>0 are normally positive in sign. They are negative in the area of x<0. That means that the material is moving away from the middle of the specimen under the AWJ action. Near the top edge there are two "eye" patterns. The

maximum and minimum *u*-field displacements are normally located in the two centers of the eyes. In the middle of the frontal surface, there is a horizontal narrow strip, as indicated in Figure 6.3(a). This narrow strip has the minimum *u*-field displacement. Along with the vertical symmetric line x=0, it forms a zero displacement region (ZDR). The height of the zero displacement region varies as the loading conditions are changed. In the *v*-field the displacement contour has two important regions, or patterns. On the top of the model is the maximum compressive region. In the lower portion of the model is the island pattern region. These regions are illustrated in Figure 6.3(b). The maximum compressive region normally lies in the upper middle area, where it has the maximum *v*-displacement *dv* with a negative sign assigned to it. The island like source pattern in the bottom half of the surface represents an area of positive displacement. Along the bottom edge of the model (z=0), the *v*- displacement is zero as shown in Figure 6.3(b). Calculated surface and mid section stress distributions in terms of isochromatic (σ_1- σ_2) and isopachics (σ_1+ σ_2) are shown in Figures 6.4(a) and 6.4(b). It is apparent that the (σ_1- σ_2) is larger than (σ_1+ σ_2) on both surface and mid section. All of them are symmetric with respect to the centerline. Figures 6.4(a) shows the stresses on the out surface, and Figures 6.4(b) shows the stresses on the mid section. At the bottom of the cavity, the (σ_1- σ_2) is not the largest. This may be because the jet forms a stagnation point at the bottom of the cavity, and the return flow exerts shear on the kerf surface.

6.3.1 Effect of the Loading Variables

The three loading pressures, i.e. impact jet pressure, normal pressure, and shear were varied to study the effect of each pressure load on the displacement field in the front surface of the model. All the simulation results are presented in the following sections for varying depths. Since the loads applied to the FEA model were in English units, in this summary the English units were kept unchanged. The pressure loads used are unit pressure for simplicity reasons.

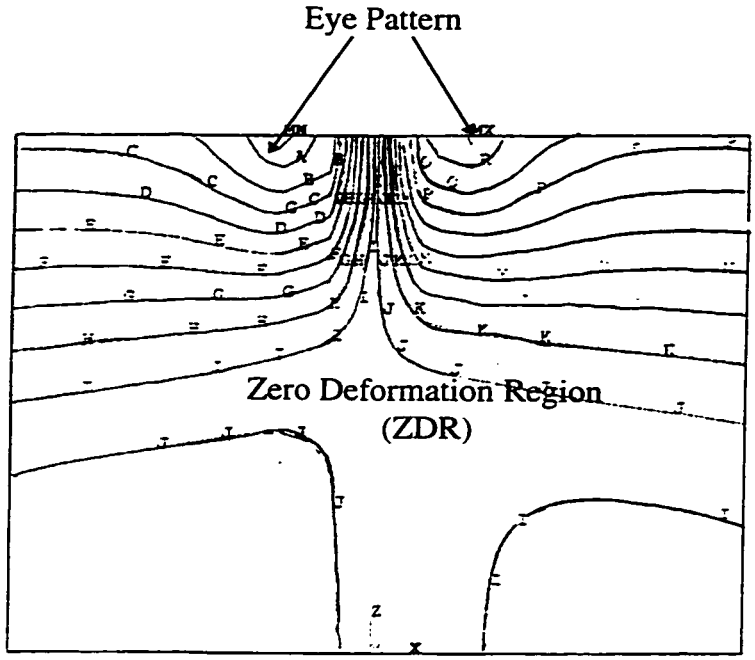

Figure 6.3(a) Typical *u*-field surface displacement distribution contours by FEA

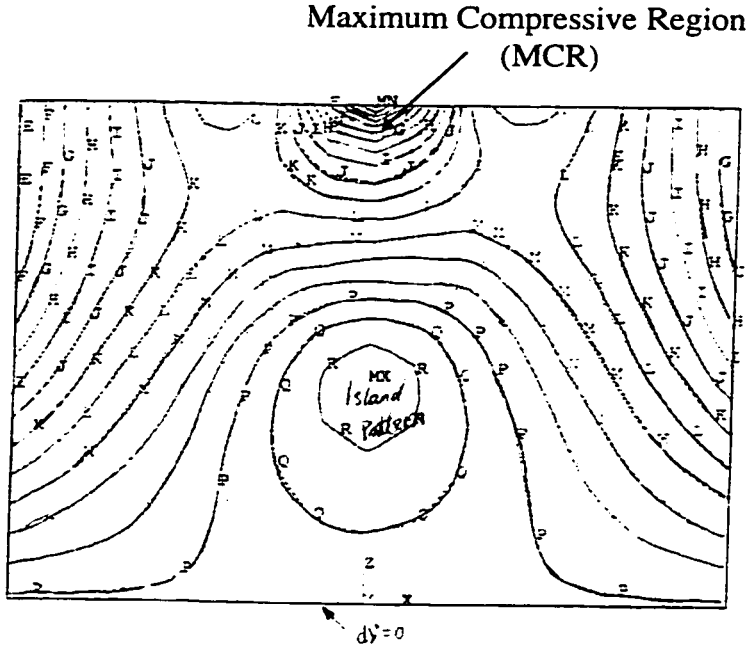

Figure 6.3(b) Typical *v*-field surface displacement distribution contours by FEA

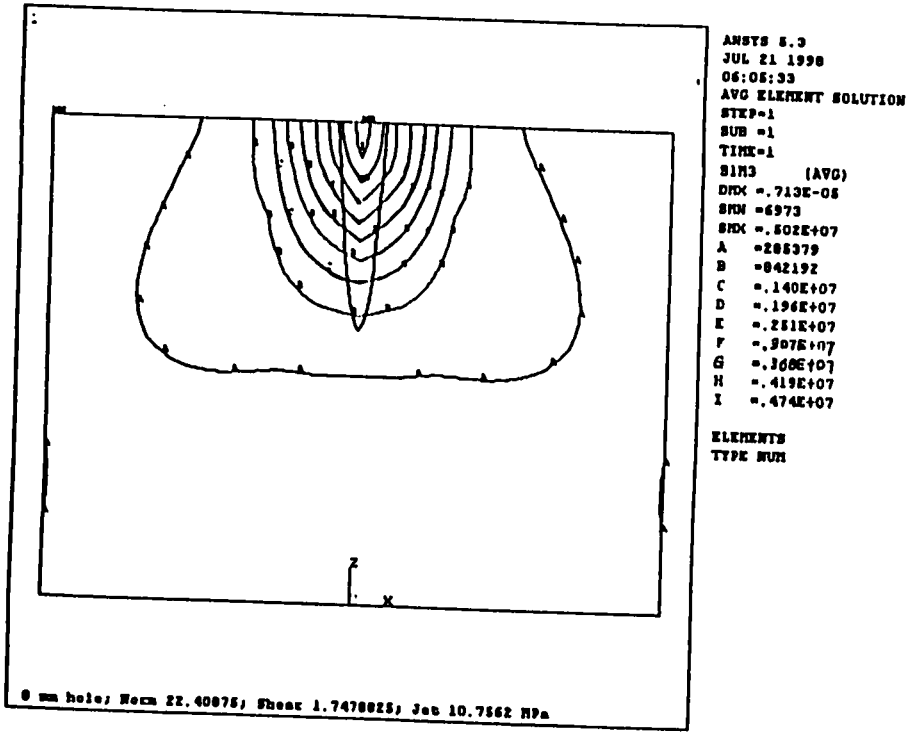

(a) σ_1-σ_3

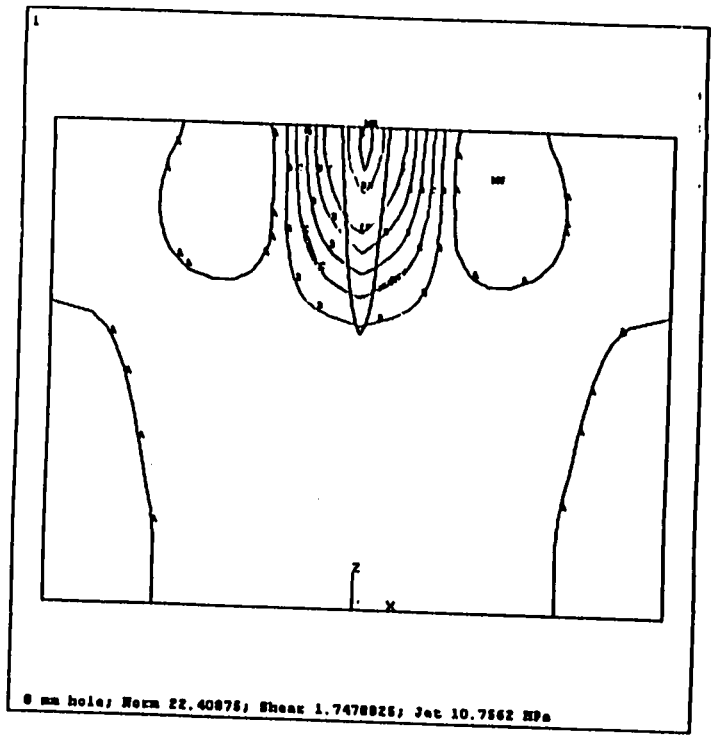

(b) σ_1+σ_3

Figure 6.4 (a), (b). Isochromatic and isopachic contours on the surface

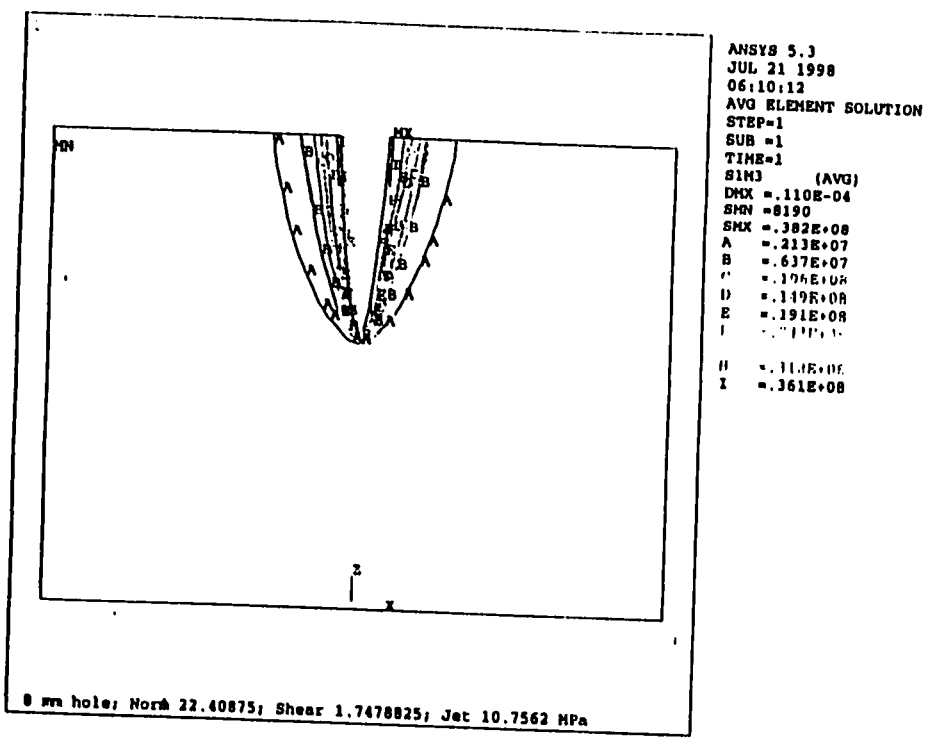

(c) σ_1-σ_3

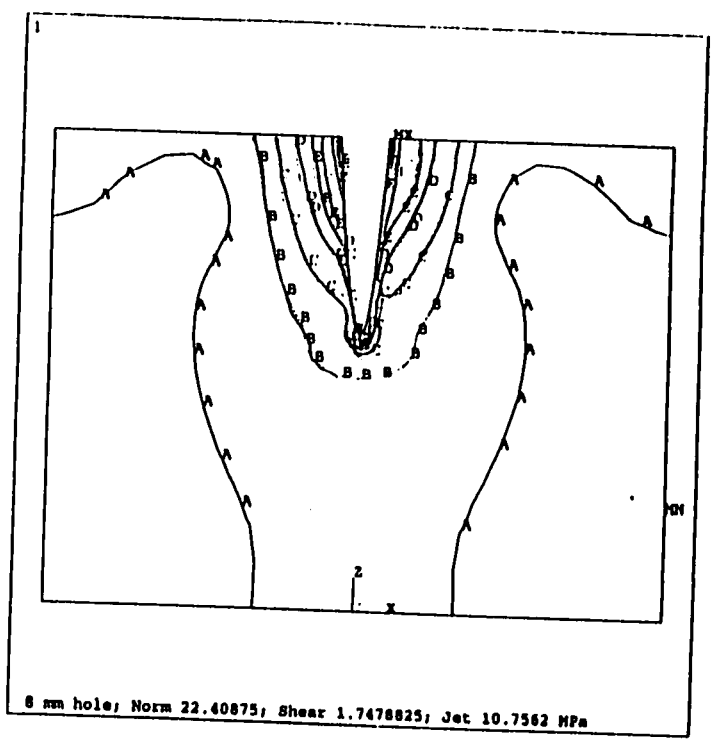

(d) σ_1+σ_3

Figure 6.4 (c), (d). Isochromatic and isopachic contours on the mid section

6.3.1.1 Jet Pressure

The displacement distributions were modeled as the jet pressure increased from 0 psi, 1 psi, 3 psi, and up to 5 psi. The shear and the normal pressure were fixed at 0.2 psi and 5 psi, respectively. The modeling results are summarized in Figures 6.5(a)-(d). In the *u*-field, increasing the impact waterjet pressure lowered the zero displacement region, and the two eyes as well. However, increasing the impact pressure from 0 psi to 5 psi only slightly reduced the maximum and minimum displacements *du* on the surface. It can be observed that the zero displacement region was raised upward as the depth of hole increased for all four loading cases.

In the *v*-field, when the jet pressure increased, the area of the minimum displacement region got larger, and the absolute value of the minimum displacement became larger too. As the jet pressure increased, the area of the *v*-displacement island contour was reduced. As the depth of hole increased, the absolute value of the minimum displacement *dv* became larger, and the maximum displacement *dv* became smaller. When the depth of hole was 2 mm, a positive displacement island region was not formed, even when the jet pressure was increased to 5 psi.

6.3.1.2 Normal Force

Shown in Figures 6.6(a)-(c) are the FEA results for normal pressure of 1 psi, 2 pa, and 5 psi respectively. The shear was fixed at 0.0025, and the jet pressure was 1 psi. In the *u*-field, it appears that the normal pressure exerted on the kerf surface has less dramatic changes to the displacement distribution on the front surface of the model . Increasing the normal pressure lowers the position of the eye pattern slightly. The absolute value of the maximum and minimum *u*-field displacements *du* increase, and are almost proportional to the normal load.

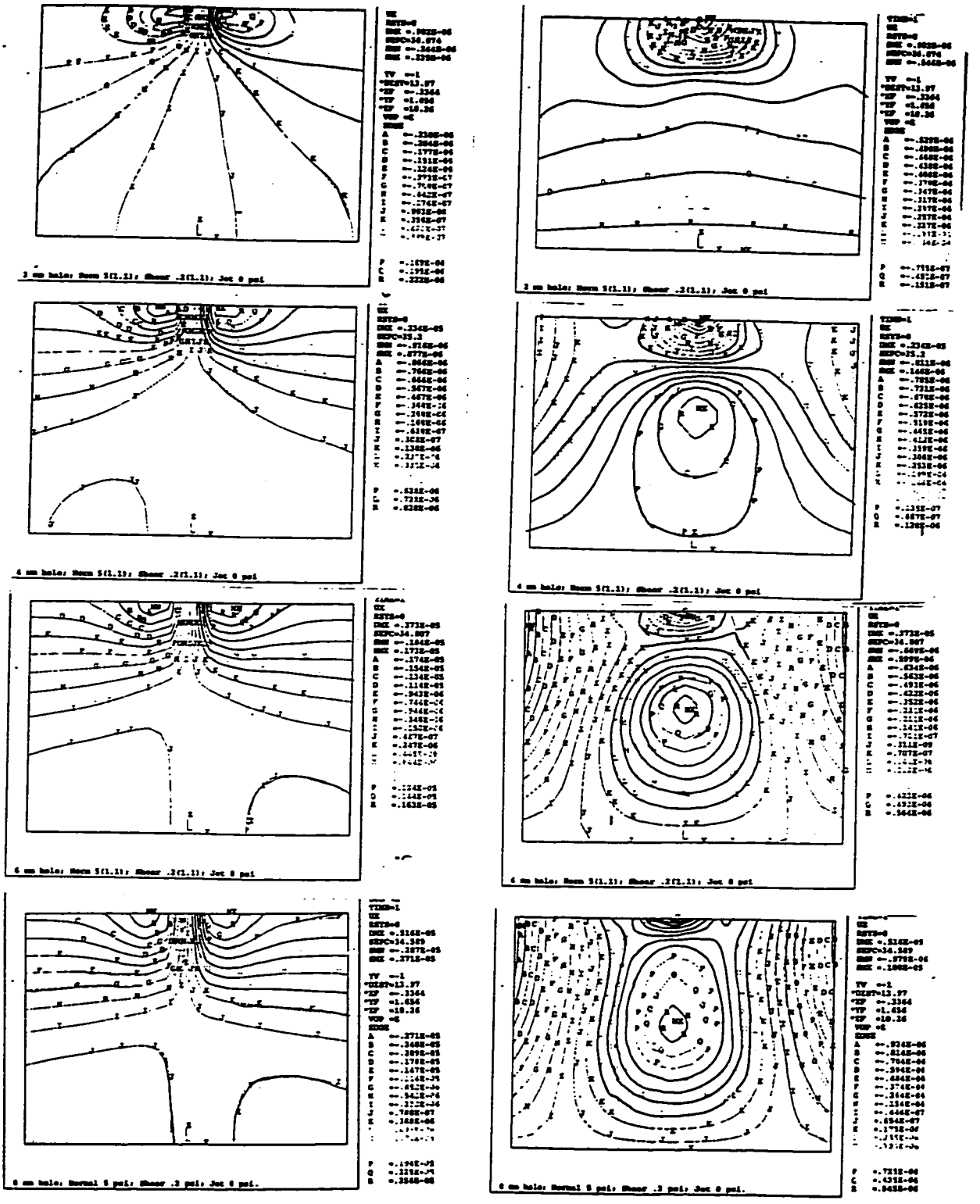

Figure 6.5(a) Effect on displacement with varying jet pressures (0)

(normal 5; shear 0.2)

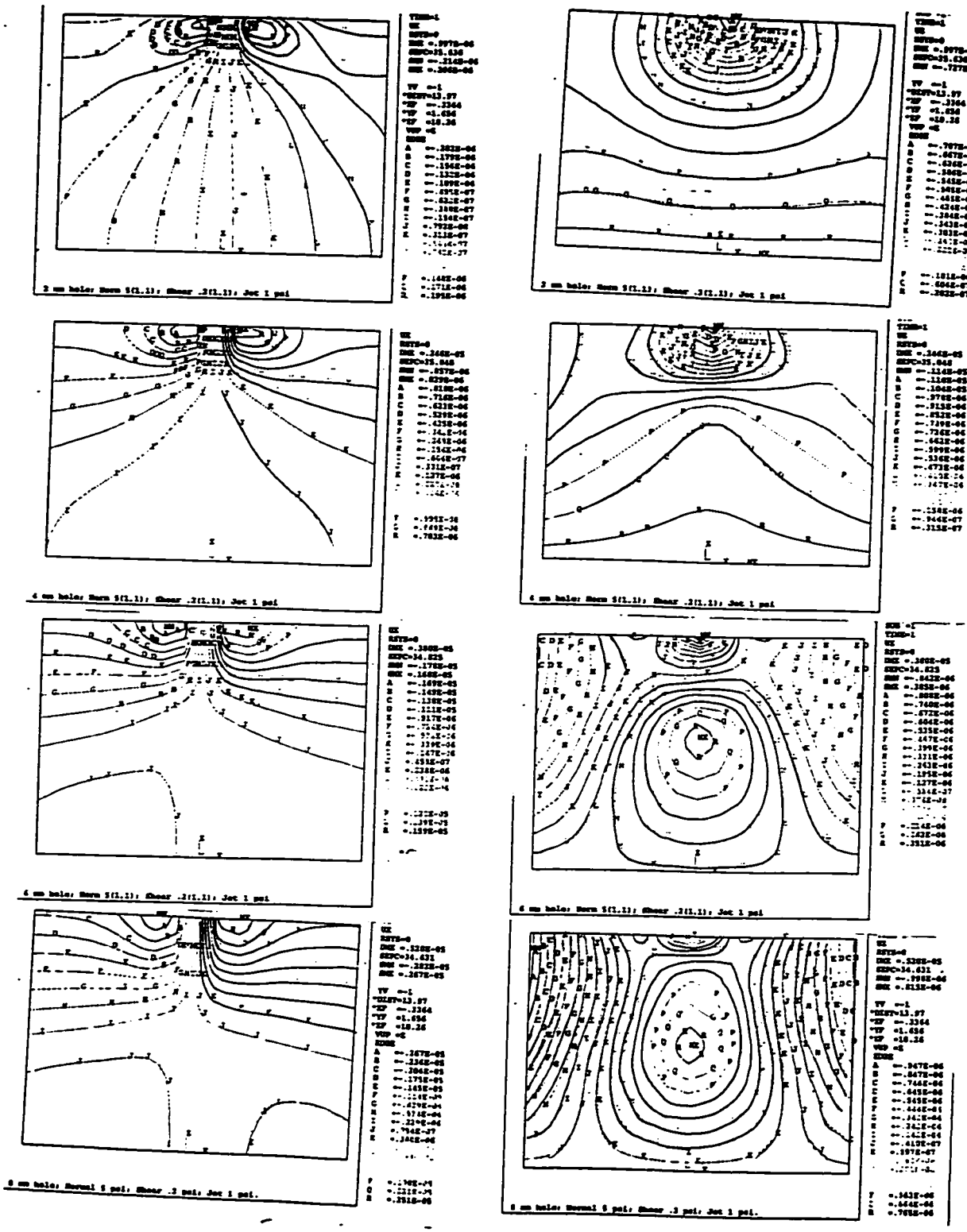

Figure 6.5(b) Effect on displacement with varying jet pressures (1)

(normal 5; shear 0.2)

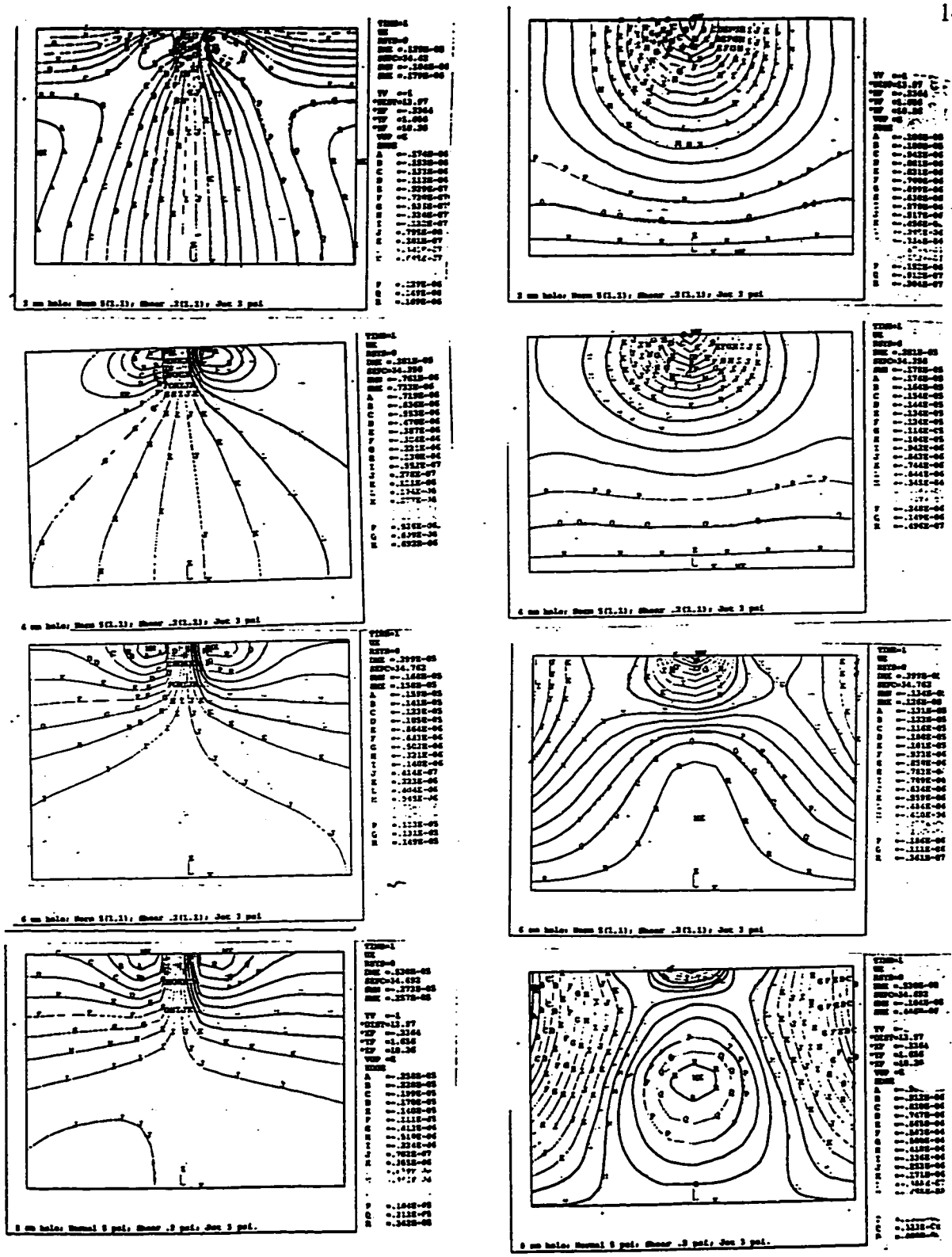

Figure 6.5(c) Effect on displacement with varying jet pressures (3)

(normal 5; shear 0.2)

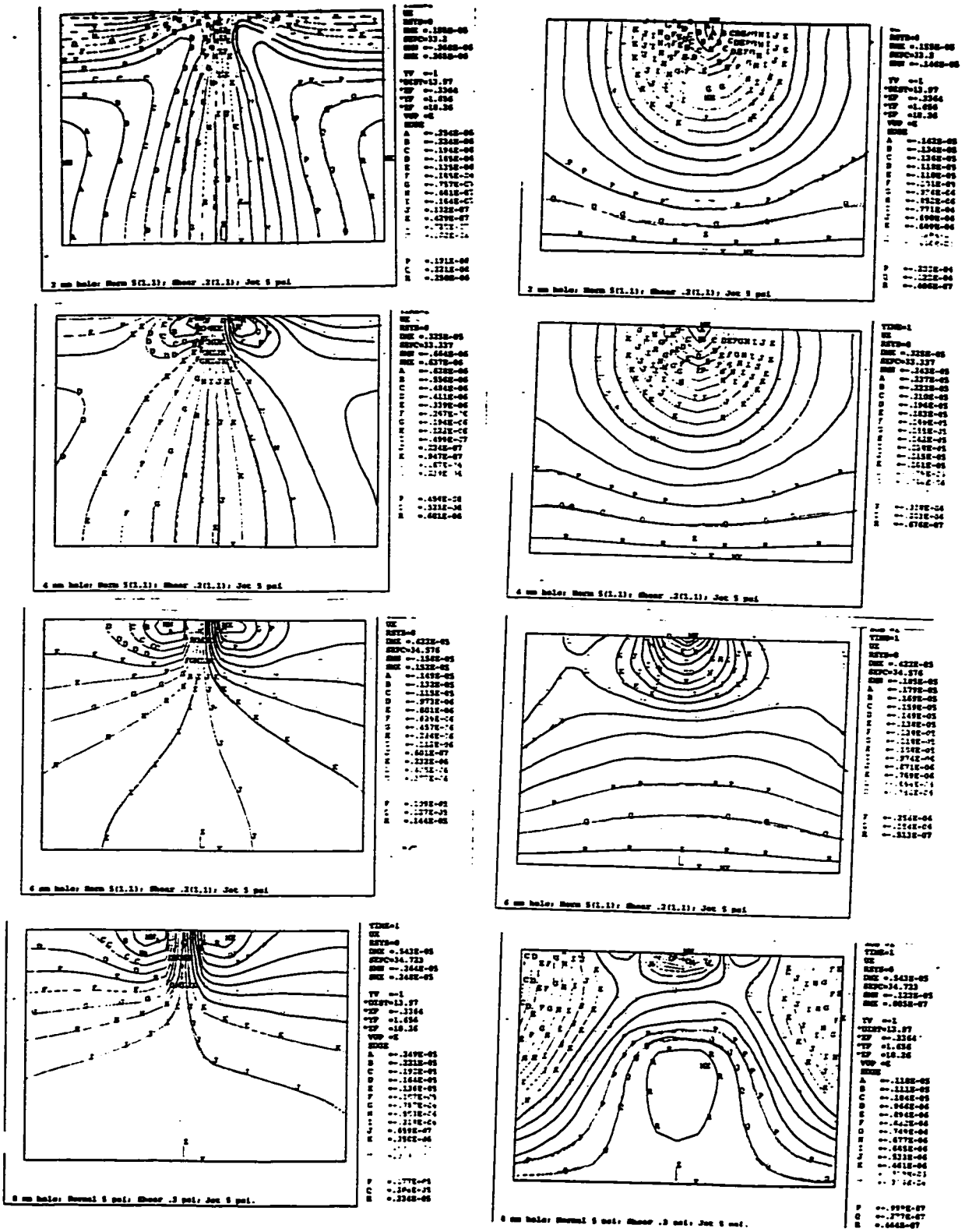

Figure 6.5(d) Effect on displacement with varying jet pressures (5)

(normal 5; shear 0.2)

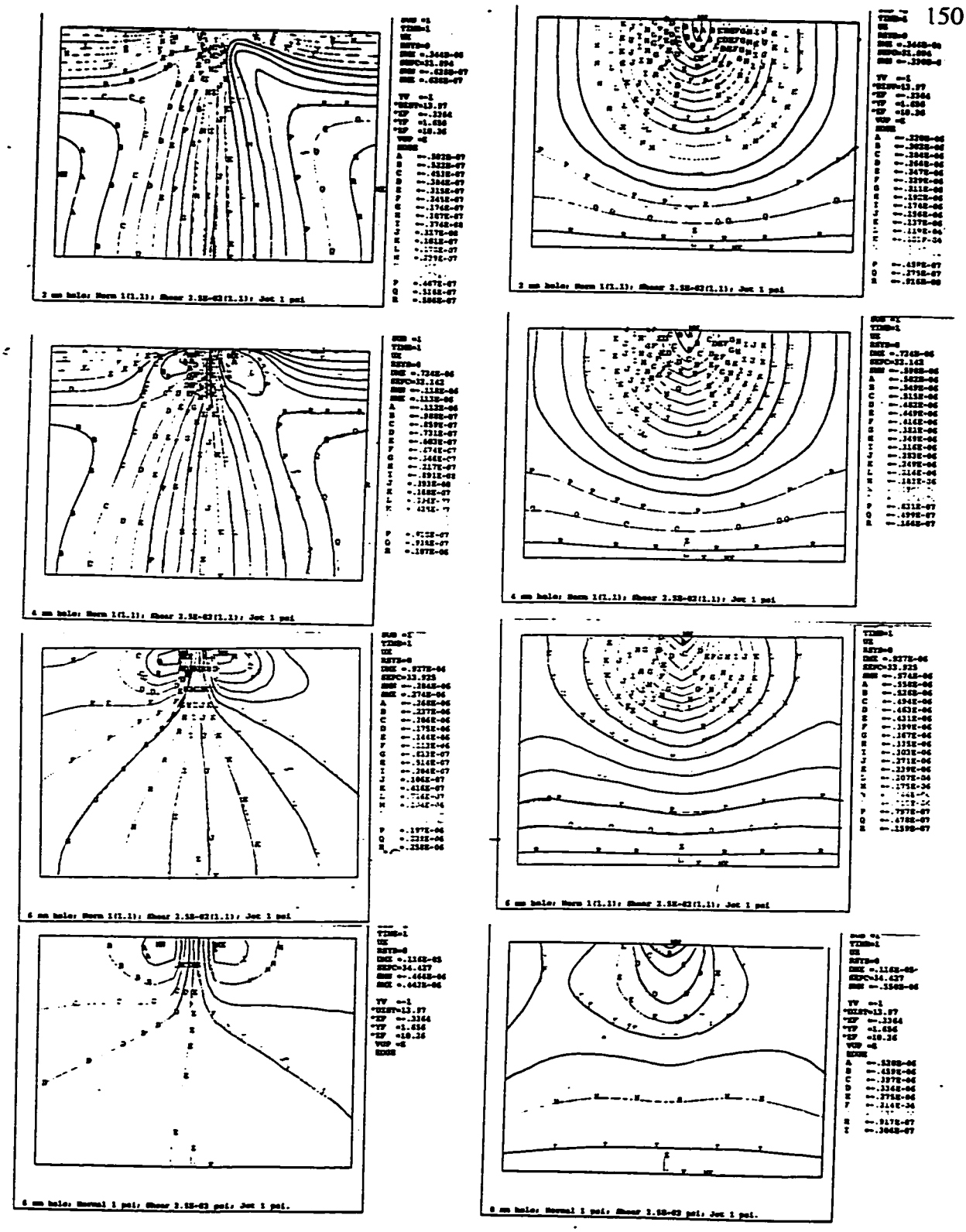

Figure 6.6(a) Effect on displacement with varying normal pressures (1)

(jet pressure 1.0; shear 0.025)

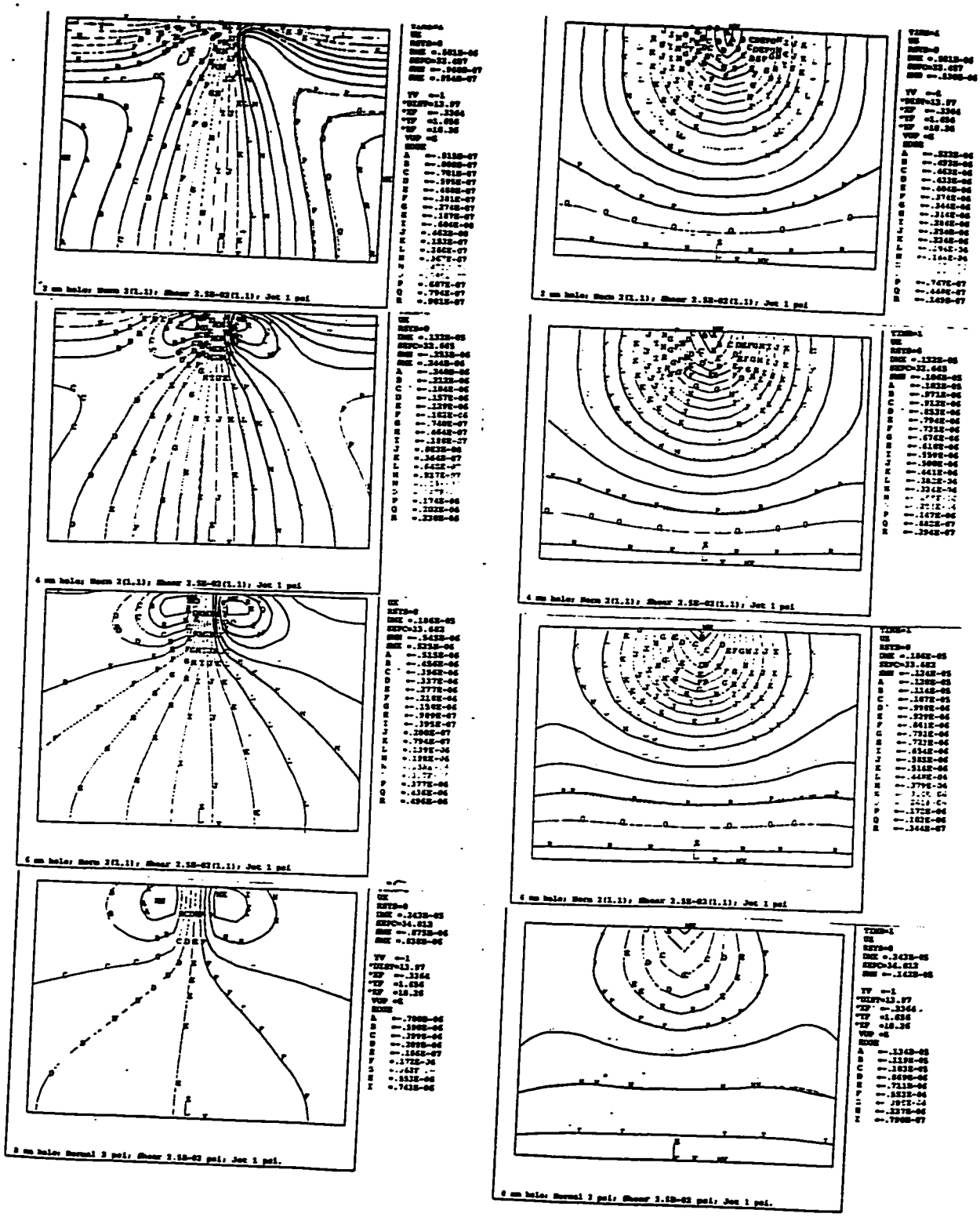

Figure 6.6(b) Effect on displacement with varying normal pressure

(jet pressure 1.0; shear 0.025)

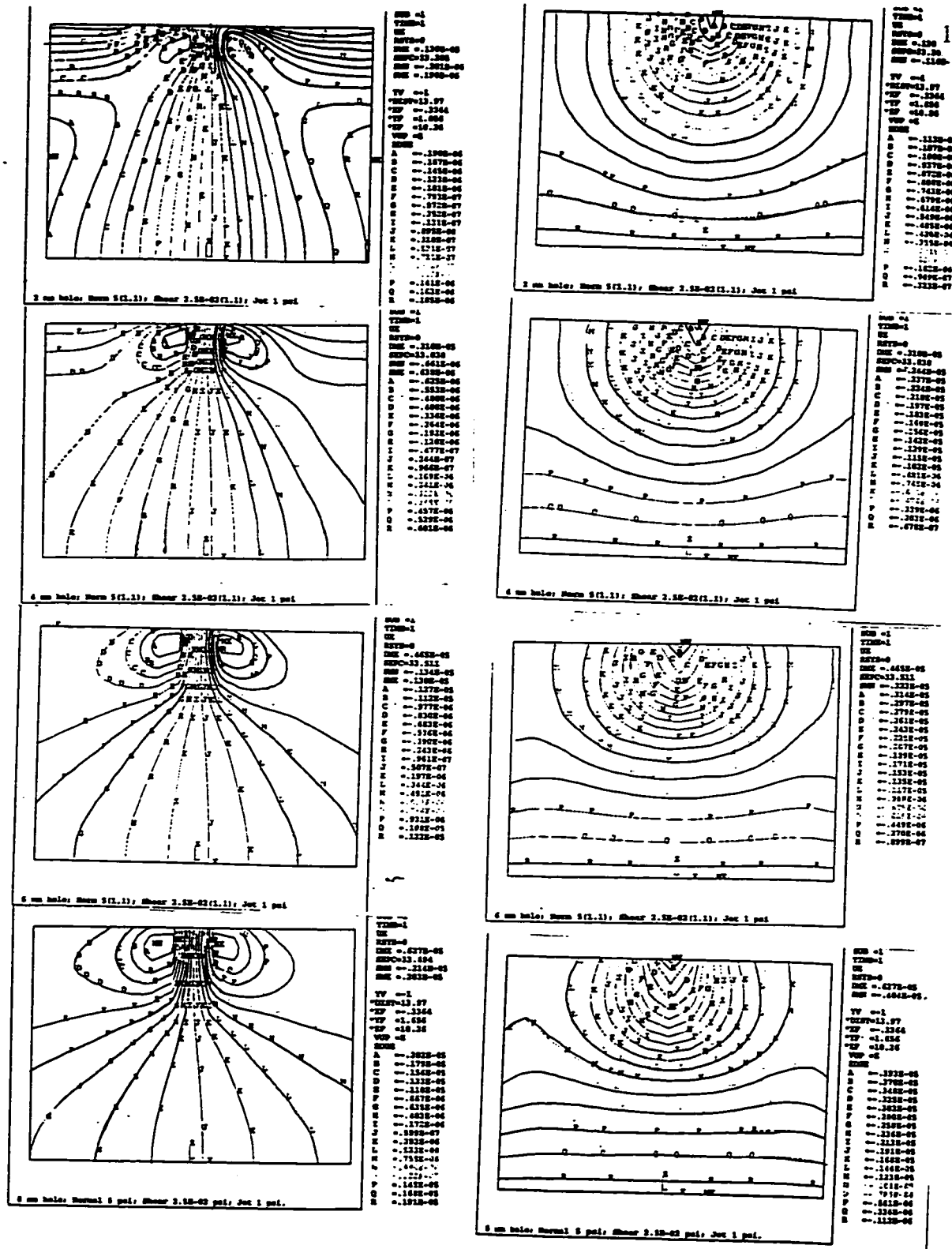

Figure 6.6(c) Effect on displacement with varying normal pressures (5)

(jet pressure 1.0; shear 0.025)

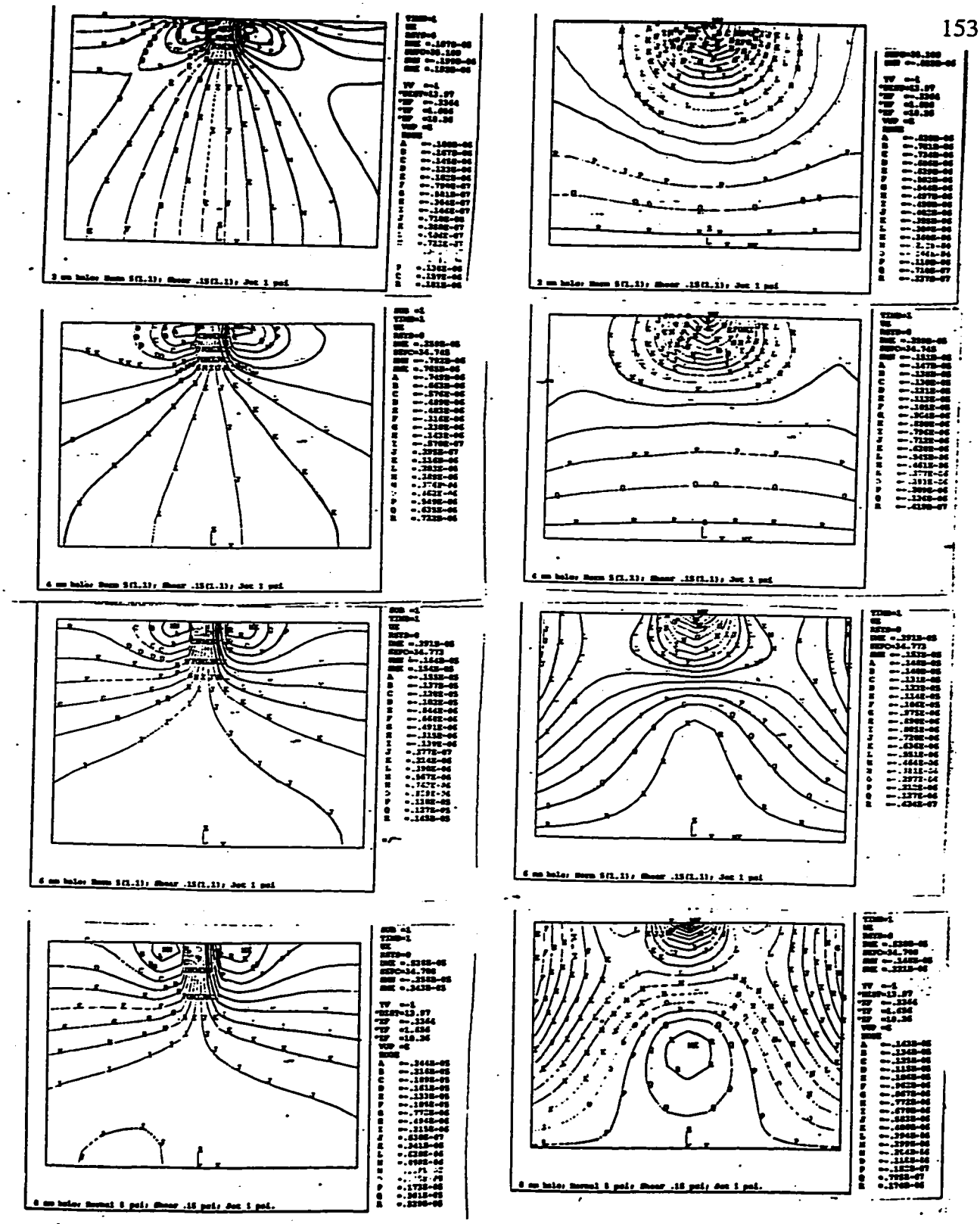

Figure 6.7(a) Effect on displacement with varying shear (0.15)

(normal pressure 5.0; jet 1.0)

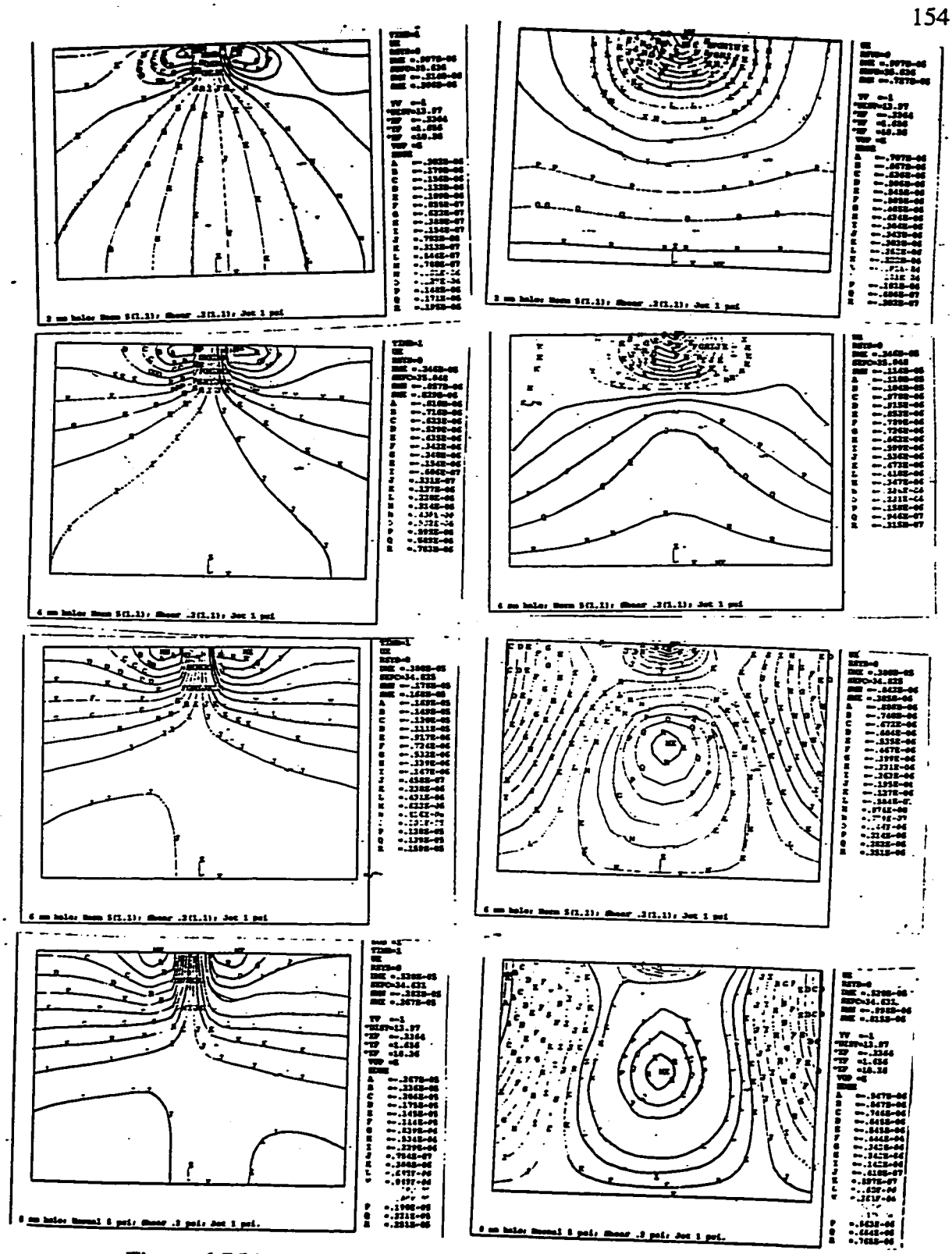

Figure 6.7(b) Effect on displacement with varying shear (0.2)

(normal pressure 5.0; jet 1.0)

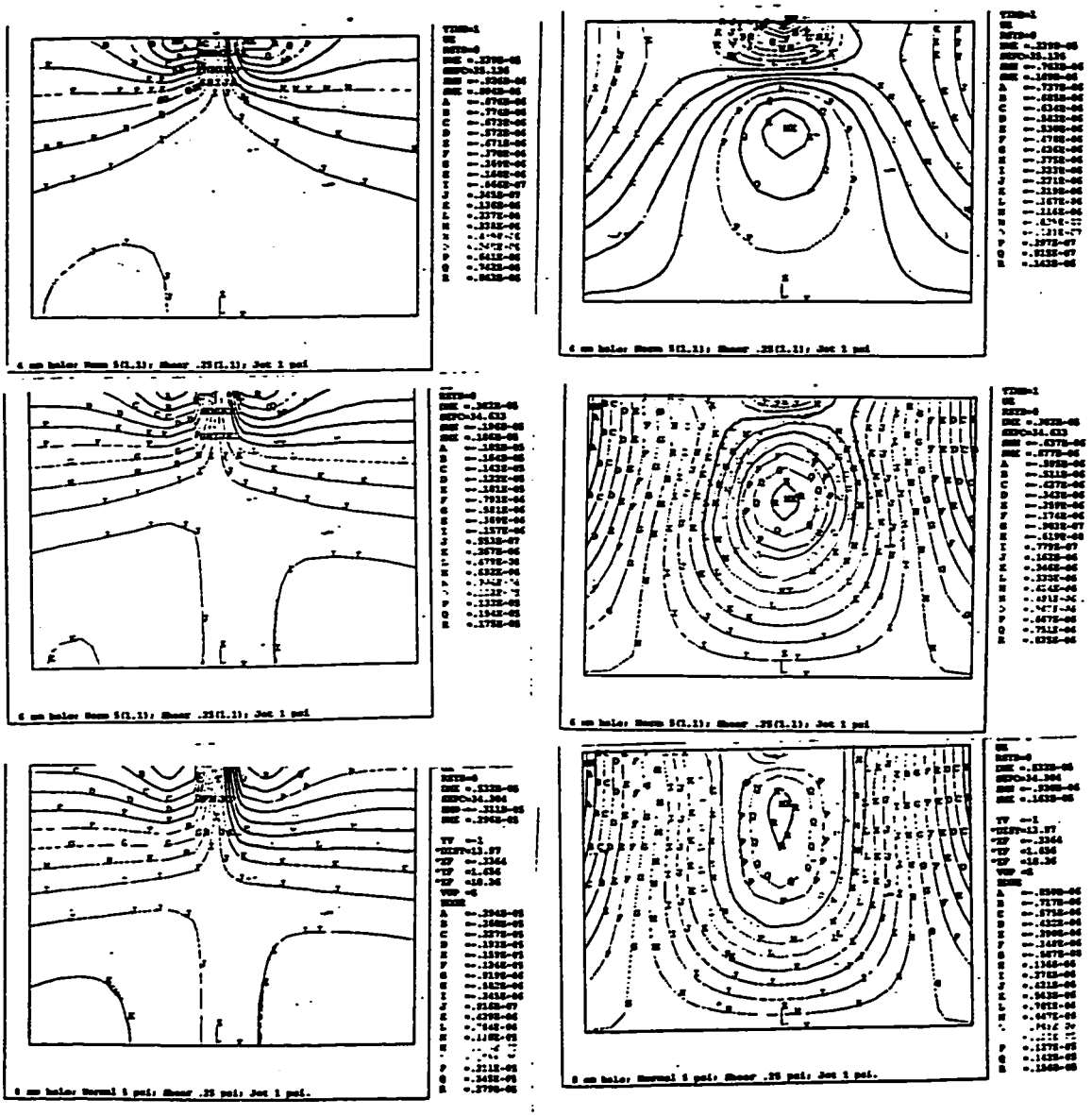

Figure 6.7(c) Effect on displacement with varying shear (0.25)

(normal pressure 5.0; jet 1.0)

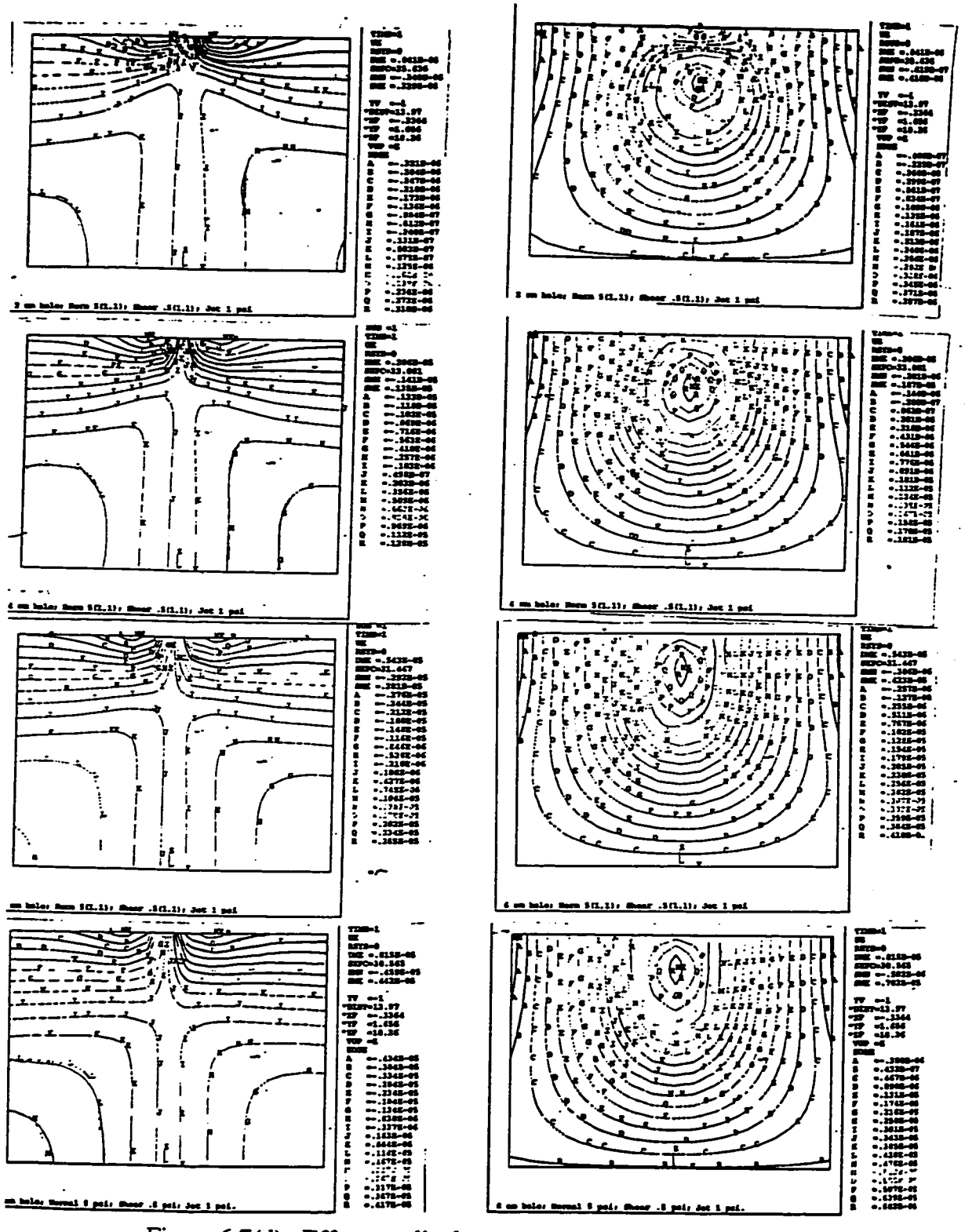

Figure 6.7(d) Effect on displacement with varying shear (0. 5)

(normal pressure 5.0; jet 1.0)

In the *v*-field, increasing the normal pressure does not change the shape of the displacement contour patterns much. However, the magnitude of the *v*-displacement represented by each contour line increases. Increasing the normal pressure will not significantly change the location of the contour patterns on the surface.

6.3.1.3 Shear

The effect of the shear on the surface displacement distribution was investigated. The normal pressure was kept constant at 5 psi, and the jet pressure at 1 psi. The shear was increased from 0.15, 0.2, 0.25, to 0.5. The FEA results are shown in Figures 6.7(a)-(d). The shear appears to produce the most profound change to the look of the moiré fringe patterns. In the *u*-field, as the shear increases, the zero displacement zone is raised upward, and the "eye" pattern is reduced in size. The absolute value of the maximum and minimum displacement also increases. When all three loads were kept the same and depth of hole was varied, the zero displacement region also moved upward. The deeper the hole, the higher the zero displacement region, and vise versa. At shear of 0.5 psi, the "eyes" almost disappear.

The depth of hole does not have a significant effect on the displacement distribution in the *v*-field with the shear at 0.025 psi, normal pressure at 5 psi,, and jet pressure at 1 psi. The compressive displacement contours dominate the full field of the front surface. When shear remains at 0.2 psi, the compressive area becomes smaller and smaller as the depth of hole increases. An island of positive *v*-displacement is formed. The position of this positive island is lowered as the depth of hole increase.

In the *v*-field, the area of the negative displacement region is reduced if the shear is increased. Eventually the negative displacement area region will disappear when the shear load is increased to a certain level. The island contour pattern, representing the positive displacement region, is formed and raised higher as the shear increases.

6.3.2 Loading Uniformity along the Depth

In the above parametric analysis, the impact jet pressure, normal pressure, and shear were applied to the kerf surface with the same magnitude. In this section, the effect of the non-uniformity of these loading variables was investigated. Figure 6.8 is an illustration of the loading non-uniformity applied to the modeled hole in FEA. The normal pressure is divided into two sections along the kerf surface. The magnitudes of the normal pressure in the upper portion and the lower portion are different. Similarly, the magnitudes of the shear in the upper portion and the lower portion are also different. Figures 6.9(a)-(c) are typical parametric FEA results. Greater normal pressure in the lower portion of the kerf than in the upper portion reduces the size of island pattern in the v-displacement field. Increasing the shear in the top portion of the kerf moves the island pattern upward. The results of this parametric study demonstrate that a uniform shear along the kerf surface of the hole produces the best displacement distribution contours matching the experimental moiré fringe patterns.

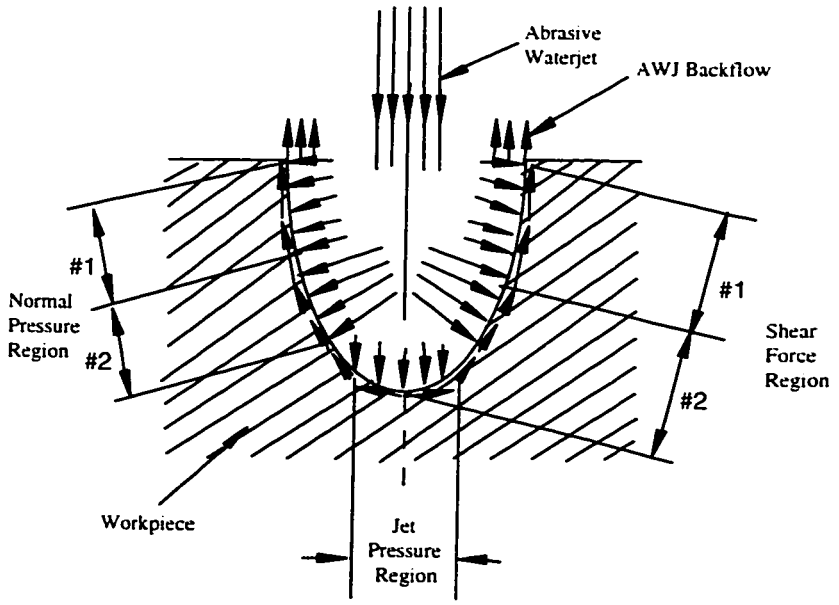

Figure 6.8 Schematic of the Un-uniform AWJ Pressure Loads

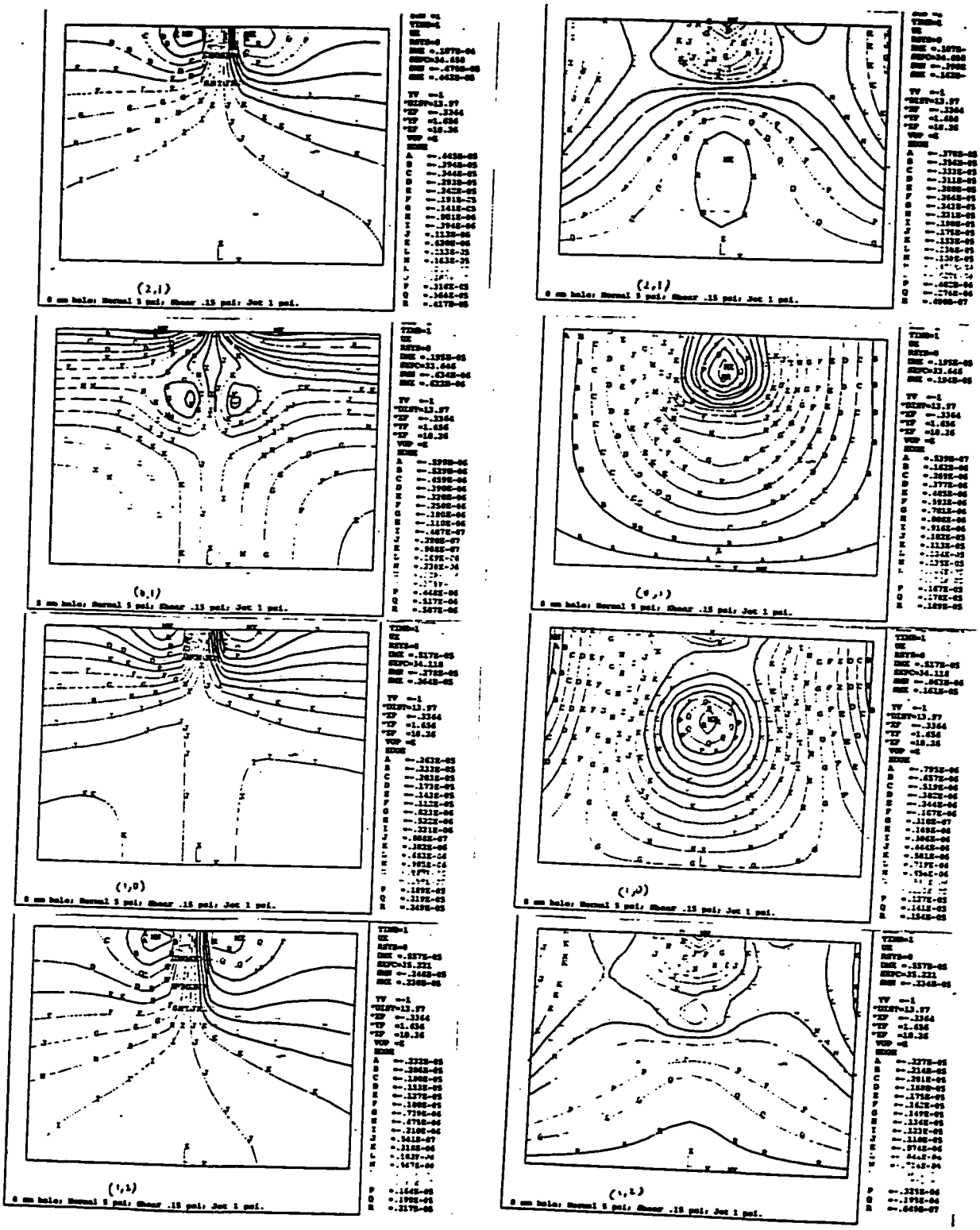

Figure 6.9(a) Effect on displacement with non-uniform normal pressure

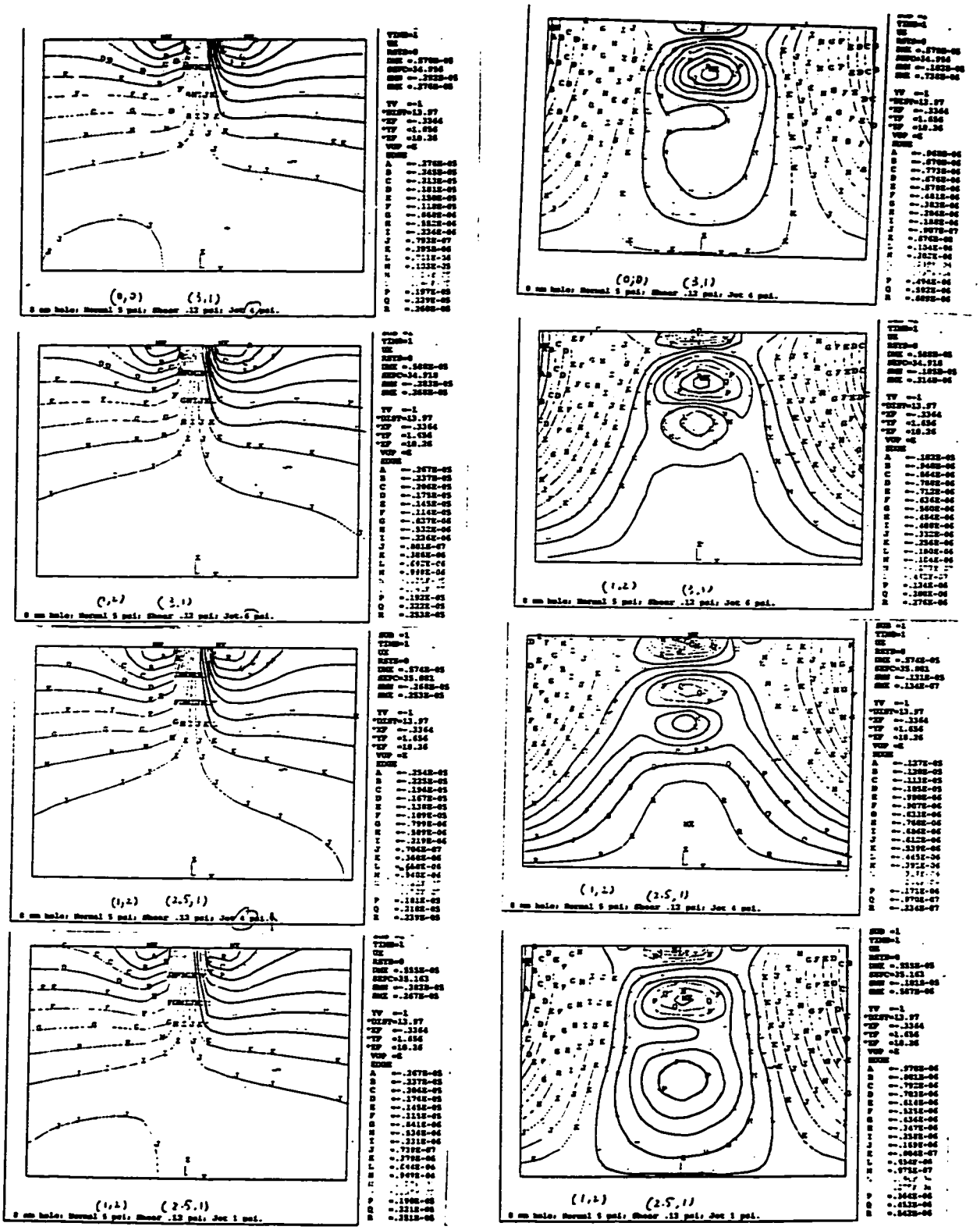

Figure 6.9(b) Effect on displacement with non-uniform shear

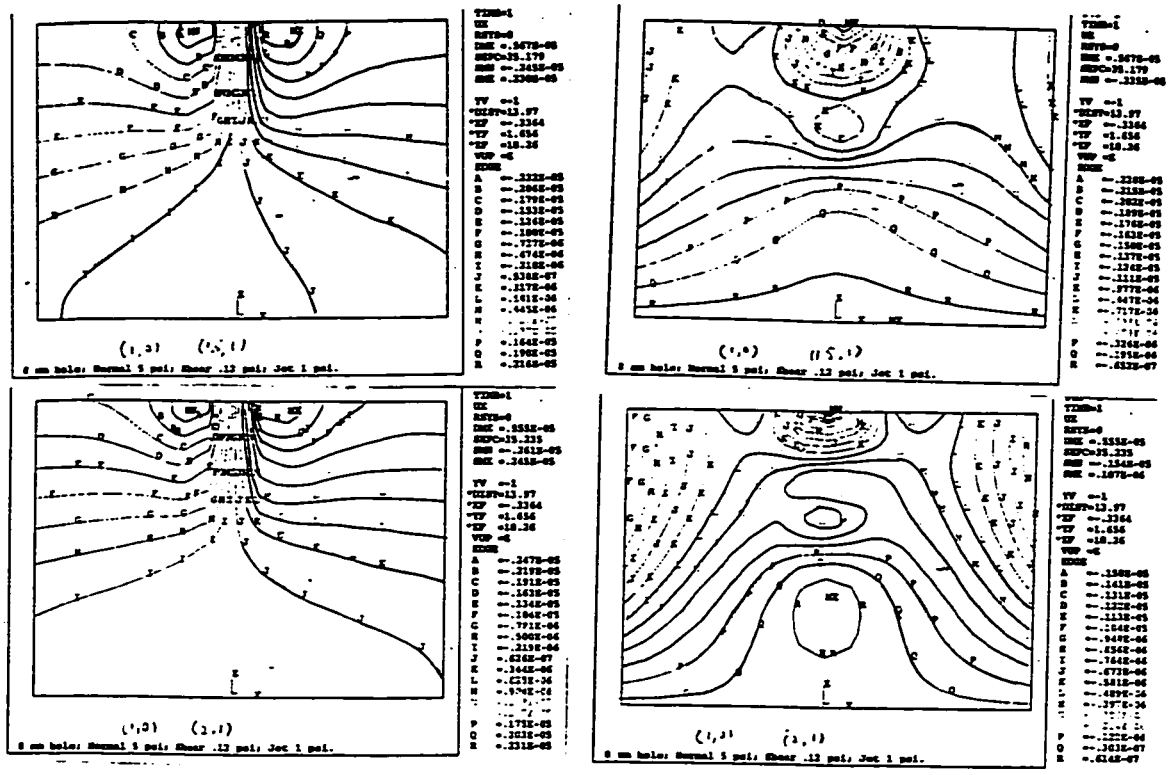

Figure 6.9(c) Effect on displacement with non-uniform shear

6.3.2 Maximum and Minimum u and v Displacements

In the above parametric study, the displacement contour patterns change as the loading conditions are changed. The maximum and minimum displacements under each loading condition are analyzed to help better understand the loading effect. The maximum and minimum displacements are plotted in Figures 6.10 to 6.15 for different shear, normal pressure and jet pressures. Figures 6.10, 6.12, and 6.14 illustrate the minimum and maximum u displacements as a function of shear force, normal pressure, and jet pressure, respectively. Figures 6.11, 6.13, and 6.15 illustrate the minimum and maximum v displacements as a function of shear force, normal pressure, and jet pressure. As can be seen, the maximum and minimum displacements are symmetric with respect to the horizontal axial in the charts. Their corresponding u-displacements are equal in value and opposite in signs. This means that all u-displacement contours are symmetric with respect to the x=0 plane.

Figures 6.11(a), 6.13(a), and 6.15(a) show the minimum v-field displacements as a function of shear, normal pressure, and jet pressure, respectively. Figures 6.11(b), 6.13(b), and 6.15(b) are the maximum v-field displacements. From these curves it appears that the v-displacement is not linearly related to the magnitude of the shear applied to the kerf surface. At jet pressure of 1 psi and normal pressure of 5 psi, if the shear is very small (for example, at 0.025 psi), the maximum v-field displacement is almost zero, while the minimum displacement possesses the largest absolute value. When the shear forces are larger, (for example, 0.5 psi), the maximum value is the largest, and the minimum value is the smallest among all the cases studied. For shear of 0.2 psi, normal pressure of 5 psi, the differences in u-field displacements for the impact jet pressure from 0 psi to 5 psi are very small. This means that the jet pressure does not significantly affect the u-field displacement.

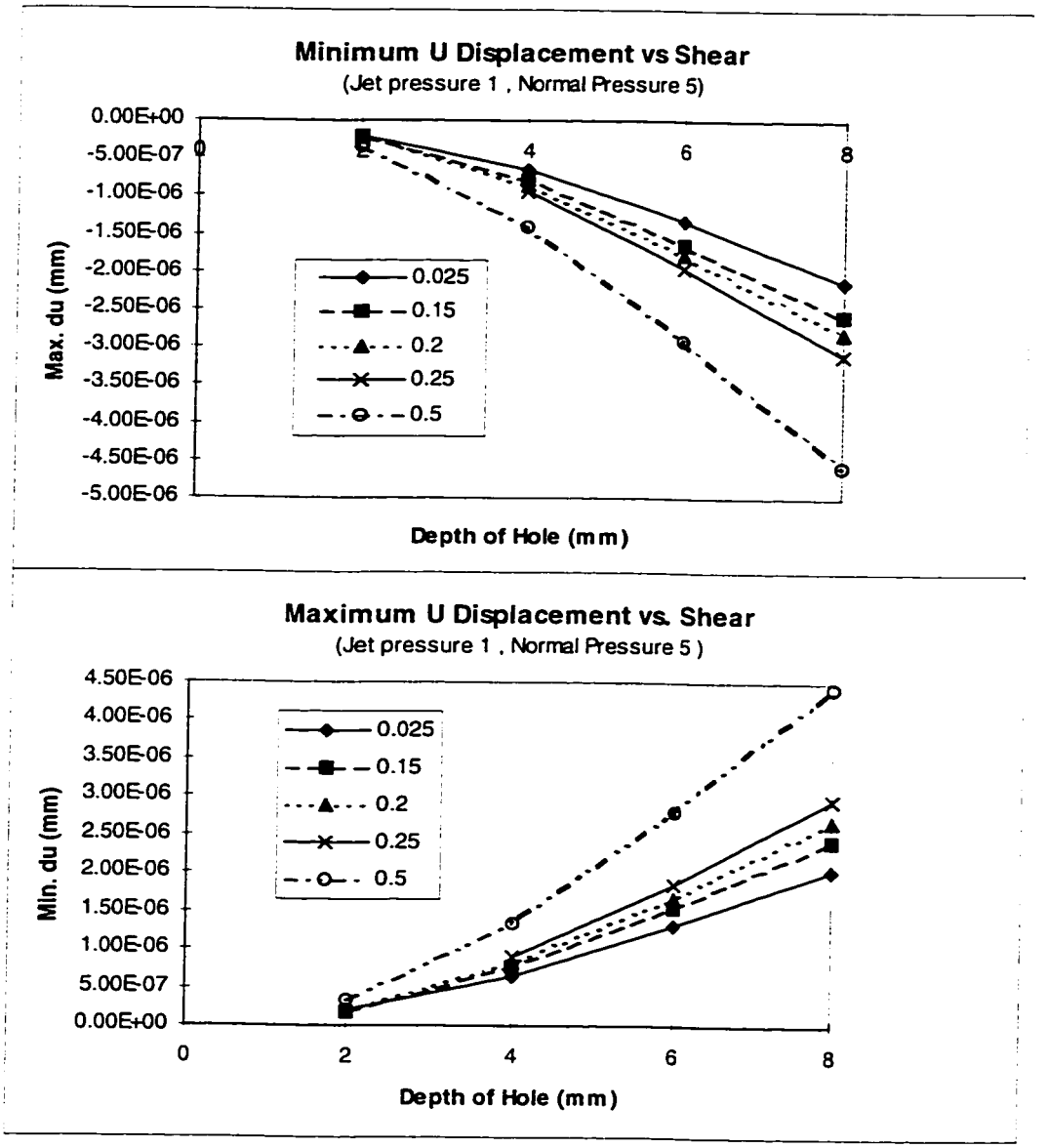

Figure 6.10 (a) (b) *u*--displacement vs. shear

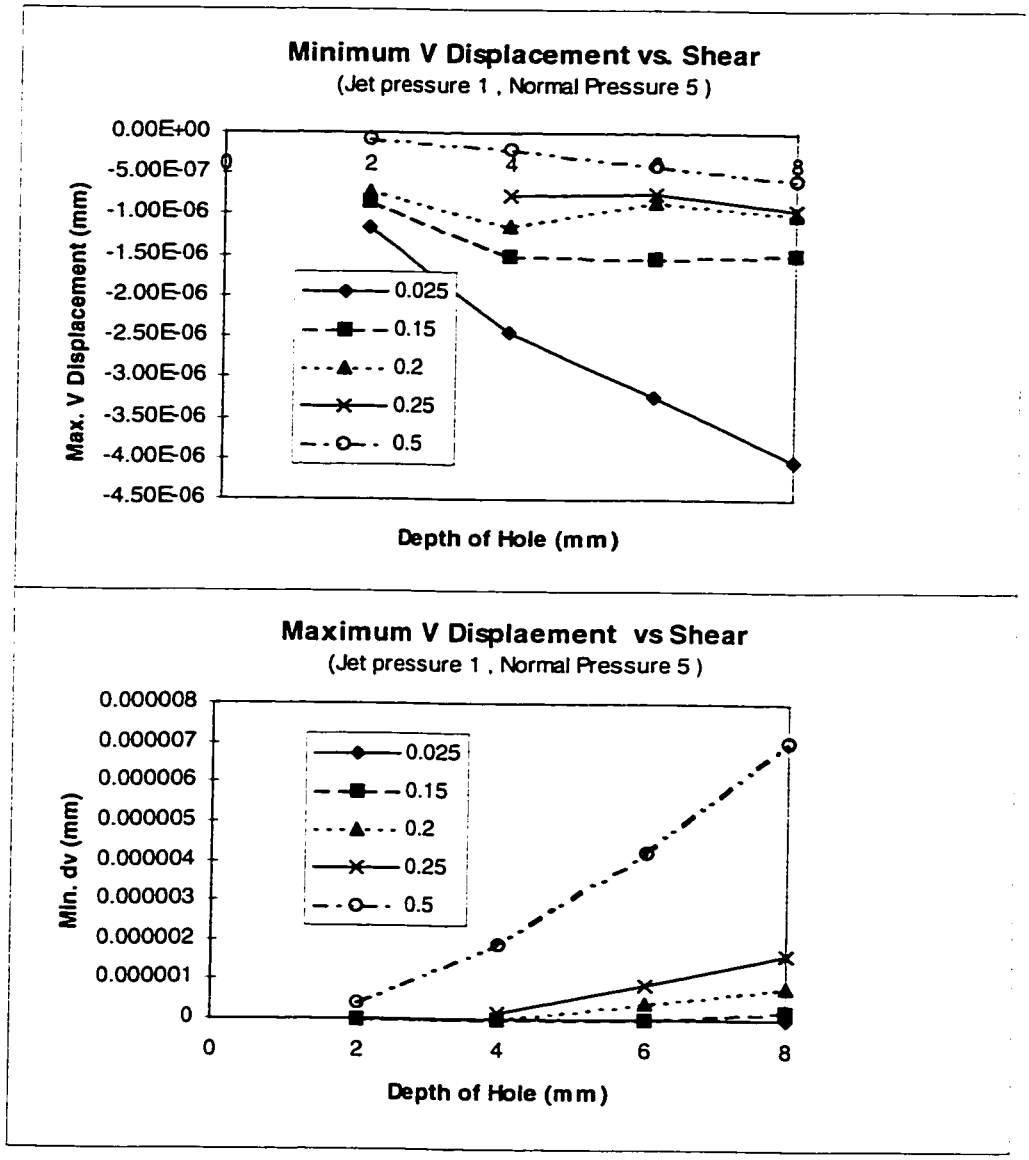

Figure 6.11 (a) (b) *v*--displacement vs. shear

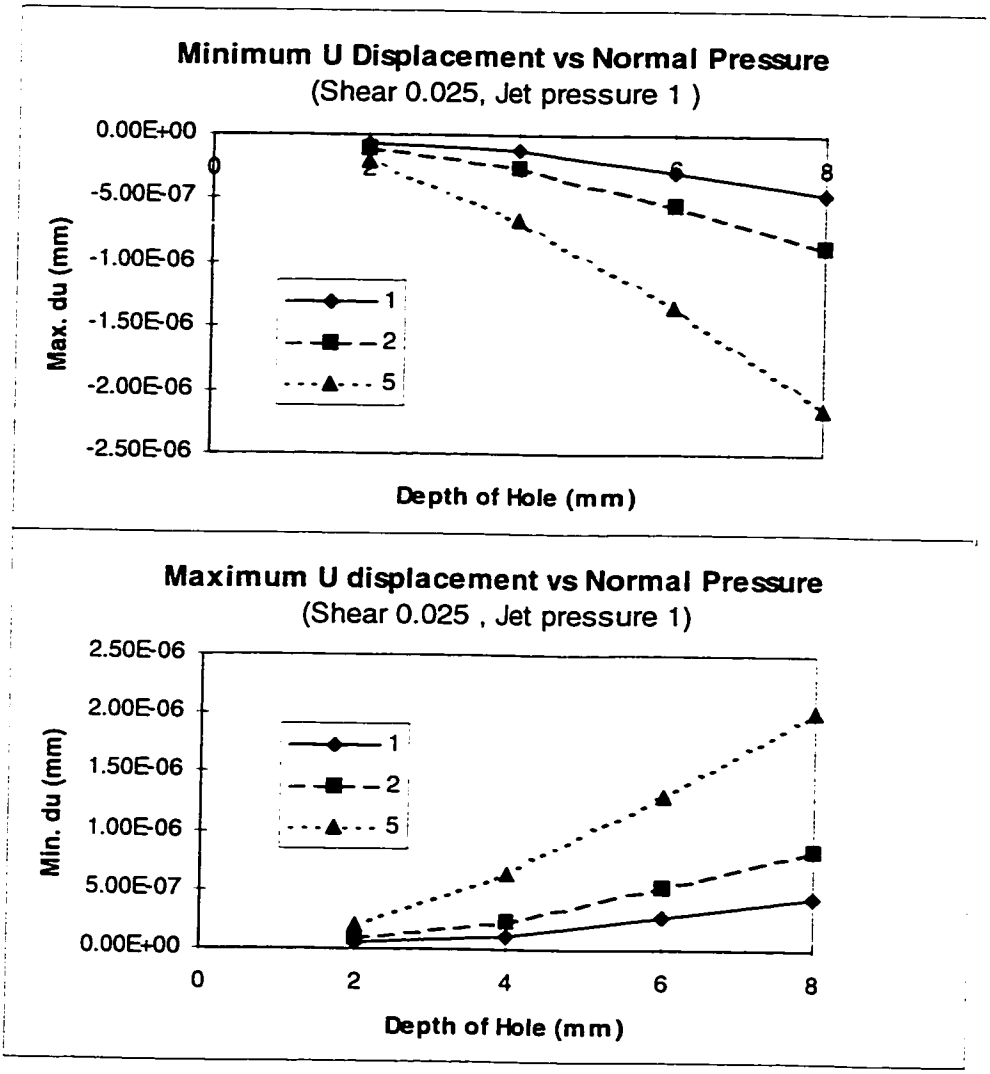

Figure 6.12 (a) (b) *u*--displacement vs. normal pressure

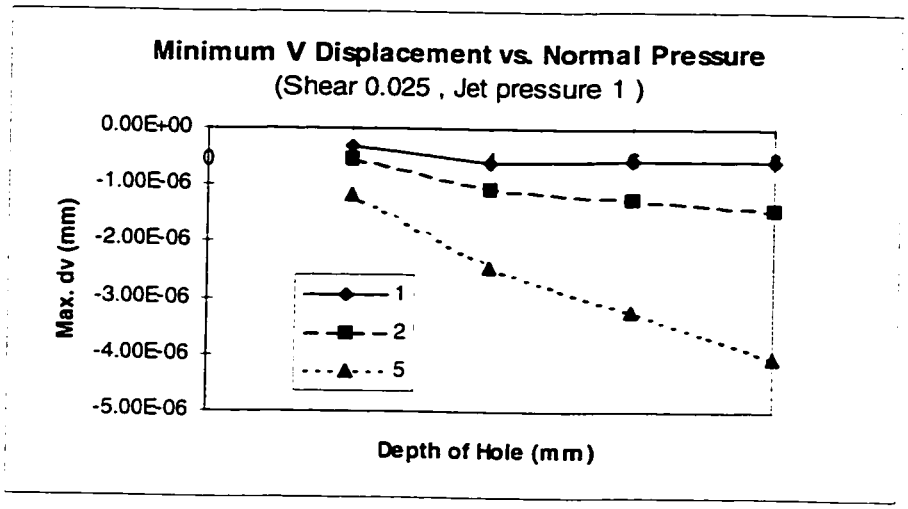

Figure 6.13 (a) (b) v--displacement vs. normal pressure

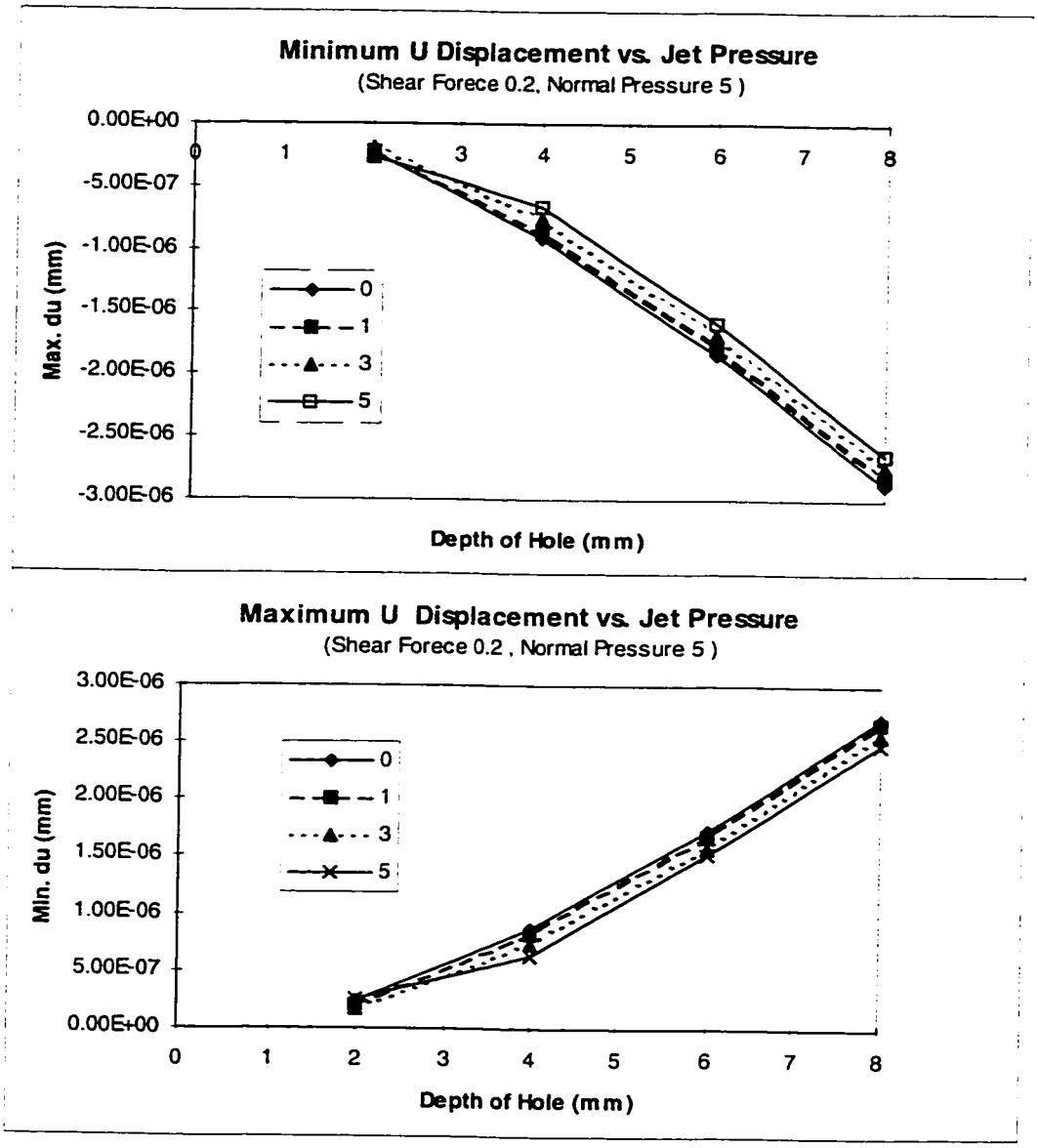

Figure 6.14 (a) (b) *u*--displacement vs. jet pressure

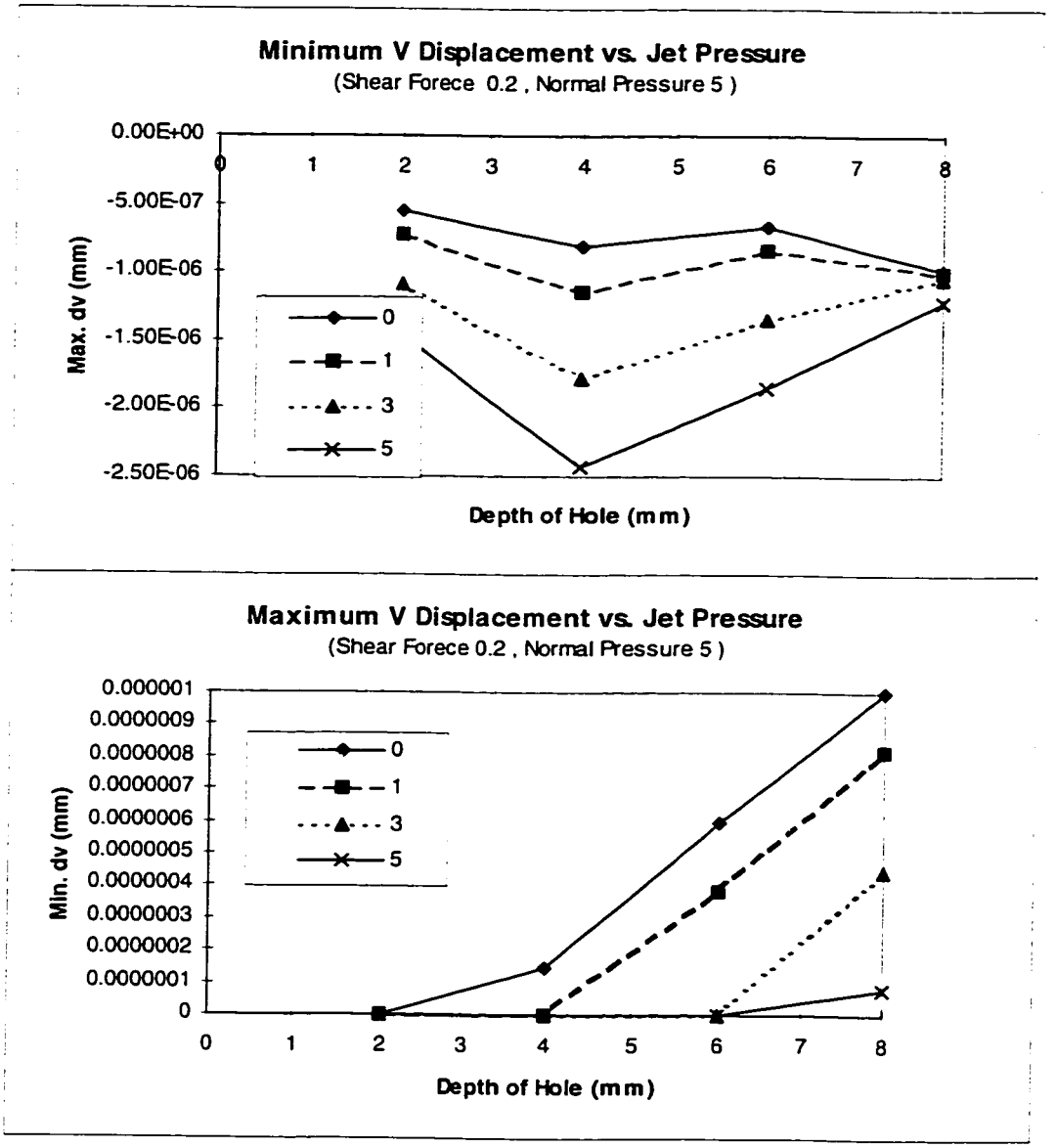

Figure 6.15 (a) (b) *v*--displacement vs. jet pressure

6.4 EXPERIMENTAL VERIFICATION WITH STATIC LOADING

A polycarbonate block with dimension of 25.4 mm x 19.5 mm x 6.25 mm under static loading was studied experimentally, numerically, and analytically. The purpose of this study is to verify the finite element model and validate the comparison between the experimental work with the numerical results. The classic analytical solution further confirms the correlation between the two. Similar comparison was conducted for ceramic materials.

6.4.1 Static Loading Experiments

Both polycarbonate and alumina specimens were tested under static loading. The specimen dimensions and fabrication were the same as those used in the dynamic optical testing. A static pressure load was applied to the top surface of a specimen by a calibrated weight through an indenter with a diameter of 2 mm. Calibrated weights were placed on a slider bar made of a light plastic. The total static load exerted on the specimen was measured with a load cell that was mounted in the middle of slider bar. The static load experimental setup, including the optical arrangement, is shown in Figures 6.16. Since this was a static experiment, only one video camera was used for moiré fringe recording. While the u-filed fringes were being recorded, the v-field view had to be blocked, and vice versa. A detailed illustration of the loading frame is in Figure 6.17(a). An indenter was threaded to the load cell, which is pictured in Figure 6.17(b). The total load was read off a load cell display, which is illustrated in Figure 6.17(c).

The specimen was coated with specimen grating with a density of 1200 lines/mm. Following the testing procedure for moiré interferometry experiments, as described previously, both u and v field moiré fringe patterns indicating the displacement could be captured. The static load was gradually increased from zero by carefully adding more weight blocks on the slider bar. The u and v fringes were each recorded with a high speed Hi8 video camera after each load increment.

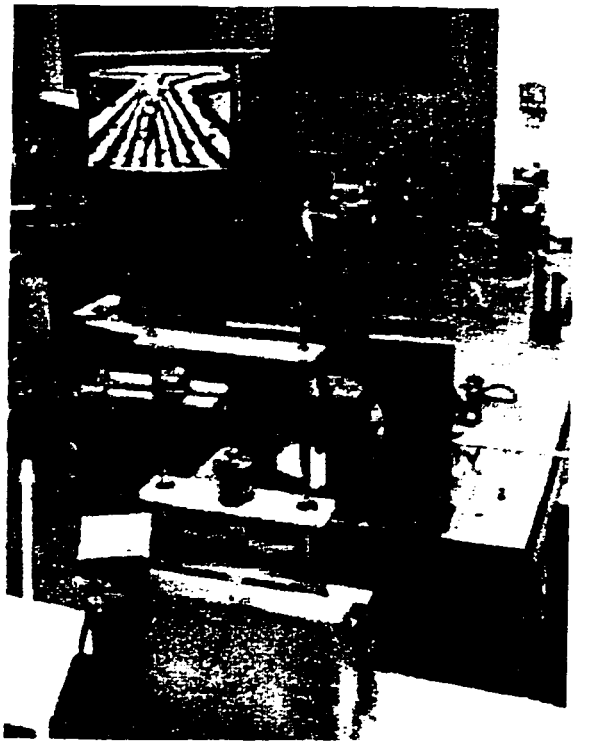

Figure 6.16 Optical experimental Setup for a Specimen under Static Loading

6.4.2 Finite Element Modeling

In the finite element analysis, the indenter was modeled as a solid cylinder with a diameter of 2 mm. Taking advantage of the symmetry of both loading and geometry, a quarter volume for the specimen and the indenter was modeled. During the optical tests, the bottom surface of the specimen was adhered to the base bar. Therefore in this FEA model, similar boundary conditions were applied. Shown in Figure 6.18(a) is a typical meshed finite element model, which has 2,548 nodes and 1,863 elements. Figure 6.18(b) shows the enlarged view of the meshed indenter. A 3-D structural solid element SOLID45 was used for both the specimen body and the indenter. The interface between the indenter and the specimen was modeled with a contact element, CONTACT49. These displacement fields modeled by the FEA meshes only represent half of the frontal surface of the specimen.

(a) Static Loading Frame

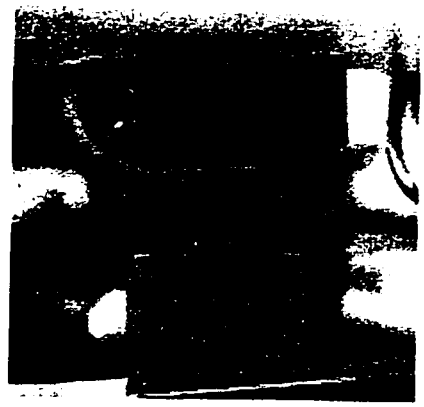

(b) Load cell, indenter and specimen

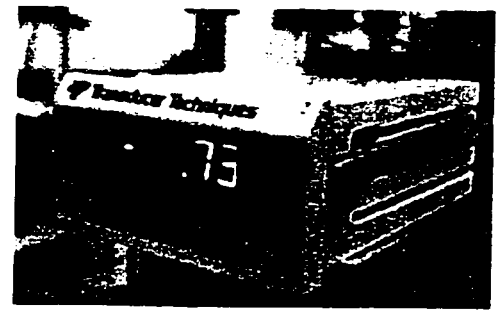

(c) Load cell display

Figure 6.17 Static Loading Apparatus

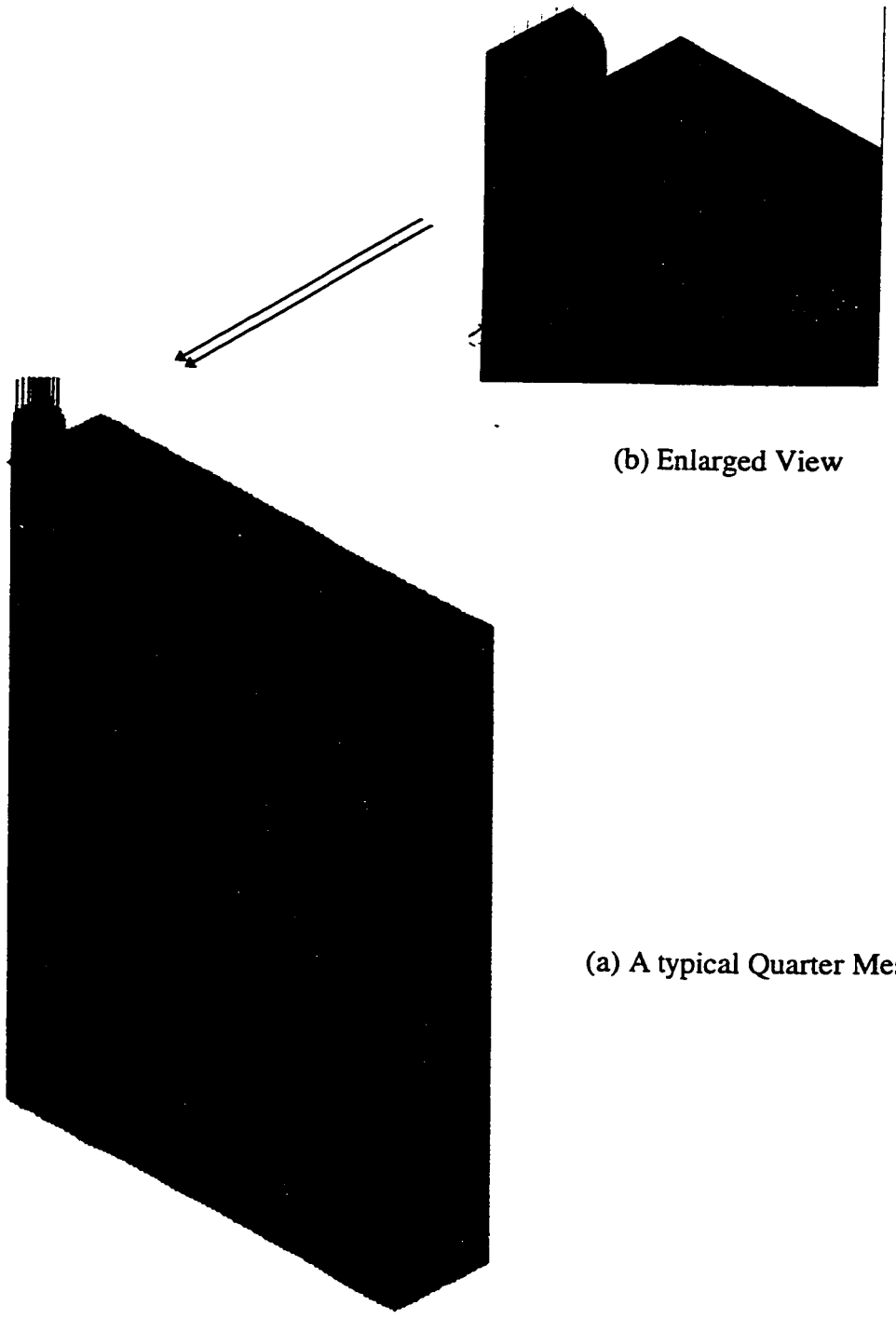

(b) Enlarged View

(a) A typical Quarter Mesh

Figure 6.18 Typical FEA mesh for the polycarbonate block under static loading

6.4.3 Results

Figures 6.19 and 6.20 are the moiré fringes for the polycarbonate specimen in both *u* and *v* fields. Each moiré fringe picture corresponds to static loads from 0 N to 44.5 N max. It is noted that both *u* and *v* fields have initial fringes at 0 N load condition. However, moiré fringes in both *u* and *v* fields are relatively symmetric with respect to the loading line. The numbers of moiré fringes were increased as the load was increased. This was especially the case for the *v* field, as shown in Figure 6.20. Figures 6.21 and 6.22 are the moiré fringes recorded for the alumina material in both *u* and *v* fields as the loads were increased from 0 N to 62.3 N. It appears that there were 2 initial fringes in the *u* field and 3 initial fringes in the *v* field. As the vertical loads were increased, the moiré fringes in both fields only shifted within the picture frames. There was no increase in moiré fringes for the alumina material.

Due to the existence of initial fringes at 0 N load, the real displacement contour for certain subsequent load with 4.45 N increment could be obtained by subtracting the initial fringes field from the corresponding moiré fringes of this load. Note that a well defined number of fringes formed for the polycarbonate material upon loading. Figures 6.23(a) and (b) are the outer surface displacement contours for polycarbonate at 44.5 N static load. Apparently the displacement contours in both *u*- and *v*- fields are symmetric with respect to the centerline of the static load. The outer surface displacement contours were plotted with each contour line representing the same amount of displacement of one fringe order, as in the recorded optical fringe patterns. At 44.5 N there are 5 fringes in the *u* field and 13 fringes in the *v* field. Figures 6.29(a) and (b) are the outer surface displacement contours for the alumina materials at 44.5 N static load. Even at 44.5 N, the maximum displacement is 7.6e-6 mm in the *u*- field, and 4e-5 mm in the *v*-field. These magnitudes of displacement are less than the equivalent displacement of one moiré fringe. This also means that the displacement for alumina material at load of 44.5 N is too small to be measured with the current moiré technique.

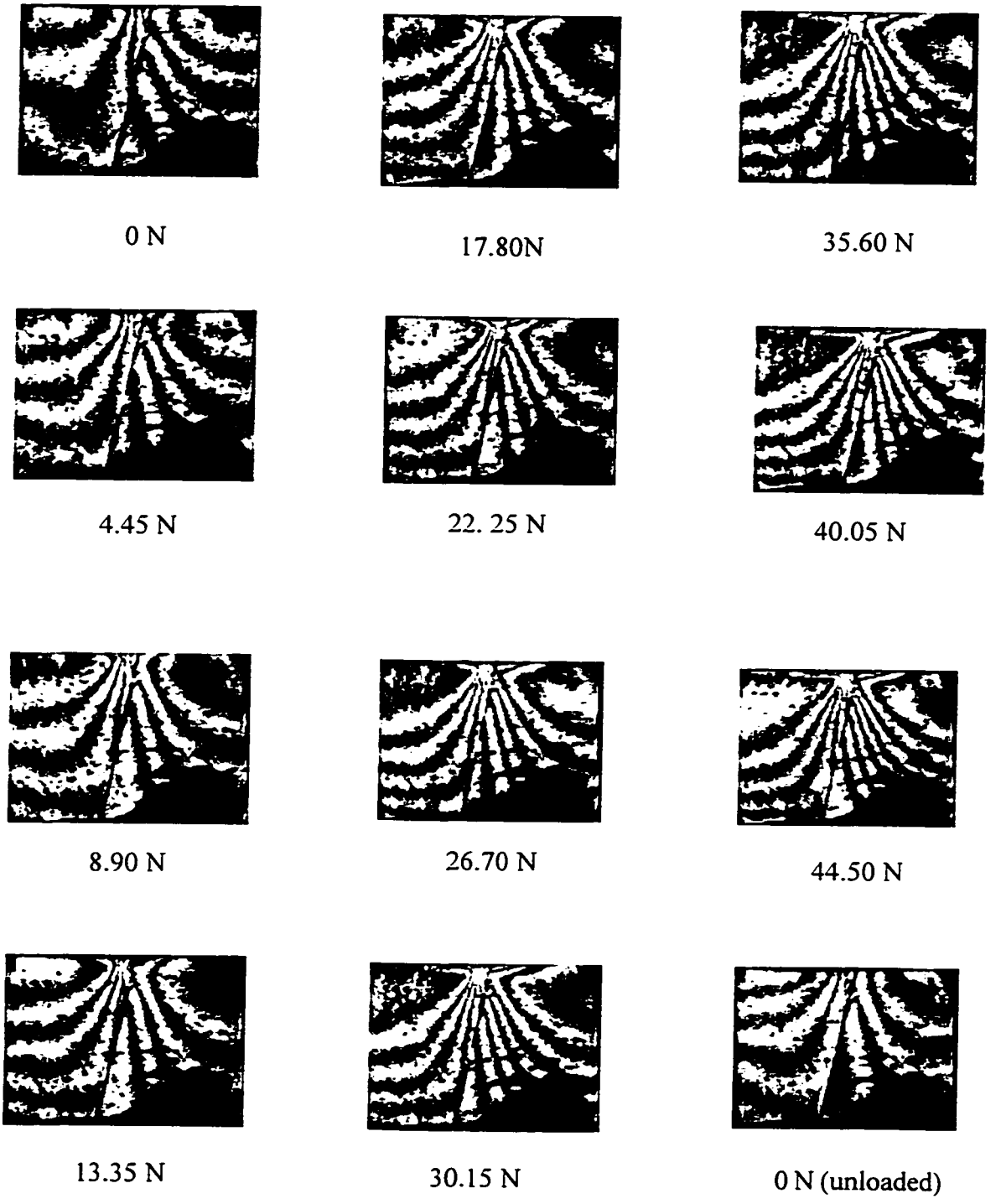

Figure 6.19 *u*-Field Moire Fringes for Polycarbonate Specimen under Static Loading

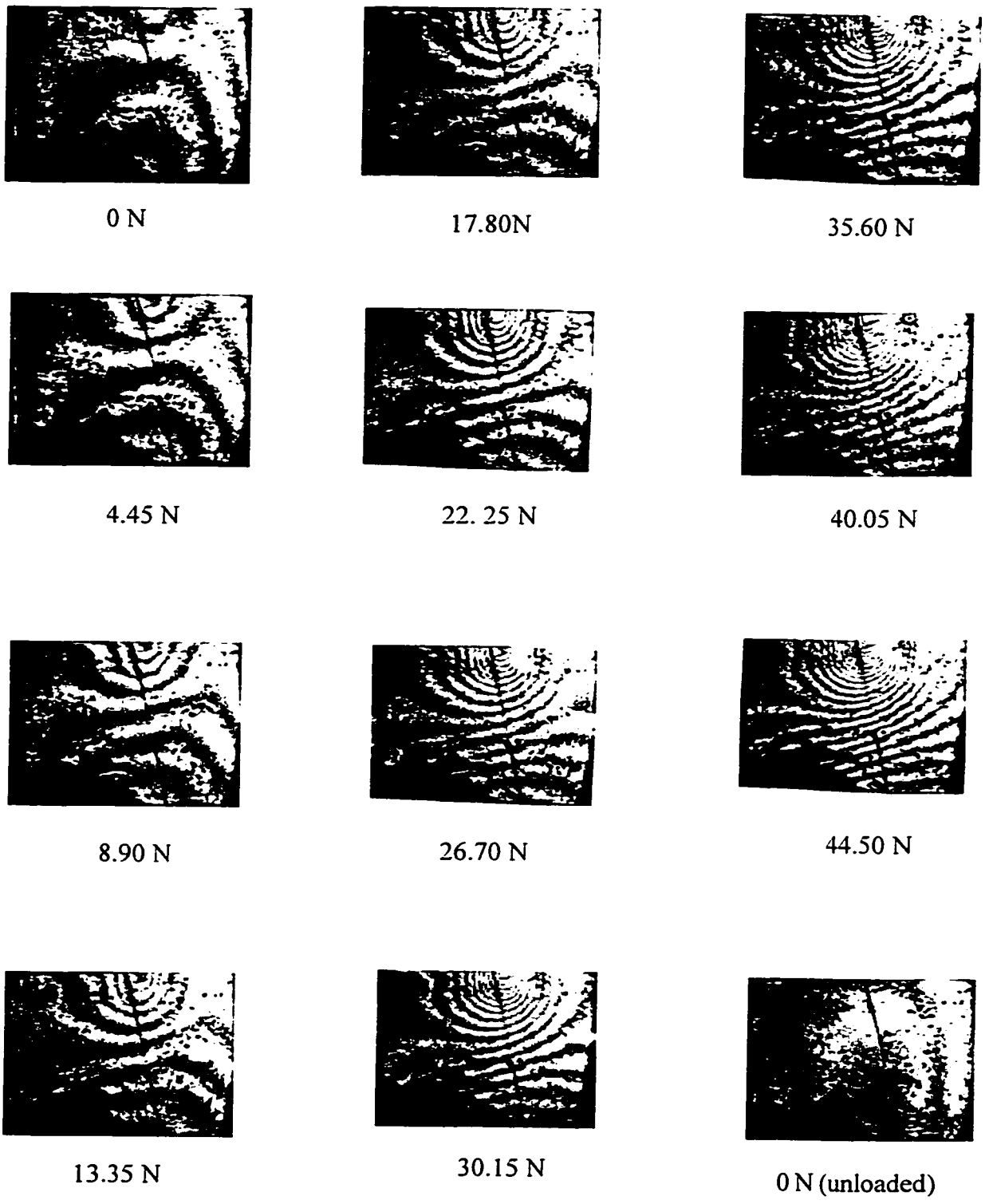

Figure 6.20 *v*-Field Moire Fringes for Polycarbonate Specimen under Static Loading

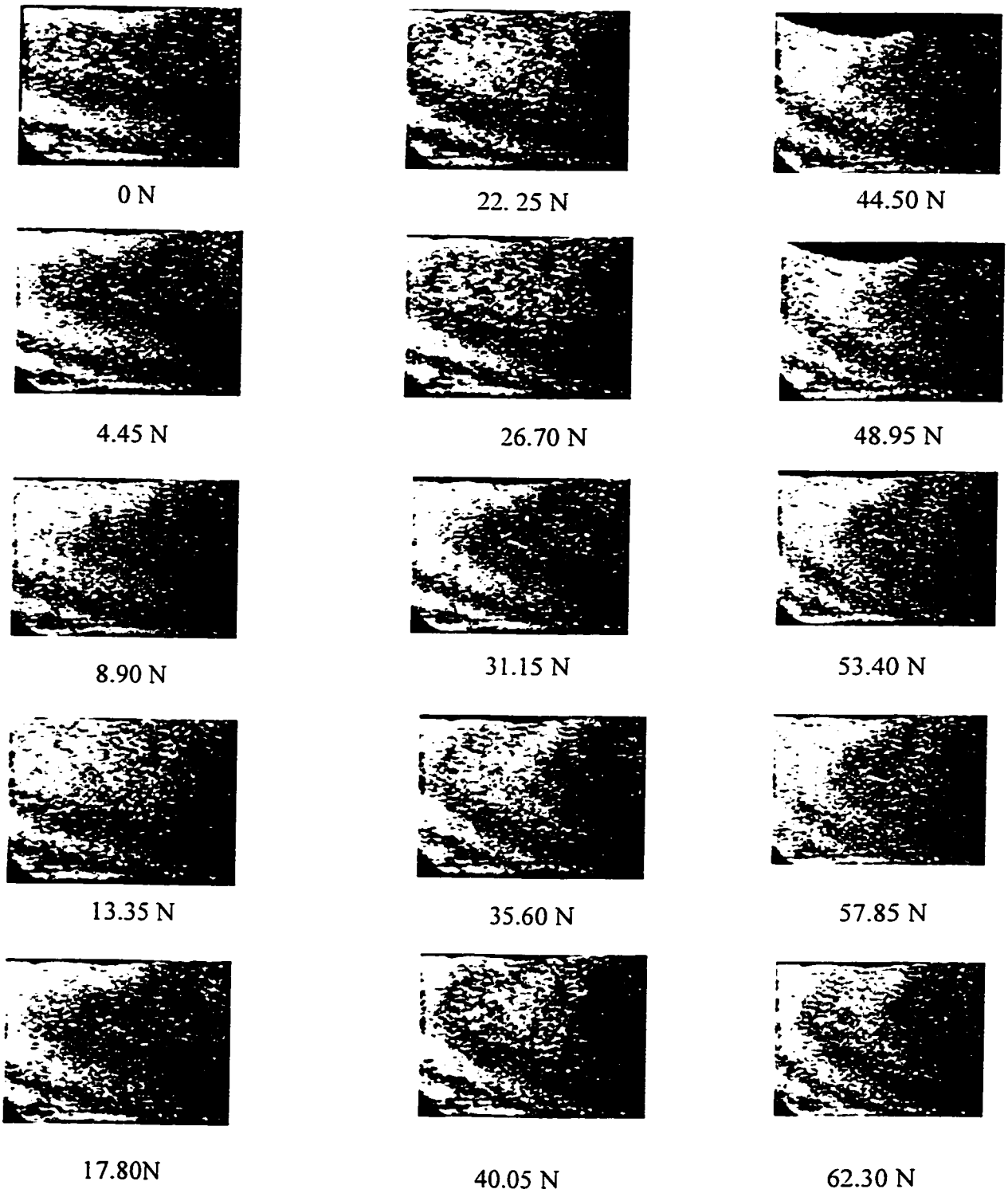

Figure 6.21 *u*-field Morie Fringes for Ceramic Specimen under Static Loading

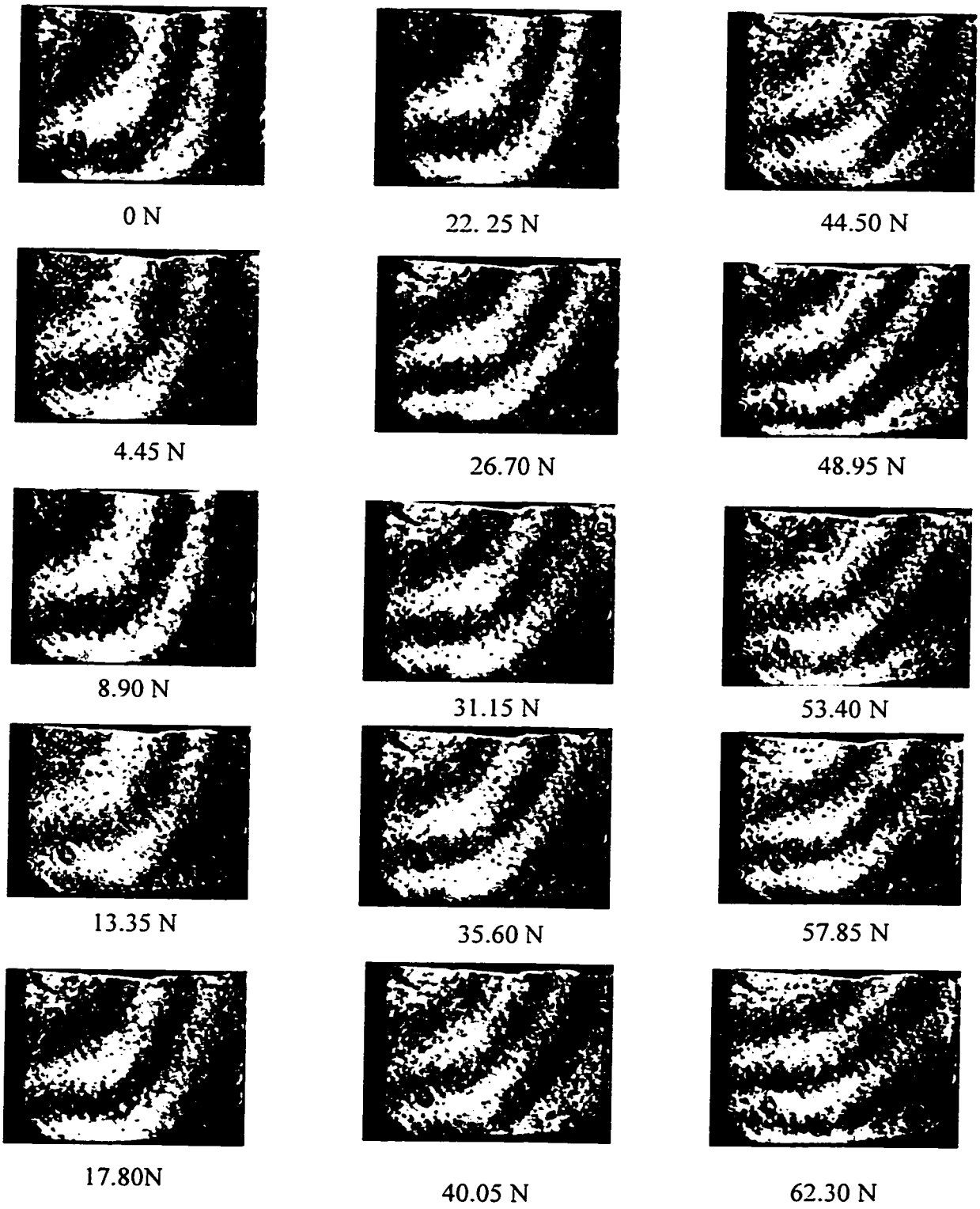

Figure 6.22 *v*-field Morie Fringes for Ceramic Specimen under Static Loading

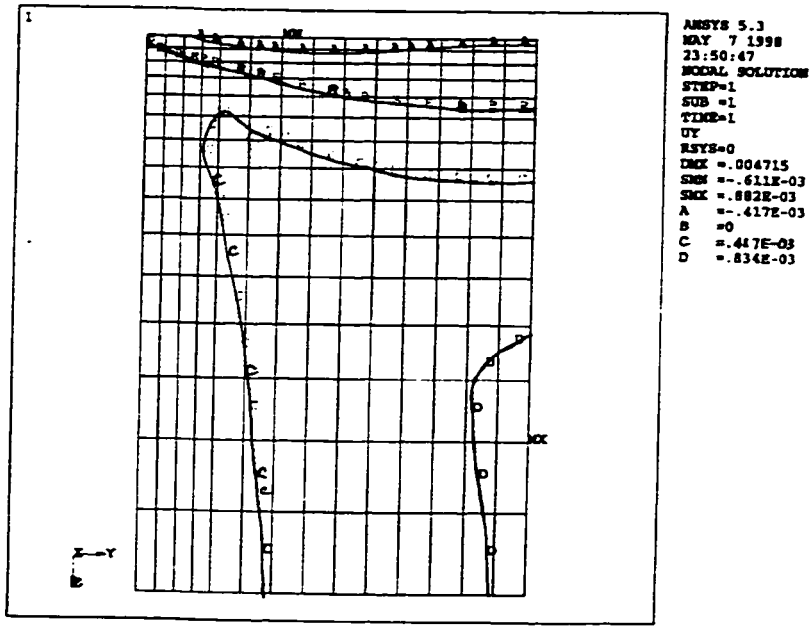

Figure 6.23(a) u-field displacement contours for polycarbonate block (44.5 N static load)

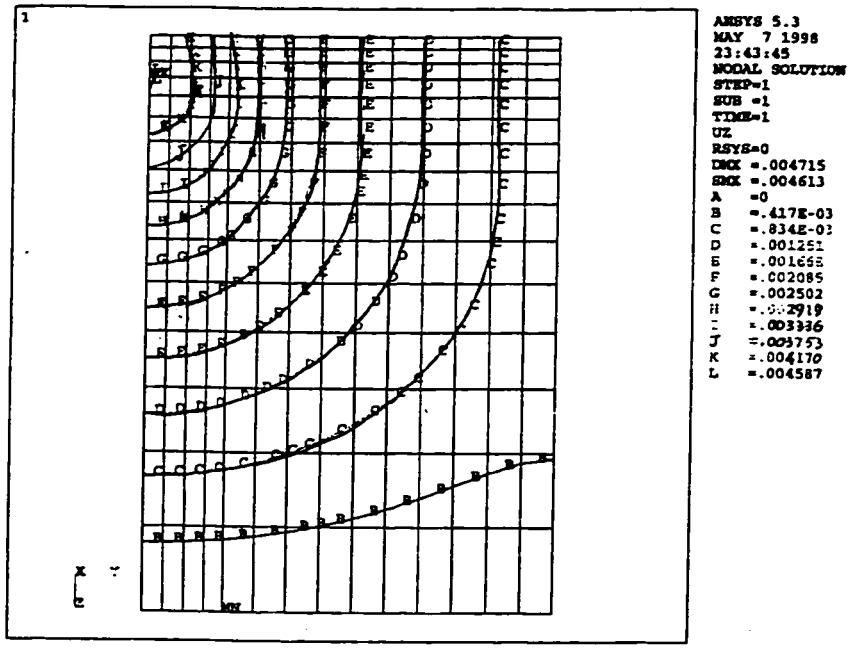

Figure 6.23(b) v-field displacement contours for polycarbonate block (44.5 N static load)

6.4.4 Discussion

The moiré fringes from the optical experiments for varying static loads in polycarbonate material were obtained successfully. The displacement contour lines in the frontal surface of the test specimen in both *u*- and *v*- fields are shown in Figures 6.19 and 6.21. Based on the finite element analysis results, the surface displacement contour was extracted and graphed. The equal-displacement contours graphs for the polycarbonate specimen in the *u*-field and *v*-field are shown in Figures 6.23(a) and (b), respectively. Each contour line represents a displacement of 0.000417 mm, which is the same as one fringe line in the moiré fringe pictures from the optical experiments. Since a closed form solution is not readily available analytically for a static loading on a small specimen block, an idealized model in a semi-infinite body under the pressure of a sharp indenter was used. The point load is illustrated in Figure 6.24. The concentrated point force *P* is applied at the origin of the cylindrical coordinate system.

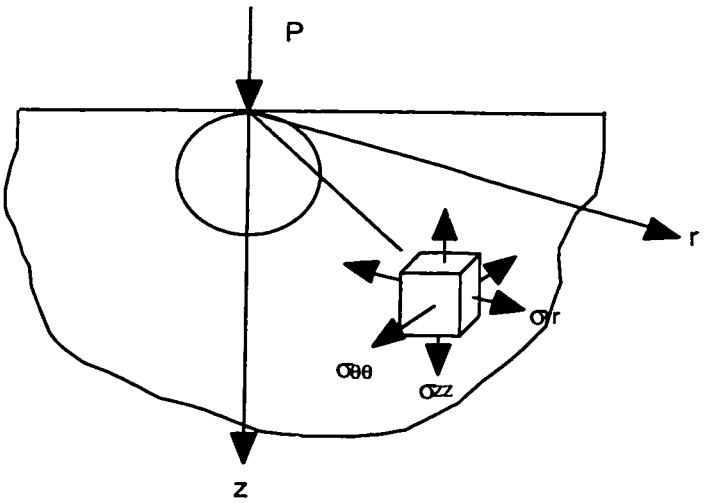

Figure 6.24 Point force P at the origin of the cylindrical coordinate system

In this cylindrical coordinate system, the displacement components in the r, θ,and z axes are denoted by u, v, and w, respectively. The stress components can be expressed as[130]:

$$\sigma_{rr} = \frac{P}{2\pi}[(1-2\nu)\frac{1}{r^2} - \frac{z}{r^2(r^2+z^2)^{1/2}} - \frac{3r^2z}{(r^2+z^2)^{5/2}}] \quad (6.1)$$

$$\sigma_{zz} = -\frac{3P}{2\pi}\frac{z^3}{(r^2+z^2)^{5/2}} \quad (6.2)$$

$$\sigma_{\theta\theta} = \frac{P}{2\pi}[(1-2\nu)[-\frac{1}{r^2} + \frac{z}{r^2(r^2+z^2)^{1/2}} - \frac{z}{(r^2+z^2)^{3/2}}] \quad (6.3)$$

$$\sigma_{rz} = -\frac{3P}{2\pi}\frac{rz^2}{(r^2+z^2)^{5/2}} \quad (6.4)$$

The displacement components u (radial direction), v (tangential direction), and w (vertical direction) can be written as[130]

$$u_r = \frac{(1-2\nu)(1+\nu)P}{2\pi Er}[\frac{z}{(r^2+z^2)^{1/2}} - 1 + \frac{r^2z}{(1-2\nu)(r^2+z^2)^{3/2}}] \quad (6.5)$$

$$v_\theta = 0 \quad (6.6)$$

$$w_z = \frac{P}{2\pi E}[\frac{(1+\nu)z^2}{(r^2+z^2)^{3/2}} + \frac{2(1-\nu^2)}{(r^2+z^2)^{1/2}}] \quad (6.7)$$

Within this semi-infinite body, a small volume of the same size of a test specimen (25.4 mm x 6.25mm x 19.5mm) centered at the origin of the coordinate system was of the most interest. The displacements in the front surface of the small volume were calculated using the above equations. The front surface was divided into a 75 x 100 mesh grid. The coordinates x and y at each grid point was calculated in a Cartesian coordinate system. Therefore, the displacement components in the Cartesian coordinates are as follows:

$$u_x = \frac{(1-2\nu)(1+\nu)P}{2\pi Er}\left[\frac{z}{(r^2+z^2)^{1/2}} - 1 + \frac{r^2 z}{(1-2\nu)(r^2+z^2)^{3/2}}\right]\sin(\arctan(x/y)) \qquad (6.8)$$

$$u_y = \frac{(1-2\nu)(1+\nu)P}{2\pi Er}\left[\frac{z}{(r^2+z^2)^{1/2}} - 1 + \frac{r^2 z}{(1-2\nu)(r^2+z^2)^{3/2}}\right]\cos(\arctan(x/y)) \qquad (6.9)$$

$$w_z = \frac{P}{2\pi E}\left[\frac{(1+\nu)z^2}{(r^2+z^2)^{3/2}} + \frac{2(1-\nu^2)}{(r^2+z^2)^{1/2}}\right] \qquad (6.10)$$

where, $r = \sqrt{x^2+y^2}$

The analytical solutions for polycarbonate material were calculated using equations 6.7 to 6.10. At 44.5 N, the displacement distribution contours in both u- and v-fields for a polycarbonate material are shown in Figures 6.25(a) and (b). The displacement contours in both u and v fields are symmetric, and the trends are very similar to experimental observations.

A comparison of the experimentally obtained displacement contours with the finite element analysis contours was conducted. The first step for the displacement comparison was to analyze the experimentally recorded moiré fringes. The next step was to place the experimental fringe pictures side by side with the FEA contour plots. It is observed in Figures 6.19 and 6.20, that the numbers of initial fringes for both u-field and v-field are not zero. The net displacements corresponding to each static load could be obtained by subtracting the initial displacement field from the displacement field of each specific loading. This was performed by digitizing the moiré fringe pattern of both initial load conditions and the loading condition of interest. A subtraction could be performed numerically for each corresponding point on the outer surface. Figure 6.26 shows examples of the digitized moiré fringe patterns for polycarbonate specimen under static load of 0 N and 44.5 N. The net displacement contour for 44.5 N load was obtained and is shown in Figure 6.27(a). The zigzagged curves and other irregularities in Figures 6.27(a) are due to the numeral noises introduced in the subtraction process. A smooth

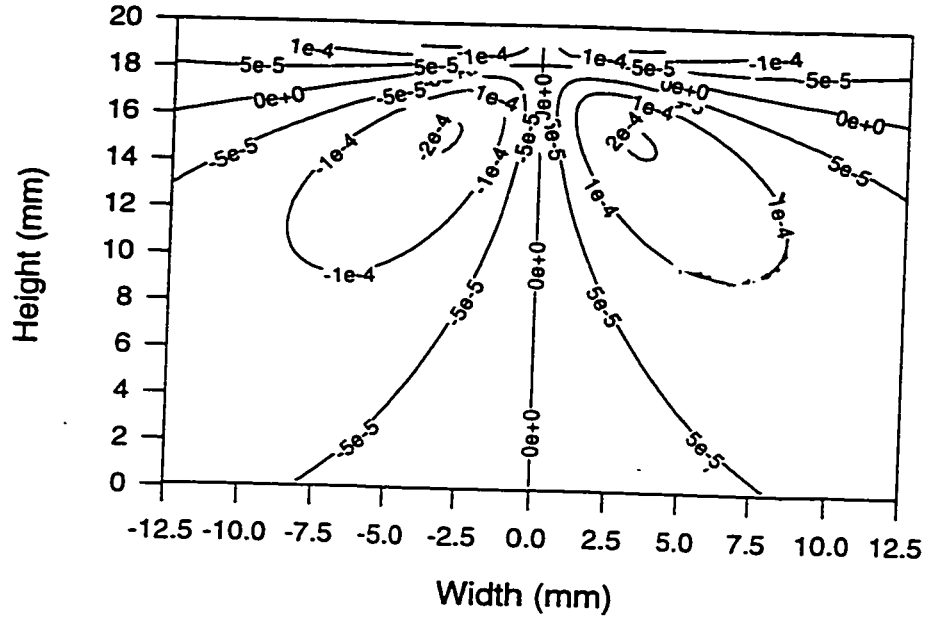

(a) *u*-field displacement Contour (mm)

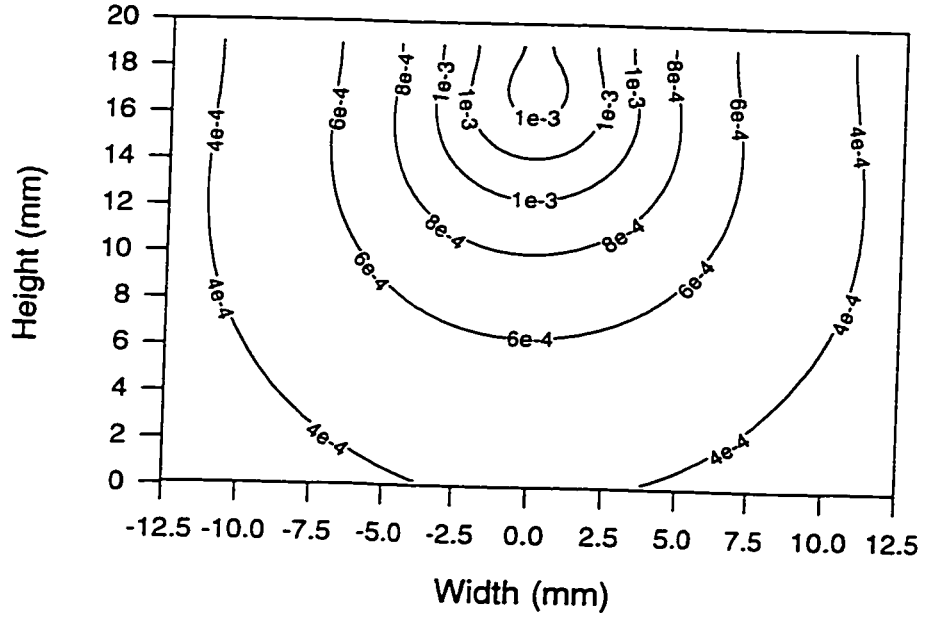

(b) *v*-field displacement Contour (mm)

Figure 6.25 Closed form solutions of displacement contours under a point load

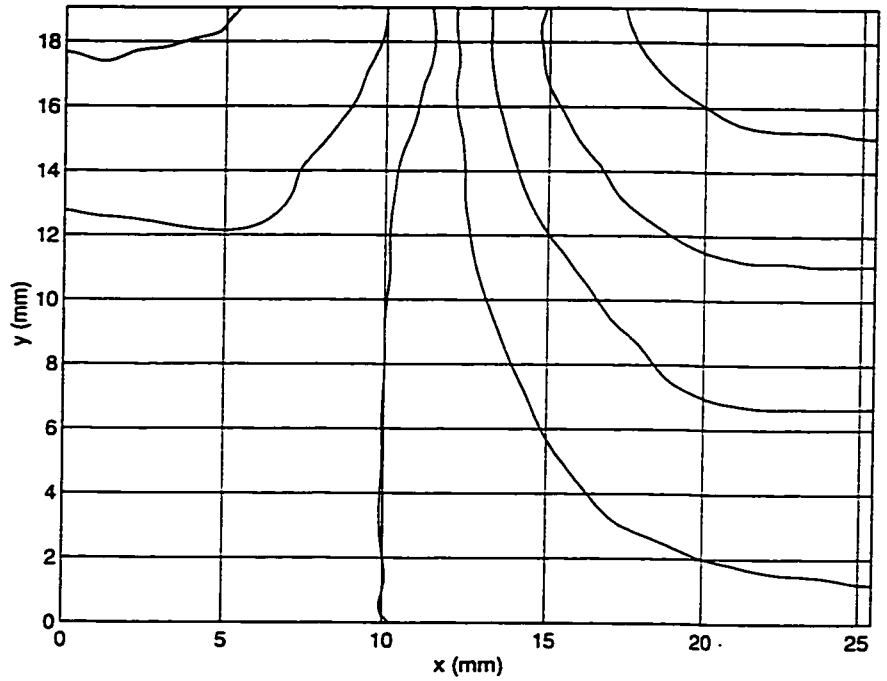

(a) Static Load 0 N)

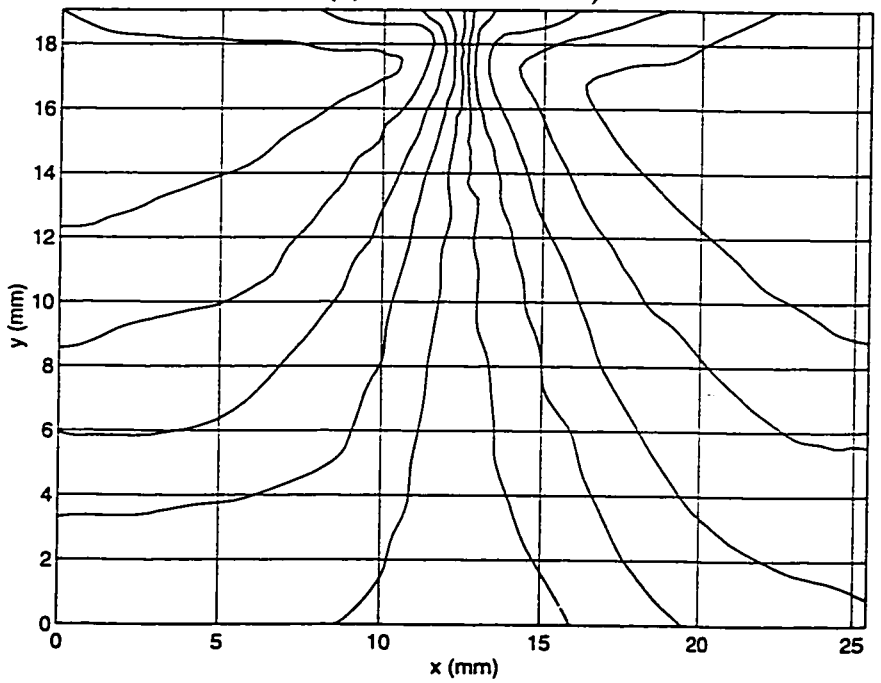

(b)Static Load 44.5 N)

Figure 6.26 Digitized u-field displacement contours for polycarbonate specimen under static loads

line would be calculated if the initial fringe pattern matched the loaded fringes patterns exactly. The contour plot algorithm used in the plotting software could be partly responsible for the irregularities in the net displacement contours.

This net displacement contour is approximately symmetric with respect to the centerline. The FEA predicted u-field displacement contours are illustrated in Figure 6.27(b) for polycarbonate specimen under static load of 44.5 N. In the net u-displacement contour graph in Figure 6.27 (a), there is an approximate symmetry with respect to the centerline of the specimen. There is no u-displacement along the symmetry line. On either side of the symmetric line there are three deformation zones. Along the top edge is the upper displacement zone, where the material moves towards the loading point and the centerline. The values of the displacements are negative. In the lower portion of the specimen surface is the lower displacement zone. In the lower displacement zone the material moves away from the centerline. The values of the displacements are positive. The maximum displacement in the lower displacement zone is approximately 0.000834 mm, which can be represented by two moiré fringes. Separating the upper and lower displacement zone is a neutral displacement zone. In the neutral zone there is no displacement. Examining the contour plot obtained from the finite element analysis, as shown in Figure 6.27(b), there are three displacement zones on either side of the specimen. The magnitudes of the displacements coincide with the experimentally obtained results in Figure 6.27(a). Therefore, the displacement fields depicted in Figure 6.27 (a) and 6.27(b) are very comparable

A similar comparison was made for the v-field displacement contours between the experimental results and the FEA results for the polycarbonate specimen. The net result of the v-field displacement contour after subtraction is shown in Figure 6.28(a), and the FEA predicted contour is shown in Figure 6.28(b). There is a general symmetry in the v-displacement field, as is shown in Figure 6.28(a), with respect to the centerline of the

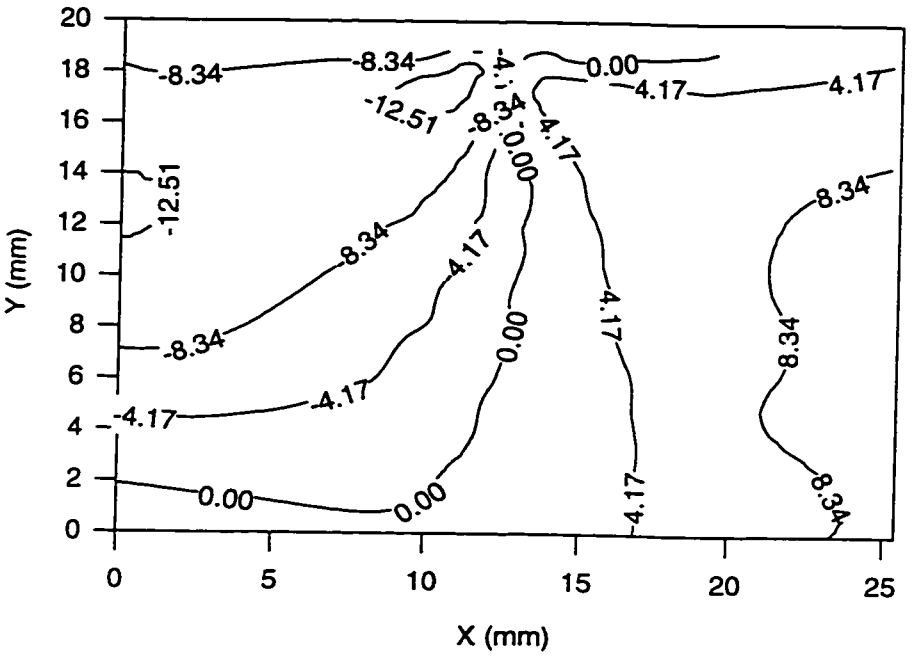

(a) *Net displacement contour ($x10^{-4}$) mm at static load 44.5 N*

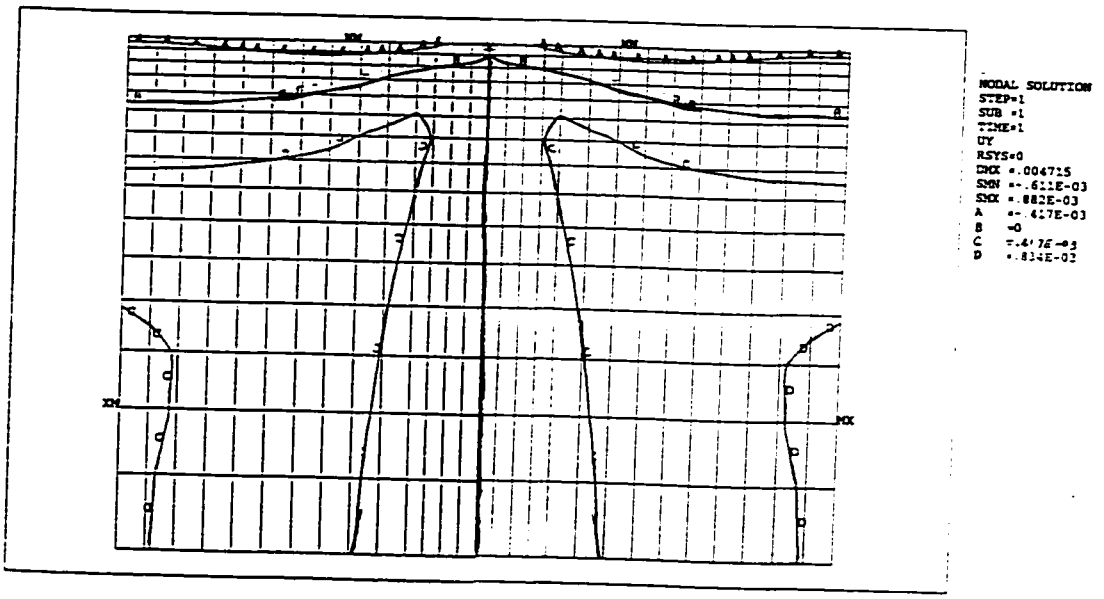

Figure 6.27 Comparison of the experimental and FEA results of the *u*-field displacement contours for polycarbonate specimen

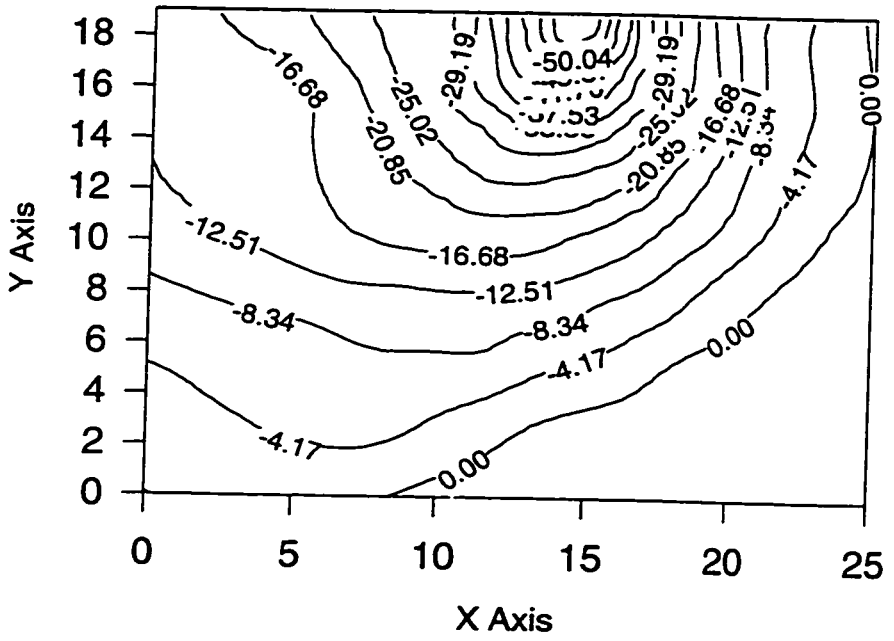

(a) *Net displacement contour ($x10^{-4}$) mm at static load 44.5 N*

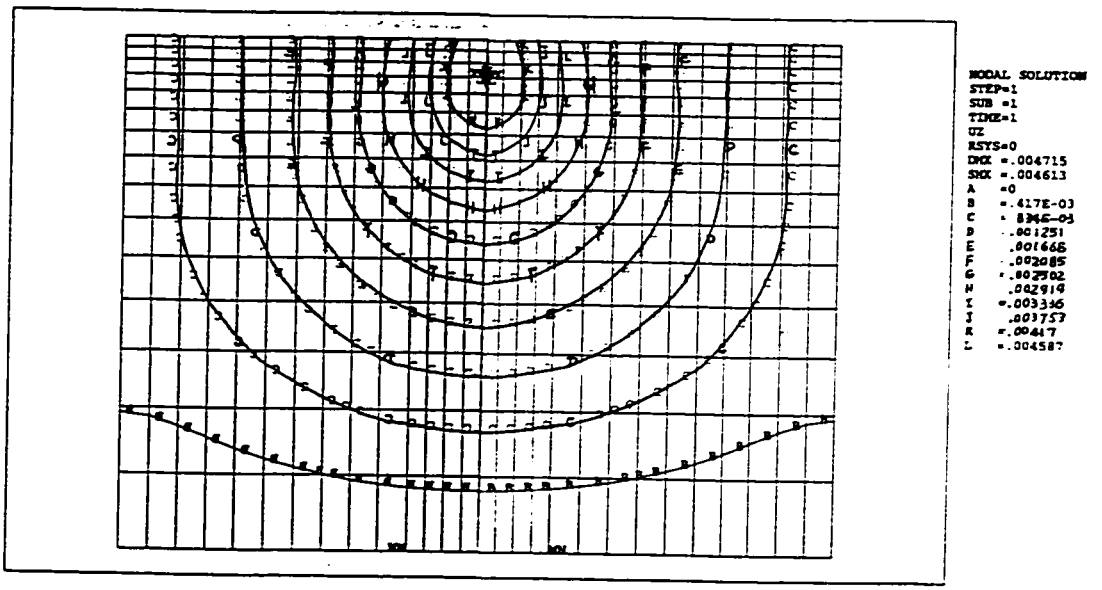

(b) FEA predicted displacement contour(mm) at static load 44.5 N .

Figure 6.28 Comparison of the experimental and FEA results of the *v*-field displacement contours for polycarbonate specimen

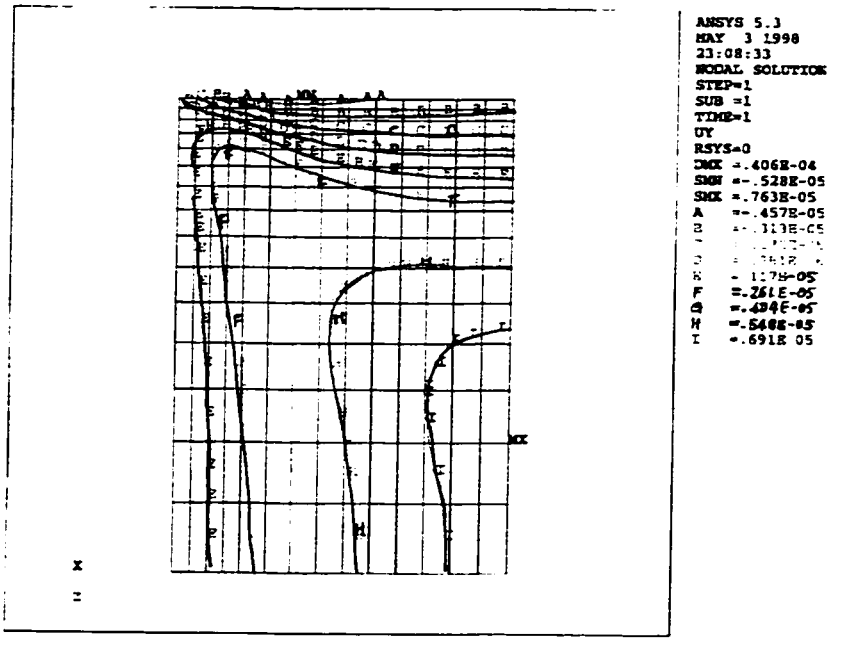

Figure 6.29(a) *u*-field displacement contours for alumina block (44.5 N static load)

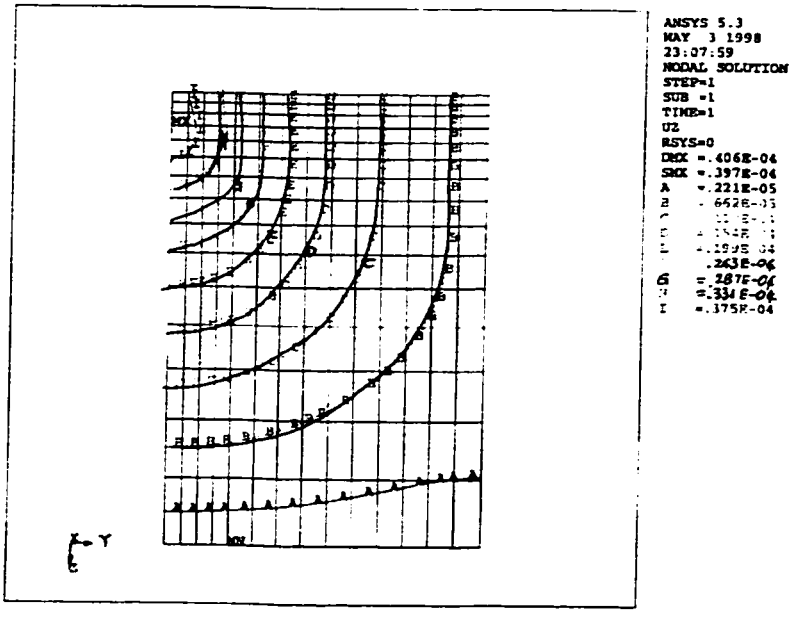

Figure 6.29(b) *v*-field displacement contours for alumina block (44.5 N static load)

specimen, which is the case for the FEA v-displacement contour plot in Figure 6.28(b). Along the lower edge the v-displacement is zero. The maximum v-displacement is at the loading point, or the center point of the upper edge. The maximum displacements from both experimental and FEA are approximately 0.005 mm. It appears that there exists a close match between the experimental results and the finite element prediction in v-displacement field also. The above comparison in both u- and v- fields demonstrates that the results from the experiments agree with that of FEA results.

Figure 6.25(a) and 6.25(b) are the contour plots from the analytical solutions described in equations 6.1 to 6.10. The contour plots represent the u- and v- displacement for a small block of material in a semi-infinite body. Comparing the u and v fields displacement contours from the analytical solution in Figures 6.25, with those from FEA and experiments in Figures 6.24(a) and (b), it is obvious that the displacement contour trends are very similar. However, the magnitude of the displacements of the analytical solution is smaller than the FEA contour indicated, and smaller than the experimentally recorded displacements at their corresponding locations. The analytical u-field displacements in Figure 6.25(a) are about 1/7 of those from the FEA or experiments in Figure 6.28. The analytical v-field displacements in Figure 6.25(b) are about 1/4 to 1/5 of those from the FEA or experiments in Figure 6.24(b). The differences in the displacements in both u- and v- fields are probably due to the different boundary condition between the semi-infinite body and those in the FEA model and experiment. For example, in the experimental setup and FEA model, both sides of the specimen were free of support. In the semi-infinite model, the specimen volume is supported by the adjacent materials, and the adjacent material prevents the material deform freely in the v-direction. Thus smaller displacement was observed in the analytical solutions. Another important factor that is attributed to the differences is that the applied load in the analytical model is a concentrated force at the center of the block volume instead of a blunt pressure load, as is in the case in the experiment and FEA models.

The optical experimental and FEA results for *alumina* material are studied and compared in this section. Figures 6.21 and 6.22 are the moiré fringes pictures from the experiments in u- and v- displacement fields respectively. Figures 6.29(a) and 6.29(b) are the contour plots obtained from finite element analysis for the alumina material. As can be seen in the experimental results shown in Figures 6.21 and Figure 6.22, the number of moiré fringes nearly remained constant in both u- and v- fields as the static loads were increased from 0 N load to 62 N in both u- and v-fields. Checking the FEA contours in the v fields, as illustrated in Figure 6.23 (b), the maximum displacement at static load of 44.5 N is 0.397e-5 mm, which is still less than that which can be represented by one moiré fringe (0.000417 mm). In the v fields, as illustrated in Figure 6.23 (a), the maximum u-displacement at static load of 44.5 N is 7e-6 mm, which is even less. The comparison between the FEA results and experimental results in u-and v- filed displacements equally demonstrates that the experimentally obtained displacements agree with those predicted by FEA for the alumina material.

From the above comparisons, it is not difficult to observe that the maximum displacement in both u- and v- fields at static load of 44.5 N on a polycarbonate material is quite different from those of ceramic material. Apparently the displacement for ceramic material is much smaller than the polycarbonate material. This is because that the alumina material is a much stiffer material than the polycarbonate. For alumina material, the displacement under the limited static loads could not be measured by moiré fringes.

6.5 SUMMARY

The numerical experimental study indicated that the normal pressure, jet pressure, and shear are the three most important parameters in determining displacement distribution and its contours. The FEA model with appropriate loads can be used to simulate the abrasive waterjet drilling. The jet pressure does not play a dominant role in

determining the u-field displacement. It was found that the shear contributes the most in shaping the displacement contours patterns. A uniform shear along the kerf proves to render distribution contours that are closest to the experimental observations.

In the verification study, both optical experimental and FEA results were compared for a polycarbonate specimen and a ceramic specimen under static loading. This step was necessary to qualify the optical system and the numerical model. In the polycarbonate specimen, the moiré interferometry results agree quite well with the finite element analysis results. However, in ceramic specimen the number of moiré fringes did not change as the load increased from 1 to 62 N. This is also consistent with the numerical prediction.

The good correlation between the FEA modeling and the experiments of the static loading on polycarbonate and alumina demonstrates that the FEA modeling is able to predict the displacement distribution for both polycarbonate and alumina material under static load. It also indicates that the FEA model used in this study is a viable model, and that the moiré interferometry setup employed in this investigation is a reliable optical experimental system.

CHAPTER 7

DYNAMIC EXPERIMENTAL AND NUMERICAL MODELING

7.1. AWJ PENETRATION DEPTHS

The drilling depth and penetration rate in both polycarbonate and alumina materials by abrasive waterjet were studied experimentally. Each hole was achieved under a predetermined jet exposure time. The depths of the hole generated by AWJ drilling were measured as a function of jet exposure time. A typical hole drilled in polycarbonate specimen is shown in Figure 7.1.

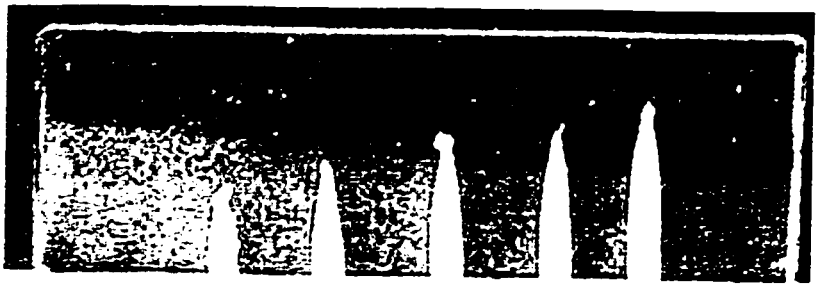

Figure 7.1 Typical hole drilled by AWJ in polycarbonate specimen

In polycarbonate material, a hole with an approximate parabolic profile was clearly visible through the transparent specimen after the abrasive waterjet drilling. Three groups of depth calibration tests were conducted. The AWJ parameters for all three AWJ tests included supply pressure of 207 MPa, SOD of 1 mm, garnet of mesh size #50, and

abrasive flow rate 30 g/s. The jet exposure time for the first group of drilling experiments ranged from 0.75 second to 2.4 seconds. The results from the first group of materials are plotted in Figure 7.2(a). Two more groups of drilling experiments were performed with jet exposure time ranging from 2 seconds to 6 seconds. The drilled depths are shown in Figure 7.2(b). As can be seen from Figures 7.2 (a) and (b), it is clear that the depth of hole in the polycarbonate material is a nonlinear function of the AWJ piercing time, and the change in the hole radius on the top of the hole is found to be insignificant. It appears that there exists a threshold time, and that material can only be removed and a hole formed if the jet exposure duration is greater than the threshold time. As can be seen from Figure 7.1, the largest slope of the curves occurs at the beginning of the AWJ drilling. The curve slope in the graph slowly tapers off as the jet drilling time increases. This suggests that the drilling capability of the abrasive waterjet stream is attenuated as the hole depth increases. This is evidenced in Figure 7.3, which shows the AWJ penetration rate through the polycarbonate material as a function of the jet exposure time. At t=2 seconds, the penetration rate is approximately 5 mm/s. Near the end of the experiment at t=6 seconds, the penetration rate becomes 3.6 mm/s. The reduced penetration rate is indicative of less kinetic energy in the abrasive waterjet. There are several causes responsible for the reduction of penetration rate. The interaction between the incoming flow and the reverse flow significantly reduces the jet speed, thus the reduction in kinetic energy. The kinetic energy of the AWJ stream also dissipates during the drilling process, which also contributes to the reduced penetration rate of the abrasive waterjet.

AWJ drilling experiments were performed on alumina material and the depths of jet penetration in alumina material were measured and recorded. These experiments were carried out at supply pressures of 124, 166, and 207 respectively. The depth of penetration is plotted in Figure 7.4(a) as a function of the jet exposure time at different supply pressures. The depth of penetration of the AWJ is highly related to the supply pressure. At jet exposure time of 10 seconds, the depth of hole is 2.2 mm for supply

pressure of 124 MPa, 3.1 mm for 166 MPa, and almost 4 mm for 207 MPa. The higher the supply pressure, the greater depth of hole produced. This agrees with the findings described in chapter 4. The AWJ penetration rate was calculated and plotted in Figure 7.4(b). The general trend is that the AWJ penetration rate is reduced as the jet exposure time is increased and is tapered off near the end. At jet exposure time of 7 seconds, the penetration rate is reduced to 1/3 of the penetration rate at t=1 second for supply pressure of 166 MPa and 207 MPa. At lower supply pressure of 124 MPa, the curve of penetration rate is almost flat, and the change in penetration rate is small. This is partly because the depth of hole created by the low pressure AWJ is relatively small, hence the smaller variation in rate of penetration. At higher pressures, such as 166 MPa and 207 MPa, the reduction in AWJ penetration rate is much more obvious

(a) 1st polycarbonate group

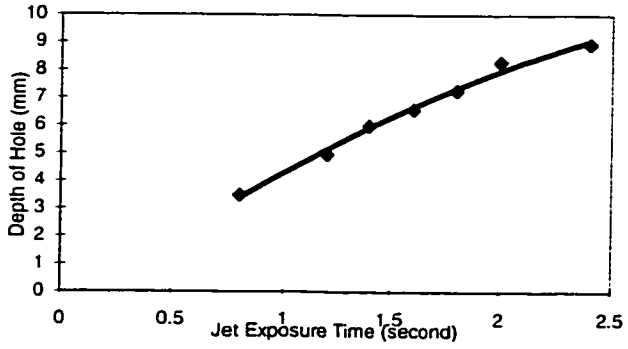

(b) 1st polycarbonate group

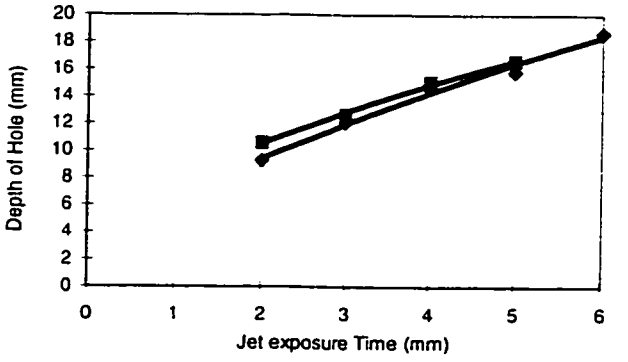

Figure 7.2 Depth of hole vs jet exposure time

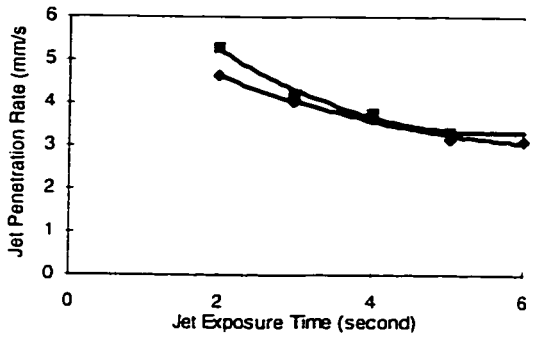

Figure 7.3 AWJ penetration rate vs jet exposure time(2nd group)

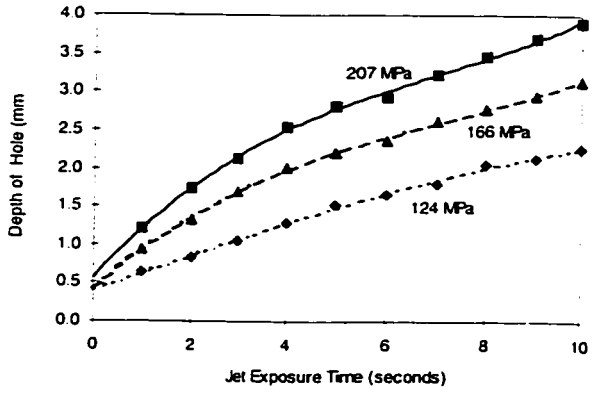

Figure 7.4(a) Depth of Hole vs. Jet exposure Time for Al_2O_3

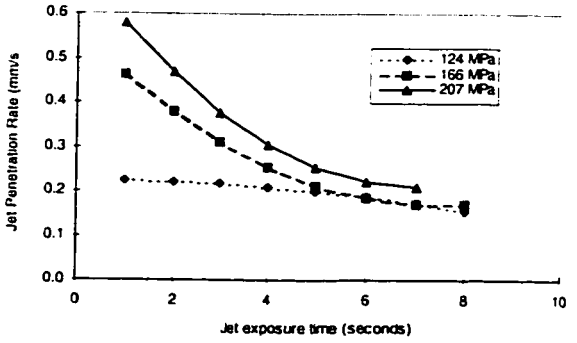

Figure 7.4(b) Jet Penetration Rate in Alumina Material

Under the same AWJ drilling conditions, the penetration rate is much greater in polycarbonate than in alumina material, as can be observed in Figure 7.3 and 7.4(b). In comparison with the energy dissipation results of AWJ drilling in polycarbonate material, the energy dissipation in ceramic material is much greater.

7.2. DYNAMIC MOIRE EXPERIMENTS

7.2.1 Polycarbonate Material

Dynamic moiré fringe patterns for both u- and v- displacement fields for polycarbonate material were recorded during the AWJ piercing process. The recorded moiré fringe patterns in two typical experiments for the polycarbonate specimens are shown in Figures 7.5 to 7.8. The conditions used in generating the moiré fringe patterns on polycarbonate were: supply pressure of 207 MPa, standoff distance maintained at 1 mm, garnet abrasive of mesh size 50, and abrasive flow rate of 30 g/s. The jet exposure times for the two experiments were approximately 2.4 seconds and 2.6 seconds, respectively. At the beginning of the jet impact process, the recorded u field started with a few fringes, while the v field only showed obscure fringes. However, when the pierced hole became deeper, clearer fringes emerged in both u- and v- fields. The blurry fringe patterns could have been due to the vibration from the intensifier pump at the onset of impact process, since the v- field tended to be affected more than the u field. In addition, stress waves in the specimen might have been induced by the impingement of the jet. After a jet exposure time of 0.6 second, the system became stabilized, and clear fringe patterns could be observed. It is also interesting to notice that some of the recorded fringe patterns in the v- field look like a skeleton, as shown in Figure 7.7.

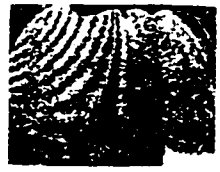

t=0.2 seconds

t=1.0 seconds

t=1.8 seconds

t=0.4 seconds

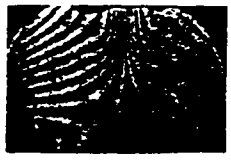

t=1.2 seconds

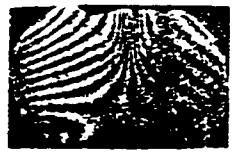

t=2.0 seconds

t=0.6 seconds

t=1.4 seconds

t=2.2 seconds

t=0.8 seconds

t=1.6 seconds

t=2.4 seconds

Figure 7.5 *u*-field Morie Fringes for Polycarbonate Specimen during AWJ Piercing
(Supply pressure 207 MPa, Garnet #50, SOD 1mm)

t=0.2 seconds

t=1.0 seconds

t=1.8 seconds

t=0.4 seconds

t=1.2 seconds

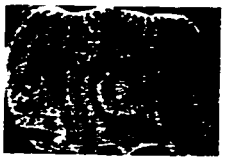

t=2.0 seconds

t=0.6 seconds

t=1.4 seconds

t=2.2 seconds

t=0.8 seconds

t=1.6 seconds

t=2.4 seconds

Figure 7.6 *v*-field Morie Fringes for Polycarbonate Specimen during AWJ Piercing
(Supply pressure 207 MPa, Garnet #50, SOD 1mm)

t=0.4 second

t=1.2 second

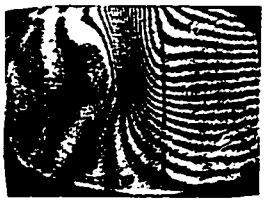

t=2.0 second

t=0.6 second

t=1.4 second

t=2.2 second

t=0.8 second

t=1.6 second

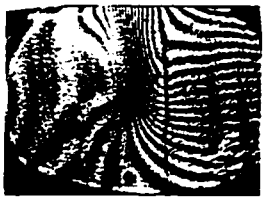

t=2.4 second

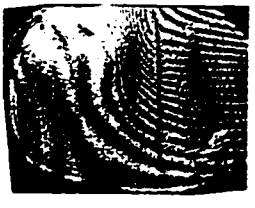

t=1.0 second

t=1.8 second

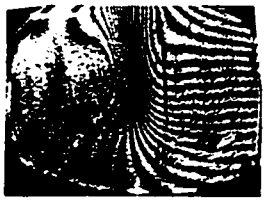

t=2.6 second

Figure 7.7 *u*-field Morie Fringes for Polycarbonate Specimen during AWJ Piercing
(Supply pressure 207 MPa, Garnet #50, SOD 1mm)

t=0.4 second

t=1.2 second

t=2.0 second

t=0.6 second

t=1.4 second

t=2.2 second

t=0.8 second

t=1.6 second

t=2.4 second

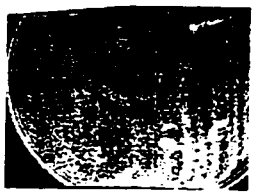

t=1.0 second

t=1.8 second

t=2.6 second

Figure 7.8 *v*-field Morie Fringes for Polycarbonate Specimen during AWJ Piercing
(Supply pressure 207 MPa, Garnet #50, SOD 1mm)

Figure 7.9 (a) shows displacement in the horizontal direction (*u-field*) along the top edge of the specimen at t=0.6 second of jet exposure time, which was plotted as a function of the horizontal coordinate. It is obvious that the *u*-field displacement at t=0.6 second already became symmetric with respect to the centerline of the specimen. At 4 mm from the vertical centerline on the top edge, the *u*-displacement *du* was 0.0025 mm moving away from the centerline. At jet exposure time t=2.4 seconds, the *u*-displacement along the top edge of the specimen was plotted as a function of the x-coordinate, and the *v*- field displacement along the centerline of the specimen was plotted as a function of the y-coordinate. The graphs are shown in Figures 7.9 (b) and (c).

A sketch of the specimen and the reference coordinate system used in the graphs is illustrated in the Figure 7.9 (a)-(c). Note that the displacement in the *u*-filed is symmetric with respect to the centerline of the specimen in the waterjet direction. Along the centerline in the *v*-field, the displacement at the bottom edge is zero. The *v*-displacement is increased almost linearly, starting at a height of 12 mm from the bottom, and reaching the maximum value near the top edge.

The moiré fringes for the polycarbonate material shown in Figures 7.5 and 7.6 are analyzed in more detail. Both *u* and *v* displacement fields for selected AWJ drilling depths of 4 mm, 6 mm, and 8mm are studied. The displacement and the strain distributions in their respective whole fields on the specimen surfaces are calculated and presented in Figures 7.10 to 7.15 for all three hole depths. In the *u*-field, as shown in Figure 7.10, 7.12, and 7.14, the horizontal displacements are symmetric with respect to the vertical centerline of the specimen. The left most and the right most points along the top edge have the largest horizontal displacements. In the general area near the vertical symmetric line, the density of the moiré fringes is the largest in the *u*-displacement field, which means that it has the largest horizontal strain in this area. In the *v*-displacement field in Figure 7.11(a), 7.13(a), and 7.15(a), the *v*-displacement along the bottom edge is zero, because the specimen is set on this platform. At the mid - point on the top edge, it

has the largest *v*-displacement *dv*. The maximum *v*-displacements are 0.00125 mm, 0.00167 mm, and 0.00208 mm for depth of hole of 4 mm, 6 mm, and 8 mm, respectively. Near the maximum *v*-displacement region, the moiré fringes are the densest. Therefore, the *v*-strain is also the largest in this area. This agrees very well with what is demonstrated in the *v*-strain contour in 7.11(b), 7.13(b), and 7.15(b).

The profile of the hole created by the AWJ drilling is drawn and overlaid both on the displacement contour plot and on the strain contour plot. These profiles of the cavities are used as reference for further analysis, because the area near or within the cavity envelope is of the most interest. On the outer surface of the specimen, the maximum *u*-displacements within the hole profile are 0.00085 mm, 0.0011 mm, and 0.0013 mm for depths of hole of 4 mm, 6 mm and 8 mm, respectively. The maximum *u*-strains within the envelopes for the three cases of different depth of hole are 0.0012 mm/mm, 0.0016 mm/mm, and 0.0016 mm/mm, respectively. At the point on the outer surface of the specimen corresponding to the bottom of the hole, the strains in the *u*-field vary from 0.0007 to 0.0014.

At the bottom of the hole on the outer surface of the specimen, the *v*-displacements are 0.00125 mm, 0.00167 mm, and 0.00208 mm. The *v*-strains are 0.0006 mm/mm, 0.0002 mm/mm, and 0.00004 mm/mm for the depths of hole of 4 mm, 6 mm, and 8 mm, respectively.

Figures 7.7 and 7.8 show the second set of moiré fringes, analyzed for jet exposure time of 0.8 second to 2.4 seconds with an increment of 0.2 second. Both *u*- and *v*- field fringe patterns were digitized, as well as the strain components ε_x, ε_z. Based on the *u*- and *v*- displacement contours, the shear strains on the front surfaces were calculated and found to be zero for all depth of holes. This implies that the principal strains ε_1,and ε_3 are the same as the strain components ε_x, and ε_z

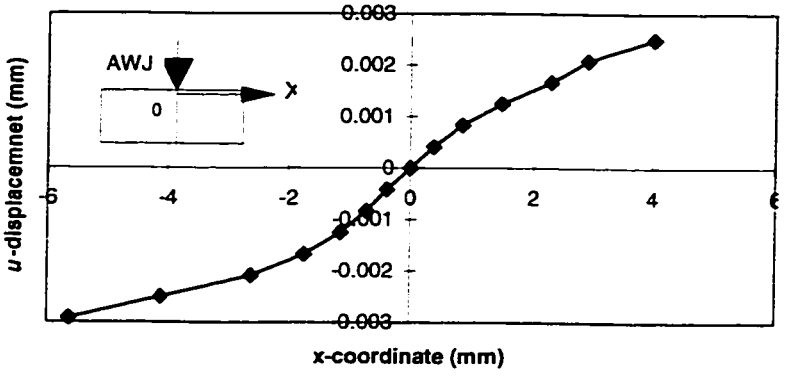

(b) U-displacement @t=2.4 seconds

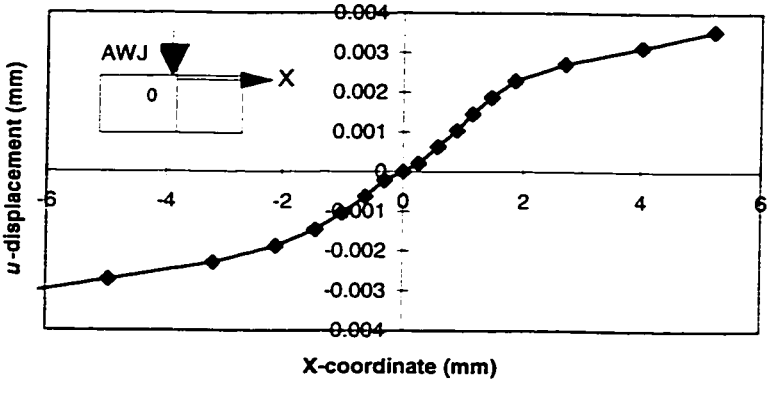

(c) *v* displacement @ 2.4 seconds

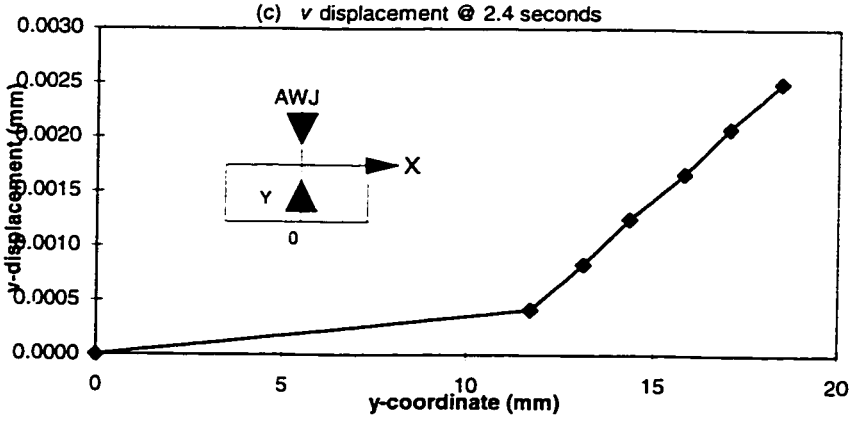

Figure 7.9 *u*-, *v*- Displacements along the Top Edges and Centerline

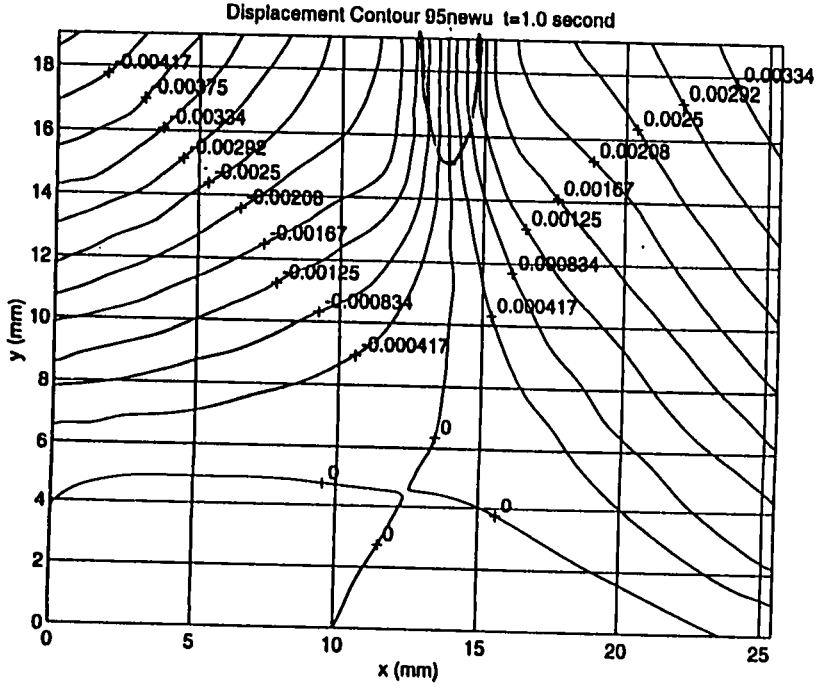

(a) Displacement Contour

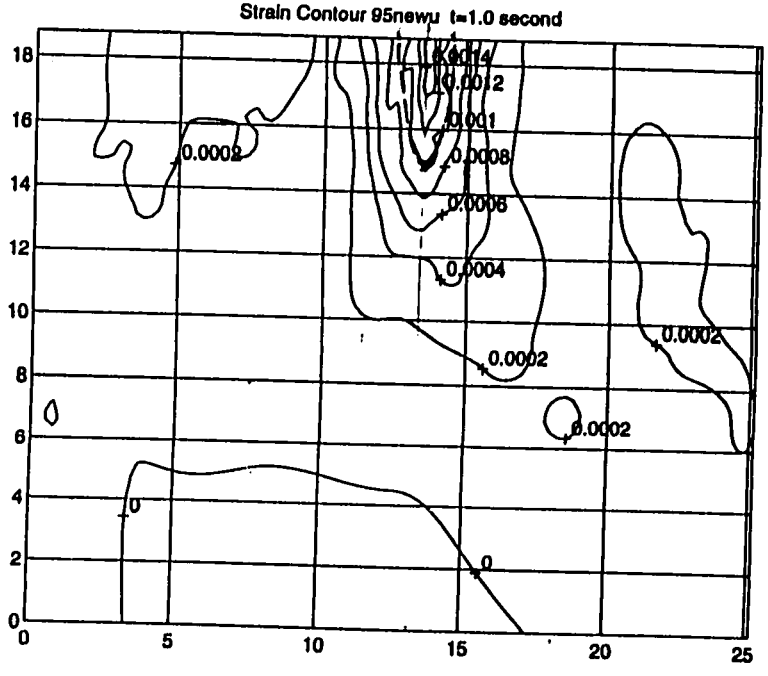

(b) Strain Contour

Figure 7.10 u-field displacement and strain contours for polycarbonate at depth of 4 mm (supply pressure 207 MPa; SOD 1mm; garnet mesh #50; AFR 30 g/s)

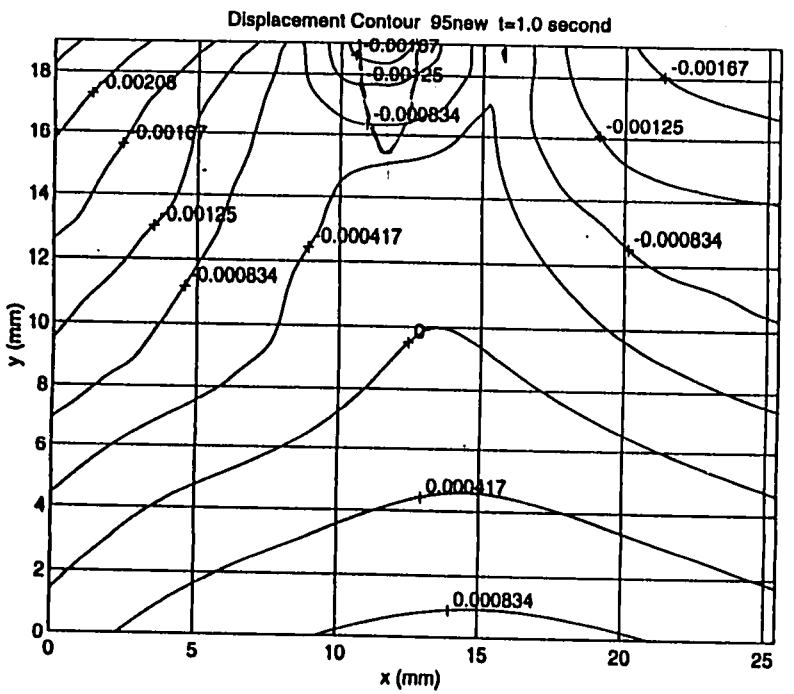

(a) Displacement Contour

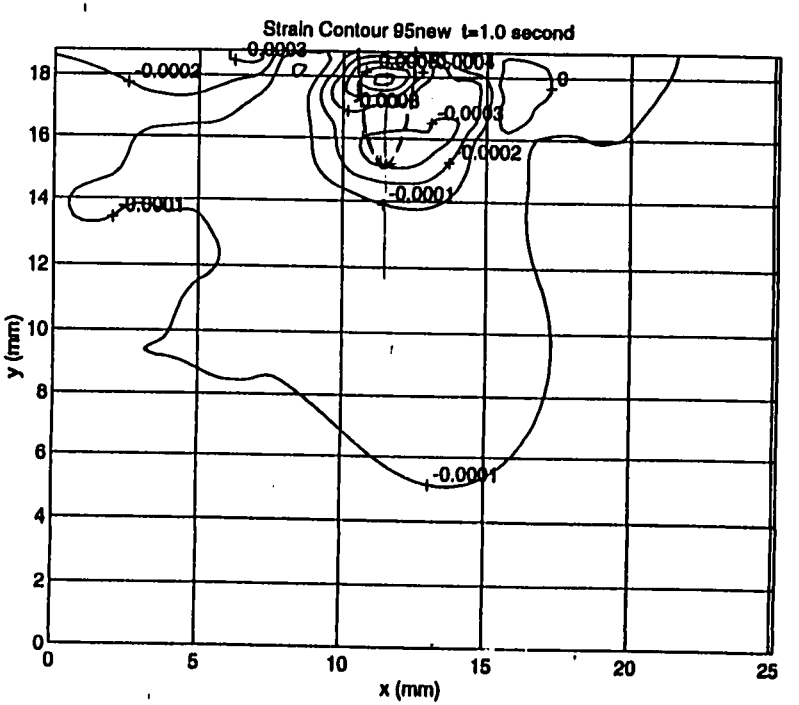

(b) Strain Contour

Figure 7.11 ν-field displacement and strain contours for polycarbonate at depth of 4 mm (supply pressure 207 MPa; SOD 1mm; garnet mesh #50; AFR 30 g/s)

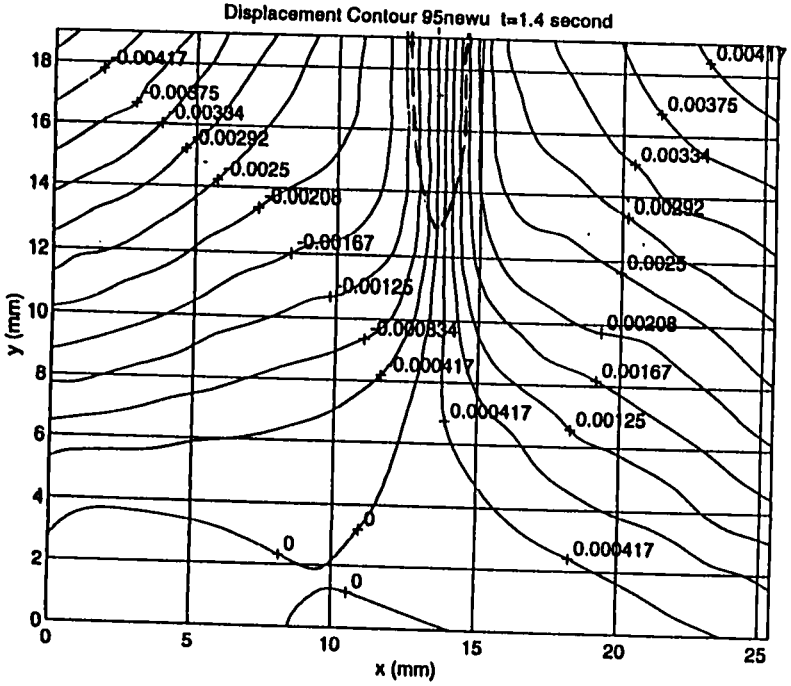

(a) Displacement Contour

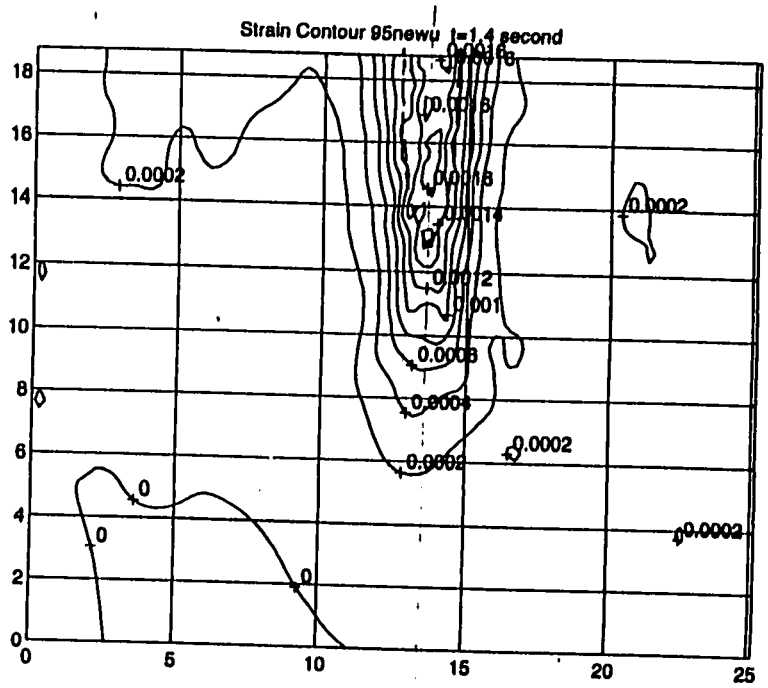

(b) Strain Contour

Figure 7.12 *u*-field displacement and strain contours for polycarbonate at depth of 6 mm (supply pressure 207 MPa; SOD 1mm; garnet mesh #50; AFR 30 g/s)

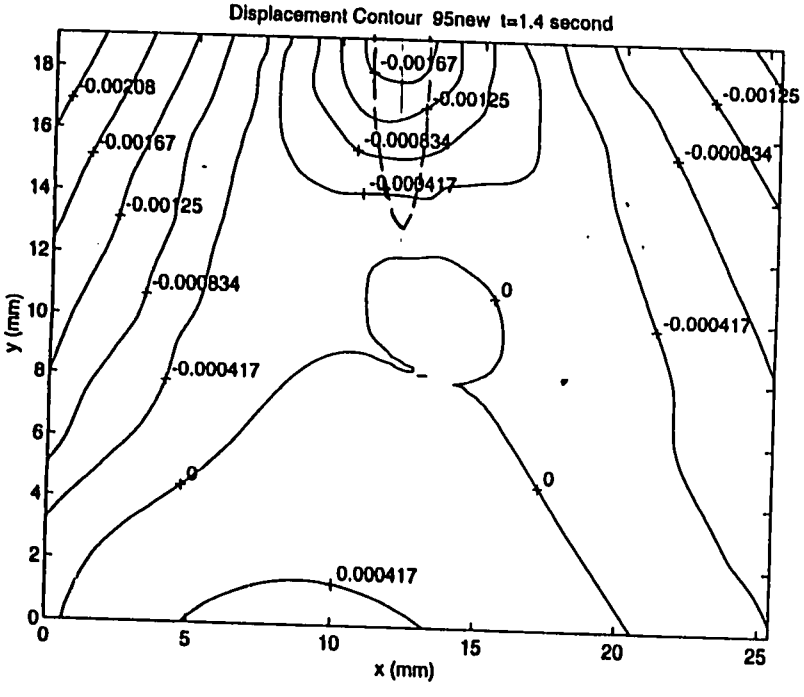

(a) Displacement Contour

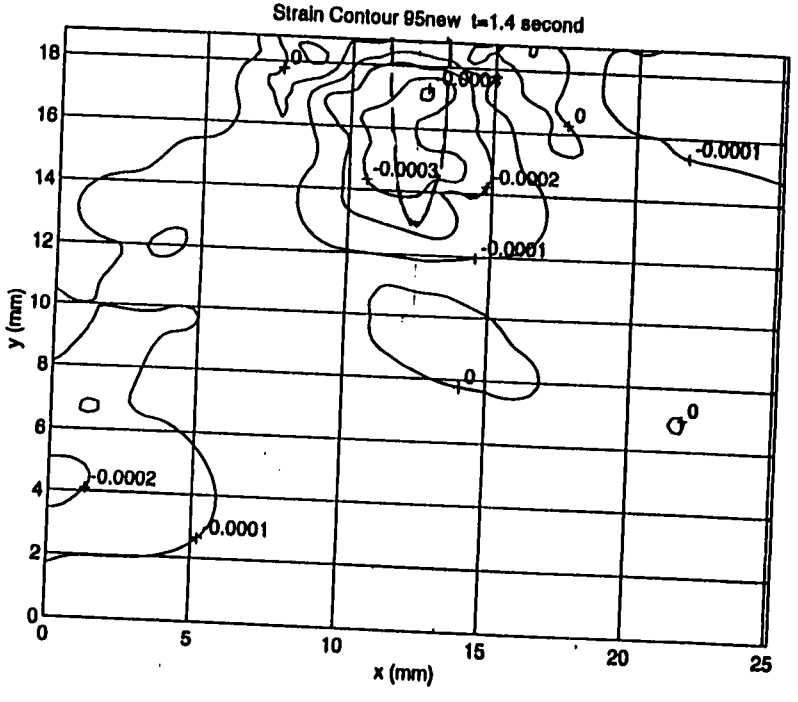

(b) Strain Contour

Figure 7.13 ν-field displacement and strain contours for polycarbonate at depth of 6 mm (supply pressure 207 MPa; SOD 1mm; garnet mesh #50; AFR 30 g/s)

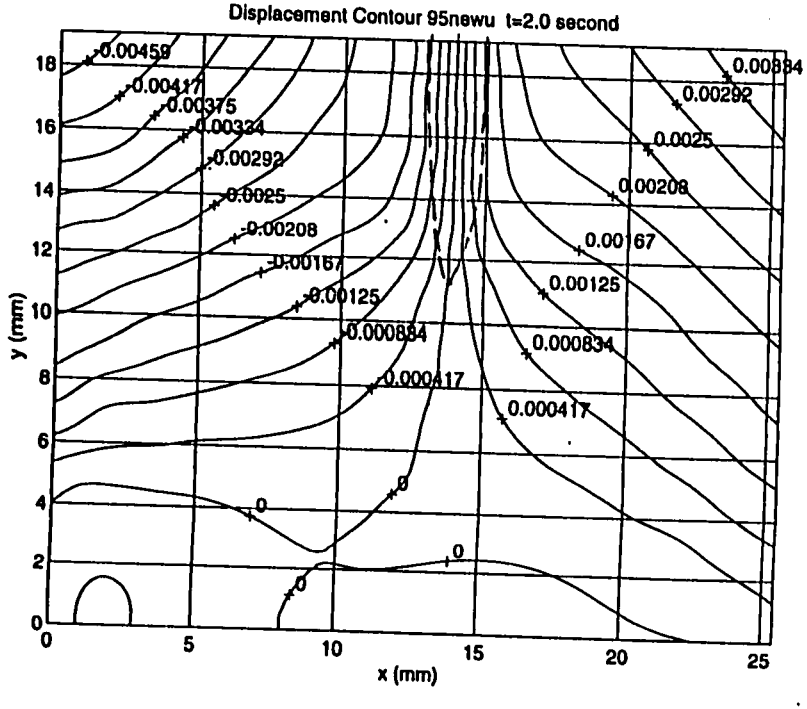

(a) Displacement Contour

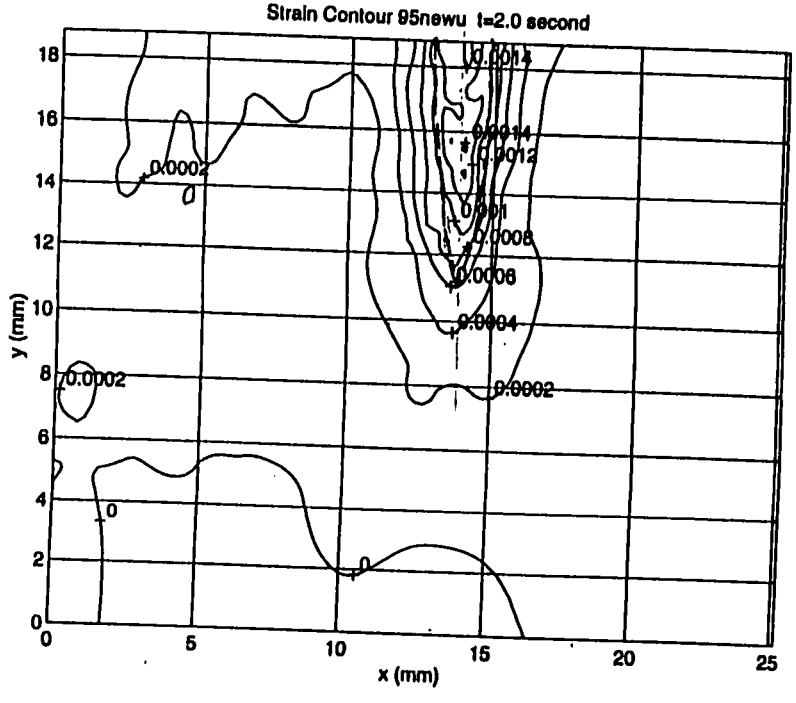

(b) Strain Contour

Figure 7.14 u-field displacement and strain contours for polycarbonate at depth of 8 mm (supply pressure 207 MPa; SOD 1mm; garnet mesh #50; AFR 30 g/s)

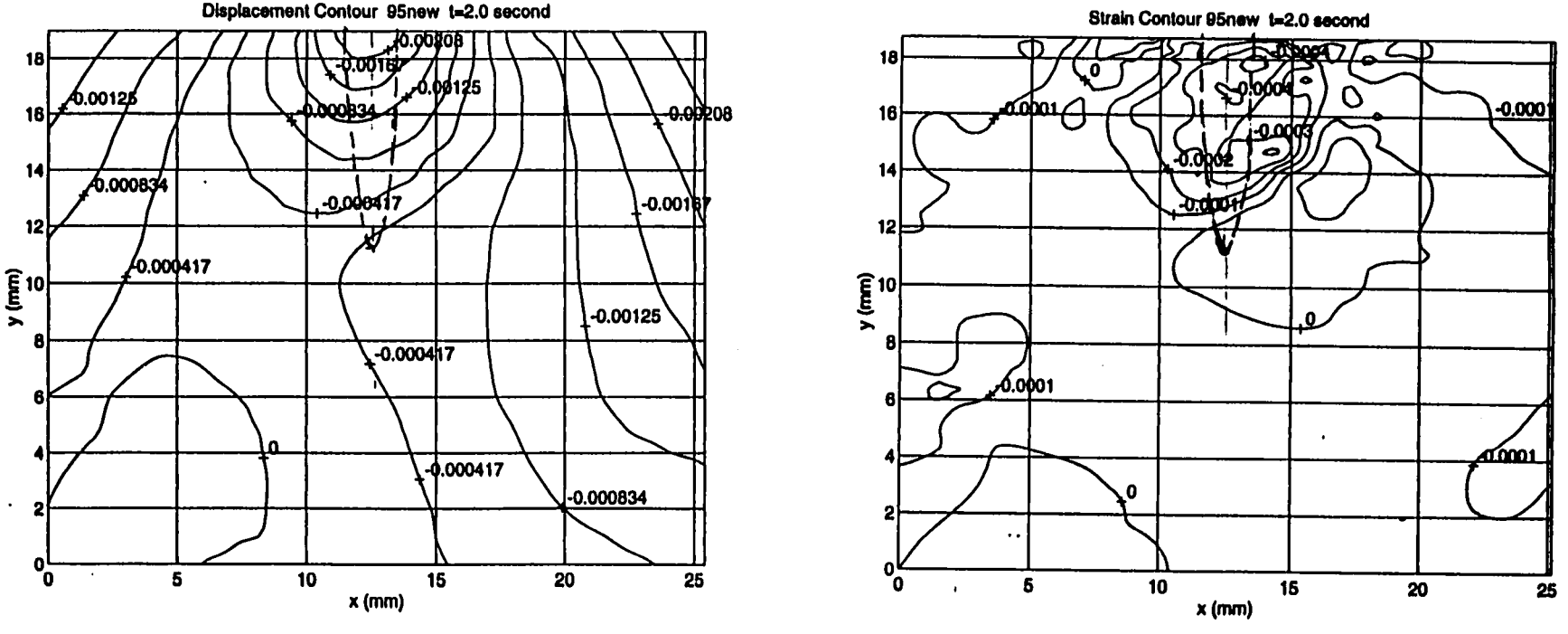

(a) Displacement Contour

(b) Strain Contour

Figure 7.15 v-field displacement and strain contours for polycarbonate at depth of 8 mm (supply pressure 207 MPa; SOD 1mm; garnet mesh #50; AFR 30 g/s)

The contour graphs for ε_1, ε_3, or ε_x, ε_z, were plotted in Figure H.1 to H.8, which are filed in Appendix H. The principal strains on the front surface at the bottom of the hole were calculated, and are summarized in Table 7.1

Table 7.1 Principal strains on the out surface at the bottom of the hole

(AWJ drilling parameters: supply pressure 207 MPa; SOD 1 mm; garnet mesh size 80, AFR 30 g/s)

Time (seconds)	Depth (mm)	ε_1 (mm/mm)	ε_2 (mm/mm)
0.8	2.60	1.3E-03	-5.0E-04
1.0	3.70	1.3E-03	-2.5E-04
1.2	4.95	1.5E-03	-5.0E-04
1.4	5.99	1.6E-03	-5.0E-04
1.6	6.58	1.6E-03	-4.5E-04
1.8	7.26	1.7E-03	-5.0E-04
2.0	8.31	1.5E-03	-2.5E-04
2.4	8.94	1.7E-03	-2.2E-04

It was noted that the principal strains ε_1 at the bottom of the notch on the outer surface of the specimen increased slightly as the depths of holes increased. The strain ε_1 increased from 0.0013 mm/mm at hole depth of 2.6 mm to 0.00175 mm/mm at hole depth of 9 mm. However, the v-field strain ε_1 varied from -0.00025 mm/mm to -0.0005. These phenomena are consistent with the results from a previous experiment.

7.2.2 Alumina Material

Three supply pressures, 124 MPa, 166 MPa, and 207 MPa, were applied in AWJ drilling experiments on alumina materials. The transient displacement moiré fringe patterns for all these experiments were recorded, and are shown in Figures 7.16 to 7.21. The AWJ drilling parameters on the alumina material included standoff distance of 1 mm, garnet abrasives of mesh size 80, orifice diameter of 0.33 mm, and carbide mixing tube diameter of 0.89 mm. The abrasive flow rates were 13 g/s, 14 g/s, and 17.5 g/s for supply

pressures of 124 MPa, 166 MPa, and 207 MPa, respectively. Since the AWJ material removal rate on the ceramic material is much less than that on the polycarbonate material, the depth of the hole achieved by AWJ drilling was much smaller than for polycarbonate materials. In all cases the jet exposure times for alumina were longer than the for polycarbonate materials. The moiré fringes shown in Figures 7.16 to 7.21 are typical fringe patterns extracted from some of the complete recordings.

For moiré fringe patterns shown in Figures 7.16 and 7.17 at supply pressure of 124 MPa, the number of moiré fringes and the fringe patterns in both u- and v-displacement fields showed some changes at the onset of the abrasive waterjet. In the u-field, the number of fringes increased from 3 to 5. In the v-field the fringe number increased from 2 to 3. As the jet exposure time was increased, the minor changes in both quantity and pattern for the moiré fringes were observed. Observable changes in moiré fringes were noticed when the supply pressure was increased to 165 MPa, as was evidenced in Figures 7.18 and 7.19. At the first second the number of fringes increased from 1 in the initial field to 4 in the u-field, and the number of fringes increased from 2 to 3 in the v-field. From the first second to the fourth second of jet exposure time, variation in the number of fringes was very small. After the fourth second, some rotational fringes were introduced, and the number of fringes increased in both u- and v-fields. For supply pressure of 207 MPa, changes of moiré fringe in both the number of fringes and fringe patterns were more obvious. In the u-field the number of the fringes was increased from 3 in the initial field to 8 at the end of the first second. The increase in number of fringes was very small as the jet exposure time was increased. In the v-field the moiré fringe increased from 1 in the initial field to 3 at the end of the first second. At the fourth second the number of fringes was increased to 4. Similar to the previous experiment, rotational fringes emerged after the fifth second of AWJ drilling.

The displacement distributions and the state of strain on the outer surface of the specimen for the dynamic AWJ drilling on alumina materials were studied in detail.

Since the process of analysis is quite lengthy, the analyzed data for the moiré fringes of AWJ drilling at a supply pressure of 207 MPa are presented in this section. The displacement and strain contours are in Figures 7.22 to 7.29. At supply pressure of 207MPa, SOD 1 mm, and abrasive flow rate of 17.5 g/s for garnet mesh of size 80, the depth of hole achieved at each of the first four consecutive seconds was, respectively: 1.25 mm, 1.75 mm, 2.15 mm, and 2.6 mm. In the u-field, the horizontal displacement du was symmetric with respect to the vertical centerline of the specimen. The horizontal displacement increased at the onset of the AWJ from 0 to 0.000417 mm at the left of the symmetric line, and to 0.000837 mm at the right of the symmetric line. From Figures 7.22, 7.24, 7.26, and 7.28, it is noticed that the horizontal displacement du did not show noticeable increase as the jet exposure time was increased. Near the bottom of the hole on the outer surface, the horizontal strains were almost maintained at 0.0002 mm/mm. In the v-field, the maximum vertical displacements for the first two seconds of jet exposure were 0.000834 mm. As the jet exposure time was increased, the vertical displacement increased to 0.001251 mm. However, the v- strain near the bottom of the hole on the outer surface increased from 1e-5 mm/mm and 2e-5 mm/mm, to 4e-5 mm/mm and 6e-5 mm/mm, as depicted in the strain contours in Figures 7.23, 7.25, 7.27, and 7.29. Similar analyses were performed for AWJ drilling on alumina with supply pressure of 167 MPa and 124 MPa. Some of the results are included in Appendix H in Figures H.9 to H.20. Under the same drilling conditions, higher supply pressure yielded a larger depth of hole, and larger displacements in both u- and v- directions. Since the bottom of the hole on the outer surface is of the most interest, the strains ε_x and ε_z are calculated and reported in Tables 7.2 to 7.5.

At the bottom of the hole on the outer surface, the strain ε_x increased from 1.5e-4 mm/mm to 2e-4 mm/mm as the supply pressure was increased from 126 MPa to 207 MPa. A minor increase in ε_z was also observed as the pressure was increased. It appears

that the absolute value of the strains of ε_x, ε_z increases as the depth of hole is increased. This can be observed from the above tables 7.2 to 7.5.

Table 7.2 Variation of strains vs. supply pressure

Supply Pressure	ε_x	ε_z
126 MPa	1.50E-04	-5.00E-05
167 MPa	1.60E-04	-4.00E-05
207 MPa	2.00E-04	-4.00E-05

Table 7.3 Variation of strains vs depth of hole (P=207 MPa)

depth of hole	ε_x .	ε_z
1.25 mm	1.50E-04	-6.00E-06
1.75 mm	1.75E-04	-2.00E-05
2.15 mm	2.00E-04	-4.00E-05
2.6 mm	2.50E-04	-7.00E-05

Table 7.4 Variation of strains vs depth of hole (P=167 MPa)

depth of hole	ε_x .	ε_z
0.94 mm	1.50E-04	9.00E-06
1.32 mm	1.60E-04	-1.20E-05
1.7 mm	1.10E-04	-1.50E-05
2.01 mm	1.60E-04	-4.00E-05

Table 7.5 Variation of strains vs depth of hole (P=126 MPa)

depth of hole	ε_x .	ε_z
2.13 mm	1.50E-04	-5.00E-05
2.5 mm	1.60E-04	-1.00E-04

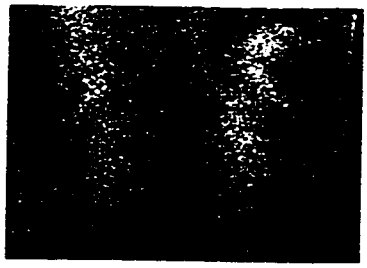

t=0 second

t=12 second

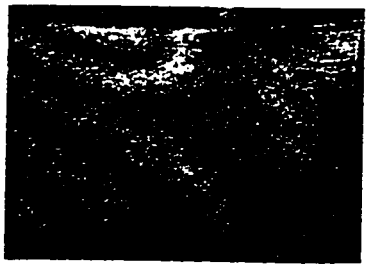

t=3 second

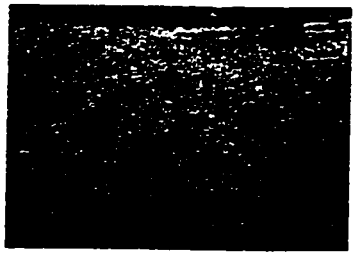

t=15 second

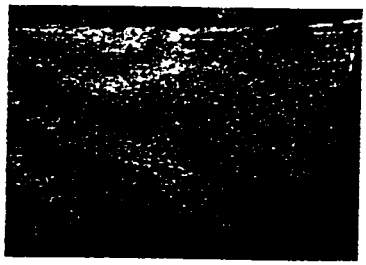

t=6 second

t=18 second

t=9 second

Figure 7.16 *u*-field Moire Fringes for Alumina during AWJ Piercing
(Supply Pressure 124 MPa, SOD 1 mm; garnet mesh 80; AFR

t=0 second

t=9 second

t=3 second

t=12 second

t=6 second

t=15 second

Figure 7.17 v-field Moire Fringes for Alumina during AWJ Piercing
(Supply pressure 124 MPa; SOD 1mm; Garnet mesh size 80)

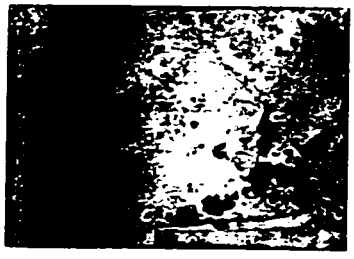

t=0 second

t=5 second

t=1 second

t=6 second

t=2 second

t=7 second

t=3 second

t=8 second

t=4 second

t=9 second

Figure7.18 *u*-field Moire Fringes for Alumina during AWJ Piercing
(Supply Pressure 167 MPa; SOD 1 mm; garnet mesh #80; AFR 17.5g/s)

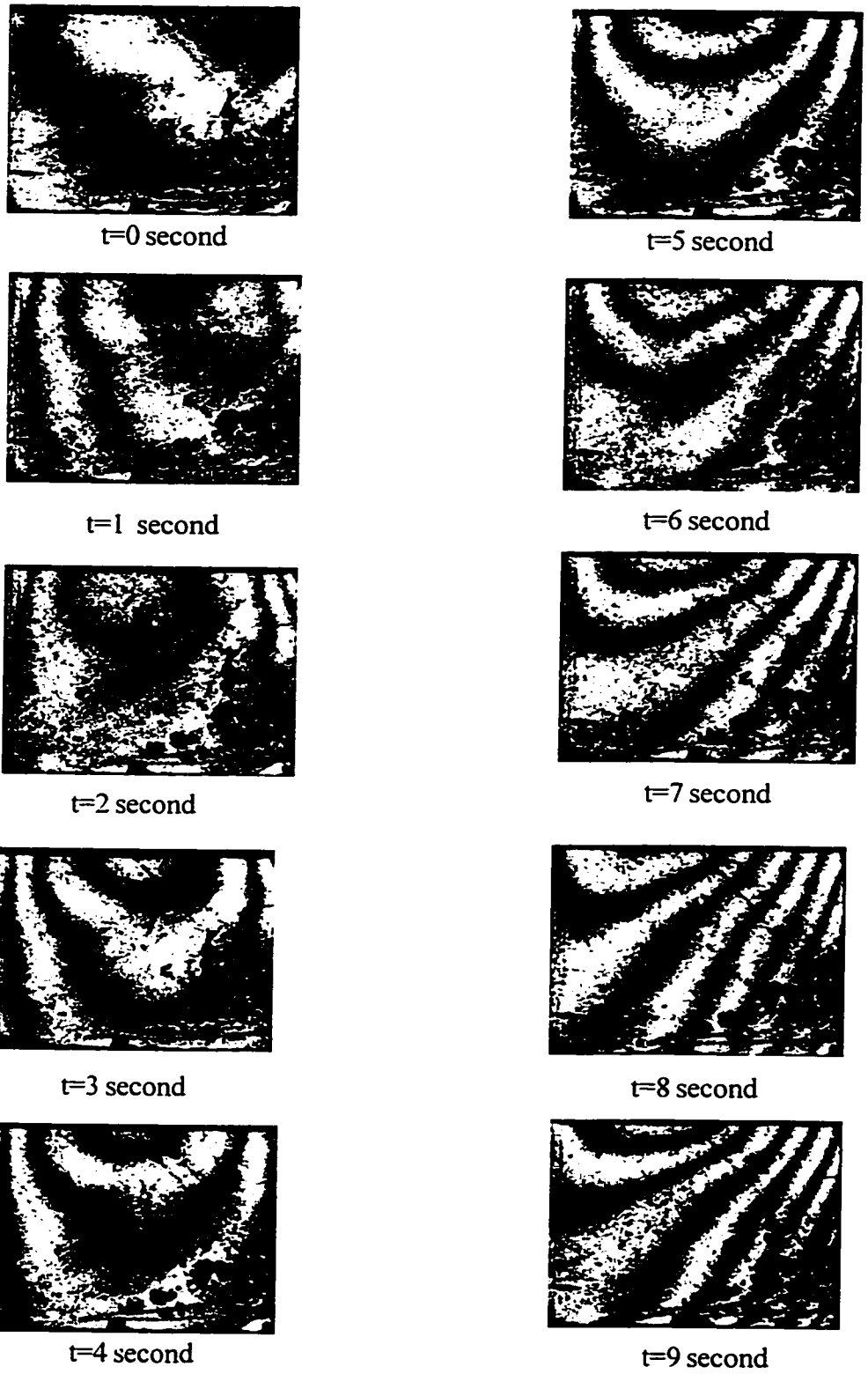

Figure 7.19 v-field Moire Fringes for Alumina during AWJ Piercing
(Supply Pressure 167 MPa)

t=0 second

t=5 second

t=1 second

t=6 second

t=2 second

t=7 second

t=3 second

t=8 second

t=4 second

Figure 7.20 u-field Moire Fringes for Alumina during AWJ Piercing (Supply Pressure 208MPa, 503)

t=0 second

t=4 second

t=1 second

t=5 second

t=2 second

t=6 second

t=4 second

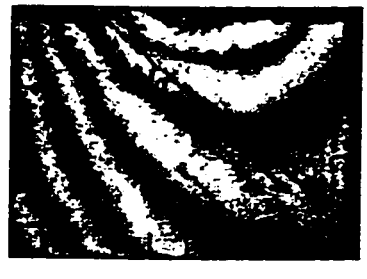

t=7 second

Figure 7.21 *v*-field Moire Fringes for Alumina during AWJ Piercing
(Supply Pressure 207 MPa, , SOD 1mm, Garnet mesh 50,503)

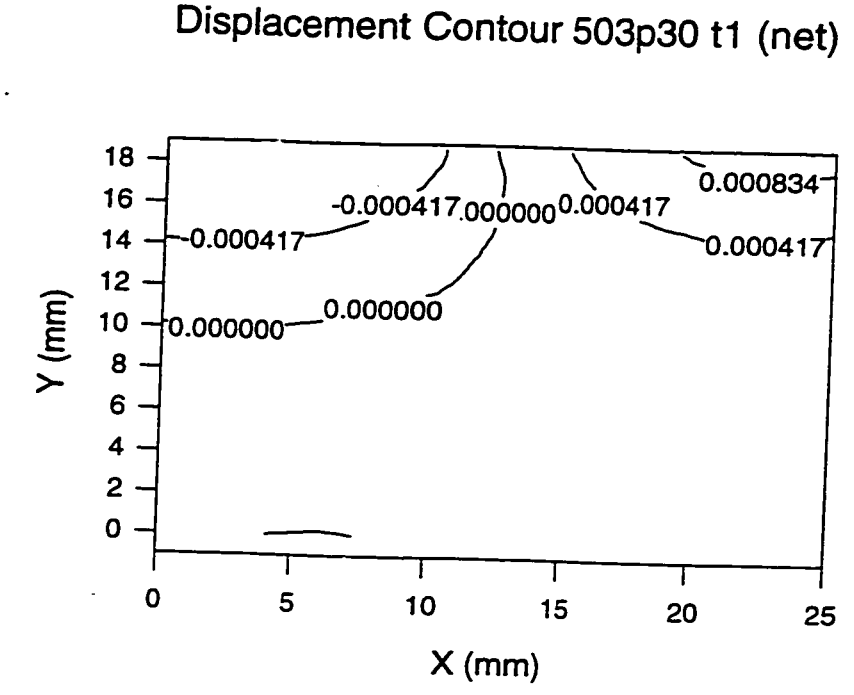

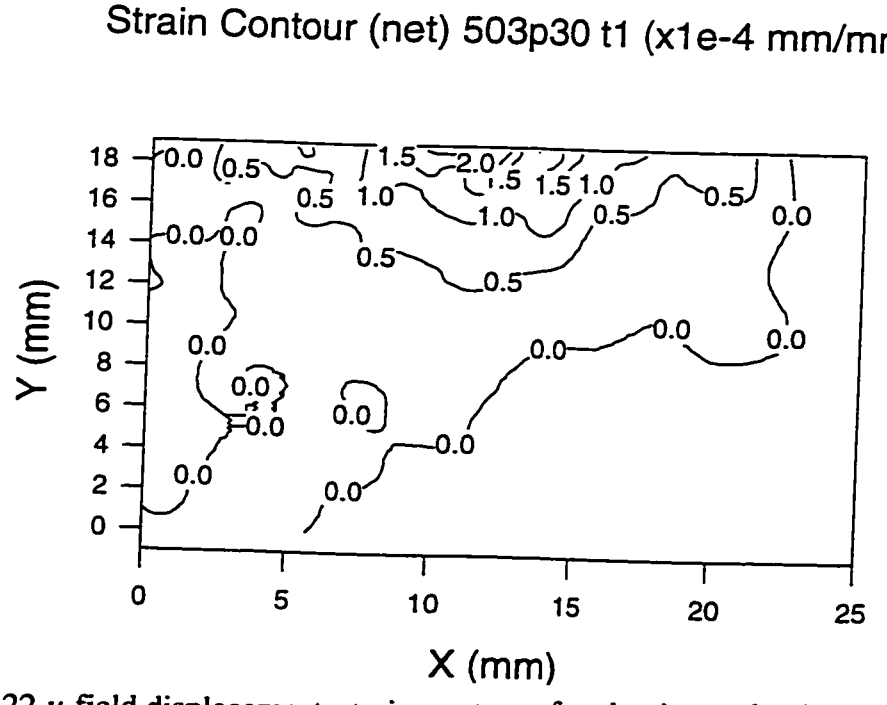

Figure 7.22 *u*-field displacement, strain contours for alumina at depth of hole 1.25 mm (supply pressure 207MPa; SOD 1mm; garnet mesh #80; AFR 17.5 g/s)

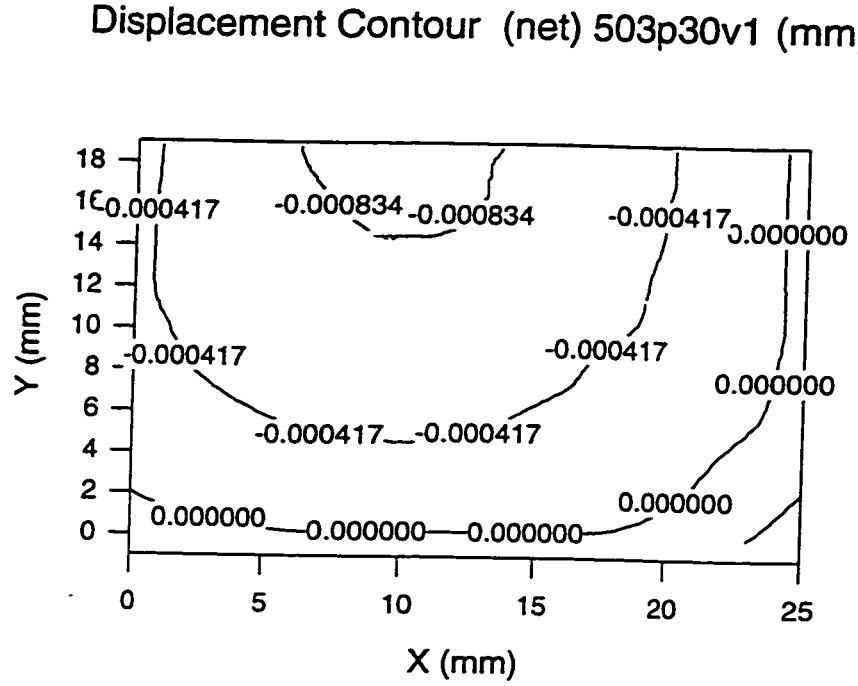

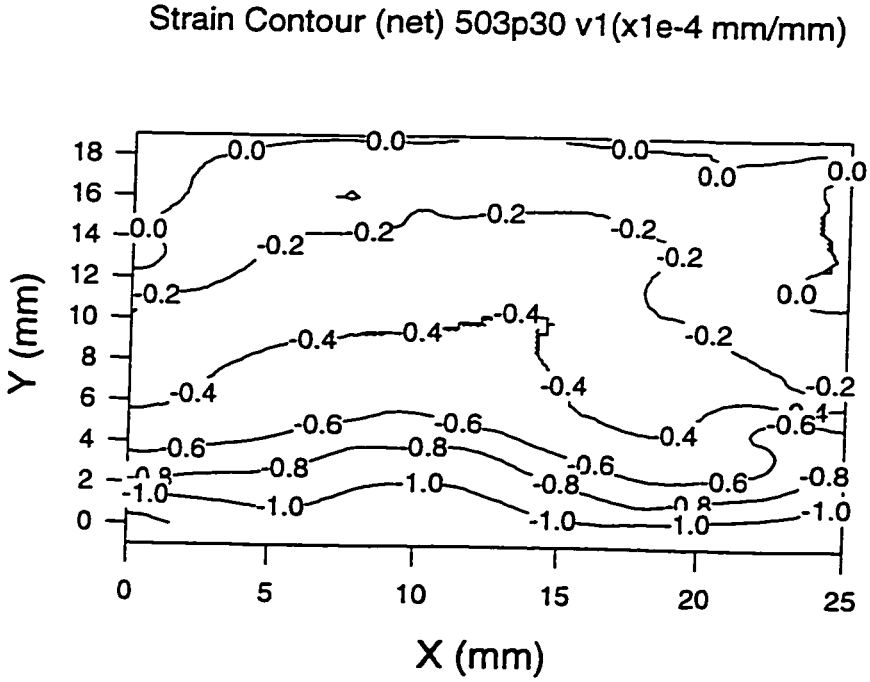

Figure 7.23 *v*-field displacement, strain contours for alumina at depth of hole 1.25 mm (supply pressure 207 MPa; SOD 1mm; garnet mesh #80; AFR 17.5 g/s)

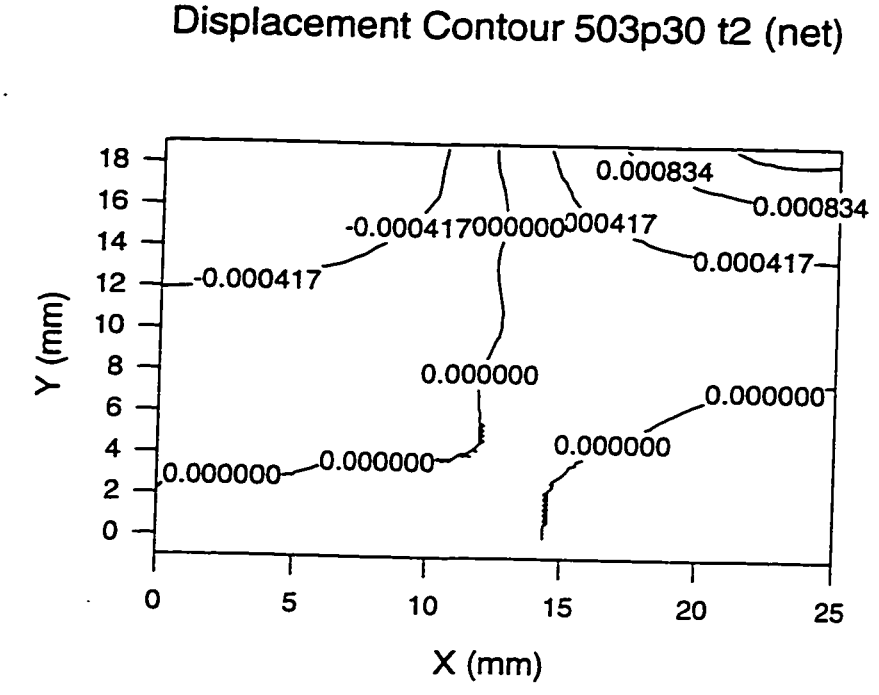

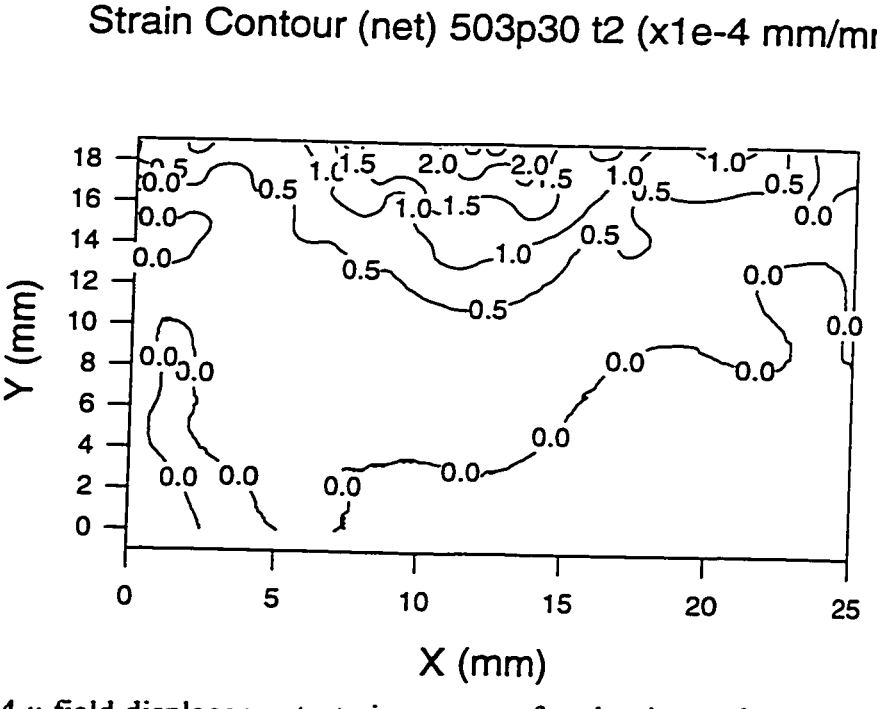

Figure 7.24 *u*-field displacement, strain contours for alumina at depth of hole 1.75 mm (supply pressure 207 MPa; SOD 1mm; garnet mesh #80; AFR 17.5 g/s)

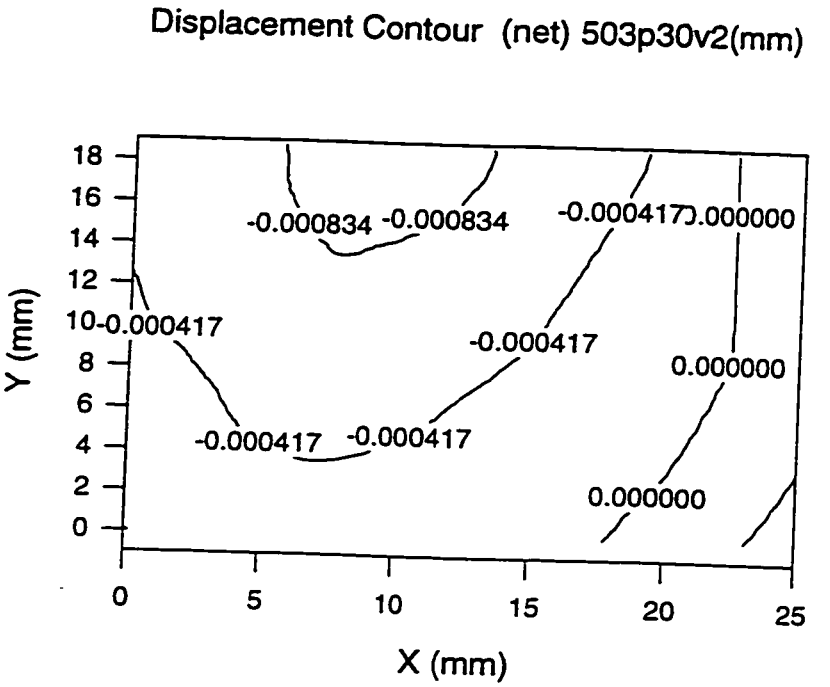

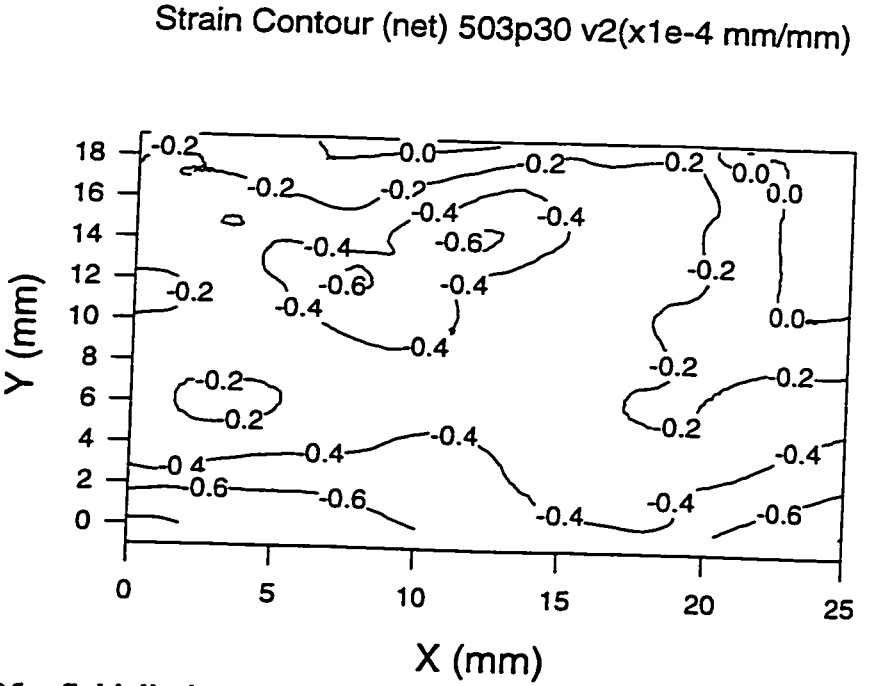

Figure 7.25 *v*-field displacement, strain contours for alumina at depth of hole 1.75 mm (supply pressure 207 MPa; SOD 1mm; garnet mesh #80; AFR 17.5 g/s)

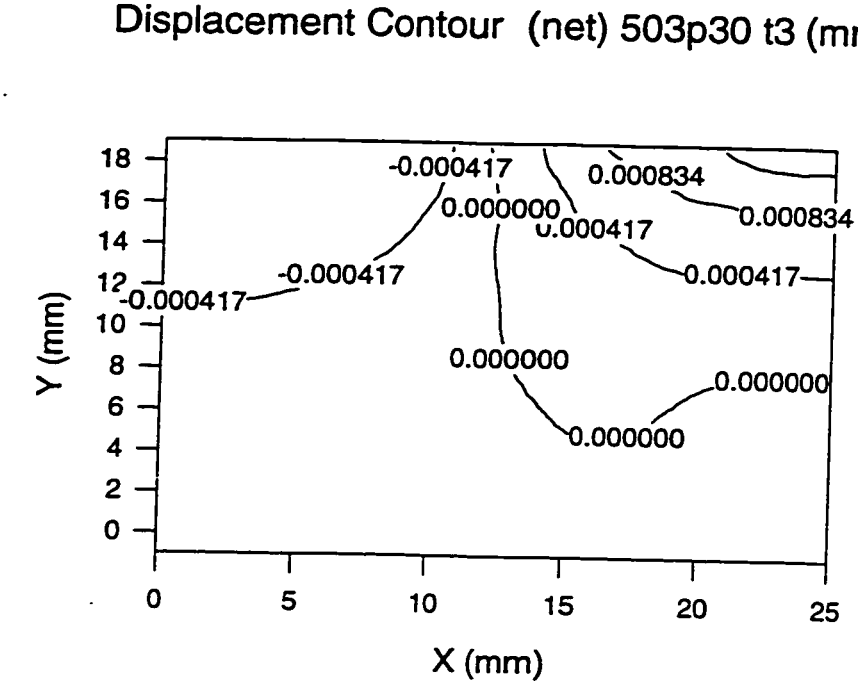

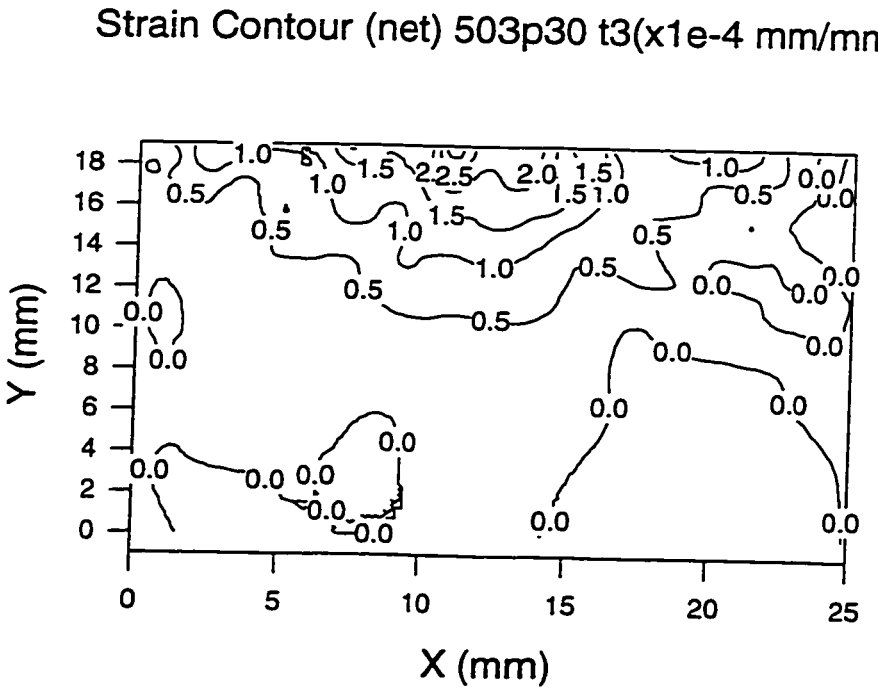

Figure 7.26 *u*-field displacement, strain contours for alumina at depth of hole 2.15 mm (supply pressure 207 MPa; SOD 1mm; garnet mesh #80; AFR 17.5 g/s)

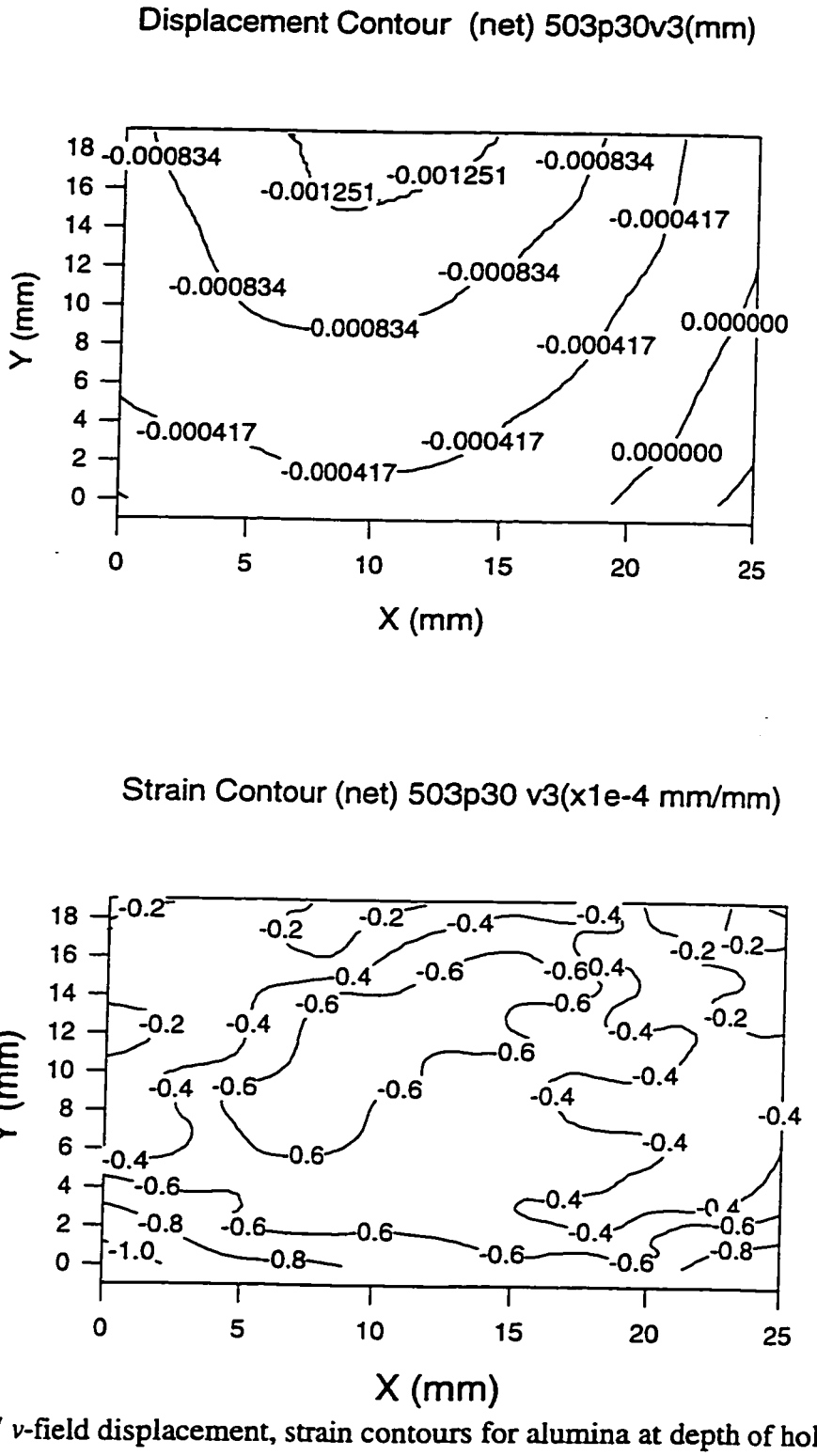

Figure 7.27 *v*-field displacement, strain contours for alumina at depth of hole 2.15 mm (supply pressure 207 MPa; SOD 1mm; garnet mesh #80; AFR 17.5 g/s)

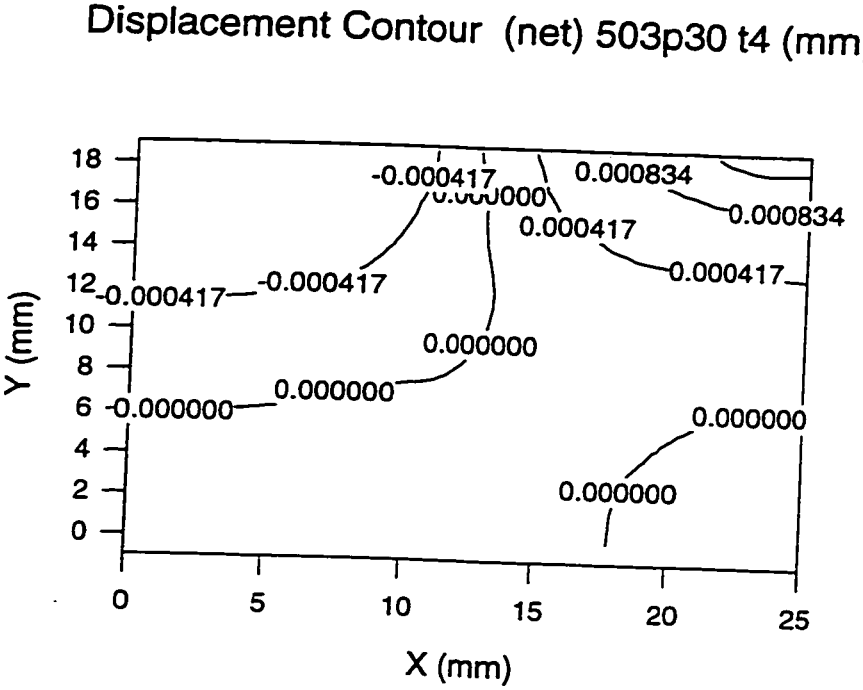

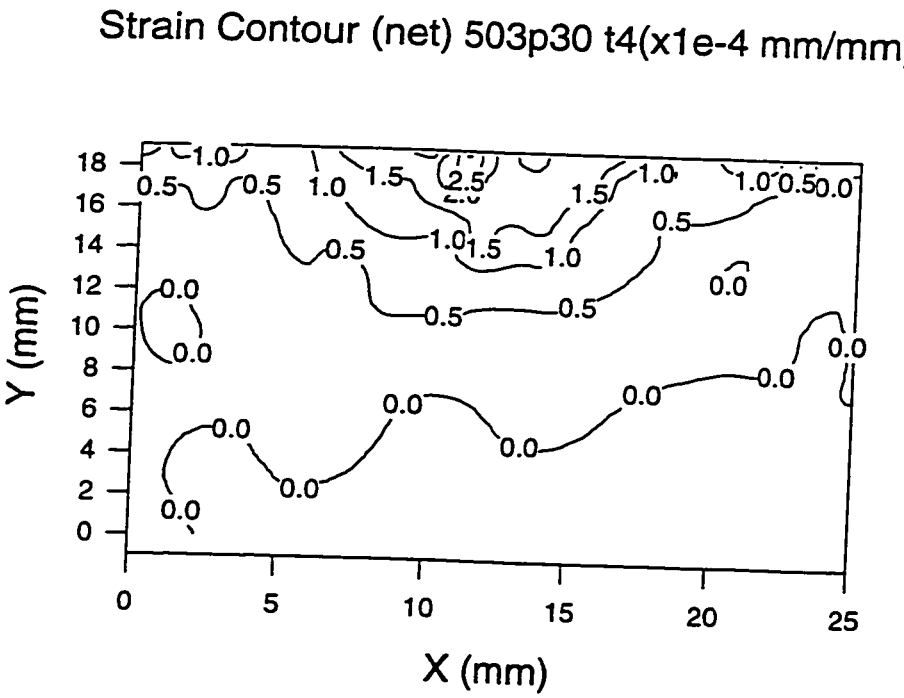

Figure 7.28 *u*-field displacement, strain contours for alumina at depth of hole 2.6 mm (supply pressure 207 MPa; SOD 1mm; garnet mesh #80; AFR 17.5 g/s)

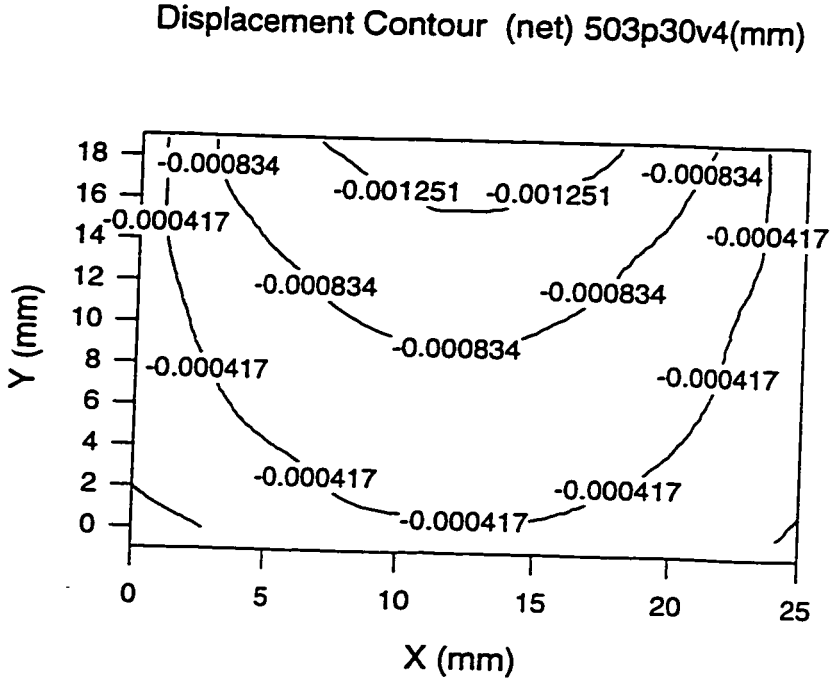

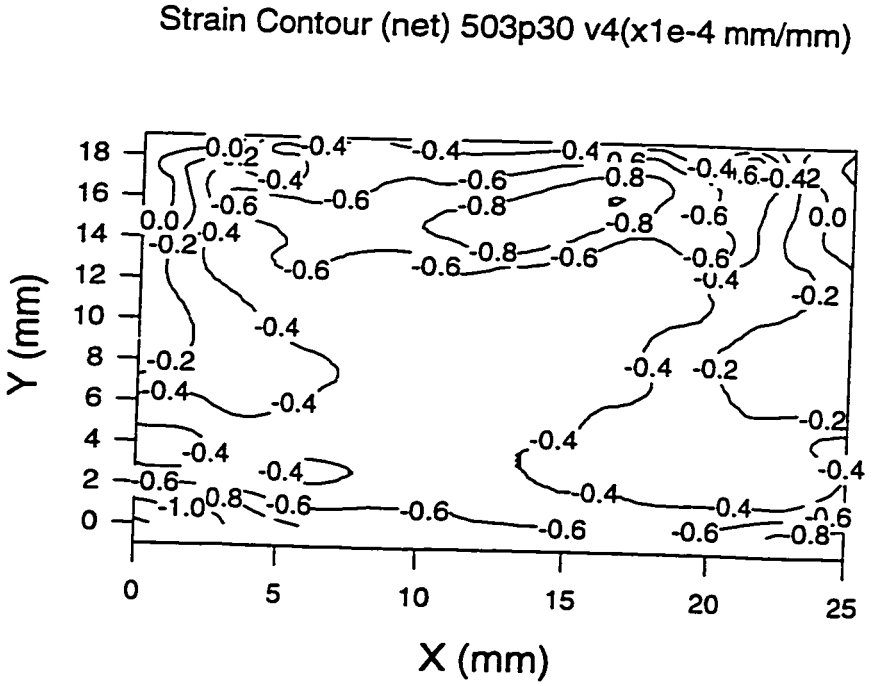

Figure 7.29 *v*-field displacement, strain contours for alumina at depth of hole 2.6 mm (supply pressure 207 MPa; SOD 1mm; garnet mesh #80; AFR 17.5 g/s)

7.3 NUMERICAL MODELING

7.3.i Pressure Loads for FEA Modeling in AWJ Piercing

The key to proper model the abrasive waterjet piercing process, is to find the simulated AWJ loads (or loading combinations) that produce displacement contours in the frontal surface that are similar to those captured in the optical experiments. Based on what was learned from the FEA parametric study presented in chapter 6, the pressure load combinations were found out through a trial and error process. There are two acceptance criteria for the assumed loads at any given depth of hole. The first one is the displacement criterion. The maximum u-displacement within the kerf profiles of the hole should be the same as those recorded in the moiré experiment, as shown in Figures 7.5. The maximum v-displacement at the center of the top edge should be the same as illustrated in Figure 7.6. The displacements from the assumed loads can be presented by contour lines, thus can be compared directly with the moiré fringe patterns. The second criterion is the reaction force criterion. The reaction forces Fz from the FEA model driven by the assumed load should be equal to the AWJ drilling forces measured. A table of the AWJ/WJ piercing forces on polycarbonate material is provided in chapter 4. As discussed in chapter 4, the abrasive waterjet piercing forces fluctuate in a certain range for any given supply pressure. The abrasive waterjet piercing process can be treated as a quasi-static loading process. In all of the above FEA trial runs, the experimental boundary conditions were employed in the finite element model.

Reported in Table 7.6 are the accepted AWJ pressure loads that yielded the closest displacement contours for polycarbonate models at selected hole depths of 4 mm, 6 mm, and 8 mm. The FEA calculated displacement contours in the u-field and v-field under their respective loads are plotted in Figures 7.30 to 7.35 for selected hole depths of 4 mm, 6 mm, and 8 mm. Each contour line in the displacement distribution graphs represents the same amount of displacement as does the corresponding moiré fringe. In these cases,

one fringe order represents a displacement of 0.000417 mm. The strain contours of their respective displacement fields are shown in the right side of the displacement contour graphs. The kerf profile of the modeled holes is superimposed on the contour plots for better visualization.

Table 7.6 Pressure loading combinations for various depth of holes

Depth of Hole (mm)	Jet Pressure (MPa)	Normal Pressure (MPa)	Shear Force (MPa)
4.0	1.79	13.44	1.48
6.0	3.58	17.93	1.61
8.0	10.75	22.40	1.75

For the convenience of discussion, the pressure loads are simplified as unit loads, and the unit loads are listed in Table 7.7.

Table 7.7 Unit pressure load for various depth of holes

Depth of Hole (mm)	Jet Pressure (Pa)	Normal Pressure (Pa)	Shear (Pa)
4	0.2	1.5	0.165
6	0.4	2	0.18
8	1.2	2.5	0.195

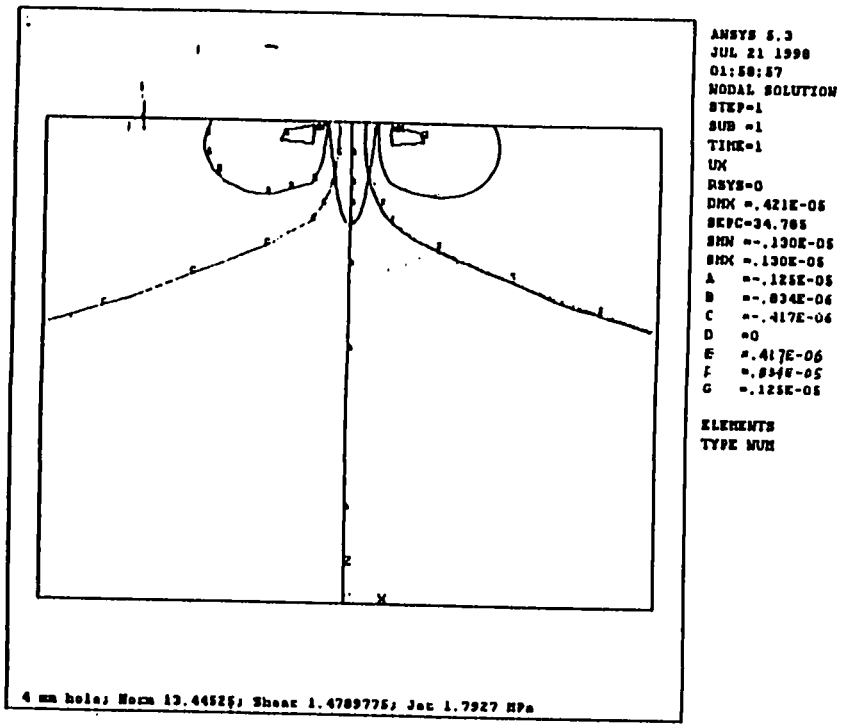

(a) Displacement Contour

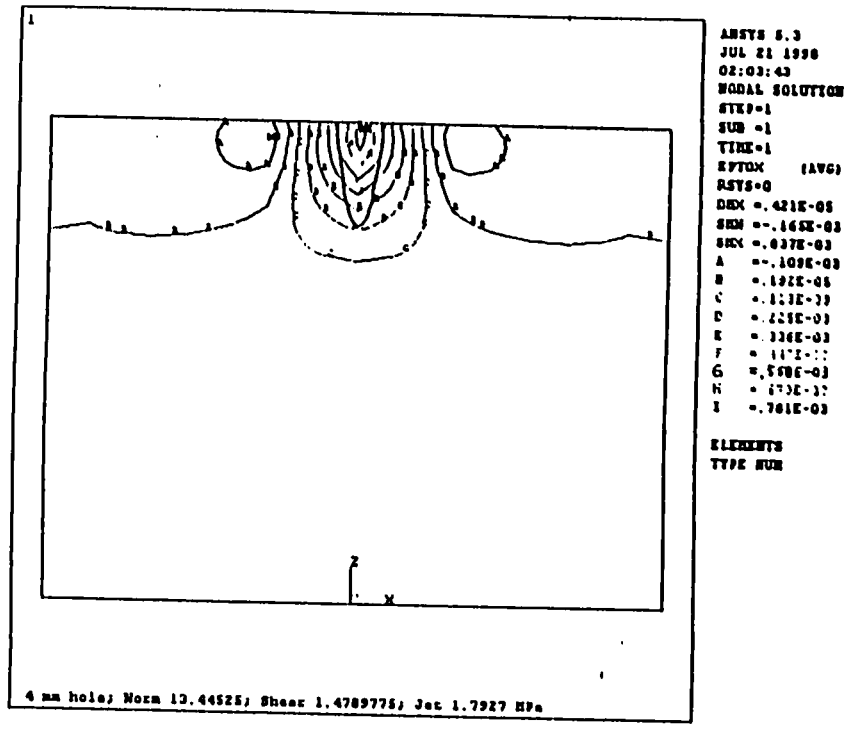

(b) Strain Contour

Figure 7.30 FEA *u*-field Displacement and Strain Contours for Polycarbonate at Depth of 4 mm

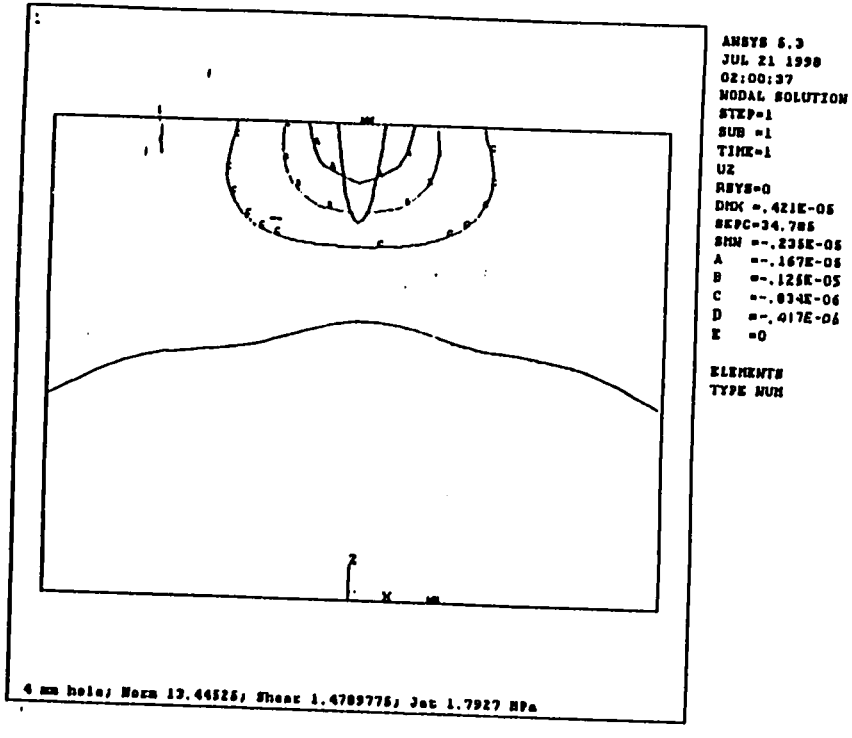

(a) Displacement Contour

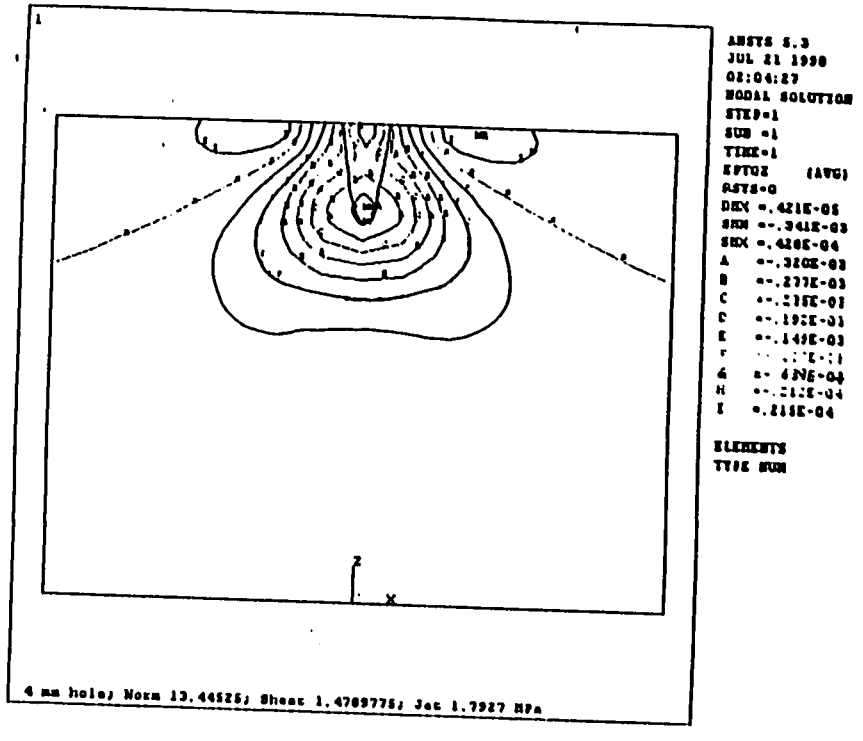

(b) Strain Contour

Figure 7.31 FEA *v*-field Displacement and Strain Contours for Polycarbonate at Depth of 4 mm

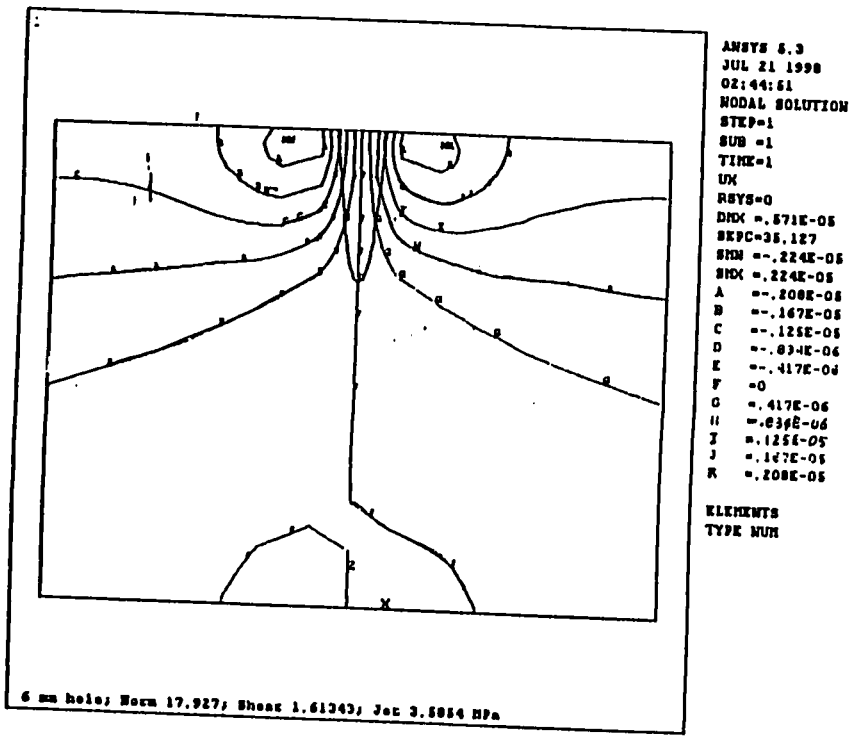

(a) Displacement Contour

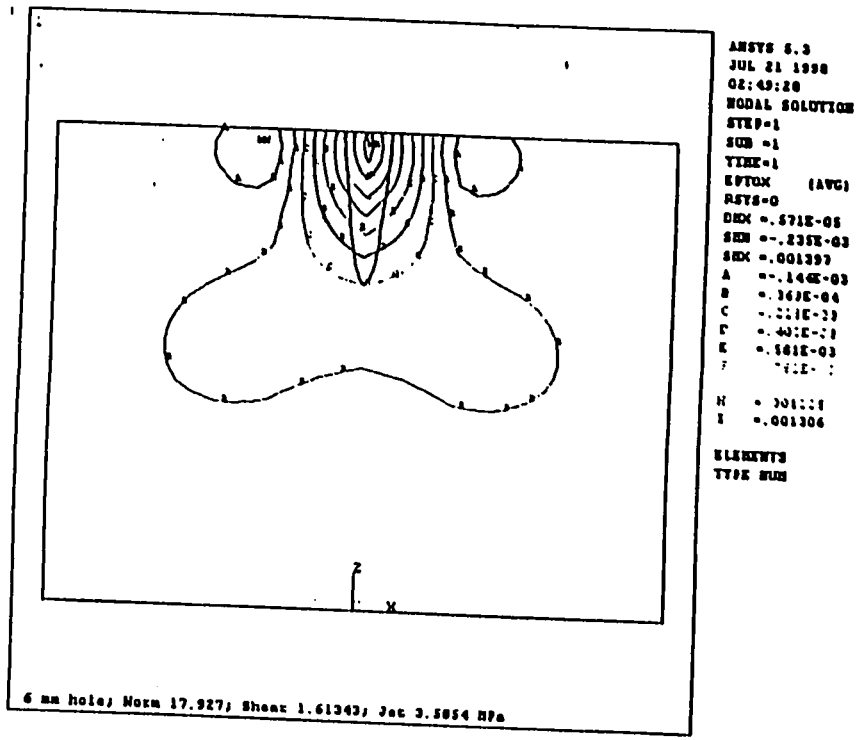

(b) Strain Contour

Figure 7.32 FEA *u*-field Displacement and Strain Contours for Polycarbonate at Depth of 6 mm

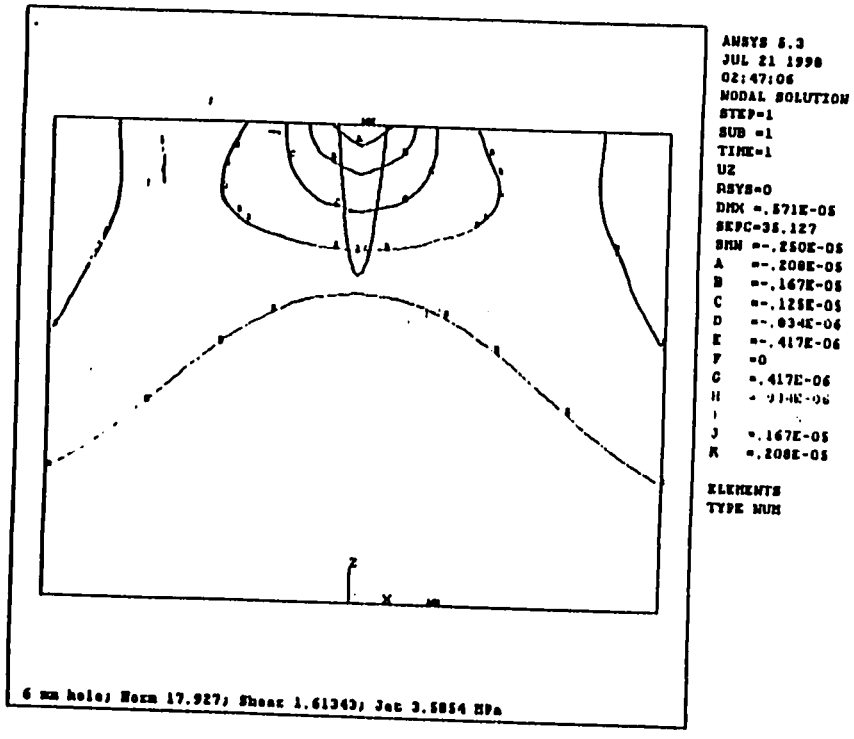

(a) Displacement Contour

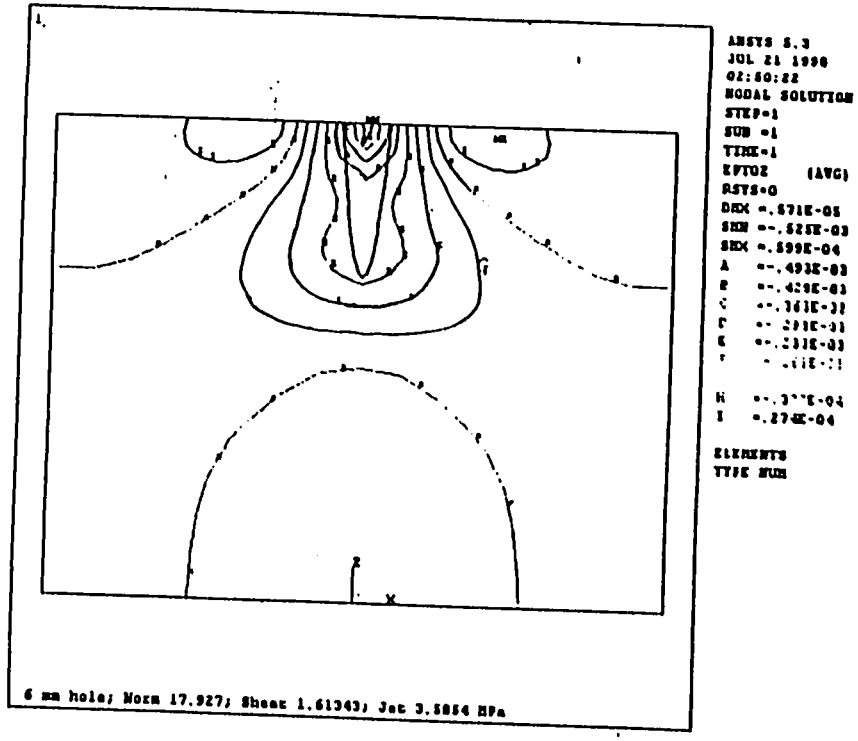

(b) Strain Contour

Figure 7.33 FEA ν-field Displacement and Strain Contours for Polycarbonate at Depth of 6 mm

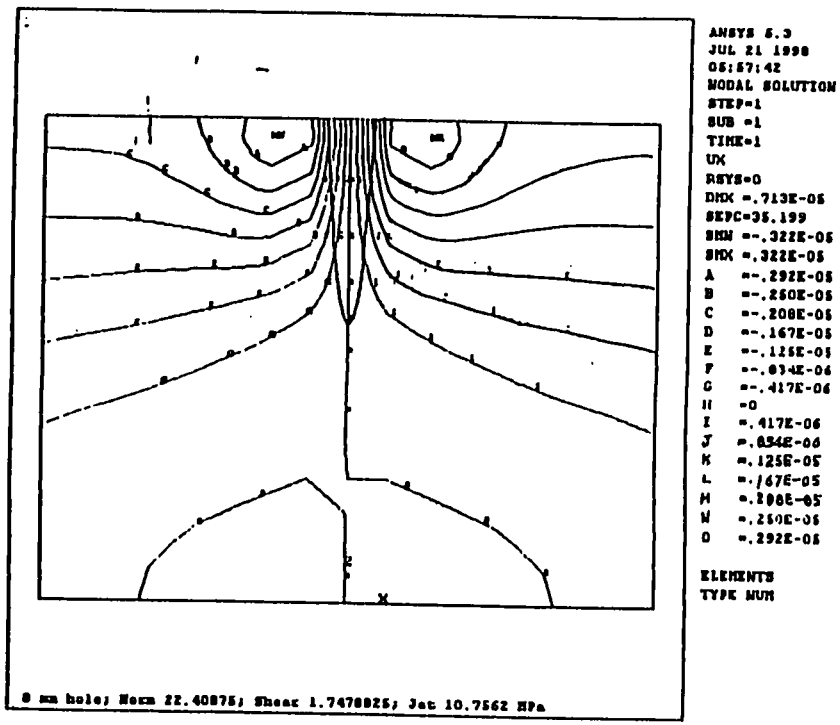

(a) Displacement Contour

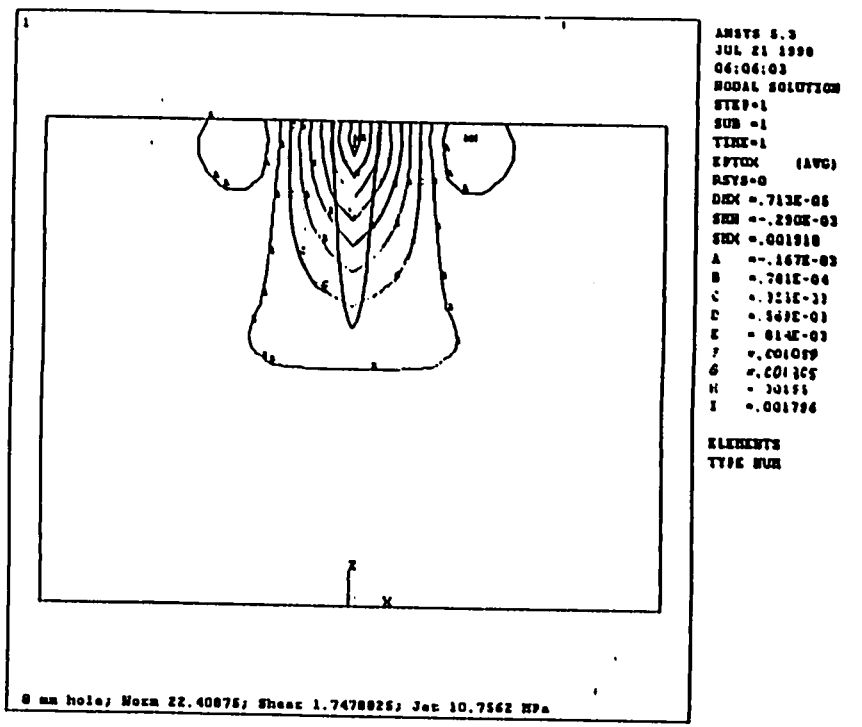

(b) Strain Contour

Figure 7.34 | FEA *u*-field Displacement and Strain Contours for Polycarbonate at Depth of 8 mm

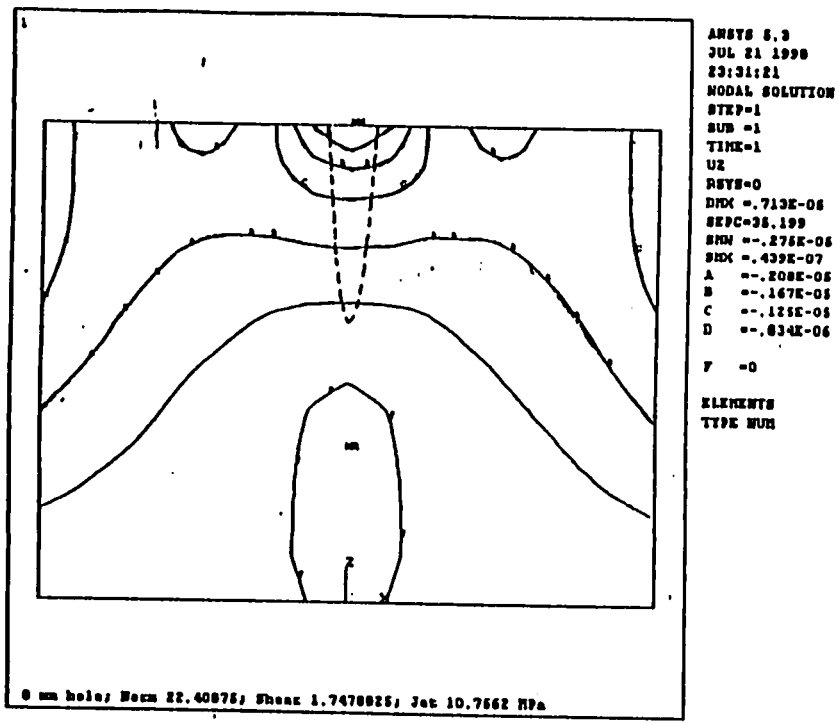

(a) Displacement Contour

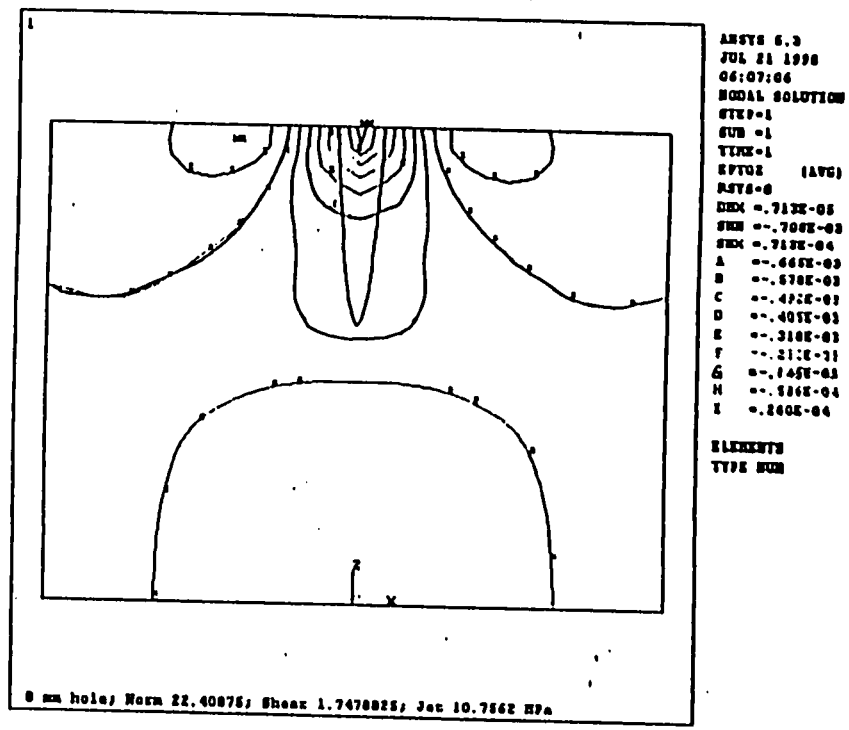

(b) Strain Contour

Figure 7.35 : FEA v-field Displacement and Strain Contours for Polycarbonate at Depth of 8 mm

The pressure loads listed in the above Table include normal pressure, jet pressure, and shear forces. In the finite element analysis, the jet pressure was applied in an area where the radius was 55% of the diameter of the maximum hole diameter, which was approximately the same size as the diameter of the abrasive waterjet stream at the workpiece. As illustrated in Figure 6.1 and 6.2, both normal pressure and shear were uniformly applied to the kerf surface from the bottom to the top. The shear represents the reversal flow of the AWJ, and the normal pressure simulates the quasi-hydrostatic pressure from the AWJ on the cavity. It can be noticed that the jet pressure increases were 0.2 Pa at 4mm hole depth, and were 1.2 Pa as the depth of hole increased to 8 mm. As the hole became deeper, the magnitude of the normal pressure also increased from 1.5 Pa to 2.5 Pa, and the shear load increased from 0.165 Pa to 0.195 Pa.

The reaction forces from the FEA simulation and the experimental testing are compared in Table 7.8. At supply pressure of 207 MPa, the average drilling forces for AWJ and WJ are 19 and 20.7 N, respectively. Standard deviations are about 2 N. The simulated reaction force was around 18 N.

Table 7.8. Comparison of Reaction forces at supply pressure of 207MP

Depth of Hole	Experiment (N)		FEA (N)
4.0 (mm)	19+/-2	20.7+/-2	18.28
6.0 (mm)	for	for	18.3
8.0 (mm)	AWJ	WJ	18.6

The maximum displacements based on these pressure loads for selected hole depths are also very similar to that observed in the optical fringes. Therefore, the assumed loads in Table 7.7 are acceptable.

7.3.2 Stresses and Strains at the Bottom of the Hole vs. Depth of Hole

After the AWJ loading in the cavity was found, the state of stress and strain in the 3-D body was analyzed using the FEA model. The finite element modeling results are analyzed and described in this section. The stresses and strains at the bottom of the hole both on the inside mid-plane and the outside surface in the FEA model are of the most interest, and are plotted in Figures 7.36 (a) and (b) to Figures 7.37(a) and (b). The stresses and strains vary with the depth of hole.

The FEA modeled stresses showed that the stress components, σ_x, σ_y, σ_z and the principal stresses, σ_1, σ_2, σ_3 are almost the same, both on the frontal surface and in the mid-plane. Similarly, the strain components ε_x, ε_y, ε_z and the principal stains ε_1, ε_2, ε_3 are also almost the same. It is interesting to note that the trend of change for the principal stresses and principal strains are very similar in both mid section and outside surface.

The stresses and strains on the outer surface are plotted in Figure 7.36. It is obvious that both σ_2 and ε_2, are nearly zero. The maximum principal stresses, σ_1 and maximum principal strain, ε_1 did not change much as the depth of hole increased. However, the minimum stress and strain, σ_3 and ε_3, both negative in sign, decreased in absolute value as the depth of hole increased.

For all three hole depths in the mid-plane, as shown in Figure 7.37, σ_1, and σ_2, are positive in sign and almost equal in magnitude, while σ_3 is negative in sign with a relatively small value. That means that tensile stresses are dominant near the bottom of the hole. As the depth of hole increases, the maximum principal stresses also increase. At 8 mm hole depth, σ_1, and σ_2 are nearly the same, with a maximum value of 35 MPa. The minimum principal stress, σ_3 changes from -7.5 MPa to -1.0 MPa. as the depth of hole increases from 4 mm to 8 mm. At hole depth of 8 mm, the maximum and minimum principal strains are almost equal in absolute value, and are opposite in signs.

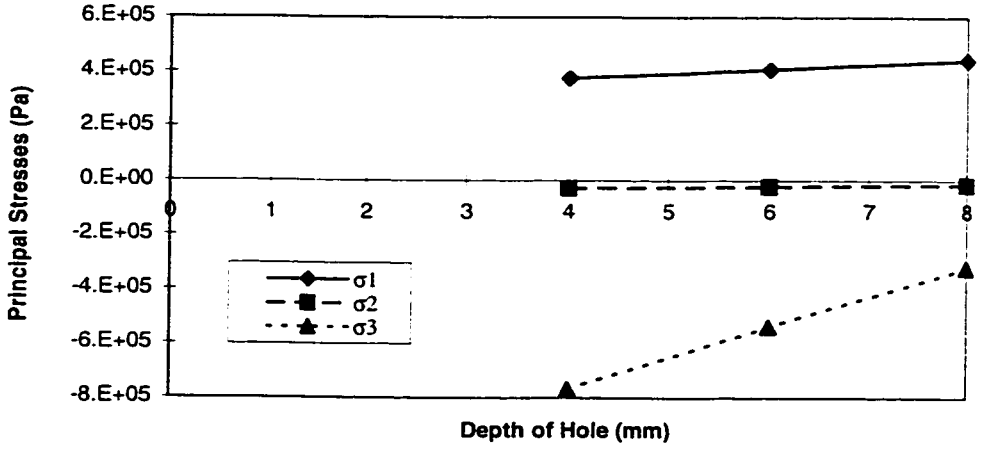

(a) Principal stresses at the bottom of the hole on the frontal surface

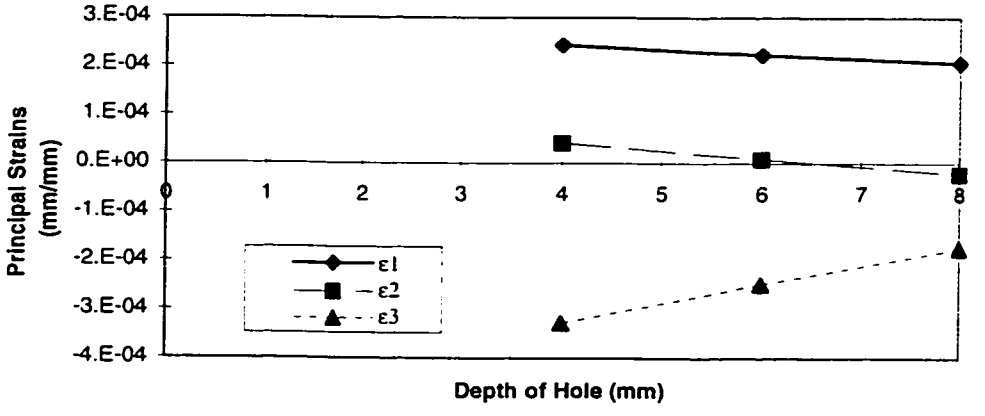

(b) Principal strains at the bottom of the hole on the frontal surface

Figure 7.36 Variations of the Principal Stresses and Strains vs. Depth of Hole

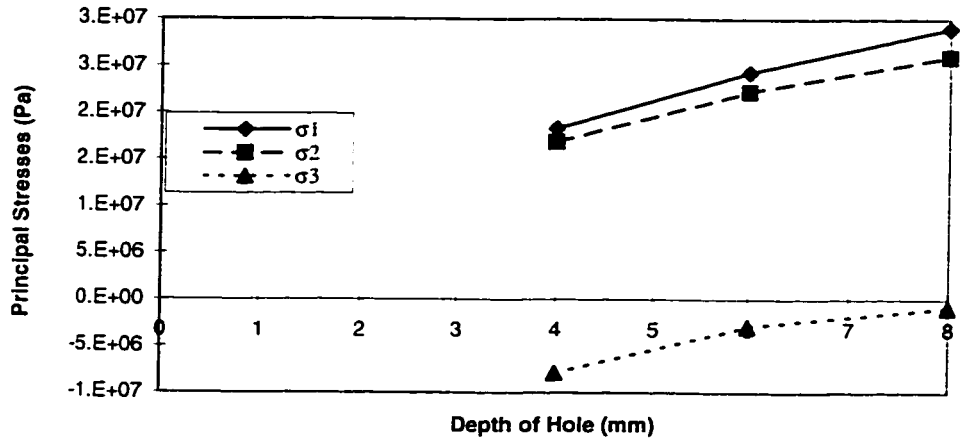

(a) Principal stresses at the bottom of the hole on the Mid-plane

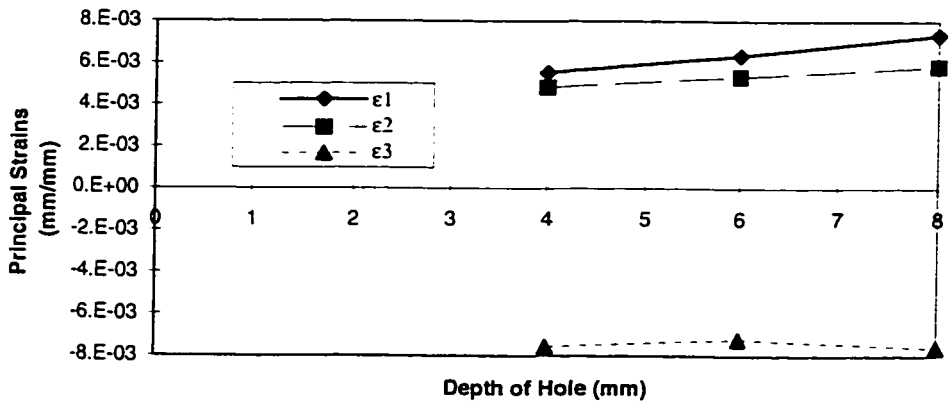

(b) Principal strains at the bottom of the hole on the Mid-plane

Figure 7.37 Variations of the Principal Stresses and Strains vs. Depth of Hole

FEA modeling of abrasive waterjet drilling on alumina was attempted. However, no correlation between the FEA results and the experimental results could be found. In the experiments of AWJ drilling on alumina material, the reaction forces from the AWJ drilling were comparable to those of polycarbonate, though fewer moiré fringes emerged in the alumina material as the jet exposure time was increased. To produce the same number of moiré fringe in the FEA simulation, the reaction forces generated by the FEA model were quite different from the recorded values. Therefore, FEA simulation of the AWJ drilling on ceramic was not possible. One of the reasons is that this material is very stiff. Other machining mechanisms may not be understood yet. Therefore, further study will be needed.

7.4 DISCUSSION

As observed in Figures 7.5 to 7.8, 7.16 to 7.21, and G.1 to G17, the moiré fringes showed obscure patterns at the onset of AWJ. This is partly due to the vibration of the AWJ pump system and the vibration of the optical setup. The stress wave induced by the impact was also responsible for the phenomenon. Even though, in most cases, the moiré fringes stabilized in about 0.6 seconds, they still showed some irregularities periodically. The dancing fringe (where the moiré fringes vibrated during AWJ machining) was another phenomenon observed during optical experiments. . The sever environment and the air currents in the abrasive waterjet lab may have been responsible for this problem. During the AWJ machining process the air current was generated by the AWJ mist after its impingement on the specimen. Since the index of refraction of air varies with pressure and temperature, and air current is motivated by both, air currents are disturbing factors[126]. Vibration is an inherent problem for the noisy waterjet pump machinery. The lack of isolation for the vibrations to the optical tables, such as using pneumatic damper supports, could have contributed to some of the irregularities. Even with the above

described problems with the experimental system, the dynamic moiré fringes recorded still showed reasonable quality in most of the cases.

In the numerical analysis of the AWJ drilling, the assumptions of the three pressure loads for AWJ are the most critical. As stated previously, the assumed AWJ loads have to meet two criteria under similar boundary conditions, as in the AWJ drilling experiments: 1)The assumed loads in the FEA model should produce similar surface displacements, as measured in the moiré experiments, And the reaction forces under the assumed loads in the FEA model should generate reaction forces that are similar to those measured in the experiments; 2) the surface strain from the experiments should be similar to that from the FEA results. In the quasi-static simulation of AWJ drilling process, it is reasonable to assume that there are three pressure loads exerted on the kerf surface in a FEA model. The normal pressure simulates the hydrostatic load applied to the kerf surface. The shear simulates the action of the return flow of the AWJ on the kerf surface. When the jet impinges on the specimen, the pressure rises in the bottom of the hole due to the stagnation point of the jet flow. Thus the third load is the pressure load applied to a small area near the bottom of the hole. The three loads superimpose to form an adequate load combination.

Using the assumed AWJ pressure load, the surface displacements from FEA were compared directly with the moiré fringes from experiments, to 7.40 in both u- and v-fields, and are shown in Figures 7.38. It can be noticed that the FEA predicted displacement distribution contours do not match exactly with all the details of the moiré fringes on the left side. However, the most important region of interest is inside and near the envelope of the kerf profiles. As can be seen, in the u-field the number of displacement contour lines from the FEA modeling is very similar to the experimentally recorded displacement moiré fringes within the kerf profile for selected hole depths of 4 mm, 6 mm, and 8 mm. However, the zero displacement zone, as shown in Figure 6.3(a), is much higher in the FEA contour graphs than that in the experimental moiré fringes'. In

the v-field, similar comparison was performed, and the close match of displacements between the FEA result and the experimentally obtained results at 4 mm, 6 mm, and 8 mm is obvious. When the reaction forces were allowed to vary in the wider range as was the case in the experimental experiments, the displacement contour can be matched even closer.

An analysis was made of the experimentally obtained and the FEA predicted strain contours. The strain contours are compared in Figures 7.41 to 7.43 for hole depths of 4 mm, 6 mm, and 8 mm respectively. The strains at the bottom of the hole on the out surface from both experiments and FEA are reported in Table 7.9

Table 7.9 Experimental and FEA Strain Comparisons

Depth of Hole (mm)	Experimental Results		FEA Results	
	ε_x	ε_z	ε_x	ε_z
4	0.00090	-0.00030	0.0002	-0.00032
6	0.00045	-0.00020	0.0011	-0.00024
8	0.00070	-0.00013	0.0013	-0.00018

The vertical strains ε_z are compressive, and decrease as the depth of hole increases. The strain values from the experimental data are very comparable to those of the FEA results. The u- strains ε_x are tensile strains due to the normal pressures exerted on the kerf surfaces. However, there are big differences in the strain value ε_z between the experimental and FEA. As mentioned previously, the zero displacement zone in the u-displacement field from the FEA (7.38) is higher than that observed in the experimental fringes (7.39). This phenomenon is largely responsible for the differences in ε_x between the experiments and the FEA In the strain contour plots for the experiments the contour lines are zigzagged and not smooth. This may be due to the noise introduced by the plotting algorithm in the plotting software.

Experimental Results

FEA Results

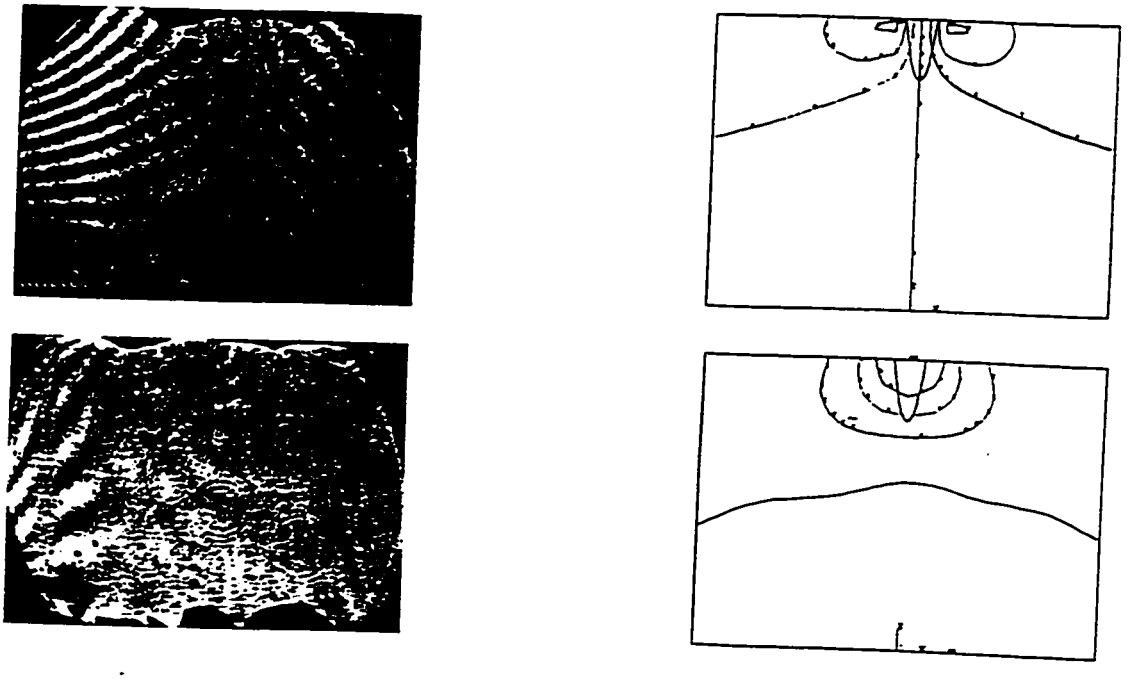

Figure 7. 38 Comparison of displacement contours at depth of hole 4 mm

Experimental Results

FEA Results

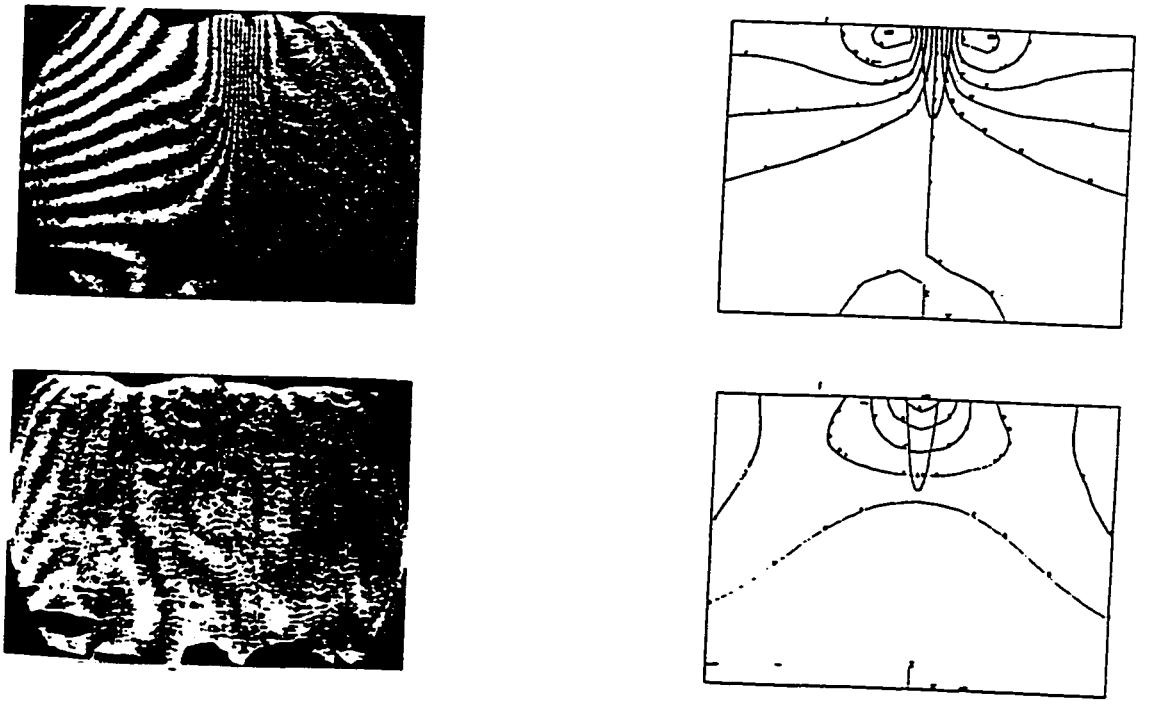

Figure 7. 39 Comparison of displacement contours at depth of hole 6 mm

Experimental Results

FEA Results

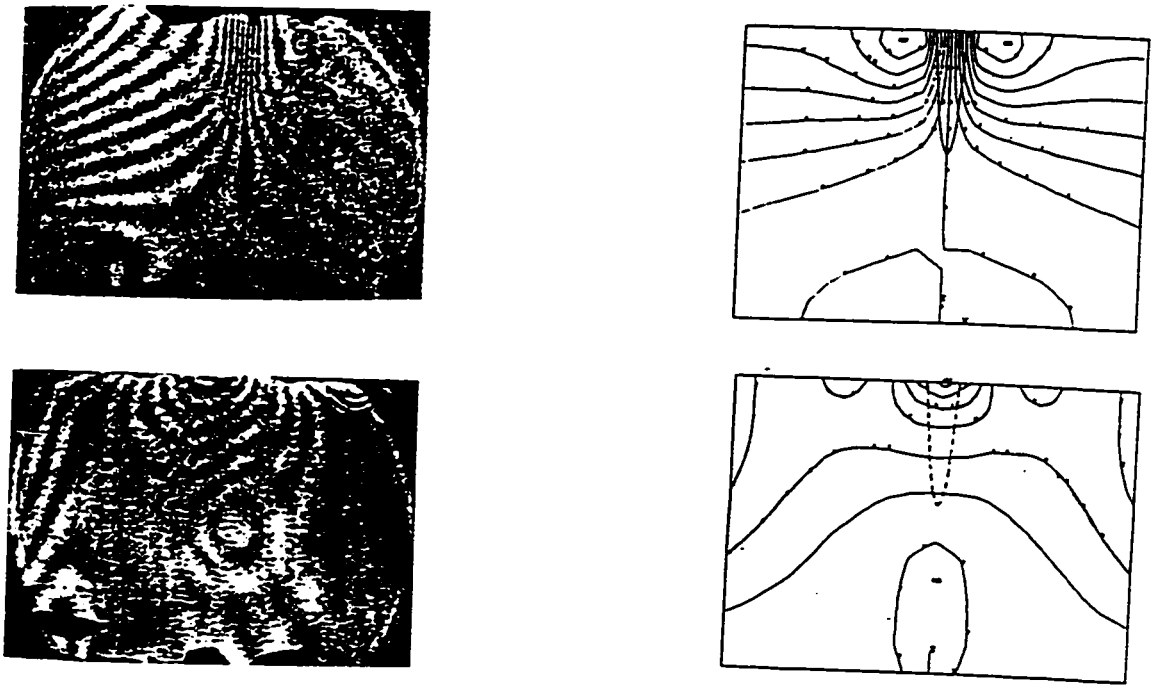

Figure 7.40 Comparison of displacement contours at depth of cut 8 mm

From the finite element analysis results, all the state of stresses in the 3-D workpiece became available. Table 7.10 summarizes the stresses σ_1-σ_3 and σ_1+σ_3 near the bottom of the hole in the mid-section and on the out-surface. The simulated isochromatic and isopachic fringes from FEA data are compared in Figures 7.44 and 7.45 for σ_1-σ_3 and σ_1+σ_3, respectively. In each figure, both stresses on the out-surface and on the mid section were placed side by side for three selected depths of hole of 4 mm, 6 mm, and 8 mm.

Table 7.10 Summary of Stresses σ_1-σ_3 and σ_1+σ_3 Near the Bottom of Hole

Depth of Hole (mm)	σ_1-σ_3 (MPa)		σ_1+σ_3 (MPa)	
	mid section	out surface	mid section	out surface
4	2.62E+07	1143580	1.04E+07	-392020
6	2.72E+07	945230	2.14E+07	-129950
8	2.99E+07	762720	2.82E+07	123260

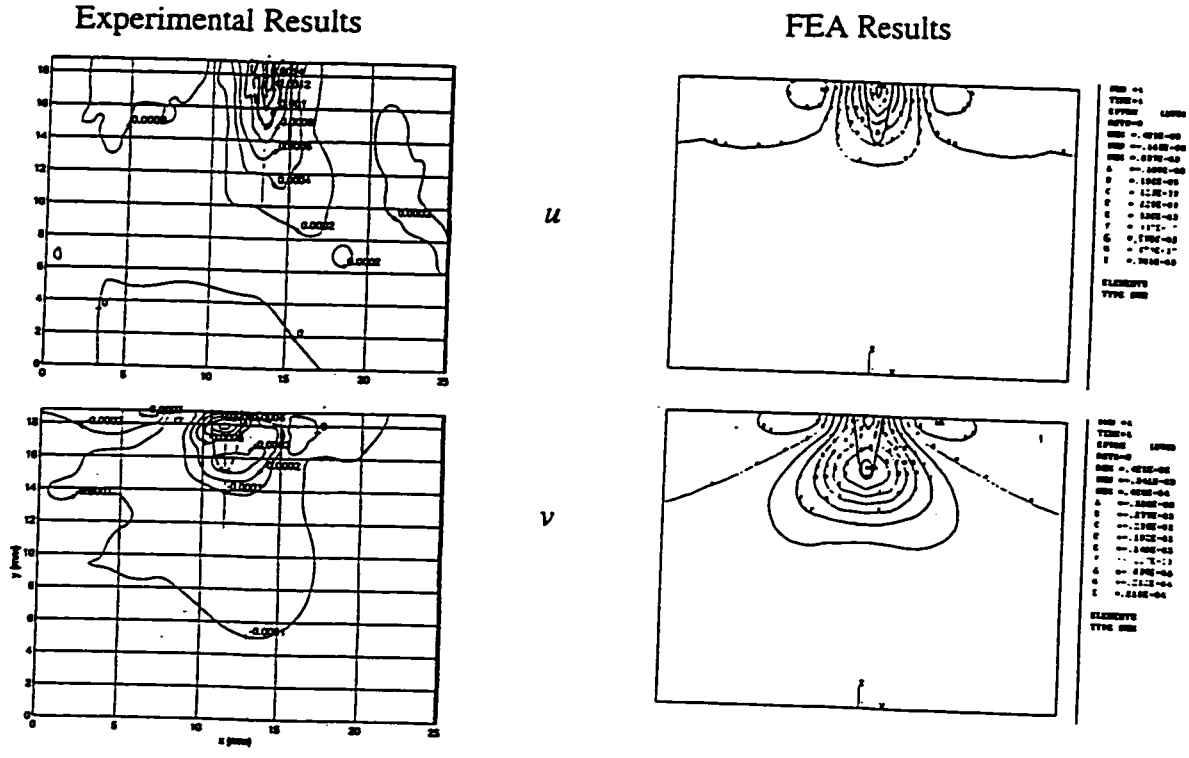

Figure 7. 41 Comparison of strain contours at depth of hole 4 mm

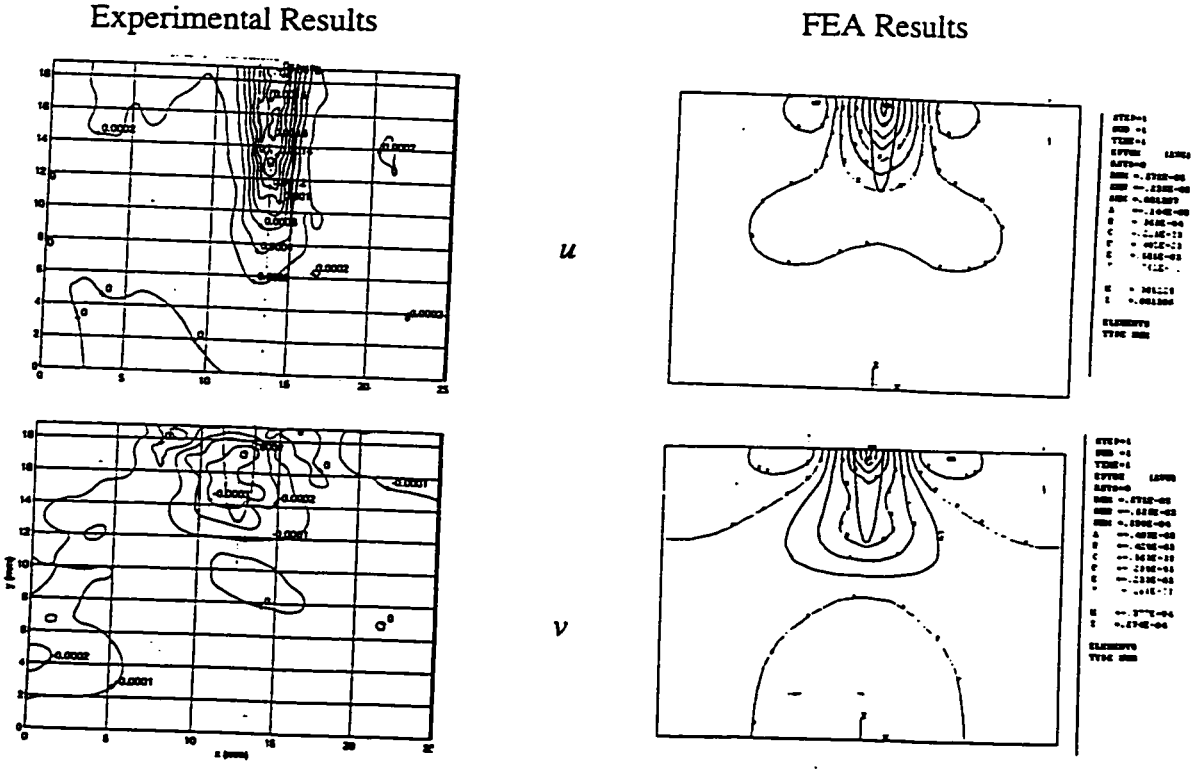

Figure 7. 42 Comparison of strain contours at depth of hole 6 mm

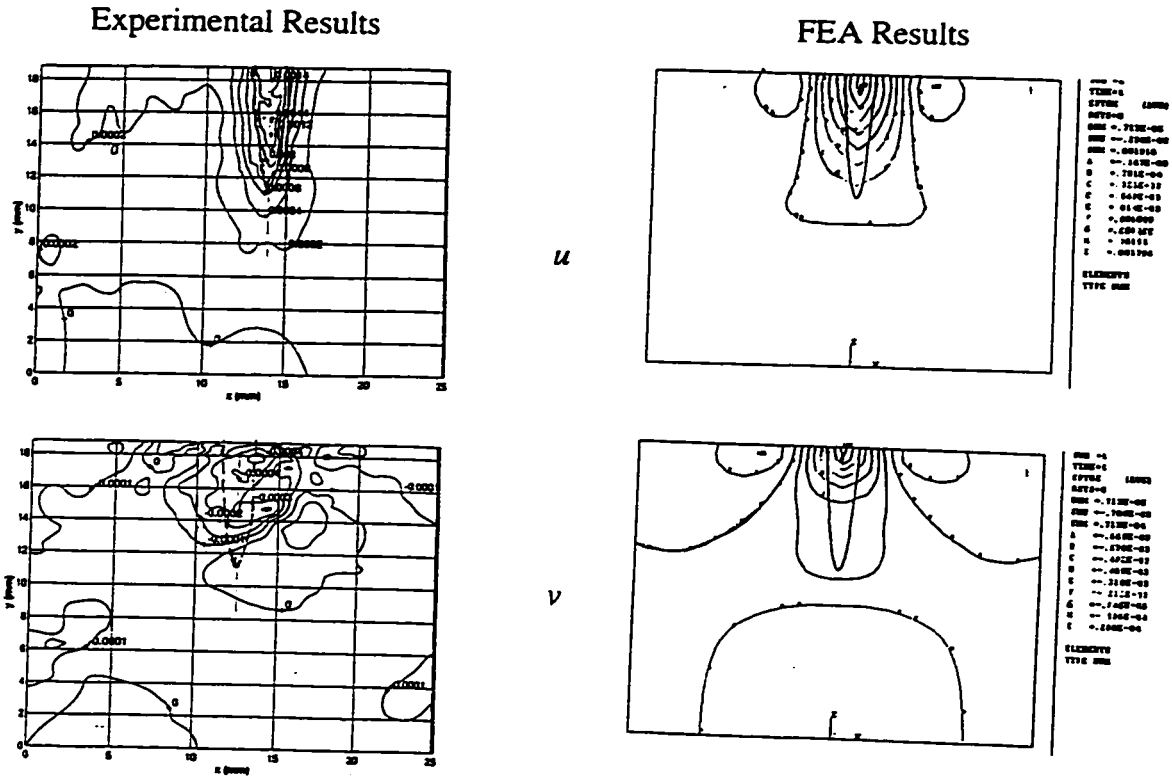

Figure 7.43 Comparison of strain contours at depth of cut 8 mm

It seems that maximum shear stress at the bottom of the hole on the mid section did not change much as the depth of hole increased. The stress values are in the same order of magnitude as those reported by Ramulu[131] in photoelasticity experiments that were conducted to measure the shear stress during AWJ drilling. but since the experimental conditions were different, no direct comparison is possible.

On the out surface, the maximum shear stress decreased as the depth of hole increased. From the isopachic fringes, the $\sigma_1+\sigma_3$ at the bottom of the hole increased in the mid section. and the other way around on the out surface.

As observed by Ramulu[17], multiple crack initiation can be generated by the AWJ. During an AWJ machining process, the sharp abrasives bombard the specimen, and micro cracks are created in the cavity. Since the cavity is filled with pressurized abrasive water mixture, if it is assumed that it is a penny shaped crack with a crack length of a, the stress intensity factor K_I can be calculated,

$$K_I = \eta\sigma\sqrt{\pi.a} \tag{7.1}$$

where η is the approximated geometry correction factor that can be found out from Murakami's stress intensity factor[132]. In the case where a crack is emanating from an elliptical hole under tension, the η is approximately 3.90. For polycarbonate materials, the initiation stress intensity factor is K_{Ici} = 2.24 MPa$\sqrt{m}$. Corresponding to a tensile stress, σ, near the bottom of the hole in the mid section, a critical crack length can be calculated.

$$c = \frac{1}{\pi}\left(\frac{K_{Ici}}{\eta\sigma}\right)^2 \tag{7.2}$$

Therefore, the critical crack lengths for selected depths of hole 4 mm, 6 mm, and 8 mm can be calculated in Table 7.11:

According to fracture mechanics, a crack propagates when KI > $K_{Ic\,i.}$ In another word, when the crack length a is greater than the critical crack length c, the crack also propagates.

Table 7.11 Critical Crack Length at Selected Depth of Hole

Depth of Hole (mm)	σ (MPa) at the bottom of the hole	Critical crack length $c=\frac{1}{\pi}\left(\frac{K_{Ici}}{\eta\sigma}\right)^2$ (mm)
4	22.5	0.208
6	30.0	0.117
8	34.0	0.0909

For garnet abrasives of mesh size 50, the average grain size is about 0.305 mm. Assuming that the crack length created by the abrasive is similar to the grain size of the abrasives, the condition $a>c$ is met, and the crack can be propagated under the tensile stresses at the bottom of the hole. Once a crack is propagated, the crack is unloaded. The cracked material will be knocked loose by the powerful AWJ. A new cycle will repeat itself. Hence, the AWJ machining mechanisms proposed by Ramulu[17] can be substantiated quantitatively. The whole process can be described as a microcrack initiation, microcutting, and erosion process.

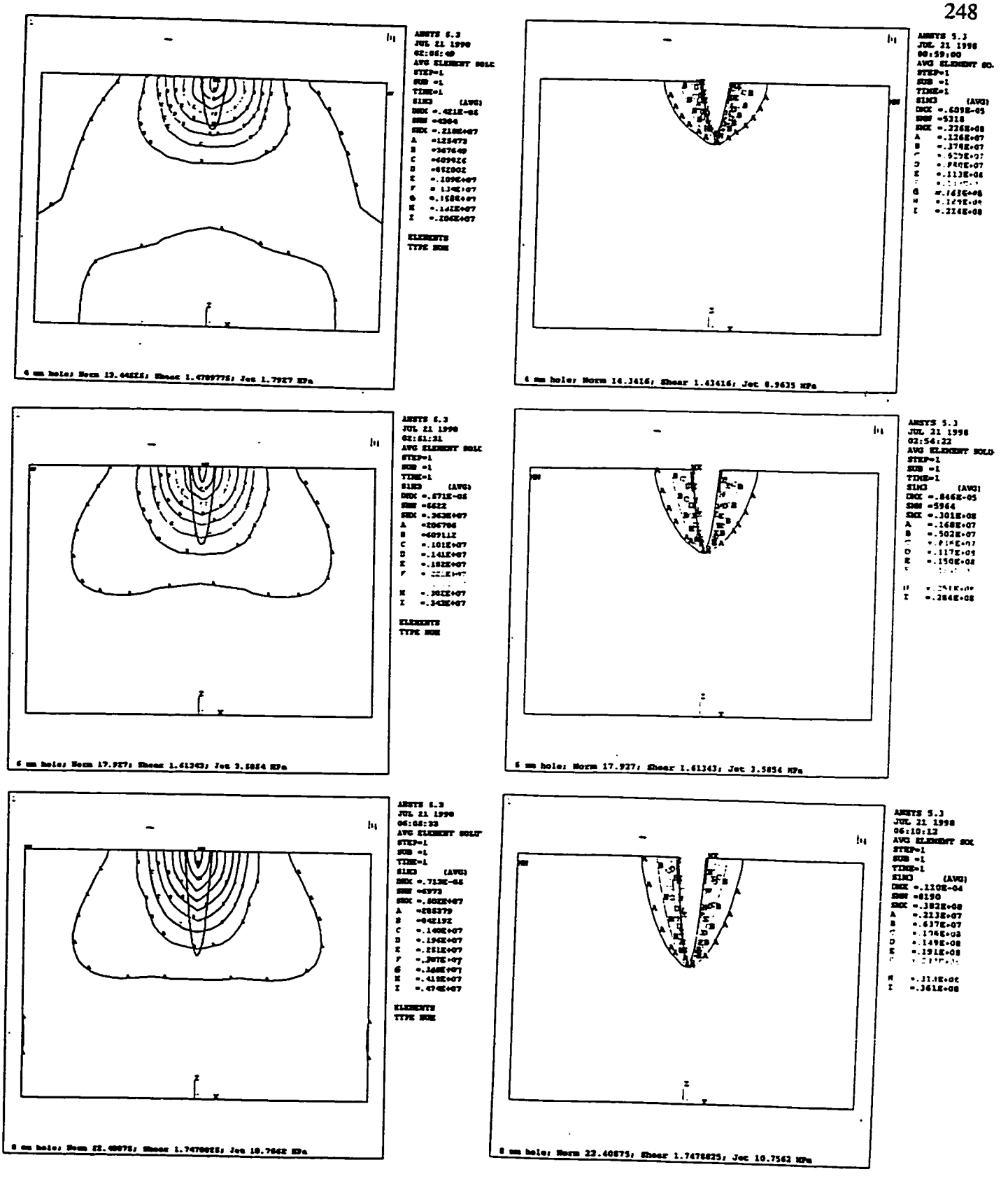

Figure 7.45 Comparison of stresses σ_1- σ_2 vs. depth of hole

(FEA simulated polycarbonate under AWJ drilling)

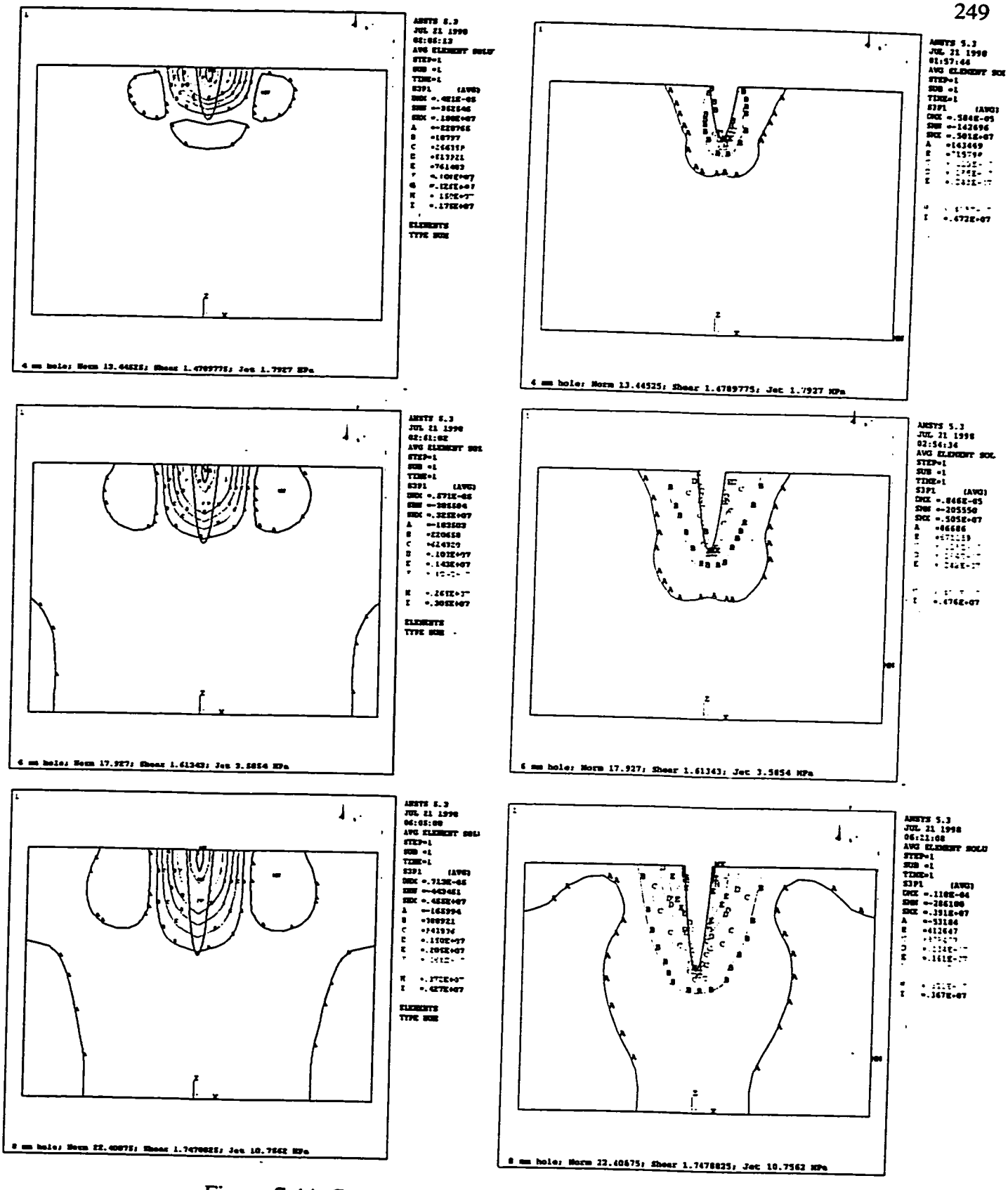

Figure 7.44 Comparison of stresses $\sigma_1 + \sigma_2$ vs. depth of hole

(FEA simulated polycarbonate under AWJ drilling)

CHAPTER 8

CONCLUSIONS

The general objective of this research was to investigate the mechanics of AWJ piercing of brittle materials, including polycarbonate and advanced ceramic materials. The specific objective was to determine the quasi-static state of stresses surrounding the micro-cracks generated in the impingement zone of target material during AWJ piercing process. The goal was achieved by using the hybrid experimental - numerical analysis approach. The moiré interferometry experimental technique was utilized. Following is a summary of the research findings:

1. The experimental parametric study helped to increase the understanding of the effect of various input parameters on the AWJ machineability of the brittle materials, as well as the reaction forces resulting in the AWJ penetration process. These force measurements and analyses were used as a foundation for the numerical modeling of the AWJ process. With the extensive study on the CFCC material, the understanding of the AWJ machining mechanisms was broadened.

2. A new and unique setup of moiré interferometry system, including a specimen protection fixture, a machining force dynamometer, etc. was developed and fabricated to facilitate the real time recording of the moiré fringe patterns. The moiré interferometry technique was successfully used to measure the dynamic surface displacement distribution on the front surface of the specimen during AWJ drilling.

3. The hybrid experimental - numerical analysis method was developed and successfully used to characterize the stress and strain state in the AWJ machining zone.

4. A three-dimensional finite element model was developed to simulate the AWJ drilling process.

The major contribution of this research is that the moiré interferometry experimentation was first utilized in measuring the transient state of displacement distribution on a workpiece during AWJ drilling. Both u- and v- field displacement fields were recorded simultaneously, either on a single frame or on two separate frames. The recorded data were deduced and used to drive a three-dimensional finite element model to study the stresses and strains in the AWJ machining zone. The state of stress and strains near the machining zone can be used to further understand and substantiate the AWJ machining mechanisms.

Based on the experimental and numerical results obtained from this research, the specific conclusions are given as follows:

1) Several structural ceramics can be machined with abrasive waterjet at a reasonable material removal rate. Under certain abrasive waterjet machining conditions a threshold supply pressure exists, below which no material can be removed. In general, large grain size abrasives and higher abrasive flow rates remove more materials. On the other hand, increasing the traverse speed decreases the material removal rate. The workpiece hardness is inversely proportional to the material removal rate.

2) The impacting force on the specimen by pure waterjet is 20% greater than that by abrasive waterjet. The supply pressure determines the amplitude of the machining forces. There exists a basic fluctuation frequency in the recorded reaction forces, which is associated with the pressure waterjet pump system. The loading and unloading process corresponding to the crack initiation and erosion also contributes to the abrasive waterjet machining force fluctuation.

3) The abrasive waterjet machined kerf consists of four surface regions, including a top initial surface damage region, a cutting or smooth surface region, and a grooving or rough surface region. This was found to be consistent with the published literature.

4) The material removal mechanisms for AWJ cutting on CFCC consist of a combination of bending, shearing, micro-machining, and erosion. The micro-mechanisms associated with AWJ hole drilling are micro-fracture of fibers and matrix, delamination, and fragmentation of fiber bundles.

5) The topographic features of the AWJ machined surfaces of CFCC are always dependent on the fiber direction or weaving pattern, with respect to the jet penetration and its relative direction to the fibers. Abrasive waterjet machining was found to be a feasible rough and medium cutting process for CFCC, due to its material removal mechanisms and reasonable surface quality generation.

6) The AWJ drilling process was numerically modeled reasonably well with the three assumed pressure loads, i.e. jet pressure, normal pressure, and shear. The results from the numerical experiments demonstrate that the shear applied on the kerf surface, simulating the AWJ return flow, most profoundly affects the surface displacement distribution.

7) The principal stress at the bottom of the hole in the mid section is increased as the depth of hole increases. In the mid section, the maximum principal stresses are tensile and dominant near the bottom of the hole. As the depth of hole increases, the maximum principal stresses also increase. On the surface, both σ_2 and ε_2, are nearly zero at the bottom of the hole. The maximum principal stresses, σ_1, and maximum principal strains, ε_1 do not change much as the depth of hole increases. However, the minimum stress and strains, σ_3 and ε_3, both negative in sign, decrease in absolute value as the depth of hole increases.

8) The material removal mechanism is a process of micro-crack initiation, micro-machining, and erosion [17], which can be substantiated by the results reported here. The micro-crack can be activated by the impingement of the AWJ by the condition of $K_I \geq K_{IIC}$.

CHAPTER 9

RECOMENDATIONS TO FUTURE WORK

The current optical equipment was set up under a very limited budget. Even though recorded moiré fringes are of reasonable quality, more improvements are needed. To further understand the interaction between AWJ and the workpiece during AWJ drilling, the following recommendations are discussed:

1) As mentioned in section 7.4, the testing environment for the optical experiments was very harsh. A better ventilation or confinement system is recommended. The optical table should be supported with pneumatic vibration dampers to minimize the interference from the AWJ pump system.

2) Another improvement to the optical system would be an extension for the optical table to which the specimen could be attached. In this case the specimen and the reference gratings would vibrate in unison, and minor vibrations could be tolerated.

3) To improve the sensitivity of the moiré system for ceramic material, a higher density of the moiré grating should be used. With the improved sensitivity of the measurement system, the testing materials could be expanded to harder materials, such as SiC, Si_3N_4, TiB_2, etc.

4) In the optical experiments more attention was given to ceramic materials, and only one supply pressure was tested on the polycarbonate material. More moiré interferometry experiments are needed using different AWJ drilling conditions. More work needs to be done to complete the analysis of the moiré fringes for the alumina material.

5) Ultimately an analytical model should be determined for the material removal of AWJ drilling.

6) A dynamic finite element model should be established for accurately predicting material removal process during AWJ drilling.

BIBLIOGRAPHY

1 Kahlman, Karlsson and Carlsson, "Wear and Machining of Engineering Ceramics by Abrasive Waterjets," *International Journal of Ceramics*, vol 72, no.8, Aug. 1993.

2 Kahlman, L., Karlsson, S. et al. "Wear and Machining of Engineering Ceramics by Abrasive Waterjets," American Ceramic Society Bulletin, vol. 72, no. 8, 1993, pp. 93-98.

3 Stinton, D. P, "Assessment of the State of the Art in Machining and Surface Preparation of Ceramics," *Oak Ridge National Laboratory, ORNL/TM* - 1-791, Nov. 1988.

4 Quinn, G. D. "Fracture mechanism maps for advanced structural ceramics, part 1: methodology and hot-pressed silicon nitride results," *Journal of Material Science*, vol. 25, 1990, pp. 4361-4376.

5 Lehman, R. L., "Overview of Ceramic Design and Process Engineering," *Ceramics and Glass*, vol 4, ASM International, 1991.

6 Weller, E. J., Nontraditional Machining Processes, 2nd ed., Society of Manufacturing Engineers Dearborn, Michigan, 1984.

7 Sheppard, L.M., "Machining Of Advanced Ceramics," *Adv. Mater. Proc.* 132, vol. 6, no. 40, 1987.

8 Rajukar, K.P., Satyanarayanan, G., Komanduru, R., (ed.) "Advanced in Non-Traditional Machining'" *ASME PED*-vol. 22, 1986.

9 Blake, P., Bifano, T., Dow, T. Scattergood, R. O., " Precision Machining of Ceramic Materials'" Ceramic Bulletin, vol. 67, no. 6, 1988, pp. 1038-1044.

10 Copley, S. M., "Shaping Ceramics with Lasers," *Interdisciplinary Issues in Materials Processing and Manufacturing Symposium*, ASME, Boston, 1987.

11 Hashish, M, "Application of Abrasive Waterjet to Metal Cutting," *Nontraditional Machining Conference*, Proceedings, Cincinnati, Ohio, 1985, pp. 1-11.

12 Hashish, M. "Cutting with Abrasive waterjets," *Carbide and Tool Journal*, 1984, pp. 16-23.

13 Hashish, M., "Aspect of Abrasive Waterjets Performance Optimization," *Proceedings of 8th International Symposium on Jet Cutting Technology*, Cranfield, Bedford, England, 1986, pp. 297-308.

14 Kovacevic, R., Hashish, M; Mohan, R; Ramulu, M; Kim, T. J.; Geskin, E.S., "State of the art of research and development in abrasive waterjet machining," *Journal of Manufacturing Science and Engineering (USA)*, vol. 119, no. 4B, Nov. 1997, pp. 776-785.

15 http://www.coorsceramics.com/matprtab.htm, Coors Ceramic Corporation, Colorado.

16 Kobayashi, A. S., "Hybrid Experimental-Numerical Stress Analysis," *Handbook on Experimental Mechanics*, ed. A. S. Kobayashi, Pretice-Hall, 1987, pp. 739-767,.

17 Ramulu, M., "Dynamic Photoelastic Investigation on the Mechanics of Waterjet and Abrasive Waterjet Machining," *Optics and Lasers in Engineering*, 19, 1993, pp. 43-65.

18 Zeng, J., Kim, T., "An Erosion Model of Polycrystalline Ceramics in Abrasive Waterjet Cutting ," *Wear*, 193, 1996, pp. 207-217.

19 Ramulu, M., and Wong, K., P., "Preliminary Investigations of Abrasive Waterjet Piercing 1987 Process by Dynamic Photoelasticity," *International Journal of Water Jet Technology*, vol. 1, no. 2, Sept. 1991, pp. 53-63.

20 Subramanian, K., and Kapp, R. N. "Production Grinding Methods and Technique," *Engineering Materials Handbook, Ceramics and Glasses*, ASM International, 1991.

21 Yanagiuchi, S. Yamaguta, H., "Cutting and Drilling of Glass by Abrasive Jet," *Proceedings of 8th International Symposium on Jet Cutting Technology*, Cranfield, Bedford, England, 1986.

22 Burnham, C., "Abrasive Waterjets Come of Age," *Machine Design*, May 10, 1990.

23 Singh, P. J., "Abrasive Fluid Jet Machining," *Engineered Material Handbook*, Vol. 4, Ceramics and Glass, ASM International, 1991

24 Hashish, M. "Optimization Factors in Abrasive-Waterjet Machining," *ASME Winter Annual Meeting*, Chicago, 180, 1988.

25 Ramulu, M., "Dynamic Photoelastic Investigation on the Mechanics of Waterjet and Abrasive Waterjet Machining," *Optics and Lasers in Engineering*, 19, 1993, pp. 43-65.

26 Hocheng, H., and Chang, K. R., "Kerf Analysis in Abrasive Waterjet Cutting of Ceramic Plates," *Proceedings of Pacific-Rim Symposium on Abrasive Waterjet Machining*, 1992.

27 Hashish, M., "Material Properties in Abrasive Waterjet Machining," *Transaction of ASME*, vol.117, Nov. 1995, pp. 578 – 583.

28 Hamatani, G. and Ramulu, M., "Machineability of High Temperature Composite by Abrasive Waterjet," *Journal of Engineering Materials and Technology*, Oct. 1990, vol. 112 pp. 381-386.

29 Chelikani, S. and Kalpakjian, S., "Hydrodynamic Machining of Fiber Reinforced Composites," *Journal of Composites Technology & Research*, JCTRER, vol. 18, no. 2, April 1996, pp. 118-126.

30 Hunt, D., Kim, T., J. and Sylvia, J. G., "A Parametric study of Abrasive Waterjet Processes by Piercing Experiment," *Eighth International Symposium On Jet Cutting Technology*, Durham, England,September, 1986, pp. 9-11.

31 Hashish, M., "On the Effects of Material properties in Abrasive Waterjet Machining"...

32 Franz, N. C., "The influence of Standoff Distance on Cutting with High Velocity Fluid Jets, " *2nd International Symposium on Jet Cutting Technology*, Cambridge, England, 1974, pp. BV3-37~B3-46.

33 Konig, W. and Wulf, C., "The influence of the Cutting Parameters on Jet Cutting Force and the Geometry of the Kerf," *7th International Symposium on Jet Cutting Technology*, Ottawa, Canada, 1984, pp. 179-191.

34 Savrun, E. and Taya, M, "Surface Characterization of SiC Whisker/2124 Aluminum and Al sub 2 O sub 3 Composites Machined by Abrasive Waterjet," *J. Mater. Sci.*, vol. 23, no. 4, Apr. 1988, pp. 1453-1458.

35 Hunt, D., Kim, T. and Mark Reuber, "Surface Finish Optimization for Abrasive Waterjet Cutting," *9th International Symposium on Jet Cutting Technology*, Sendai, Japan, 4-6 Oct., 1988.

36 Mohan, R; Kovacevic, R; Zhang, Y. M., "Characterization of Surface Texture Generated by High Energy Jets," *Winter Annual Meeting of the American Society of Mechanical Engineers*, Anaheim, CA, USA, 11/08-13/92, ASME Prod Eng Div Publ Ped., ASME, New York, NY (USA),., vol. 62, 1992, pp. 203-218.

37 Burnham , C. D. and Kim, T. J., "Statistical Characterization of Surface Finish Produced by a High Pressure Abrasive Waterjet," *5th American Waterjet Conference*, August 29-31, 1989: Toronto, Canada.

38 Kovacevic, R., Mohan, R., Zhang, Y. M., "Cutting Force Dynamics as a Tool for Surface Profile Monitoring in Abrasive Waterjet," *Transactions of the ASME*, vol. 117, Aug. 1995, pp. 340-350.

39 Chao, J., Zhou, G., Leu, M. C., Geskin, E., "Characteristics of Abrasive Waterjet Generated Surfaces and Effects of Cutting Parameters and Structure Vibration," *Journal of Engineering for Industry*, vol. 117, Nov. 1995, pp516-525.

40 Tan, D. K. M., "A Model for the Surface Finish in Abrasive Waterjet Cutting," *Proceedings of the 8t h International Symposium on Jet Cutting Technology*, Cranfield, Bedford, England, 1986, pp. 309-313.

41 Hashish, M, "Characteristics Of Surfaces Machined With Abrasive-Waterjets", ED: Editor Ramula, M; Hashish, M; American Society of Mechanical Engineers, Mat.Div., *Machining Characteristics of Advanced Materials San Francisco*, 10-15 December, 1989, American Society of Mechanical Engineers, Mat.Div.; MD.-vol.16, pp.23-32.

42 Kovacevic, R; Mohan, R; Zhang, Y. M., "Cutting Force Dynamics as a Tool for Surface Profile Monitoring in AWJ," *J. Eng. Ind. (Trans. ASME) (USA)*, vol. 117, no. 3, Aug. 1995, pp. 340-350.

43 Hashish, M., "Pressure Effects in Abrasive -Water (AWJ) Machining," *Journal of Engineering Material and Technology*, Vol. 111, 1989, pp. 221-228.

44 Momber, A. W., "Investigations in Abrasive Waterjet Erosion Based on Wear Particle analysis," *Journal of Tribology*, Vol. 118, Oct. 1996, pp. 759-765.

45 Geskin, E. S., et al., "Investigation of Anatomy of an Abrasive Waterjet," *5th American Waterjet Conference*, Toronto, Canada, 1989, pp. 217-230.

46 Momber, Andreas W. Pfeiffer, Dirk; Kovacevic, Radovan; Schuenemann, Rene, "Influence of abrasive grain size distribution parameters on the abrasive waterjet machining process," *The 1996 24th NAMRC Conference*, Ann Arbor, MI, USA, 05/21-23/96 Tech Pap Soc Manuf Eng Mr, Sme, Dearborn, MI, (USA), 1996.

47 Ansari, A. I., Ohadi, M. M. and Hashish, M., "Effect of Waterjet Pressure on Thermal Energy Distribution in The Workpiece During Cutting with an Abrasive Waterjet," in *Research and Technological Developments in Nontraditional Machining*, vol. ASME PED vol. 34, ed. 1988, pp. 141-148.

48 Arola, D., Fadale, T., Ramulu, M, "Heat Flux at the Erosion Boundary During Abrasive Waterjet Machining of Metals," Jetting Technology, 1996, pp 735-752.

49 Li, H. Y., Geskin, E. S. and Chen, W. L., "Investigation of Force Exerted by an Abrasive Waterjet on a Workpiece," *5th American Water Jet Conference*, Toronto, Canada, 1989, pp. 69-77.

50 Momber, AW; Kovacevic, R," Quantification of energy absorption capability in abrasive water jet machining," *Proc Inst Mech Eng Part B J Eng Manuf*, Vol. 209, no. B6, 1995pp. 491-498.

51 Kim, T. J., Sylvia, J.G. and Posner,L., "Piercing and Cutting of Ceramics By Abrasive Waterjet," *ASEM PED*-vol. 17, pp. 19-24.

52 Ansari, A. I., Hashish, M., "Effect of Abrasive Waterjet Parameters on Volume Removal Trends in Turning," *Journal of Engineering for Industry*, Nov. 1995, vol.117, 475-484.

53 Hashish, M., "An Investigation of Milling with Abrasive Waterjet," *Journal of Engineering for Industry*, vol. 111, 1989, pp.158-166.

54 Hashish, M., "Turning with Abrasive Waterjet - A First Investigation," *Journal of Engineering for Industry*, vol. 109, 1987, pp. 281-290.

55 Hashish, M., "Visualization of the Abrasive Waterjet Cutting Process," *Experimental Mechanics*, 1986, pp.159-169.

56 Hashish, M., "Turning with Abrasive Waterjet - A Preliminary Investigation," in *Advances in Non-Traditional machining*, vol. PED 22, ed. ASME, 1986, pp. 79-100.

57 Hashish, M, "Milling With Abrasive-Waterjet: a Preliminary Investigation," *Proceedings of the Fourth U.S. Water Jet Conference, Berkeley*, California, USA, 26-28, Aug. 1987, American Society of Mechanical Engineers, 1987, pp. 1-10.

58 Hashish, M., "Machining of Advanced Composite Abrasive Waterjet," *Manufacturing Review*, vol. 2, 1989, pp. 142-150.

59 Hashish, M., Whalen, J., "Precision Drilling of Ceramic Coated Components with Abrasive waterjets", *Transaction of ASME*, vol. 115, Jan. 1995, pp. 148-154.

60 Hashish, M. "Waterjet Machining Of Advanced Composites," *Mater. Manuf. Processes*. vol.10, no.6, 1995, pp.1129-1152.

61 Paul, S. , Hoogstrate, A. M., van Luttervelt, C. A., Kals, H.J.J. "An Experimental Investigation of Rectangular Pocket Milling with Abrasive Water jet," *J. Of Material Processing Technology* 73, 1998, pp. 179-188.

62 Wada, S, "Effects Of Hardness And Fracture Toughness Of Target Ceramics And Abrasive Particles On Wear Rate By Abrasive Water Jet," *J Ceram. Soc. Jap.* vol.104, no.4, 1996, pp. 247-252.

63 Wong, WCK; Chen, L; Siores, E, "Optimizing abrasive waterjet cutting of ceramic materials," Journal of Materials Processing Technology (Netherlands), vol. 74, no. 1-3, Feb. 1998, pp. 251-254.

64 Wada, S; Kumon, Y, "Effects Of Impact Angles Of Jet Stream In The Abrasive Water Jetcutting Of Si3n4 Ceramics", *J. Ceram. Soc. Jap.* 101, no.11, 1993, pp.1297-1301.

65 Tikhomirov, et al., "High-Pressure Jetting," *ASME Press Translations*, 1992.

66 Hashish, M., "A Model for Abrasive-Waterjet Machining," Transactions of the ASME, *J. of Engr. Mat and Tech.*, vol. 111, 1989, pp. 154-162.

67 Bitter, J. G. A. , "A Study of Erosion Phenomenon, Part I, II," *Wear*, Vol. 6, 1963, pp. 5-21 169-190.

68 Raju, S., "Modeling of Hydro-Abrasive Erosive Wear during Abrasive Waterjet Machining," *Ph. D. Dissertation*, University of Washington, 1994.

69 Zeng, J., "Mechanisms of Brittle Material Erosion Associated with High Pressure Abrasive Waterjet Processing -- A Modeling and Application Study," *Ph.D Dissertation*, University of Rhode Island, 1992.

70 Tilly, G. P., "Erosion Caused by Airborne Particles," *Wear*, vol. 14, 1969, pp. 63-79

71 Rickerby, D. G. and MacMillan, N. H., "The erosion of Aluminum by Solid Particle Impingement at Oblique Incidence," *Wear*, vol. 60, 1980, pp. 369-382.

72 Tilly, G. P., "Erosion Caused by Airborne Particles," *Wear*, vol. 23, 1969, pp. 87-96.

73 Smeltzer, C. E., Gulden, M. E., Compton, W. A., "Mechanisms of Metal Removal by Impacting Dust Particles," *Journal of Basic Engineering*, September 1970, pp. 639-654.

74 Ives., I. K. and Ruff, A. W., "Electron Microscopy Study of Erosion Damage by Copper," *Erosion: Prevention and Useful Applications*, ASTM STP 664, W. F. Alder, Ed., *American Society for Testing and Materials*, 1979, pp. 5-35.

75 Naerheim, A., "The Effect of Mechanical Properties on Erosion," *Wear*, vol. 121, 1988, pp. 307-324.

76 Stringer, J. and Wright, I., G., "Some Views on the Formation of Ripples on Eroded Surfaces," *Proceedings of the Seventh International Conference on Erosion by Liquid and Solid Impact*, Cambridge, UK, Sept. 7-10, 1987, pp. 47-1/47-7.

77 Reddy, A. Venugopal and Sundararajan, G., "Erosion Behavior of Ductile Materials with a Spherical Non-Friable Erodent," *Wear*, vol. 111, 1986, pp. 313-323.

78 Chaudhri, M. M.,Wally, S. M., "A High - Speed Photographic Investigation of the Impact Damage in Soda-Lime and Borosilicate Glasses by Small Glass and Steel Spheres," *Symposium on the Fracture Mechanics of Ceramics*, vol. 3, Plenum Press, New York, 1978, pp. 349-364.

79 Bowden, F. P. and Field, J. E., "The Brittle Fracture of Solids by Liquid Impact, by Solid Impact, and by Shoch," *Proceedings of the Royal Society of London, Series A*, Vol. 282, 1964, pp. 331-352.

80 Sheldon, G. L., Finnie, I., "The Mechanism of Material Removal in the Erosive Cutting of Brittle Materials," *Journal of Engineering for Industry*, ASME, November 1966, pp. 393-400.

81 Finnie, I, "The Mechanism of Erosion of Ductile Metals," *Proceedings of 3rd US National Congress of Applied Mechanics*, ASME, New York, 1958, pp. 527-532.

82 Finnie, I, "Erosion of Surfaces by Solid Particles," *Wear*, vol. 3, 1960, pp. 87-103.

83 Evans, A. G., "Impact Damage in Ceramics," Fracture Mechanics of Ceramics, vol. 3, ed. Bradt, B. C., Hasselman, D. P. H., and Lange, F. F., 1978, Plenum Press, New York, pp. 303-330.

84 Hochey, B. J., Wiederhorn, S. M., and Tohnson, H., " Erosion of Brittle Materials by Solid Particle Impact," *Fracture Mechanics of Ceramics*, vol.3, ed. Bradt, B. C., et al, 1978, Hasselman, D. P. H., and Lange, F. F., 1978, Plenum Press, New York, pp. 379-402.

85 Paul, S. , Hoogstrate, A. M., van Luttervelt, C. A., Kals, H.J.J. "Analytical Model for the Total Depth of Cut in the Abrasive Water Jet Machining of Polycrystalline Brittle Material," *J. of Material Processing Technology* 73 (1998) 179-188.

86 Paul, S. Hoogstrate, A. M., van Luttervelt, C. A., Kals, H.J.J. "Analytical and Experimental Modeling of the Abrasive Water Jet Cutting of Ductile Material," *J. of Material Processing Technology* 73, 1998, pp. 189-199.

87 Arola, D., Ramulu, M., "Micro-mechanisms of Material Removal in Abrasive Waterjet Machining," *Processing of Advanced Materials* 4, 1994, pp. 37-47.

88 Momber, A. W., Kovacevic, R., "A Fracture Model for Hydrodemolition," *8th American Water Jet Conference*, August 26-29, 1995, Houston, Texas.

89 Hashish, M., "Material Properties in Abrasive Waterjet Machining," *Transaction of ASME*, vol.117, Nov. 1995, pp578 - 583.

90 Momber, AW; Eusch, I; Kovacevic, R, "Machining Refractory Ceramics With Abrasive Water Jets," *Journal of Materials Science (UK)*, vol. 31, no. 24, 15 Dec. 1996, pp. 6485-6493.

91 Zeng, J; Kim, TJ, " Machineability of engineering materials in abrasive water jet machining," *International Journal of Water Jet Technology (Canada)*, vol. 2, no. 2, Apr. 1995, pp. 103-110.

92 Chen, L., Siores, E. and Wong, W. C. K., "Kerf Characteristics in Abrasive Waterjet Cutting of Ceramic Materials," *Int. J. Mach. Tools Manufact.* vol. 36, no.11, pp 1201-1206, 1996.

93 Ramulu, M. and Arola, D., "Water jet and Abrasive Waterjet Cutting of Unidirectional Graphite/Epoxy Composite," Composites , vol. 24, no. 4, 1993, pp. 299-308.

94 Ramulu, M., Prasad, E., Malakodaiah, G., and Guo, Z., "Secondary Processing Effects and Damage Mechanisms in Continuous Fiber Ceramic Composites," Thermal and Mechanical Test Methods and Behavior of CFCCs, *ASTM STP 1309*, ed. Jenkins. M., et al., *American Society for Testing and Materials*, 1996.

95 M. Ramulu, M. G. Jenkins, and Z. Guo, "Abrasive Waterjet Drilling and Cutting Mechanisms in Continuous-fiber Ceramic Composite," *9th American Waterjet Conference, Aug. 23-26, 1997*, Dearborn, Michigan.

96 Daniel, I. M., Lowlands, R. E. and Labs, T. J., "Photoelastic Study of Water Jet Impact," *Proceedings of the 2nd International Symposium on Jet Cutting Technology*, 2nd-4th, April, 1974, Cambridge, UK.

97 Daniel, I. M., "Experimental Study of Water Jet Impact on Rock and Rocklike Materials," *Proceedings of the 3rd International Symposium on Jet Cutting Technology*, 11th-13th May, 1976, Chicago.

98 Przylenk and Schlatter ,"Simulation of the cutting process in water Jetting with the Finite Element Method," *8th International Symposium on Jet Cutting Technology*, Durham, England,September, 1986, pp.9-11.

99 Martin Rosenblatt, Y. Marvin Ito and Larry DeAngelo "Numerical Simulations of Ceramic Target Response to Water Drop Impacts Including Effects of Surface Flaws and Pores," *Proc. 5th Int. Conf. On Erosion by Solid and Liquid Impact*, 4:1.

100 Fukunishi, Y., Kobauashi, R. and Uchida, K., "Numerical Simulation of Striation Formations on Waterjet Cutting Surface," *Proceeding of the 8th American Water Jet Conference*, August 26-29, 1995, Houston, Texas, pp. 657-670.

101 Liaw, N. W., Kobayashi, A. S., and Emery, A. F., "Effect of Loading Rate on Dynamic Fracture of Reaction Bonded Silicon Nitride," pp. 95-107.

102 Mark, K, Y., and Jenkins, M., G., "Numerical Modeling of the Mechanical Response of a Continuous Fiber Ceramic Composite in Flexure," *Ceram.Eng. Sci. Proc.* vol.18, no.3, 1997, pp. 485-493.

103 Sheppard, L. M., "Machining of Advanced Ceramics," *Advanced Materials & Processes*, vol. 132, no. 6, 1987, pp. 40-48.

104 Karnitz, M. A., Craig, D. A., and Richlen, S. L., *Ceramic Bulletin*, vol. 70, no. 3, 1991, pp. 430-435.

105 Jahanmir, S., (ed), Machining of Advanced Materials, NIST Special Publication 847, *National Institute of Standards and Technology*, Washington, DC, 1993.

106 Snoeys, R., Staelens, F., and Dekeysev, W., CIRP Annuals, vol. 35, no.2, 1986, pp. 467-480.

107 Wang, D. H., Ramulu, M., and Arola, D., *International Journal of Machine Tools and Manufacture*, vol. 35, no. 6, 1995, pp. 1623-1638.

108 Wang, D. H., Ramulu, M., and Arola, D., *International Journal of Machine Tools and Manufacture*, vol. 35, no. 6, 1995, pp. 1639-1648.

109 Colligan, K. and Ramulu M., " An Experimental Investigation into Pitting of Hole Surfaces When Drilling Graphite Epoxy Composite" *ASME Bond Volume*, MD vol. 35, 1992, pp.11-25.

110 Colligan, K. and Ramulu, M., "The Effect of Edge Trimming on Composite Surface Plies," *Manufacturing Review*, vol. 5, no. 4, 1992. pp.274-283.

111 Hashish, M., "Machining of Advanced Composite with Abrasive Waterjet," *Manufacturing Review*, vol. 2, no. 2, 1989, pp. 142-150.

112 Ramulu, M., "EDM Sinker Cutting of TiB_2-SiC Composite," *Advanced Ceramic Materials*, vol. 3, no. 4, 1988, pp. 324-327.

113 Ramulu, M., and Arola, D., *International Journal of Machine Tools and Manufacture*, vol. 34, no. 3, 1994, pp. 295-313.

114 Gonczy, S. T., Lara-Curzio, E., Riester, L., Butler, E., Danforth, S., Cannon, W., "Low cost machining of ceramic - fiber reinforce ceramic composites (2-D) and the effects on tensile properties," The 1994 International Mechanical Engineering Congress and Exposition, Chicago, IL, USA, 11/06-11/94, ASME. Materials division Publication, ASME, New York, NY, 1994, vol. 52, pp.217-238.

115 McMurty, C. H., Boecher, W. D. G., Seshadri, S. G., Zangki, J. E., "Micro-structure and Material Properties of SiC-TiB2," *Ceramic Bullitin*, vol. 66, no. 2, 1987, pp. 325-332.

116 Jenkins, M. G., Piccola, Jr., J. P., Mello, M. D., Lara-Curzio, E., and Wereszczak, A. A., *Ceramic Engineering and Science Proceedings*, vol. 15, no. 4, 1994, pp. 209-218.

117 Piccola, J. P., Jr., "Effects of Test Parameters on Tensile Mechanical Behavior of a Continuous Fiber Ceramic Composite (CFCC)," *Master of Science thesis*, University of Washington, 1994.

118 Hashish, M., "Modeling Study of Metal Cutting with Abrasive Waterjets," *Journal of Engineering Materials Technology, ASEM Translations*, Jan. 1984, pp.88-100.

119 Hodgman, C. D., (ed.), "Handbook of Chemistry and Physics," The chemical Rubber Co., Cleveland, 1942.

120 American National Standards: Surface Texture, Surface Roughness, Waviness, And Lay, ANSI B 46.1-1978.

121 Neusen, K. F., Gores, T. J., Labus, T. J., "Measurement of particle and drop velocities in a mixed abrasive waterjet using a forward-scatter LDV system," Jet Cutting Technology, ed Lichtarowicz, A., 1992, pp. 63-73.

122 Momber, A. W. Cherukuthota, C Kovacevic, R. "Calculation of Exit Jet Energy in Abrasive Water Jet Cutting," *ASME International Mechanical Engineering Congress Exposition*, vol. 68, Part 1, PED, 1994, pp.361-366.

123 Chelikani and Kalpakjian. International Journal of Water Jet Technology, vol. 2, no. 2, 1995, pp. 111-118.

124 Laermann, K. H., "Hybrid Analysis of Pale Problems," *Exp. Mech.*, 21 (Oct. 1981), pp. 386-388.

125 Manufactured by Micromeasurement, Raleight, NC.

126 Post, D., Han, B., Ifju, P., "High Sensitivity Moiré Experimental Analysis for Mechanics and Materials," *Springer-Verlag*, New York, Inc. 1994.

127 Guild, J., " The Interference System of Crossed Diffraction Gratings'," *Clarendon Press*, Oxford, 1956.

128 Dally, J. W. and Riley, W. F., "Experimental Stress Analysis," *3rd Edition, McGraw-Hill*, New York, 1991.

129 ANSYS Corporation., "ANSYS User's Manual for Reversion 5.3," 1995.

130 Timoshenko, S, Goodier, J. N, "Theory of Elasticity," McGraw-Hill Book Company, Inc., 2nd ed. , 1951, pp362-366.

131 Wong, Kwok-Pew, Photoelastic Investigation of abrasive Waterjet Machining," Master Thesis, University of Washington, 1990.

132 Murakami, Y, "A method of stress intensity factor calculation for the crack emanating from an arbitrarily shaped hole or the crack in the vicinity of a arbitrarily shaped hole," *Transaction of Japan Soc. Mech. Engrs*, vol, 44, no 378 (1978), pp.423-432.

133 Koepke, B. G., Stokes, R. J., "Grinding Damage in Ceramics," *Society of Manufacturing Engineers Publication No. EM77-358*, 1977.

134 Ishikawa, K. and Ichikkawa, K., "Study on Precision Slicing of Hard and Brittle Materials by the Vibratory Multi-Blade Cutting Method," *Bull. Jpn. Soc. Precise.* Eng. 17(2), (1983), pp. 135-137.

135 Subramanian, K., "Precision Finishing of Ceramic Components with Diamond Abrasives," *Ceramics Bulletin*, Vol. 67, , June 1988, pp. 1026-1029.

136 Schwartz, M. M., "Handbook of Structural Ceramics," *McGraw-Hill, Inc.*, 1992

137 Indge, H. , "Lapping, Honing, and Polishing," *Engineered Material Handbook, vol. 4, Ceramics and Glasses*, ASM International, 1991

138 Tuersley, IP; Jawaid, A; Pashby, IR, "Various methods of machining advanced ceramic materials," *J. Mater. Process. Technol. (Netherlands)*, vol. 42, no. 4, pp. 377-390, 1 May 1994

139 Firestone, R. F., "Lasers And Other Nonabrasive Machining Methods For Ceramics," *Advanced Ceramics '87. Proc. Conf. held at Cincinnati*, Ohio, February 17-19 1986. Dearborn, Mi., Soc. Manuf. Eng., 1987. Paper MR87-112

140 Petrofes, N. F., Gadalla, "Electrical Discharge Machining of Advanced Ceramic," *Ceramic Bulletin*, Vol. 67, No. 6, 1988, pp. 1048-1052

141 Snoeys, R., "Non-Conventional Machining Techniques, The State of the Art," Advances in Nontraditional Machining, ASME PED vol. 22, pp. 1-20, *Winter Annual Meeting of ASME*, Dec. 1986

142 Moreland, M. A. Moore, D. A., "Versatile Performance of Ultrasonic Machining," *Ceramic Bulletin*, Vol. 67, No. 6, 1988, pp. 1045-1047

143 Kirchner, H. P., and Conway, J. C. Jr., Richard, D. M., "Fragmentation and Damage Penetration During Abrasive Machining of Ceramics," *The science of Ceramic Machining and Surface Finishing*, II ed. pp. 23-42,1985

144 Li, H. -Y., "Investigation of Waterjet-Workpiece Interaction," *Ph. D. Dissertation*, New Jersey Institute of Technology, 1992

145 Sedlacek, Halden and Jorgensen, "On the Strength of Ceramics as a Function of Microstructure, Grinding Parameters, Surface Finish, and Environmental Conditions," *The Science if /ceramic Machining and Surface Finishing*, I ed. NBS Special Publication 348, U. S Government Printing Office,.1972

146 Tressler, Langensiepen and Bradt "Surface Finish Effects on Strength- vs.-Grain-Size Relations in Polycrystalline Al_2O_3," *Journal of American Ceramic Society*, 57(5), pp. 226-227, 1974

147 Post, D.," Moiré Interferometry," *Handbook on Experimental Mechanics*, ed. A. S. Kobayashi, Prentice-Hall, pp. 314-387, 1987

148 Tuttle, M. E., and Klein, R., J., "Compression Measurements Using Moiré Interferometry," *Optical engineering*, Vol. 27(8), pp. 630-635, 1988.

149 Wang, F. X., Kang, B., S., -J. And Lin, K., Y., "Full-Field Displacements by Four-Beam Moiré Interferometry," *Proceedings of the 1986 SEM Spring Conference on Experimental Mechanics*, Milwaukee, WI, pp. 278-284, 1991

APPENDIX A
CERAMIC MACHINING PROCESSES

Ceramic material can be machined using mechanical, chemical or thermoelectric energies. A flow chart that illustrates all machining processes is shown in Figure A.1. This flow chart can be further categorized as traditional machining processes and non-traditional machining processes. Fundamental principles and machining mechanisms of these processes are presented in the following sections.

A.1 CONVENTIONAL MACHINING PROCESSES FOR CERAMICS

Abrasive machining, including cutting, grinding, lapping, and polishing, is the most popular and basic process for ceramics machining. Flat surfaces of ceramic workpieces are either ground with a revolving grinding wheel, lapped with a free-rolling abrasive, or polished with fine abrasives. Conventional ceramic machining processes consist of a sequence of grinding steps of decreasing severity to remove material from the workpiece[133]. A "normal" machining operation can consist of three to five steps[134]. The first step is rough grinding using coarse diamond grit wheels at the traverse removal rate of 25 mm/pass. Machining at reduced material removal rates is needed following rough grinding. Finish grinding with fine abrasives, for example, 325 μm diameter abrasive, is then performed to obtain smooth surfaces. Lapping or polishing is conducted to obtain the desired surface finish and to minimize the subsurface damage. Each of these machining techniques is discussed in the following subsections.

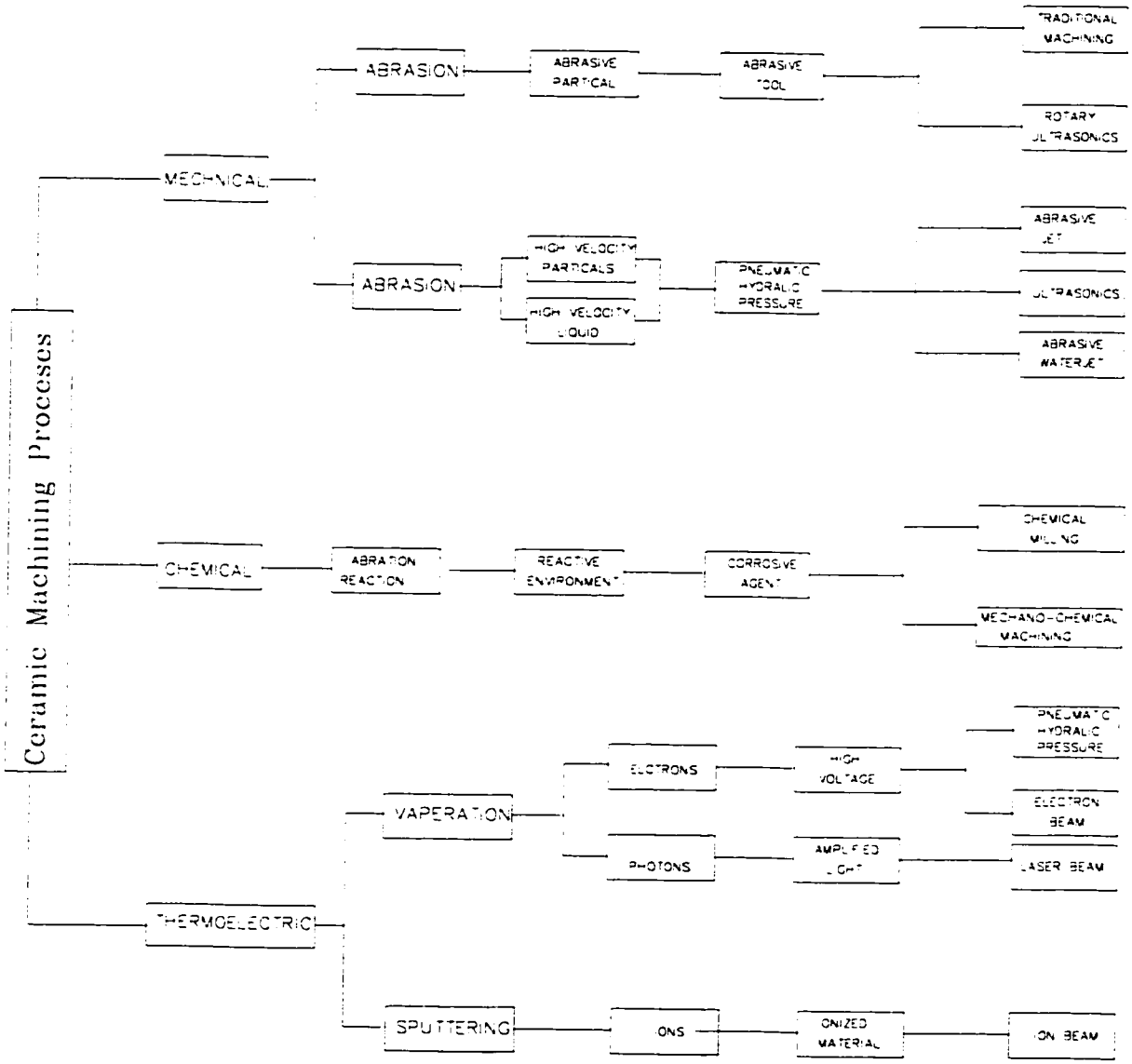

Figure A.1 A flow chart illustrating all machining process [146]

(1) Grinding

Grinding is a chip-generation process. The shape, size and efficiency of this chip-generation process determine the geometry and quality of the surface produced. The rate and efficiency of chip production determine the economics of the grinding process [135]. Grinding uses diamond grit abrasives bonded on a grinding wheel, and pressure applied against the work surface in a variety of configurations. The most efficient diamond grit abrasive finishing method requires a system approach that addresses four key aspects of the grinding process: machine tool, wheel selection, work material properties, and operational factors. The grinding process has been able to remove stock at a faster rate, utilize higher horse-power, process more workpieces per load, and achieve acceptable accuracy. This method for ceramics machining is a well established abrasive machining process that is extensively used in electronic ceramics, such as magnetic heads, microchips, and substrates. In the fabrication of cutting tools, ball bearings, and engine components, grinding is also a very popular process. As demands for closer tolerances become greater and materials become more exotic, grinding processes are now being challenged by sophisticated precision lapping and polishing processes.

(2) Lapping

Lapping uses loose or bonded abrasives in a low - pressure, low - speed operation to achieve high geometric accuracy, to correct minor shape errors, to improve surface finish, or to provide tight fits between mating surfaces. Lapping takes place when abrasive grains in a liquid vehicle, often known as a slurry, are guided across the surface to be lapped and backed up by a lapping plate[136]. When a relative motion is induced and pressure applied, the sharp edges of the grains are forced into the ceramic materials to be lapped. They either make an indentation or cause the material to chip away microscopic particles. The hardness and the size of the abrasive grain determine the surface finish. The finer the abrasive grains are, the smoother the finish is. When lapping is used for

sintered type ceramic materials, it seems that there often exists a limit to the smoothness on the surface. This is true in the case of very fine abrasive grains, in which a rolling abrasive cutting action causes the sintered particles to break away from the bond.

(3) Honing

Honing resembles lapping in principle, but usually it is reserved for finishing internal surfaces of cylindrical spherical parts. Flat honing is sometimes called fine grinding [137]. The abrasive grain is mixed into a bonded wheel or a disk that also acts as the reference surface. The abrasive grains are oriented in a random way with sharp edges exposed to the surface of a part. A uniform pressure is applied between the wheel and the part. The protruding abrasive edges penetrate the workpiece surface and scratch away materials.

(4) Polishing

The polishing process normally uses a fine powder as a medium applied to a tool, and uses a relative motion between workpiece and the tool to improve the surface finish on the workpiece. The polishing tool used for a softer workpiece is a fabric or other soft material such as pitch. For a harder workpiece, harder abrasives are embedded into a firmer material, causing a portion of the abrasive particles to protrude from the tool. The abrasive acts as a scraping cutting tool, shearing off microscopic peaks of the surface being polished. The smoothness of the surface depends on the size and the quality of the abrasive and the technique used. A controlled polishing process is able to produce a product of size in an increment of 10 millionths of an inch.

The just mentioned abrasive machining processes account for most of the total material removal processes for ceramics at present. However, many problems still need to be overcome [5]. For example, it may be impossible to machine a part with complex shapes. The main problems with traditional ceramic machining are low machining

efficiency, high expense, tool cost, and problematic machining accuracy. Non-conventional machining processes must be utilized to achieve fine finishes for advanced ceramic products. In the following section, non-conventional ceramic machining processes are introduced.

A.2 NON-CONVENTIONAL CERAMICS MACHINING PROCESSES

Non- conventional ceramic machining processes are classified into two groups: abrasives or non abrasives. Non-abrasive techniques include chemical machining, electron beam machining, laser machining, electrical discharge machining, etc[138]. Abrasive techniques include ultrasonic machining, abrasive jet machining, and abrasive waterjet machining.

A.2.1 Non-Abrasive Machining Technique

(1) Chemical Machining

Chemical machining is a technique, which is able to remove or dissolve material from the surface of a glass or ceramic very gently, i.e., with no mechanical force. It is based on a chemical reaction between the workpiece and etching fluid. Some areas of the workpiece can be masked to prevent reaction. Generally, thin layers are removed. Thus, making chemical machining preferred for manufacturing small or middle-sized parts. Although the process is not very complex, the machining results still depend on masking and the etching reagent selected.

(2) Electron-Chemical Machining

Another process involving chemicals is electron-chemical machining. The material removal in electron-chemical machining (ECM) is based on the anodic dissolution during electrolysis. The tool electrode is used as a cathode while the

workpiece is the anode. The electrolysis process takes place in a salt solution. The major advantage is the absence of tool wear and any thermal load on the workpiece. The major drawback is "overcut", that is, the undesired and uncontrolled electrochemical over-dissolving of the workpiece [3].

(3) Electron Beam Machining

Electron beam machining is a thermal process that removes material through melting and vaporization. The material to be removed is exposed to a focused beam of electrons, and then heated. This process is able to drill a very small hole of less than 50 μm, utilizing the small size electron beam that can be positioned using a magnetic field. A series of electromagnetic lenses focus the beam on the target on a vacuum chamber. Even though the process can be highly automated with high productivity of attainable high precision, it is only suitable for small parts and only in a vacuum environment [141].

(4) Laser Machining of Ceramics

Laser machining is a non-contact thermal process and is not limited by the hardness or strength of the ceramic[139]. It can be used in processes for hard, brittle, and abrasive materials, such as drilling, cutting, welding, etching, surface processing, and material composition [10]. Laser energy is focused on a workpiece to melt or evaporate material at the focal point. High pressure gas jets blow the melted material away from the groove or hole being machined. Laser machining eliminates tool wear problems, machine tool deflections and vibrations, and cutting forces on the workpiece. It has the ability to drill, cut, thread, or groove a wide range of materials because the hardness has no effect on machining rates. However, because of high heat during the machining process and the use of high-intensity energy, the process produces a heat affected zone on the workpiece that may reduce the strength of the materials. Laser beam machining is

preferred for thin workpieces. For thick material, a high-power laser generator is essential, which increases the cost dramatically.

(5) Ion Beam Machining

Ion beam machining produces the least amount of damage to the workpiece of all the techniques described. Energy from an incident beam of ions is transferred to surface atoms that are ejected from the surface. Movement of the ion beam is rapid and quite simple because electrical control of a magnetic field moves the beam from one location to another. Although, the material removal rate is very small, the strength of workpiece machined by this technique will normally be greater than a specimen machined by an abrasive technique.

(6) Electrical Discharge Machining (EDM)

EDM is an electro-thermal process. It uses thermal energy to remove material through melting or vaporization, by means of discharging an electric arc between an electrode (cutting tool) and a cathode (workpiece). The electric arc generates high temperatures in close proximity to the arc. The workpiece is submerged in a dielectric fluid. This process is controlled, so that many small arcs are produced across a dielectric fluid between a workpiece and the tooling. In EDM process, the specimen has to be electric conductive, which includes certain carbides, borides, and nitrides. The cutting tools are very inexpensive because they are made of soft conductive materials like brass, stainless steel, and graphite. However, the process is very slow and the material removal rate is very slow also.

There are two types of machines used for EDM operation: die sinking and wire cutting. Die sinking can be used for tapping, cutting holes, and helical machining. Here the workpiece is a cathode and the shaping tool (die) is the anode. The materials are removed from the workpiece by the high heat, until the workpiece takes the form of the

reverse image of the three-dimensional tool. A schematic of a die sinking machining by electrical discharge is in Figure A.2. The machineability of a TiB_2 particulate SiC matrix ceramic composite material has been studied by Ramulu [112] and Petrofes et al[140]. In wire-cutting (EDM), a thin metallic wire under tension is used to "cut" material like a jigsaw.

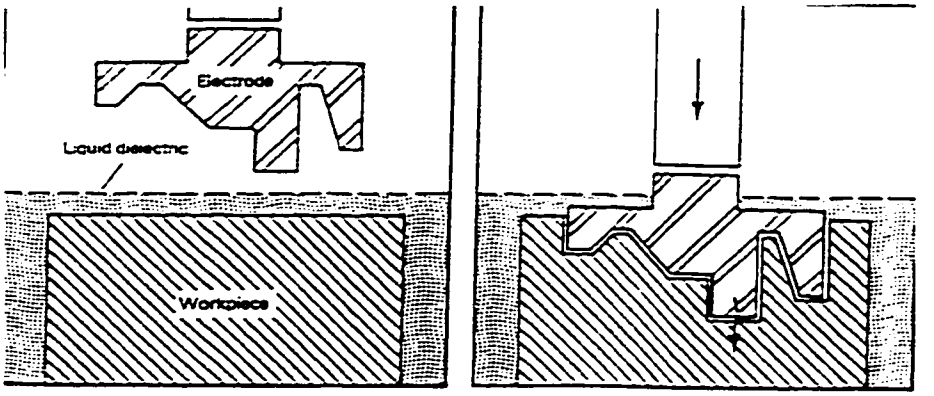

(a) Before EDM (b) After EDM

Figure A.2 Schematic of Electrical Discharge Machining [146]

(7) Plasma Beam Machining (PBM)

A plasma is an electrically conductive gas state[141]. Plasma can be obtained by an electric discharge between an anode and cathode, which yields an ionized gas at very high temperature (~ 20,000°C). Typical gases include argon, helium or nitrogen. In plasma machining(PBM), the plasma torch is constructed in such a way that the plasma is constricted in a narrow column with a diameter of the order of 1 mm.

A plasma arc beam and a plasma jet beam are applied respectively for electric conductive and non-conductive materials [141]. The material is removed by melting and

evaporating. However, because of the high temperature involved, PBM has the same problems as other thermally based machining techniques

A.2.2 Abrasive Machining Technique

(1) Ultrasonic Machining

Ultrasonic machining (USM) is also known as ultrasonic abrasive machining, which is a more widely used technique for the fabrication of hard and brittle ceramic components[142]. A schematic of an ultrasonic machine is shown in Figure A.3. The cutting tool is ultrasonically vibrated normal to the workpiece (no rotary action) while a slurry of abrasive particles is pumped between the tool and the workpiece. Machining occurs within regions where the tool contacts the workpiece or its close proximity. The abrasive particles erode the material, and the workpiece takes on the exact form of the tool. Because no pressure is directly applied from the tool to the workpiece, the grinding pressure rarely exceeds 0.1 MPa. The low force and cool abrasive slurry prevent significant thermal and mechanical stresses from building up in the material. The gentle grinding pressure result in very little strength-limiting damage to the surface of the workpiece. In Figure A.3, part (a) illustrates the transducer assembly and tooling assembly, and part (b) shows the close-up view of tooling assembly being used in machining of ceramics.

(2) Rotary Ultrasonic Machining

Rotary ultrasonic machining (RUSM) utilizes a rotating diamond tool that vibrates ultrasonically at about 20 kHz during machining. This technique produces much faster machining rates and superior surface finishes. It also exerts very light tool pressures on the workpiece, which minimizes chipping and damage to the surfaces being machined. It makes it possible to drill very straight deep holes, and adjacent holes or grooves with a very thin dividing wall. Ultrasonic vibration of the coolant provides

benefits such as a cleaning action of the tool to eliminate binding and loading of the diamond matrix. The low pressures and clean cuts produced by this technique are ideal for ceramic composites, because the gentle action presents minimum delamination of the fibers and the matrix. The depth-to-diameter ratio of holes drilled by this technique can be very high (300:1) compared to other techniques. Rotary ultrasonic machining can also be used for milling, threading, and grinding applications. However, the disadvantage of RUSM is that its uses are limited to round tool configurations only.

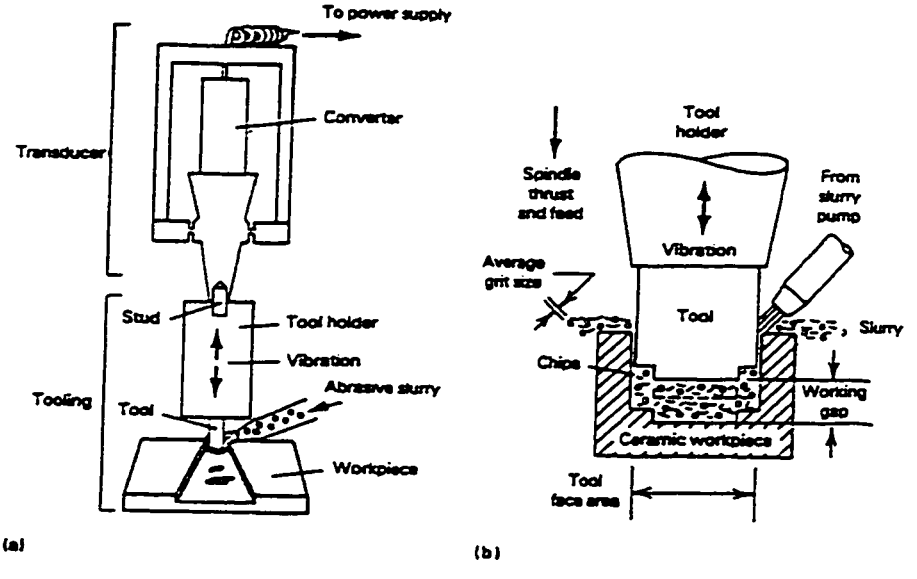

Figure A.3 Schematic of a Ultrasonic Machine[146]

(3) Mechano-Chemical Machining

Mechano-chemical machining is a very gentle abrasive technique used primarily in the electronic field to polish or lap a workpiece. A soft abrasive material that normally would not scratch or damage the workpiece is used to polish a much harder brittle material. However, in mechano-chemical polishing, the abrasive material is carefully

selected to react with the workpiece, and form a reaction product on surface aspirates of the workpiece. The very thin reaction product is then abraded because it is either poorly bonded to the workpiece or it possesses a reduced hardness. Materials polished by this mechano-chemical technique include sapphire by SiO_2, silicon nitride by Fe_2O_3, SiC by $SrCO_3$ or MgO. The polishing rate can be increased by polishing dry to generate higher temperatures.

(4) Abrasive Jet Machining

In Abrasive Jet Machining (AJM), the material is removed by mechanical impact of a high velocity air jet with abrasive particles. There is limited force on the specimen and no thermal problems occur in the process because of the cooling effect of the expanding jet. This process, however, is very slow and the abrasive powder can not be reused. Because of its nature, abrasive jet machining usually requires some kind of dust-collecting system.

(5) Abrasive Waterjet Machining

In abrasive waterjet machining, the workpiece material is removed by the mechanical impact of a high velocity waterjet. The high pressure water can be accelerated to very high speed waterjet through a nozzle. The waterjet is used to entrain and accelerate the abrasive particles. Unlike air jet, the waterjet can be confined to a small diameter without spreading, and it can accelerate the particle in a relatively short distance. Similar to AJM, the water takes away the heat generated in the machining process, so there is no degradation of the ceramics resulting from the thermal effect.

So many conventional and non-conventional machining techniques for hard-to-machine material, in particular for ceramics, were presented in this appendix. However, there are some limitations on most of these machining processes. A single process can not complete the whole machining process from stock removal to final finish. Machining

using electrical energy, such as electrical discharge machining, electrochemical machining, is limited to machining only on electric-conductive ceramics. Machining processes with thermal energy remove material by means of vaporization and fusion. These processes include electrical discharge machining, electron beam machining, laser beam machining, and plasma arc machining. And electron beam machining, plasma arc machining require that the machining be done in a vacuum environment. Obviously these two processes can not be used for stock material removal. In the case of laser beam machining very powerful laser is needed in order to machine bigger or thicker size workpiece. Chemical machining processes are based entirely on chemical reaction. However, not all materials are chemically active with available chemicals. It is a very slow process.

A.3 ABRASIVE MACHINING MECHANISMS OF CERAMICS

Ceramic material has its peculiar high hardness and brittleness. Abrasive machining methods are the most common processes for ceramics and diamond is the most popular abrasive for the process. It is necessary to understand the mechanisms associated with abrasive machining of ceramic materials.

Kirchner and Conway[143] studied the material removal mechanisms for single-point grinding of ceramics. As shown in Figure A.4, a groove is machined at a low speed (less than 1 mm/s) by a single point diamond. In the contact region between the material and the single abrasive point plastic deformation occurs, due to the high stress and elevated temperatures induced in the machining process. The dominant mechanism of material removal during diamond grinding of ceramics is brittle fracture. It was observed that not only many chips were removed in front of the point by brittle fracture, but also that a substantial number of chips separated from the workpiece. Plastic deformation occurred within the machined groove, and the brittle fracture occurred along the groove. Similar behavior also occurs with multi-point abrasive material removal during grinding and

cutting operations. Li noticed that the damage mechanism under waterjet impact is due to cavitation erosion induced by cyclic longitudinal stress waves generated by impact [144]. It was concluded that the abrasive waterjet cutting mechanism is comprised of individual abrasive particles micro-cutting and non-directional fatigue phenomena

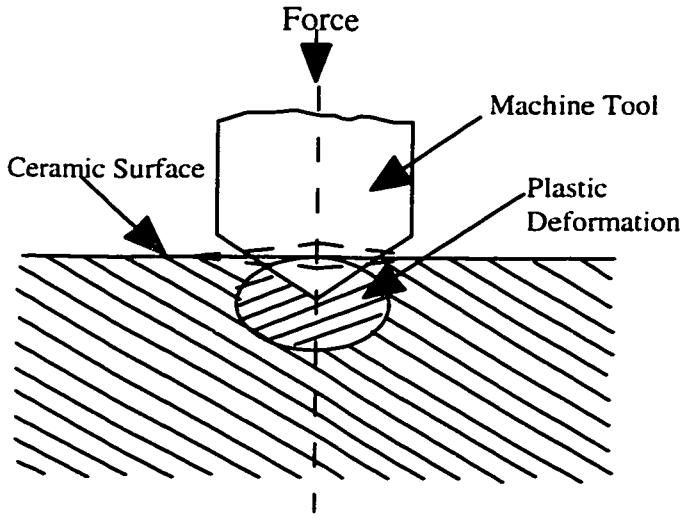

Figure A.4 A groove machined by a single point diamond

Another common model describing the material removal mechanism is the indentation fracture model. This model is used to describe the process of surface generation in ceramics (see Figure A.5). It is assumed that the grain acting as an indenter is subjected to a normal load [20]. A vertical crack originates directly below the plastically deformed region, called the median crack. After the large median crack is initiated, tensile stresses are generated at the interface of the elastically deformed region and the plastically deformed region. Therefore, the lateral crack or vent crack is then propagated back to the surface, thus removing or lifting a piece of material off the work surface. Lateral cracks initiate runs parallel to the machining groove and perpendicular to the

surface. The third type of cracks is called the radial cracks. These cracks initiate at numerous points along the length of the grinding groove and are perpendicular to the sample surface. Radical cracks result from high tensile stresses that exist at the trailing edge of the point contact.

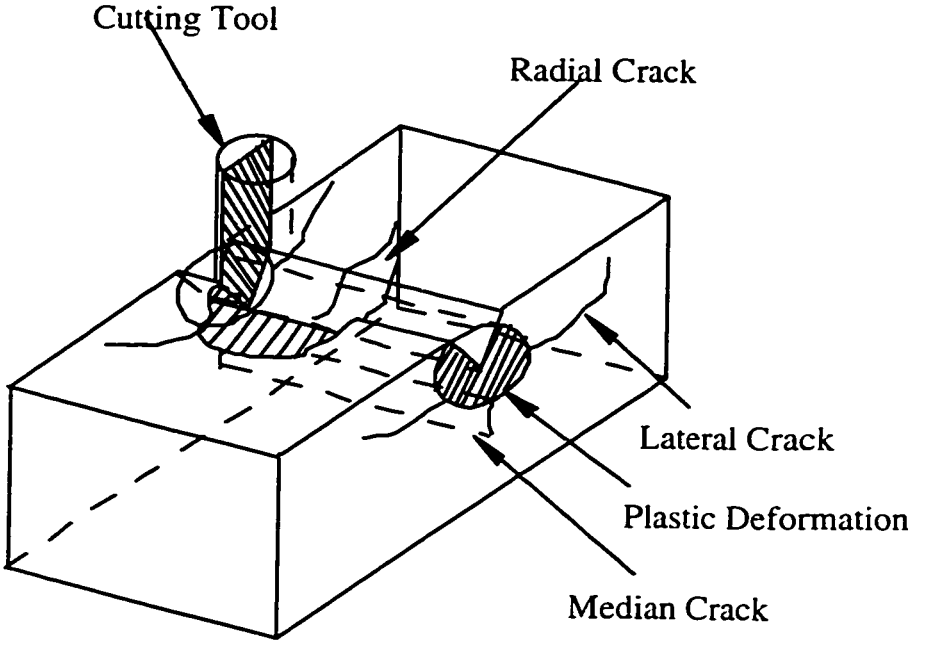

Figure A.5 An Indentation Fracture Model

The strength of ceramics is related to its microstructures, grinding parameter, surface finish, and environmental conditions[145]. It is indicated that the damage caused by machining operations significantly affect the strength of the ceramic. Ceramics with very dense fine grains normally have high strength. However, the machining induced flaws in these ceramics are often larger than preexisting processing flaws in the material, and thus they degrade considerably during machining [146]. On the other hand, ceramics with coarse grain and uniformly distributed porosity creates flaws comparable to or even smaller than

existing flaws in the material during machining. Therefore, the degradation of strength is much less susceptible[146].

Some other studies also disclosed that the orientation of the grinding operation also has a significant effect on strength. As described in the above paragraph, the strength of the ceramic is controlled by the size of the flaws within the tensile portion of a test specimen. For grinding in the transverse direction, stresses concentrate at median cracks. For grinding in the longitudinal direction (parallel to the length of a flexure bar) stresses concentrate at radial cracks. Since median cracks are much more severe, transverse grinding will result in significantly more strength reduction than longitudinal grind.

APPENDIX B

CALIBRATION CURVES OF ABRASIVE FLOW RATE

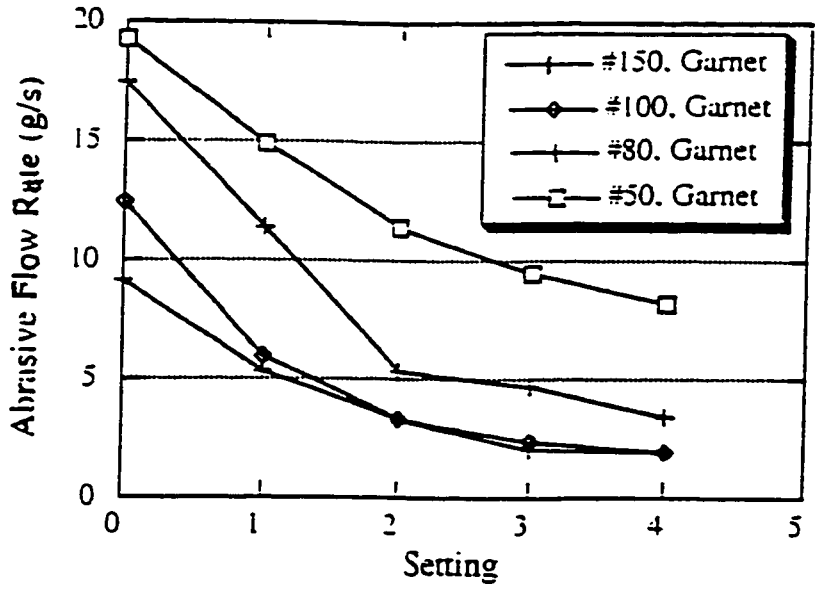

Figure B.1 Abrasive Flow Rate at Supply Pressure 75.8 MPa

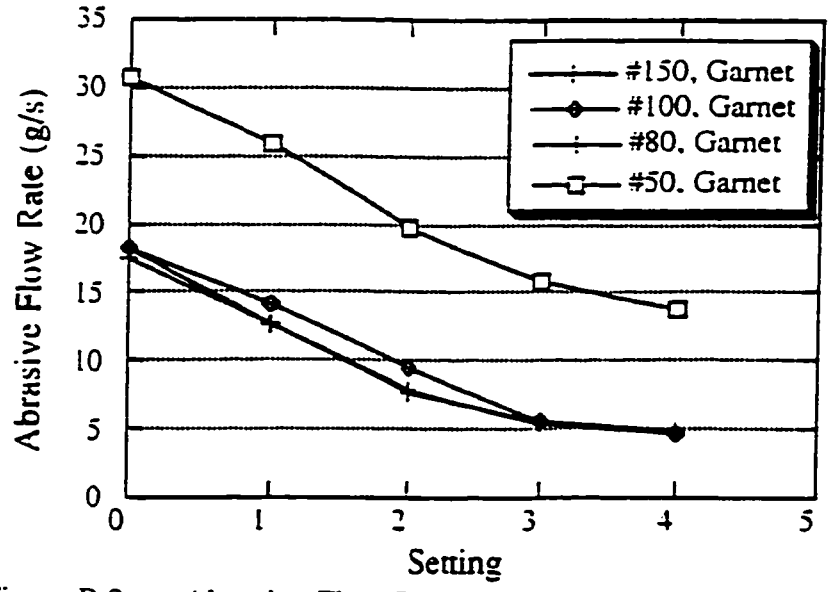

Figure B.2 Abrasive Flow Rate at Supply Pressure 241 MPa

APPENDIX C
FUNDAMENTALS OF MOIRÉ INTERFEROMETRY

Moiré phenomena occur when two beams of lights interfere. The discussion begins with a two-beam superposition. The superposition of two coherent beams of light is called two-beam interference. Assume the two coherent beams made up of long wave trains of a unique wave length λ, designated as beam 1 and beam 2, are of equal intensities. And the two beams are traveling in the same direction, as shown in Figure C.1. The amplitude of wave train I_1 and I_2 is assumed to vary with time as

$$A_1 = a\cos 2\pi\omega t \tag{C.1}$$

and

$$A_2 = a\cos 2\pi(\omega t + \frac{\delta}{\lambda}) \tag{C.2}$$

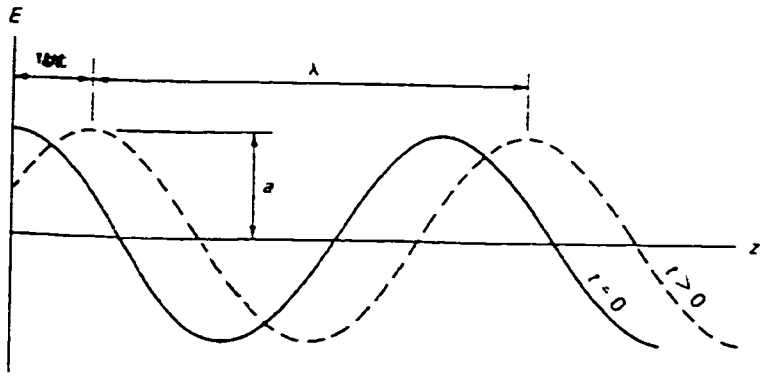

Figure C.1 Two Parallel Beams Interference

The superposition of these two beams of lights is

$$A = a\cos 2\pi\omega t + a\cos 2\pi(\omega t + \frac{\delta}{\lambda}) = K\cos 2\pi(\omega t + \varphi) \qquad \text{(C.3)}$$

where $K = \sqrt{2a^2(1+\cos 2\pi(\omega t + \frac{\delta}{t})}$ (C.4)

The resultant intensity of the superimposed light is K^2 or I:

$$I = 2a^2\left(1+\cos 2\pi\frac{\delta}{\lambda}\right) = 4a^2\cos^2\pi\frac{\delta}{\lambda} \qquad \text{(C.5)}$$

where ratio δ/λ is the relative phase, indicating the position of one wave with respect to the other. When the ratio equals an integer value n,

$$\frac{\delta}{\lambda} = n \qquad \text{n} = 0, 1, 2, \qquad \text{(C.6)}$$

then $I = 4a^2$, this interference effect is a case of constructive. If the ratio

$$\frac{\delta}{\lambda} = \frac{n+1}{2}, \qquad \text{n} = 0, 1, 2, \qquad \text{(C.7)}$$

then $I = 0$, which is the minimum intensity. This interference effect is destructive. Since both of the waves are parallel to the Z axis, the interference is the same at every point in space (x, y, z) where both beams of light exist.

When two collimated beams of light are with an angle 2θ (either diverging or intersection) as illustrated in Figure C.2, interferences occur also. Assume the two beams are produced by a single coherent light source with the same phase ($\delta = 0$), their wavefronts F_1 and F_2 are perpendicular to their beams and they too intersect at an angle 2θ. The resultant intensity of these beams is

$$I = I_1 + I_2 \pm 2I_1 I_2 \cos(2\pi\frac{\delta}{\lambda}) \qquad \text{(C.8)}$$

where I_1 and I_2 are the intensities of the interfering beams; δ/λ is the path difference.;

here since $I_1 = I_2$, thus

$$I = 2I_1\left\{1 \pm \cos(2\pi\frac{\delta}{\lambda})\right\} \qquad \text{(C.9)}$$

thus I=0, and $I = 2I_1$, when δ/λ equals to different values. This can be explained by optical interferences, where I=0 there exists constructive interference, $I = 2I_1$ constructive interference.

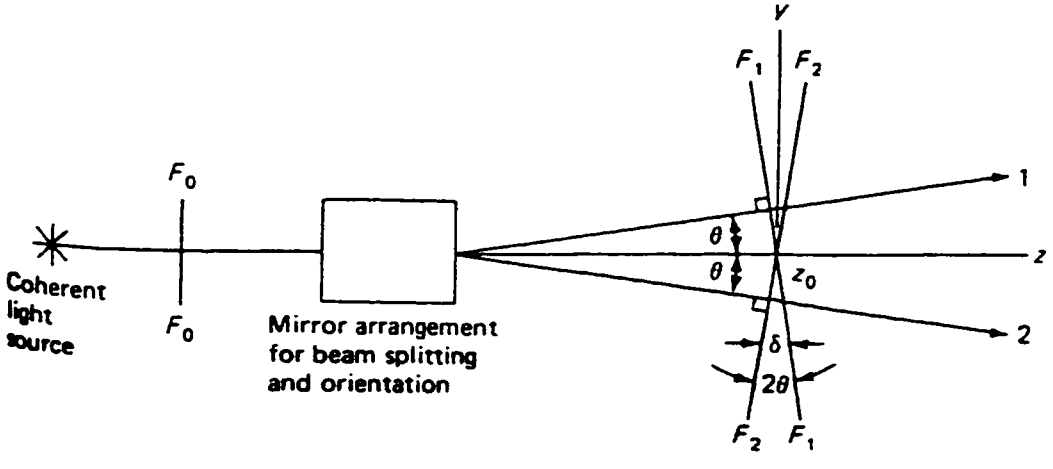

Figure C.2 Two Collimated Beams at an Angle Interference

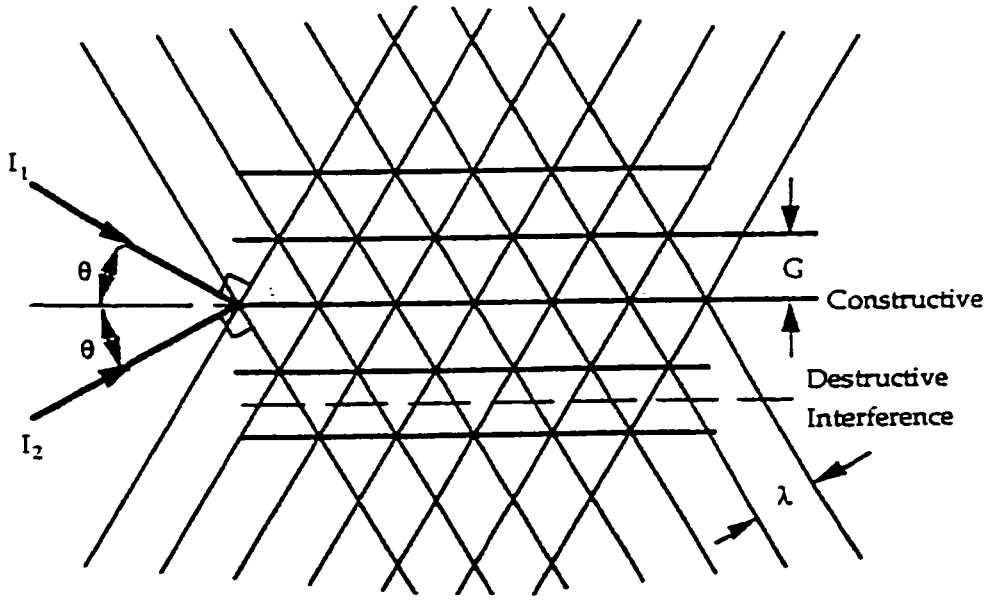

Figure C.3 Constructive and Destructive Beams

As illustrated in Figure C.3, the constructive and destructive interferences are equally spaced parallel lines. The relationship between the incident angle θ and the wave length λ can be found through the geometric analysis.

$$\sin\theta = \frac{\lambda}{2G} = f\frac{\lambda}{2} \qquad \text{(C.10)}$$

where G is the interference pitch; f is the frequency of the fringes (fringes/mm), and

$$f = \frac{1}{G} \qquad \text{(C.11)}$$

Thus the frequency of the fringe is determined by

$$f = \frac{2\sin\theta}{\lambda} \tag{C.12}$$

the fringe order N is given by the following equation:

$$N = \frac{s}{\lambda} = 0,\ 1,\ 2,\ 3,\ \ldots\ldots \tag{C.13}$$

Where s is the path length difference traveled by the two beams.

Figure C.4 is a schematic of the moiré interferometry method. Two beams of coherent light, A and B, of the wave length λ illuminates the specimen grating from specified angles (+α and -α). These two beams interfere and construct a virtual reference grating in space. The interfere mechanism was described in the above paragraphs. In this case the frequency of the reference grating equals 2x of that of the specimen gratings, and the frequency of the virtual reference grating is given by:

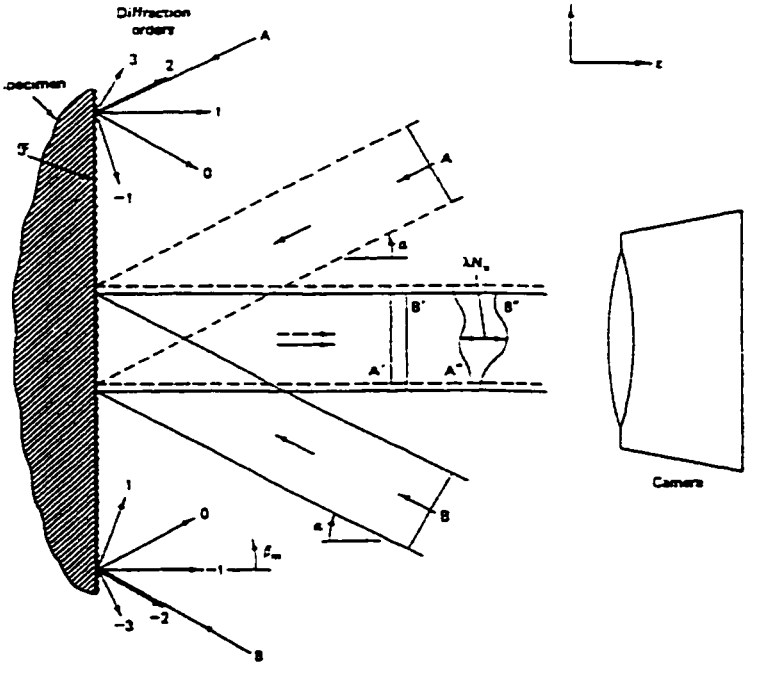

Figure C.4 Schematic Diagram of an Interferometer for Moiré Interferometry [147]

$$f = \frac{2\sin\alpha}{\lambda} \tag{C.14}$$

When the incident light beams hit the specimen grating, diffraction occurs. The diffracting lights, +1 and -1 orders of the incident beam A and B, respectively , interact with the virtual reference grating in space. If the specimen is deformed, a moiré fringe is formed and can be viewed and recorded by a camera. These moiré fringes represent in-plane displacements of every point on the specimen surface as contour maps of equal-displacement. Quantitatively, for each point in the fringe pattern,

$$u = \frac{N_x}{f} \tag{C.15}$$

$$v = \frac{N_y}{f} \tag{C.16}$$

where u, v are components of displacements in the x and y directions, respectively. N_x and N_y are fringe orders in the u- and v-displacement fields, respectively.

APPENDIX D

RECORDING OF FRINGES FOR DISPLACEMENT FIELDS

The four-beam moiré interferometry system has been used in the measurement of *u*- and v-displacement fields. Four-beam moiré interferometry system splits a collimated laser beam into four smaller beams [69, 148, 149] In static testing a two-step recording technique can be used to record the *u*- and v-field one after another, as long as the displacement fields remain stationary for each loading. When recording *u*-field, the *v*-filed is blocked, and vice verse.

In order to record both *u*- and *v*-displacement fields simultaneously, special optical setup is arranged. In this four-beam moiré interferometry system a *U*-V set is used. A U-V set splits a collimated laser beam into four small beams. The two beams in the vertical direction generate a moiré pattern that reflects the V displacement field, and the two beams in the horizontal direction generate a moiré pattern that reflects the U field displacement. The optical arrangement of the moiré interferometry in U or V field is illustrated in Figure D.1. The two horizontal beams are first reflected by the inner mirrors and to the outer mirrors, and finally directed toward the specimen through the outer mirrors. These two incident beams to the specimen surface form a vertical reference grating, which is perpendicular to the horizontal plane. The reference grating interferences with the first order diffraction beam exiting from the specimen grating and produces a moiré fringe pattern, which is the *u*-displacement field. In the same token, *v*-displacement field is also formed. The moiré patterns are reflected to the camera by means of a mirror mounted in the center of the U-V set and a specially designed mirror set, or image separation mirror set. The image separation mirror set has two mirrors. The *u*-field moiré pattern and *v*-field moiré pattern are reflected by the mirror mounted in the center of the U-V set and focused on the two image separation mirrors. Then the mirror

can reflect the beam into different spots, either on a single frame of film or on two different frames. And the images are recorded.

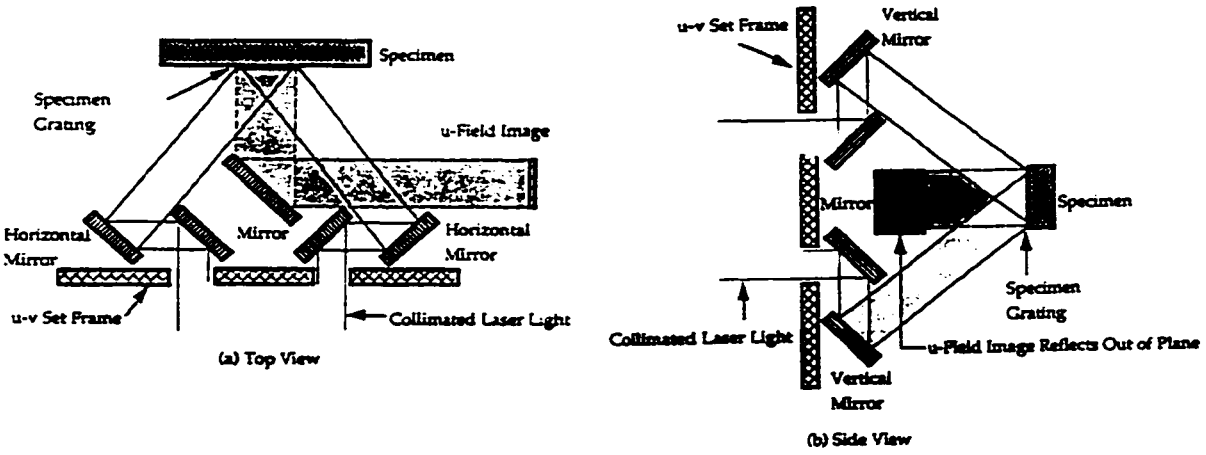

Figure D.1 U-V Field Optical Arrangement

APPENDIX E

MATLAB PROGRAM FOR ANALYTICAL SOLUTION

```
% assign 1st col. to x, 2nd col. to y, and 3rd col. to z
p=10*9.8*.45;
mu=.36;
pi=3.14;
E=2.72e9;

% define meshgrid and interpolate data to create displacement surface

xmin=-0.5*.0254;  %min x meshgrid value
xmax=0.5*.0254;  %max x meshgrid value
dx=0.01*.0254;   % x meshgrid gap
zmin=0.0;  %min y meshgrid value
zmax=0.75*.0254;  %max y meshgrid value
dz=0.01*.0254;   % y meshgrid step size

txi = xmin:dx:xmax;
tzi = zmin:dz:zmax;
Y=.125*.0254;
[X,Y,Z] = meshgrid(txi,Y,tzi);
%ZZ = griddata(x,y,z,XX,YY);
R=(X.^2+Y.^2).^.5;
R2=R.^2;
R3=R.^3;
Z2=Z.^2;
Z3=Z.^3;
RZ=(R.^2+Z.^2).^(-.5);
RZ3=RZ.^3;
RZ5=RZ.^5;
alpha=atan(X./Y);
u=p.*1000*((1-2*mu)*(1+mu).*(Z.*RZ-1+R2.*Z.*RZ3./(1-2*mu))./(2*pi*E.*R)).*sin(alpha);
w=p.*1000*((1+mu).*Z.^2.*RZ3+2*(1-mu^2).*RZ)/(2*pi*E);

sr=(p/(2*pi))*((1-2*mu)*(R.^(-2)-Z.*RZ./R.^2)-3.*R2.*Z.*RZ5);
sz=(-3*p/(2*pi)).*Z3.*RZ5;
```

```
stheta=(p/(2*pi))*(R.^(-2)+Z.*RZ.*R.^(-2)+Z.*RZ.^3);
Srz=(-1.5*p/pi).*R.*Z2.*RZ5;

% calculate dv-dy & dv_dx derivative
j=1:(((zmax-zmin)/dz))+1;
i=1:(((xmax-xmin)/dx))+1;
xx=X(i,j);
zz=Z(i,j);
yy=.125;
uu=u(i,j);
ww=w(i,j);
ssr=sr(i,j);
ssz=sz(i,j);

%convert matrix to column vector and save to ascii file
xcord=xx(:);
ycord=yy(:);
zcord=zz(:);

dispu = uu(:);
dispv= ww(:);
sr1=ssr(:);
sz1=ssz(:);

data=[xcord,zcord,dispu,dispv,sr1,sz1];
```

APPENDIX F

FINITE ELEMENT SIMULATION INPUT FILES

```
/prep7
!*
hole=8
!*
const=6.895e3     !1 psi=6.895e3 Newton/mm^2
!
jet=7*1300
!
normal=6.5*1300
Nup=1
Nlow=1
!
shear=0.20*1300
Sup=1
Slow=1
!*
Pnormal=normal*const
Pjet=jet*const
Pshear=shear*const
!
rjet=1.0e-3
ratio=hole
depth=rjet*ratio
thck=3.25e-3
width=25.4e-3
height=.75*25.4e-3
dip=depth/40
SAVE
!
j=Pjet*1e-6
h=ratio
s0=Pshear*1e-6
s1=sup
s2=slow
n0=Pnormal*1e-6
n1=nup
n2=nlow
/title, %h% mm hole; Norm %n0%; Shear %s0%; Jet %j% MPa
!/title, %ratio% mm hole; Norm %normal% (Nup,; Shear %shear% psi; Jet %jet% psi.
!
ET,1,SOLID64
```

```
MP,EX,1,395000*const      !Ex=2.72 GPa
MP,PRXY,1,.36,
!
ET,2,22
MP,EX,2,0
!*
/auto,all
CLOCAL,11,1,,,
N,1, rjet, 0.         height
N,81,rjet, 90,        height
FILL,1,81,3,21,20,
!fill,n1,n2,nfill,nstrt,ninc,itime,inc,space
csys,0
N, 10, thck, 0,   height
N, 30, thck, thck/2,height
N, 50, thck, thck, height
N, 70, thck/2,thck, height
N, 90, 0,     thck, height
!
N, 19, width/2, 0,    height
N, 39, width/2, thck/2,height
N, 59, width/2, thck, height
!
N, 1500,      ,     , height-depth
N, 1600,      ,     , height-depth-dip
!NGEN,5,20,1601,
!ngen,itime,inc,n1,n2,ninc,dx,dy,dz,space
N, 1610, thck,      , height-depth
N, 1630, thck,  thck/2, height-depth
N, 1650, thck,  thck,  height-depth
N, 1670, thck/2, thck,  height-depth
N, 1690, 0,     thck,  height-depth
!Curve nodes assignment
CLOCAL,12,0,,,height-depth
k=depth/(2*rjet**2)          !z=2kx^2 @ (rjet,depth)
m=.3                         !L1/LN=m=r**(N-1)
r=m**(1/(1-16))  !r=m**(1/(1-N))
lsum=0
*do,i,1,16
lsum=lsum+(r**(i-1)-r**i)*depth/(1-r**16)
zi=lsum
xi=(zi/(2*k))**0.5
nnumb=1+(16-i)*100
n,nnumb,xi,0,zi
*enddo
!
CLOCAL,11,1,,,
NGEN,5,20,1,1501,100,0,90/4
!
```

```
csys,0
h1600=nz(1600)
NGEN,2,100,1501,1581,20,0,,-depth/20
NGEN,17,100,10,90,20,0,0,-depth/16,0.4
h1601=nz(1601)
NGEN,14,100,1610,1690,20,0,0,-(height-depth)/13,7
NGEN,14,100,1601,1681,20,0,0,-h1601/13,7
NGEN,14,100,1600, , ,0,0,-h1600/13,7
NGEN,30,100,19,59,20,0,0,-height/29,2
!
*DO,m,1,15
m100=(m-1)*100
FILL,1+m100,10+m100,8,2+m100,1,5,20,3
FILL,10+m100,19+m100,8,11+m100,1,3,20,3
!fill,n1,n2,nfill,nstrt,ninc,itime,inc,space
*ENDDO
!
*DO,m,16,30
m100=(m-1)*100
FILL,1+m100,10+m100,8,2+m100,1,3,40,3
FILL,21+m100,30+m100,8,22+m100,1,2,40,2
FILL,10+m100,19+m100,8,11+m100,1,3,20,3
!fill,n1,n2,nfill,nstrt,ninc,itime,inc,space
*ENDDO
!
/VIEW,1,-0.03,-1,-0.2
/vup,1,z
eintf,1e-6
type,1
mat,1
E,181,161,61,81,182,162,62,82
EGEN,4,-20,-1    !4
EGEN,9,1,-4      !20
EGEN,10,1,-2
eplot
EGEN,15,100,-54
EPLOT
!
E,1501,1521,1541,1500,1601,1621,1641,1600
E,1541,1561,1581,1500,1641,1661,1681,1600
!
E,1562,1582,1581,1561,1662,1682,1681,1661
EGEN,4,-20,-1    !
EGEN,9,1,-4      !
EGEN,10,1,-2     !
eplot
EGEN,14,100,-56
EPLOT
!
```

```
nsym,x,3000,all
esym,,3000,all
EPLOT
NUMMRG,NODE, 1e-8
EPLOT
nsel,s,node,,1,81,20
nsel,a,node,,101,181,20
*repeat,15,,,,100,100
nsel,a,node,,1500
nsel,a,node,,3001,3061,20
*repeat,16,,,,100,100
type,2
mat,2
esurf
!
!SFCUM, pres, add
!JETJET!JETJET!JETJET!JETJET!JETJET!JETJET!JETJET!JETJET!!!!!
!
allsel,all
csys,1
NSEL,s,loc,x,0,rjet*.55
esln,s,1
esel,r,type,,2
SFE,all,5,PRES, ,Pjet,0,0,-1
!
!SHEAR!SHEAR!SHEAR!SHEAR!SHEAR!SHEAR!SHEAR!!!!!!!!!!!!
!
allsel,all
csys,1
NSEL,s,loc,x,0.0001,rjet
esln,s,1
esel,r,type,,2
SFE,all,3,PRES, ,Pshear*Sup
!
!NORMALPRESSURE!NORMALPRESSURE!NORMALPRESSURE!N!!!!!!!!!!
!
!
allsel,all
csys,1
NSEL,s,loc,x,rjet*0.55,rjet
esln,s,1
esel,r,type,,2
SFE,all,1,PRES, ,Pnormal*Nlow
!
!
/PSF,PRES,TANY,2
/PBF,DEFA, ,1
!/PBC,ALL, ,1
/REP
```

```
!*
EPLOT
ALLSEL,ALL
csys,0
nsel,s,loc,x,0
D, all,ux,0
nsel,s,loc,y,0
D, all,uy,0
nsel,s,loc,z,0
D, all,uz,0
allsel,all
fini
/solu
solve
fini
!/input,post,txt
!fini
!
/POST1
/GRESUME,plotctrl, ,
/contour,1,18

allsel,all
/VIEW, 1 ,,,1
!ETABLE,s1,s,1
!ETABLE,s2,s,2
!ETABLE,s3,s,3
!SADD,s1p2,s1,s2,1,1
!SADD,s1m2,s1,s2,1,-1
!SADD,s2p3,s2,s3,1,1
!SADD,s2m3,s2,s3,1,-1
!SADD,s3p1,s3,s1,1,1
!SADD,s3m1,s3,s1,1,-1
!
ALLSEL,ALL
!lpath,1500,1690
!PDEF,s1,S,1,AVG
!PDEF,s2,S,2,AVG
!PDEF,s3,S,3,AVG
!PDEF,e1,EPTO,1,AVG
!PDEF,e2,EPTO,2,AVG
!PDEF,e3,EPTO,3,AVG
/VIEW, 1 ,,-1
/ANG, 1
/REP
allsel,all
!
!
/PLOPTS,INFO,1
```

```
/PLOPTS,LEG1,1
/PLOPTS,LEG2,0
/PLOPTS,LEG3,1
/PLOPTS,FRAME,1
/PLOPTS,TITLE,1
/PLOPTS,MINM,1
/PLOPTS,VERS,0
/PLOPTS,WINS,1
!
NSEL,S,LOC,Y,thck
PLNSOL,U,z,0
!/NOERAS
!NSEL,S,LOC,Y,
!ESLN,S
!EPLOT
```

APPENDIX G

MORIE FRINGE PHOTOGRAPHS OF AWJ DRILLING

The moiré fringe pictures were taken during AWJ experiments on alumina and polycarbonate materials. The AWJ drilling conditions are provided in each figure. These attached pictures represent only part of the experiments conducted.

t=0 second

t=1.2 second

t=0.2 second

t=1.4 second

t=0.4 second

t=1.6 second

t=0.6 second

t=1.8 second

t=0.8 second

t=2.0 second

t=1.0 second

t=2.2 second

Figure G.1 *u*--field Morie Fringe Pattern for Alumina Specimen Drilling with AWJ (Pressure=207 MPa; Garnet Mesh 80; Stanfoff Distance 1 mm, grating resolution 66l/mm)

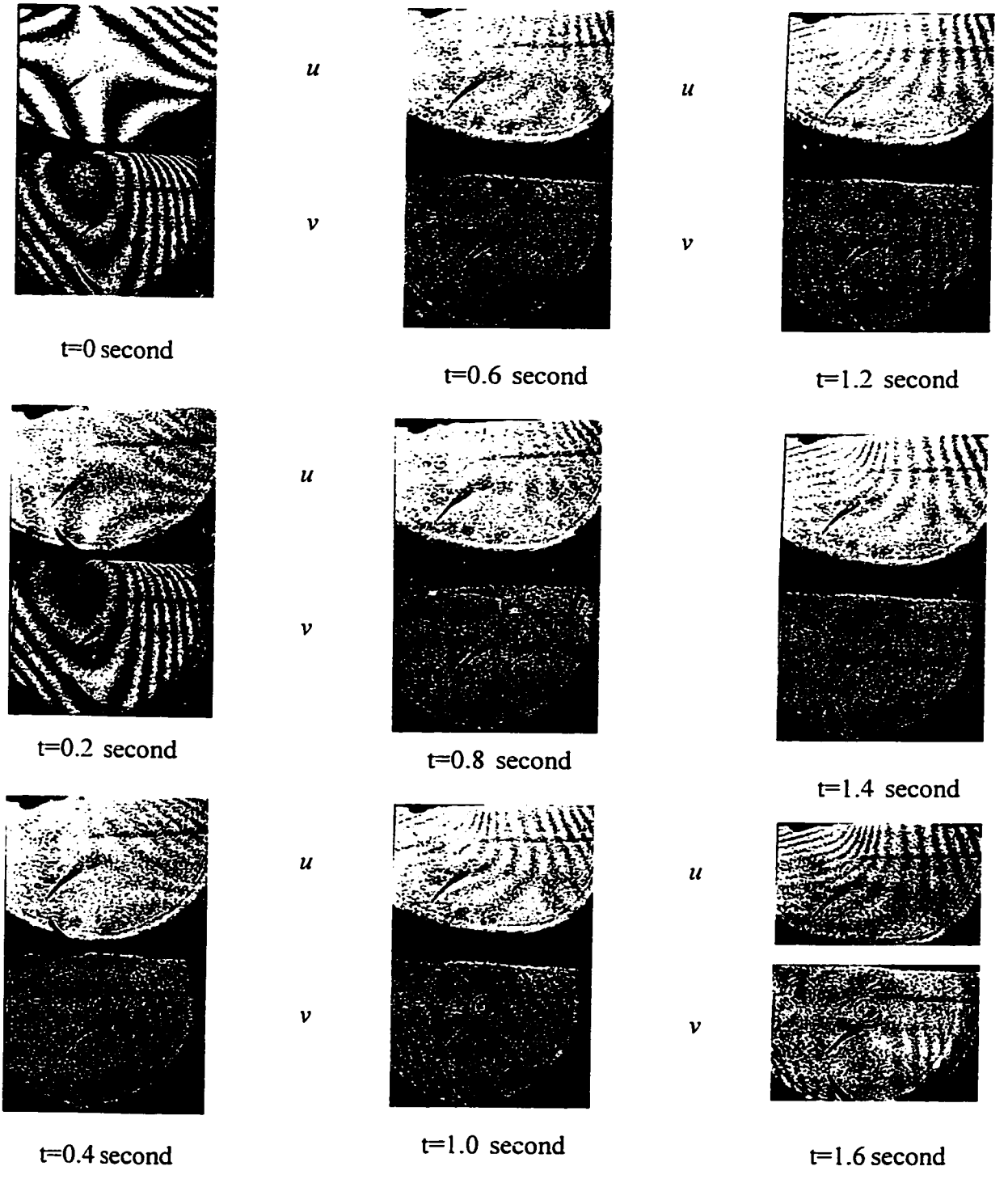

Figure G.2 Moire Fringe Patterns for AWJ Drilling of Polycarbonate
(pressure207 MPa; Garnet Mesh #80; Stanfoff Distance 1 mm)

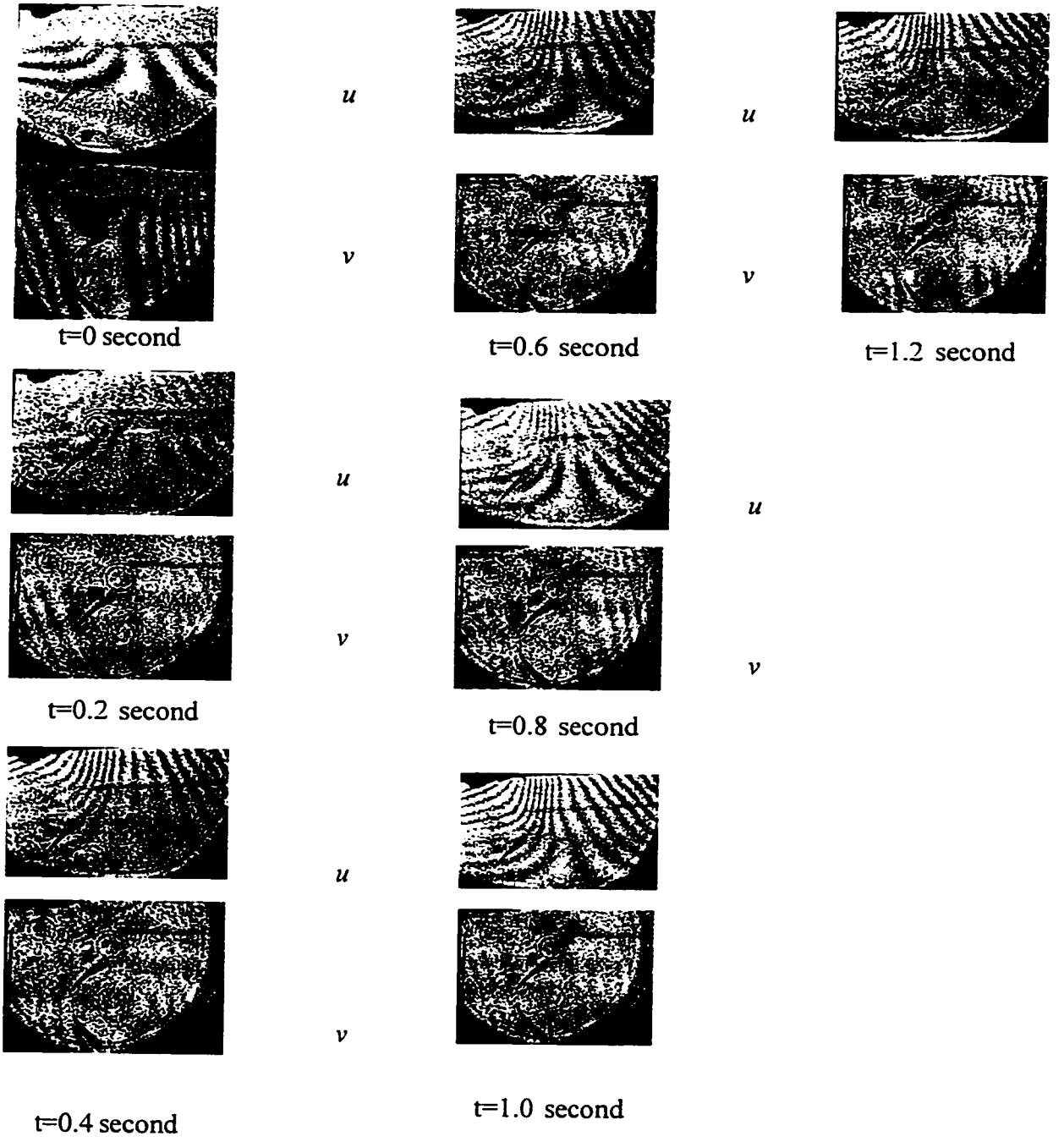

Figure G.3 Moire Fringe Patterns for AWJ Drilling of Polycarbonate
(pressure207 MPa; Garnet Mesh #80; Stanfoff Distance 1 mm)

t= 0.2 second

t= 1.2 second

t= 2.2 second

t= 0.4 second

t= 1.4 second

t= 2.4 second

t= 0.6 second

t= 1.6 second

t= 2.6 second

t= 0.8 second

t= 1.8 second

t= 2.8 second

t= 1.0 second

t=2. 0 second

Figure G.4 *v*-field Moire Fringe Patterns for Polycarbonate Material
(Supply pressure 207 MPa, Garnet #50, SOF 1mm, 120693)

t=0.0 seconds

t=0.8 seconds

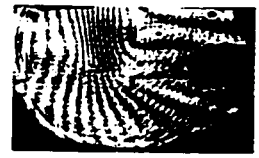

t=1.6 seconds

t=0.2 seconds

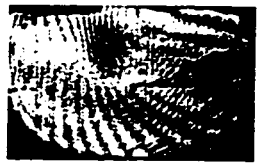

t=1.0 seconds

t=1.8 seconds

t=0.4 seconds

t=1.2 seconds

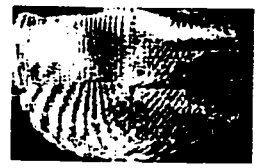

t=2.0 seconds

t=0.6 seconds

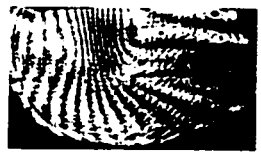

t=1.4 seconds

Figure G.6 *u*-field Morie Fringes for Polycarbonate Mateiral during AWJ Piercing (supply presusre 207 MPa, stanfoff distance 1 mm; garnet #50)

t=0.0 seconds

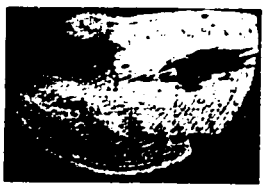

t=0.8 seconds

t=1.6 seconds

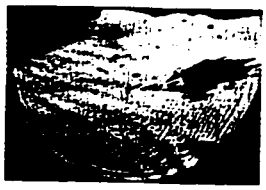

t=0.2 seconds

t=1.0 seconds

t=1.8 seconds

t=0.4 seconds

t=1.2 seconds

t=2.0 seconds

t=0.6 seconds

t=1.4 seconds

Figure G.7 *u*-field Morie Fringes for Polycarbonate Mateiral during AWJ Piercing
(supply presusre 207 MPa, stanfoff distance 1 mm; garnet #50)

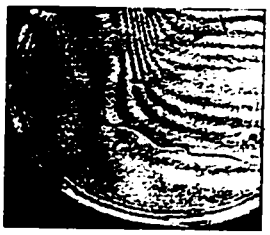

t= 0 second

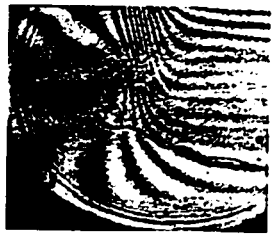

t= 0.8 second

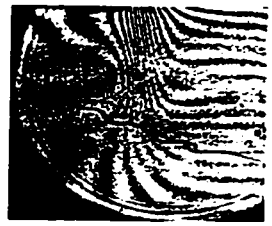

t= 1.6 second

t= 0.2 second

t= 1.0 second

t= 1.8 second

t= 0.4 second

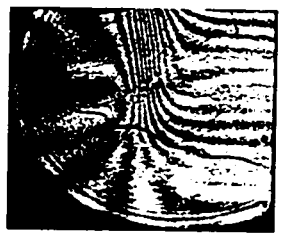

t= 1.2 second

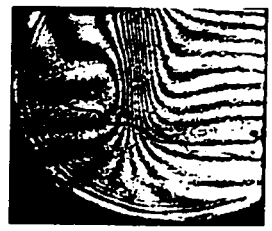

t=2. 0 second

t= 0.6 second

t= 1.4 second

Figure G.8 *u*-field Moire Fringe Patterns for Polycarbonate Material
(Supply pressure 207 MPa, Garnet #50, SOF 1mm,113093b)

t= 0 second

t= 0.8 second

t= 1.6 second

t= 0.2 second

t= 1.0 second

t= 1.8 second

t= 0.4 second

t= 1.2 second

t=2. 0 second

t= 0.6 second

t= 1.4 second

Figure G.9 *v*-field Moire Fringe Patterns for Polycarbonate Material
(Supply pressure 207 MPa, Garnet #50, SOF 1mm,113093b)

t= 0 second

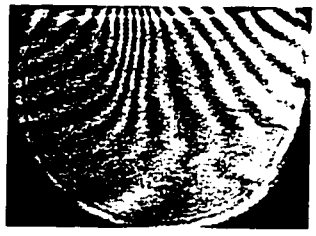

t= 1.0 second

t=2. 0 second

t= 0.2 second

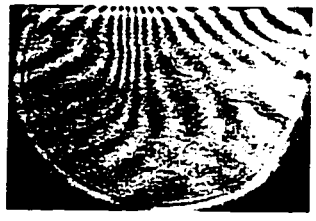

t= 1.2 second

t= 2.2 second

t= 0.4 second

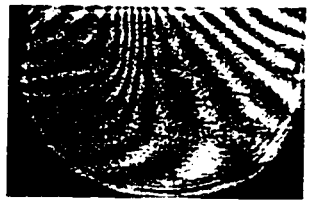

t= 1.4 second

t= 2.4 second

t= 0.6 second

t= 1.6 second

t= 2.6 second

t= 0.8 second

t= 1.8 second

Figure G10. *u*-field Moire Fringe Patterns for Polycarbonate Material
(Supply pressure 207 MPa, Garnet #50, SOF 1mm)

t= 0 second

t= 1.0 second

t=2. 0 second

t= 0.2 second

t= 1.2 second

t= 2.2 second

t= 0.4 second

t= 1.4 second

t= 2.4 second

t= 0.6 second

t= 1.6 second

t= 2.6 second

t= 0.8 second

t= 1.8 second

Figure G.11 *v*-field Moire Fringe Patterns for Polycarbonate Material
(Supply pressure 207 MPa, Garnet #50, SOF 1mm,113093)

t= 0.2 second

t= 1.2 second

t= 2.2 second

t= 0.4 second

t= 1.4 second

t= 2.4 second

t= 0.6 second

t= 1.6 second

t= 2.6 second

t= 0.8 second

t= 1.8 second

t= 1.0 second

t=2. 0 second

Figure G.12 *v*-field Moire Fringe Patterns for Polycarbonate Material
(Supply pressure 207 MPa, Garnet #50, SOF 1mm, 122693)

t= 0.2 second

t= 1.2 second

t= 2.2 second

t= 0.4 second

t= 1.4 second

t= 2.4 second

t= 0.6 second

t= 1.6 second

t= 2.6 second

t= 0.8 second

t= 1.8 second

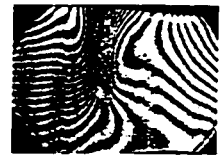

t= 2.8 second

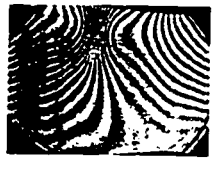

t= 1.0 second

t=2. 0 second

Figure G.13 *u*-field Moire Fringe Patterns for Polycarbonate Material
(Supply pressure 207 MPa, Garnet #50, SOF 1mm,122693)

t= 0.2 second

t= 1.2 second

t= 2.2 second

t= 0.4 second

t= 1.4 second

t= 2.4 second

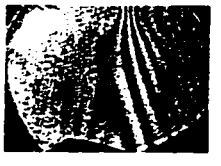

t= 0.6 second

t= 1.6 second

t= 2.6 second

t= 0.8 second

t= 1.8 second

t= 2.8 second

t= 1.0 second

t=2. 0 second

Figure G.14 *u*-field Moire Fringe Patterns for Polycarbonate Material
(Supply pressure 207 MPa, Garnet #50, SOF 1mm, 010494)

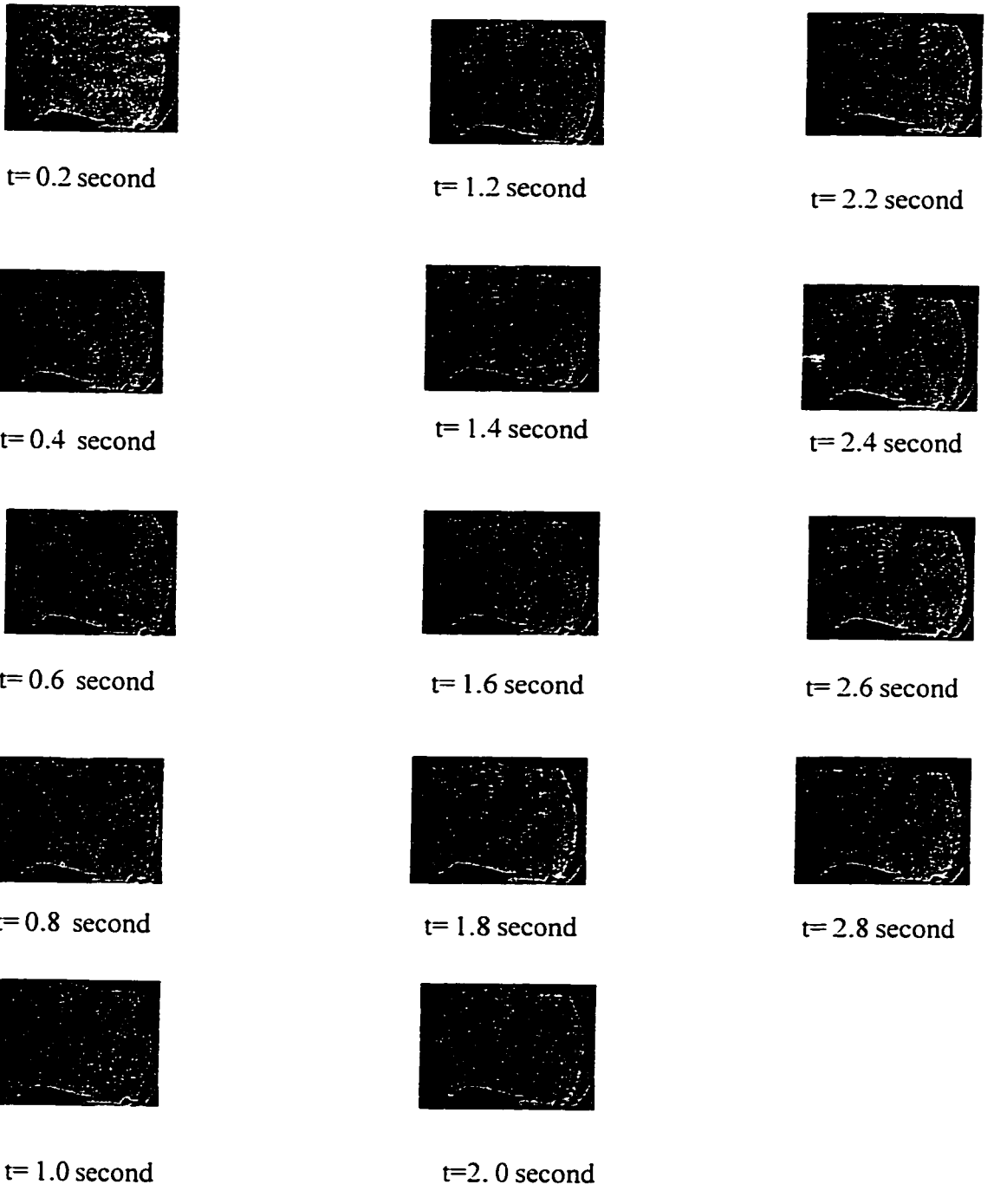

Figure G.15. *v*-field Moire Fringe Patterns for Polycarbonate Material (Supply pressure 207 MPa, Garnet #50, SOF 1mm, 010494)

APPENDIX H

DEDUCED RESULTS OF DYNAMIC MOIRE FRINGES

Included in this appendix are the displacement and strain contours from the moiré fringes patterns on the AWJ drilling of polycarbonate and alumina.

Strain Contour ε_1(x10^{-3}) Polycarbonate (94) t=0.8 second

P=207MPa; SOD=1mm;Abrasive:garnet,#50; AFR=25g/s

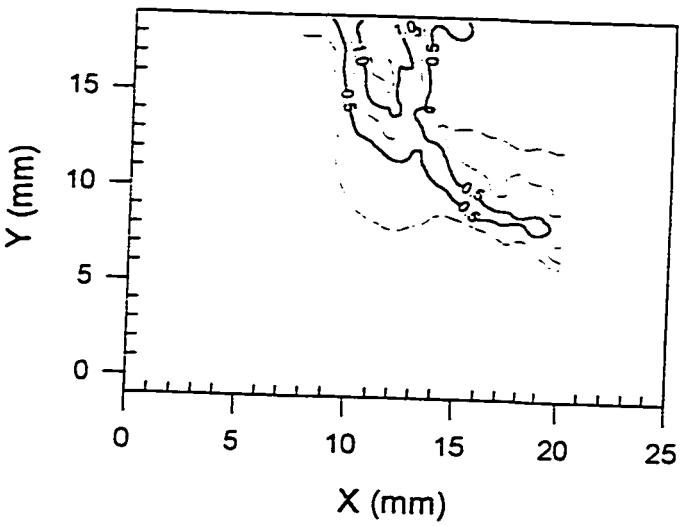

Strain Contour ε_2(x10^{-3}) Polycarbonate (94) t=0.8 second

P=207MPa; SOD=1mm;Abrasive:garnet,#50; AFR=25g/s

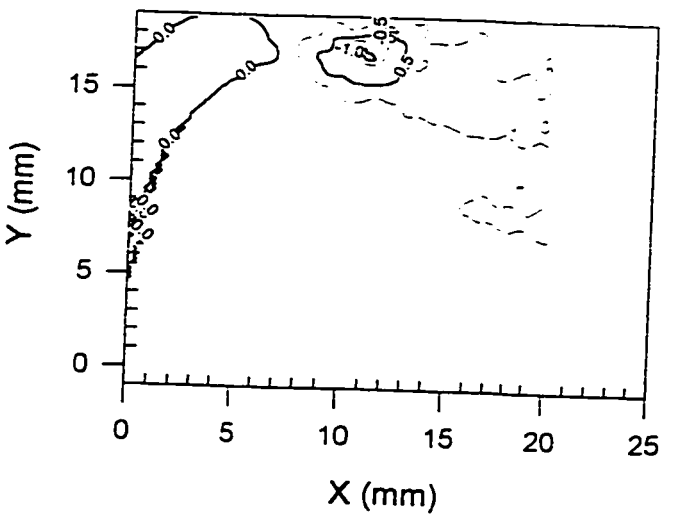

Figure H.1 Strain Contours for polycarbonate at t=0.8 second

Strain Contour ε_1(x10^{-3}) Polycarbonate (94) t=1.0 second

P=207MPa; SOD=1mm;Abrasive:garnet,#50; AFR=25g/s

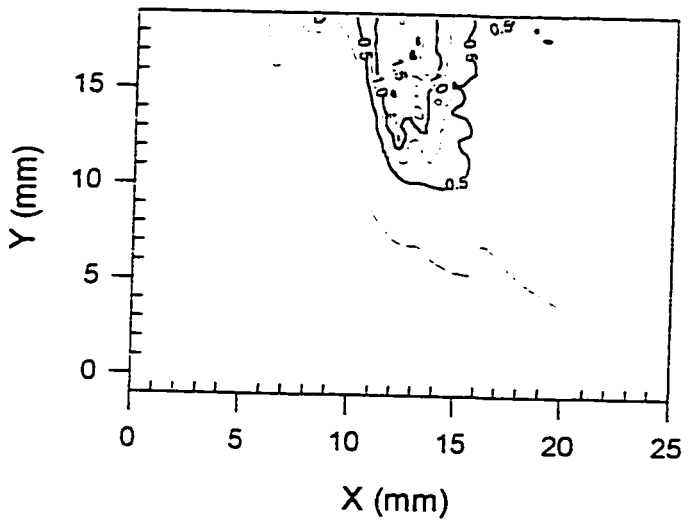

Strain Contour ε_2(x10^{-3}) Polycarbonate (94) t=1.0 second

P=207MPa; SOD=1mm;Abrasive:garnet,#50; AFR=25g/s

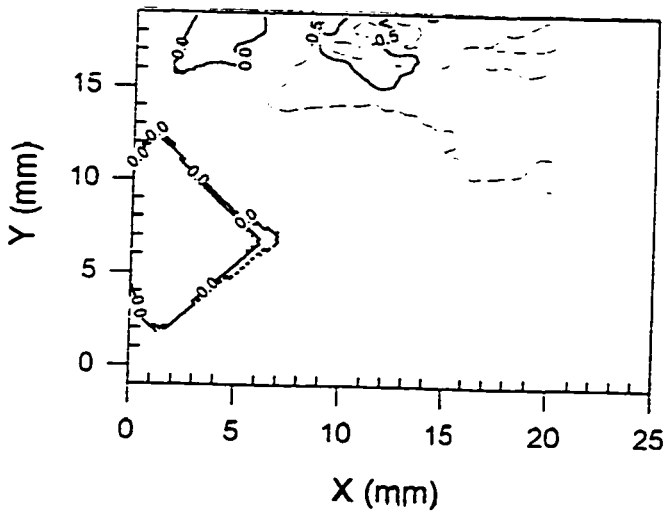

Figure H.2 Strain Contours for polycarbonate at t=1.0 second

Strain Contour ε_1(x10^{-3}) Polycarbonate (94) t=1.2 second

P=207MPa; SOD=1mm;Abrasive:garnet,#50; AFR=25g/s

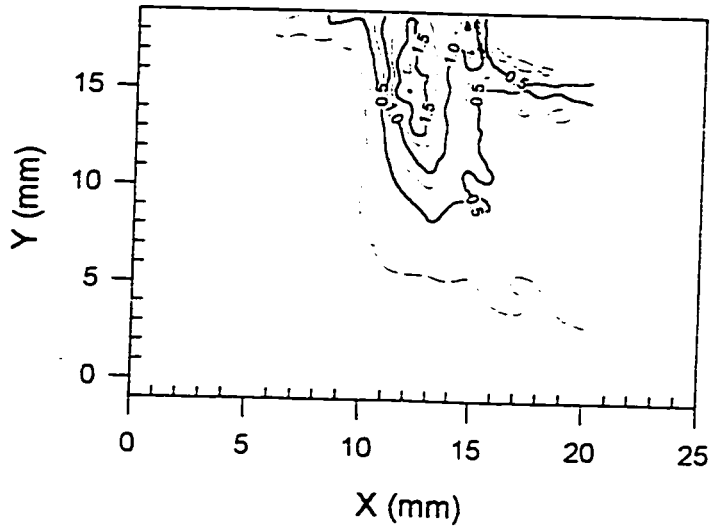

Strain Contour ε_2(x10^{-3}) Polycarbonate (94) t=1.2 second

P=207MPa; SOD=1mm;Abrasive:garnet,#50; AFR=25g/s

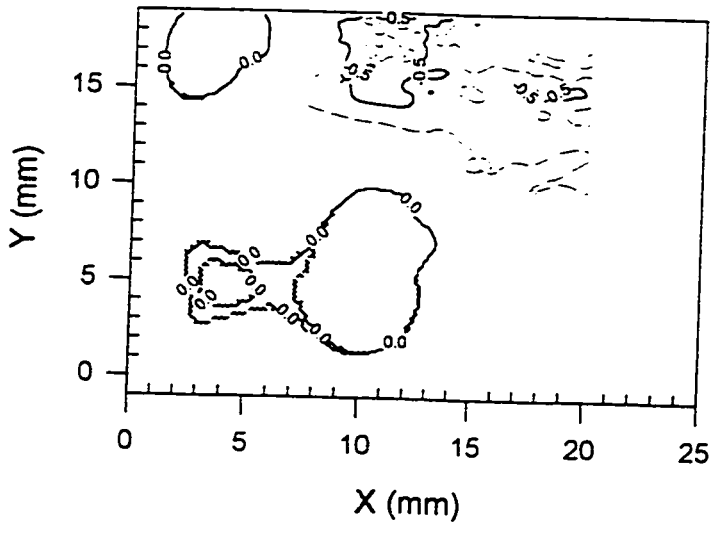

Figure H.3 Strain Contours for polycarbonate at t=1.2 second

Strain Contour ε_1(x10^{-3}) Polycarbonate (94) t=1.4 second

P=207MPa; SOD=1mm;Abrasive:garnet,#50; AFR=25g/s

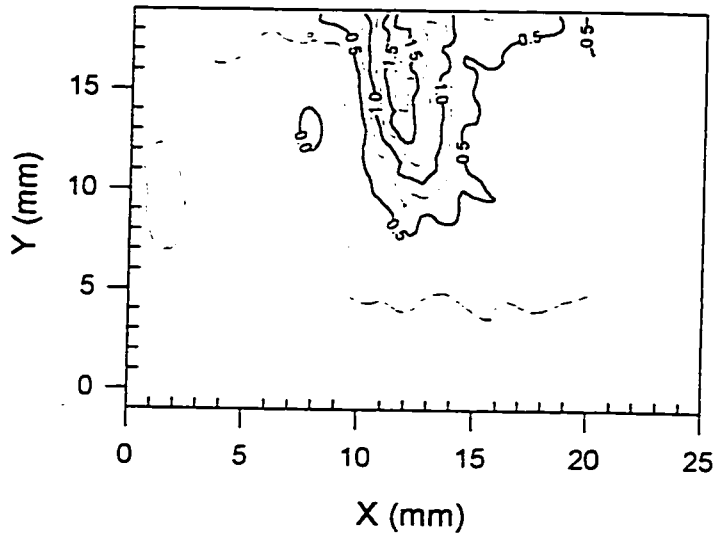

Strain Contour ε_2(x10^{-3}) Polycarbonate (94) t=1.4 second

P=207MPa; SOD=1mm;Abrasive:garnet,#50; AFR=25g/s

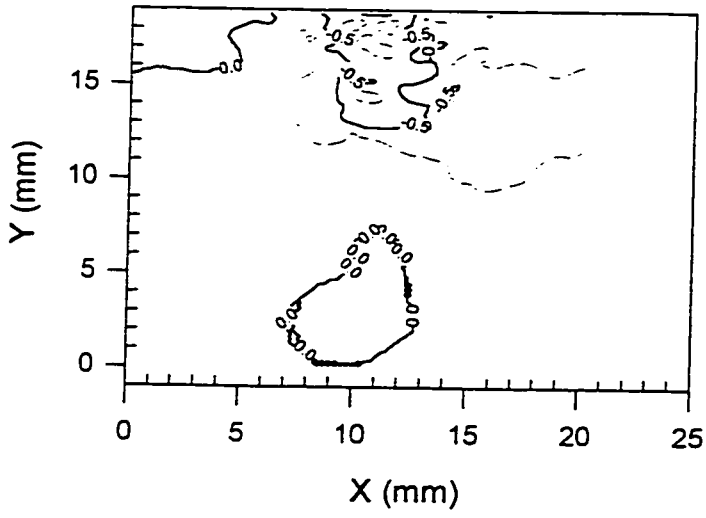

Figure H.4 Strain Contours for polycarbonate at t=1.4 second

Strain Contour ε_1(x10^{-3}) Polycarbonate (94) t=1.6 second

P=207MPa; SOD=1mm;Abrasive:garnet,#50; AFR=25g/s

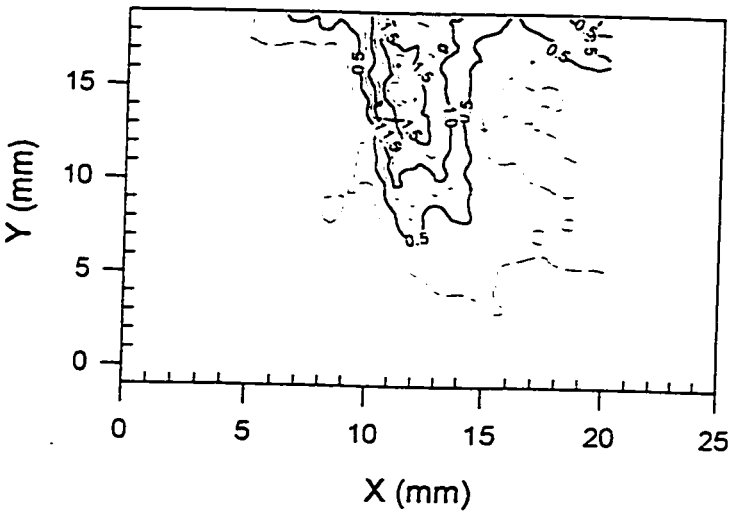

Strain Contour ε_2(x10^{-3}) Polycarbonate (94) t=1.6 second

P=207MPa; SOD=1mm;Abrasive:garnet,#50; AFR=25g/s

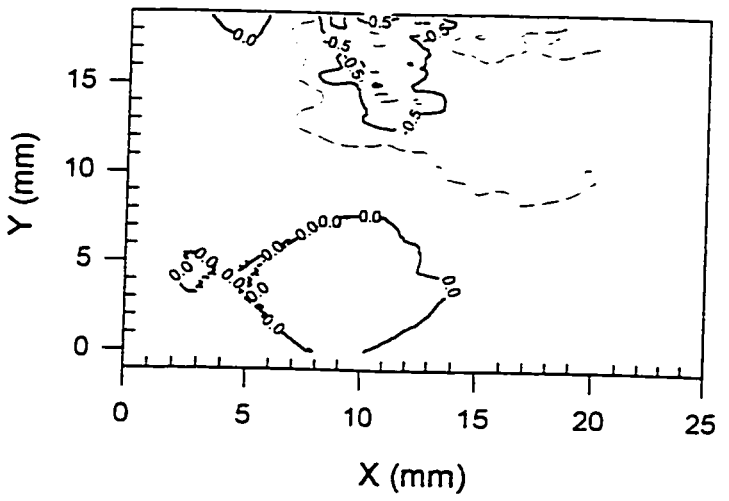

Figure H.5 Strain Contours for polycarbonate at t=1.6 second

Strain Contour ε_1(x10^{-3}) Polycarbonate (94) t=1.8 second

P=207MPa; SOD=1mm;Abrasive:garnet,#50; AFR=25g/s

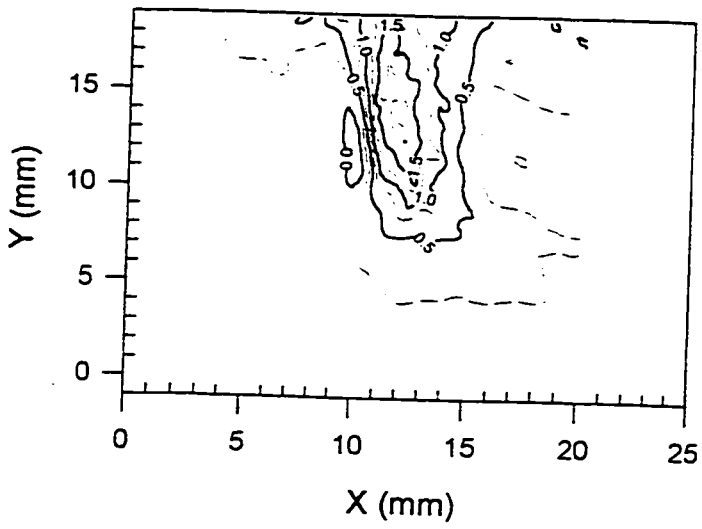

Strain Contour ε_2(x10^{-3}) Polycarbonate (94) t=1.8 second

P=207MPa; SOD=1mm;Abrasive:garnet,#50; AFR=25g/s

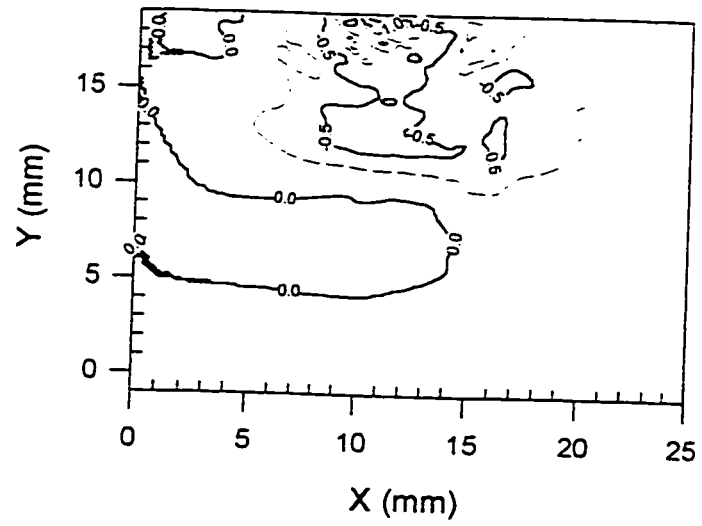

Figure H.6 Strain Contours for polycarbonate at t=1.8 second

Strain Contour ε_1(x10^{-3}) Polycarbonate (94) t=2.0 second

P=207MPa; SOD=1mm;Abrasive:garnet,#50; AFR=25g/s

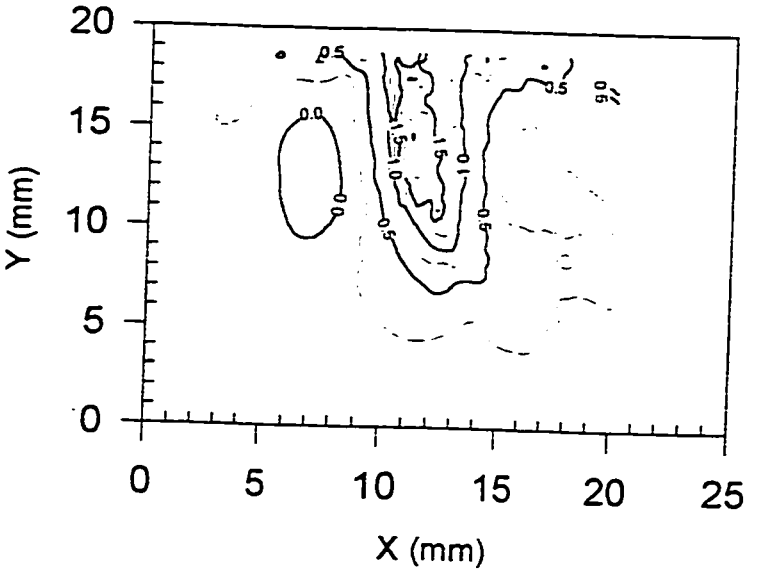

Strain Contour ε_2(x10^{-3}) Polycarbonate (94) t=2.0 second

P=207MPa; SOD=1mm;Abrasive:garnet,#50; AFR=25g/s

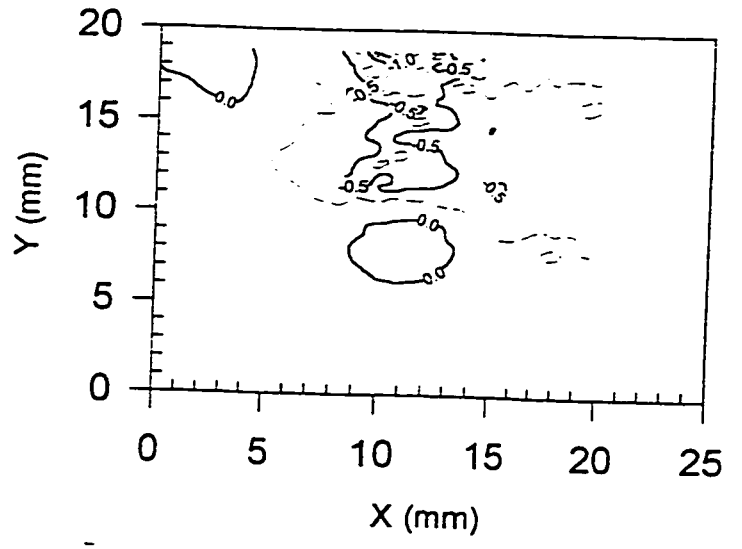

Figure H.7 Strain Contours for polycarbonate at t=2.0 seconds

Strain Contour ε_1(x10^{-3}) Polycarbonate (94) t=2.4 second

P=207MPa; SOD=1mm;Abrasive:garnet,#50; AFR=25g/s

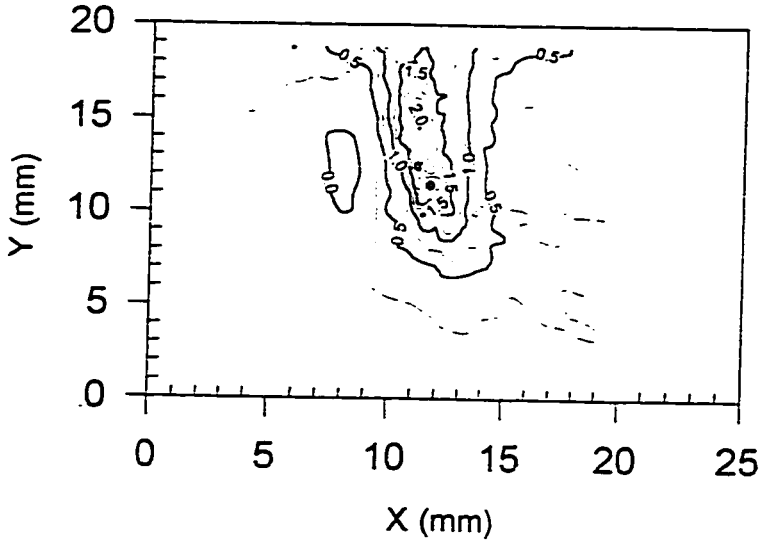

Strain Contour ε_2(x10^{-3}) Polycarbonate (94) t=2.4 second

P=207MPa; SOD=1mm;Abrasive:garnet,#50; AFR=25g/s

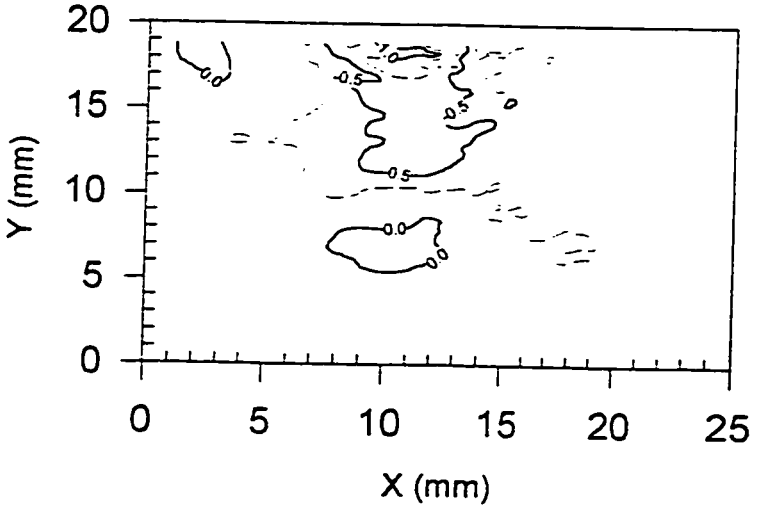

Figure H.8 Strain Contours for polycarbonate at t=2.4 seconds

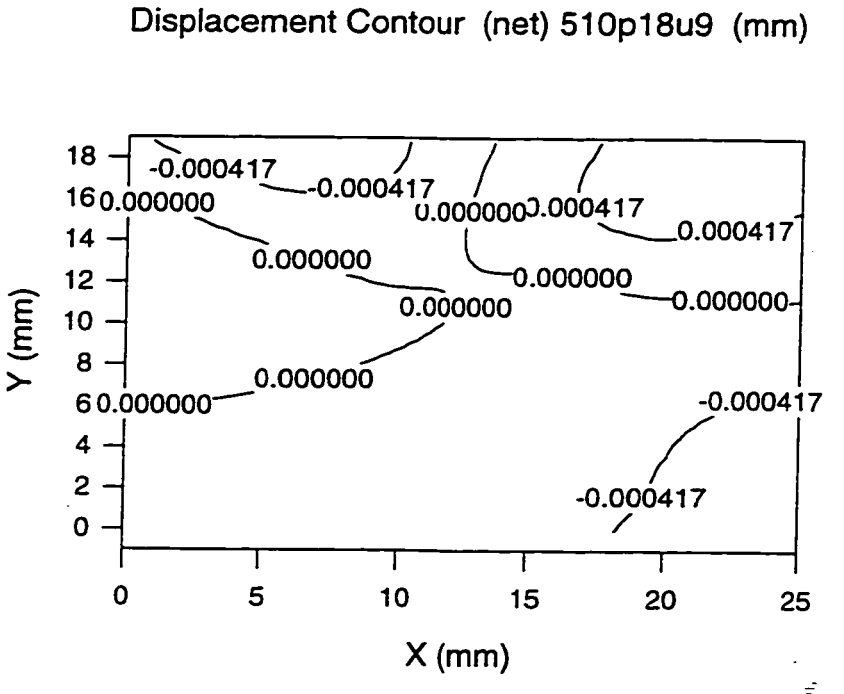

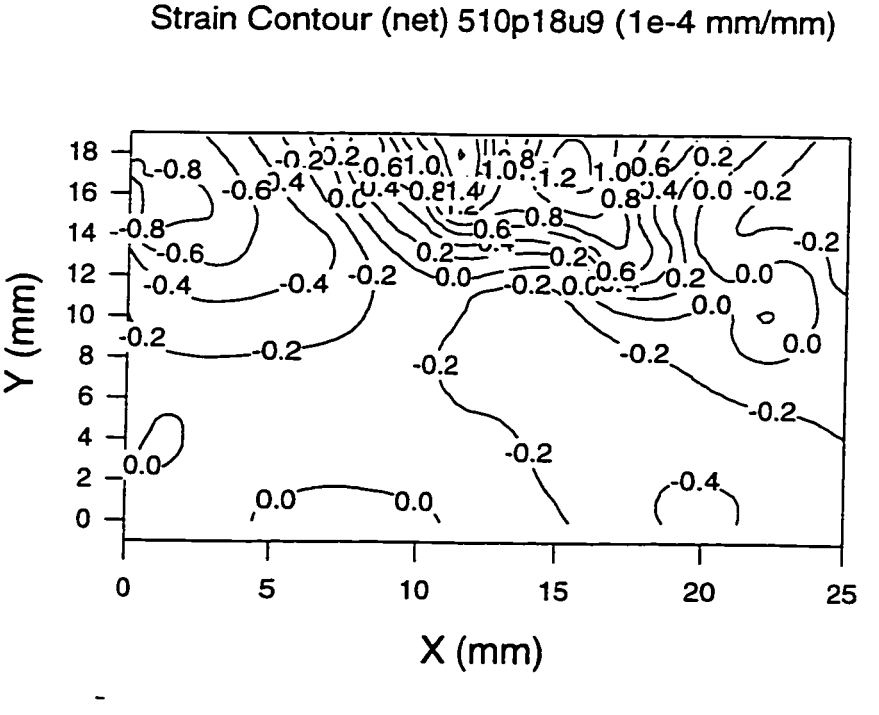

Figure H.9 u-field displacement and Strain contours for alumina at hole depth 2.13 mm (supply pressure 126 MPa, SOD 1 mm; garnet mesh 80; AFR 13 g/s)

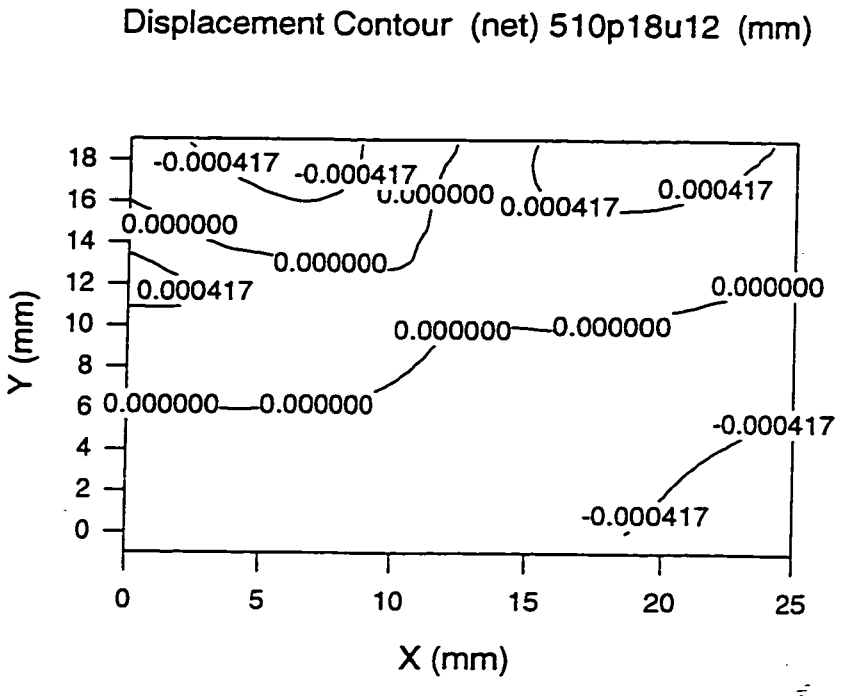

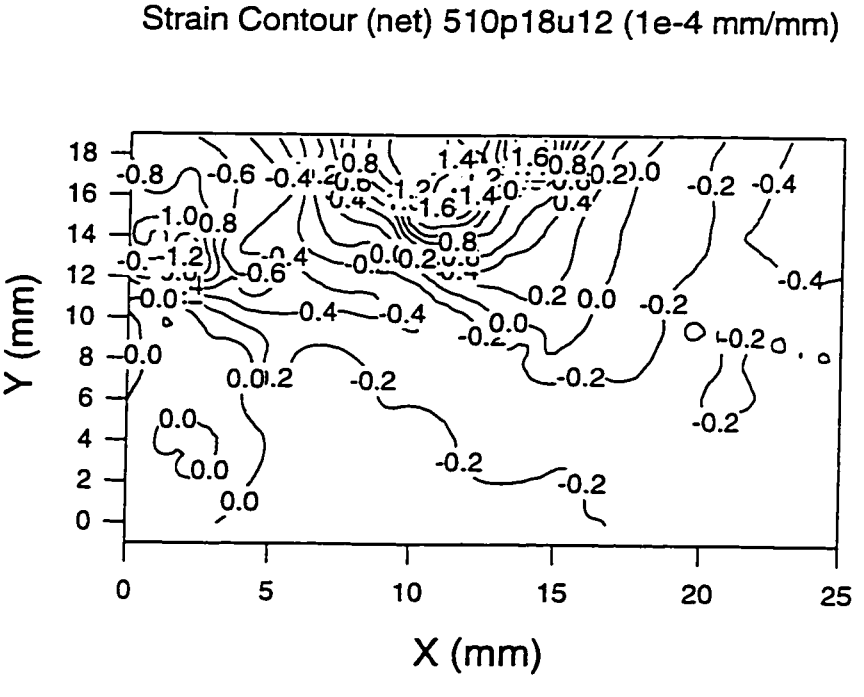

Figure H.10 *u*-field displacement and Strain contours for alumina at hole depth 2.5 mm (supply pressure 126 MPa, SOD 1 mm; garnet mesh 80; AFR 13 g/s)

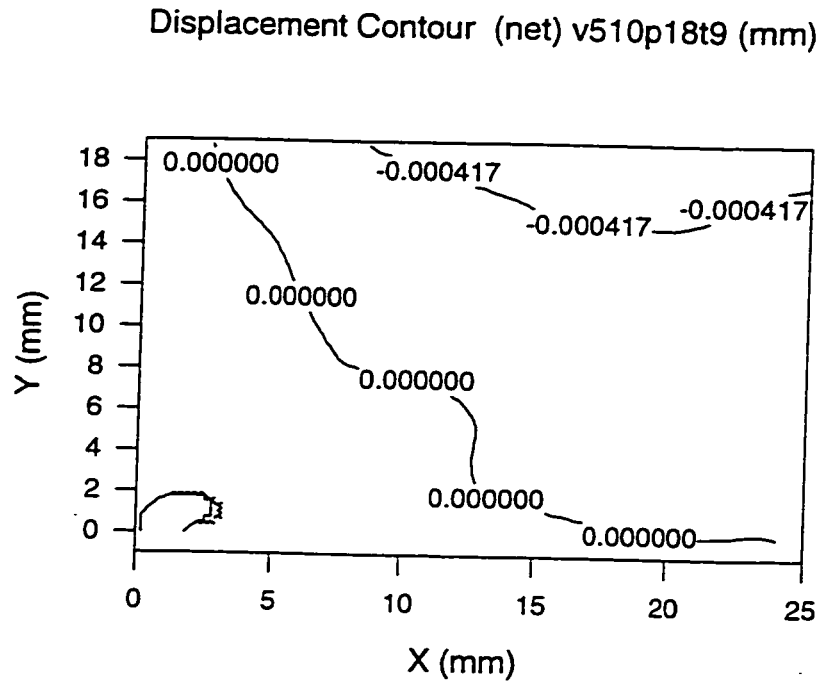

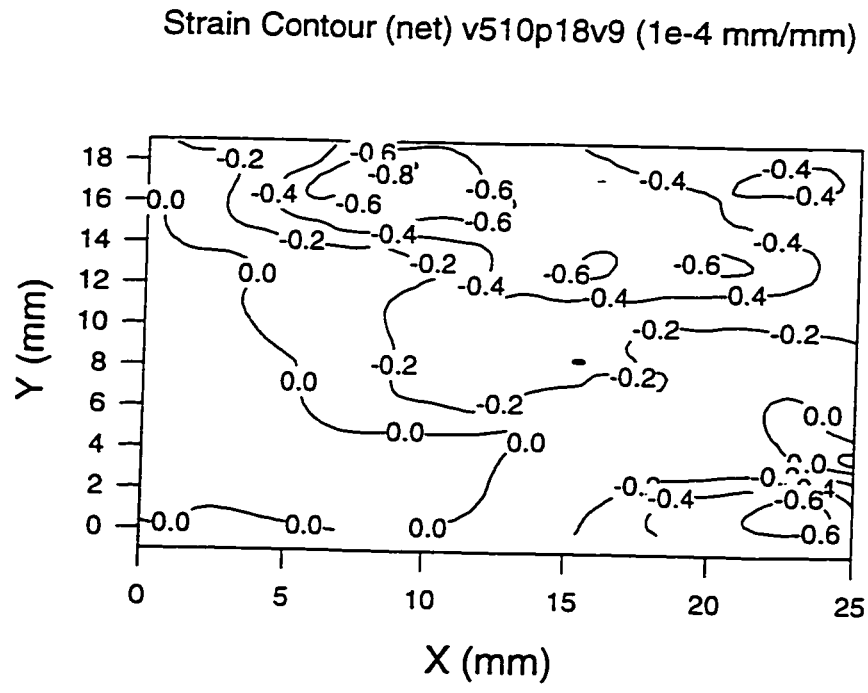

Figure H.11 v-field displacement and Strain contours for alumina at hole depth 2.13 mm (supply pressure 126 MPa, SOD 1 mm; garnet mesh 80; AFR 13 g/s)

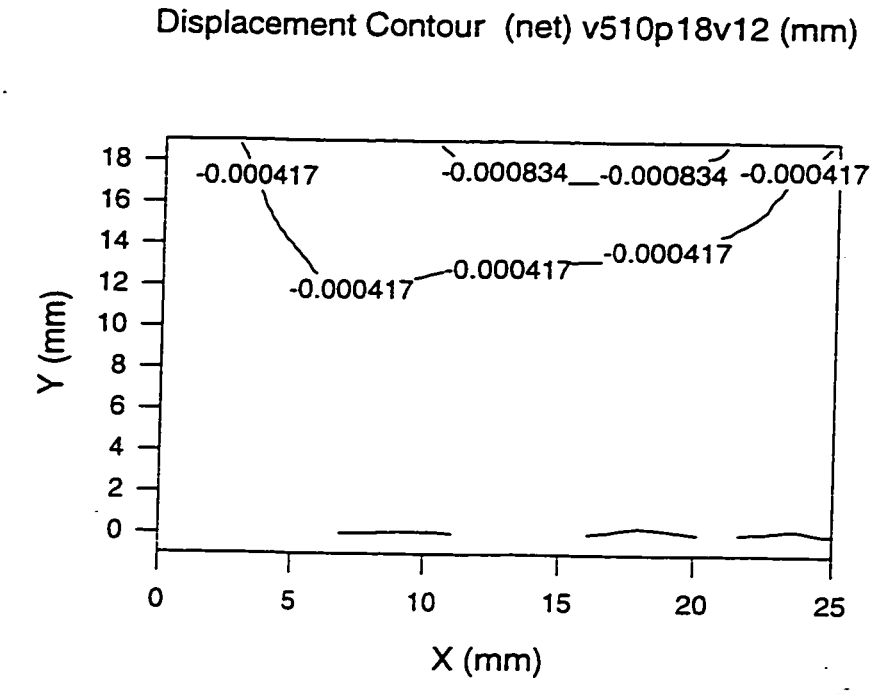

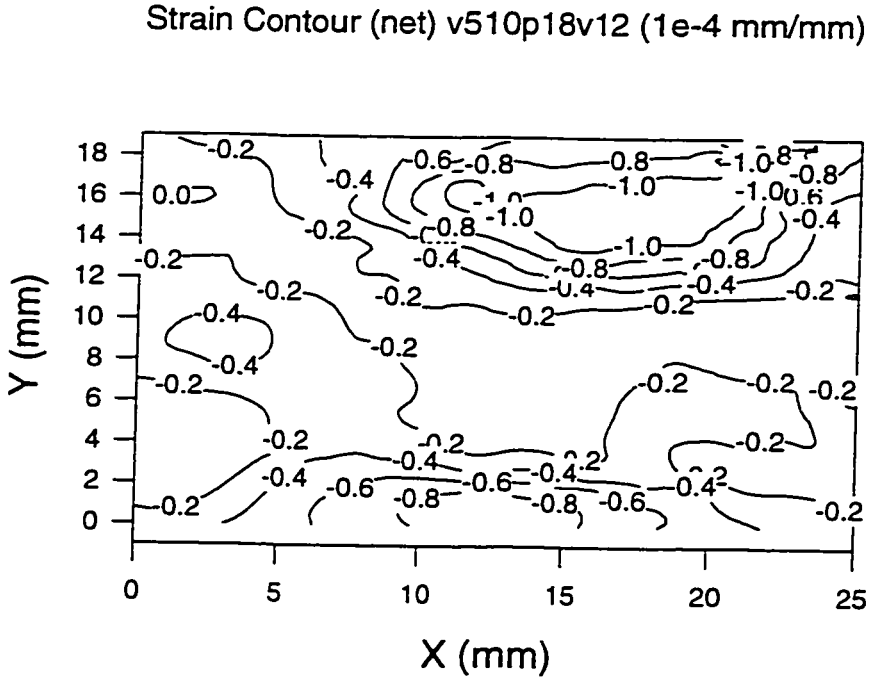

Figure H.12 *v*-field displacement and Strain contours for alumina at hole depth 2.5 mm (supply pressure 126 MPa, SOD 1 mm; garnet mesh 80; AFR 13 g/s)

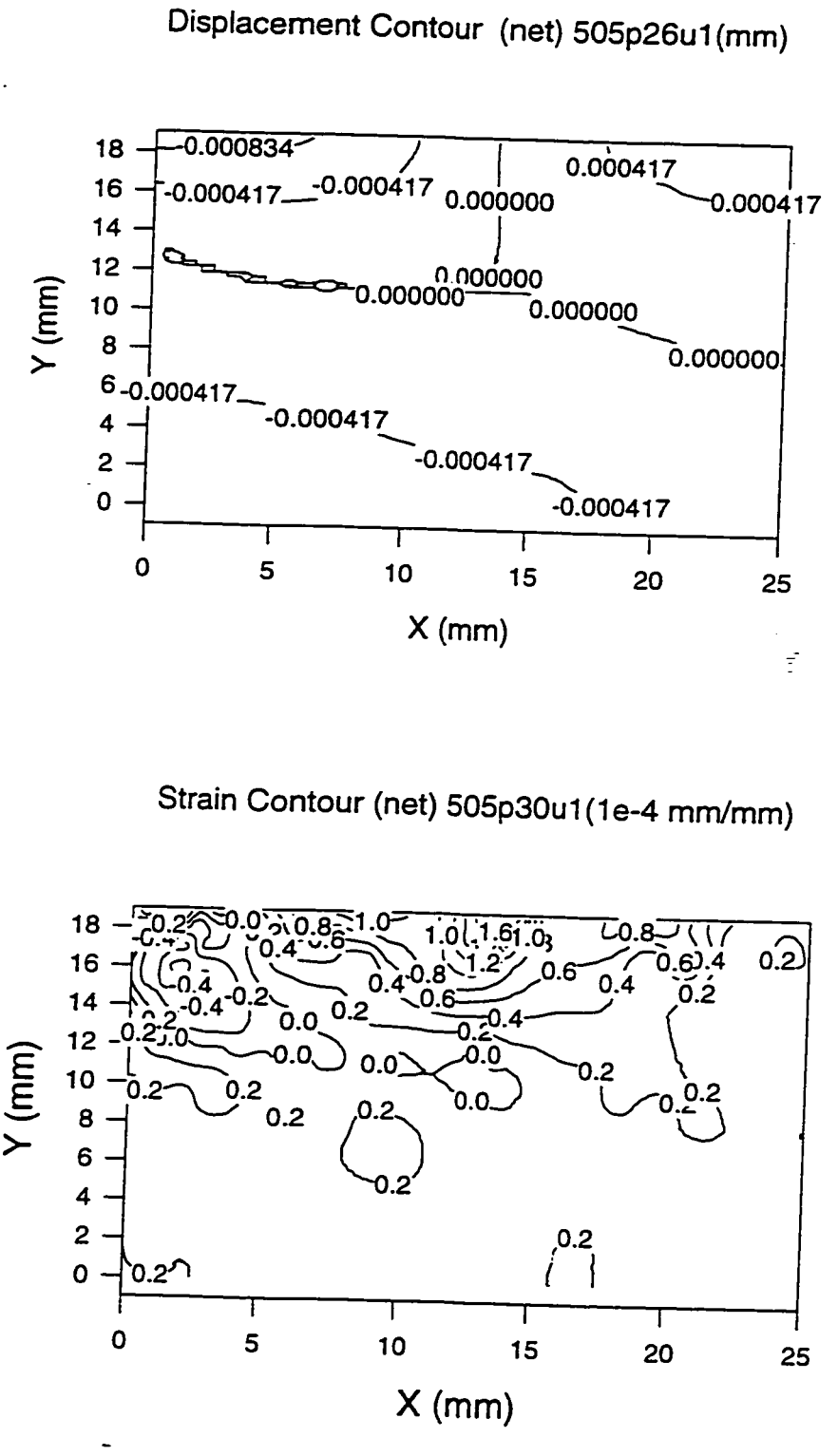

Figure H.13 *u*-field displacement and Strain contours for alumina at hole depth 0.94 mm (supply pressure 167 MPa, SOD 1 mm; garnet mesh 80; AFR 14 g/s)

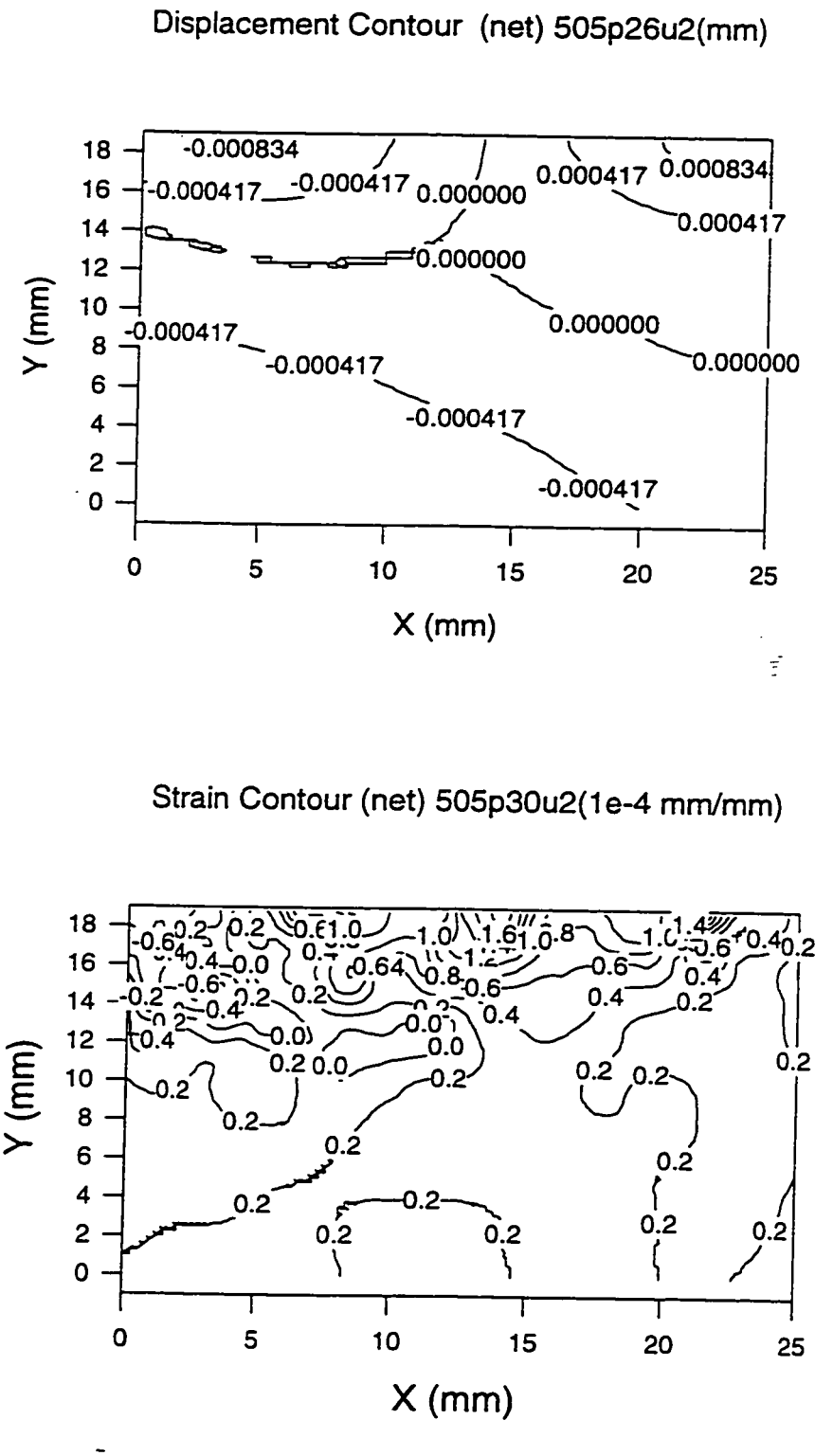

Figure H.14 *U*-field displacement and strain contours for alumina hole depth of 1.32 mm
(supply pressure 167 MPa; SOD 1 mm; garnet mesh 80; AFR 14 g/s)

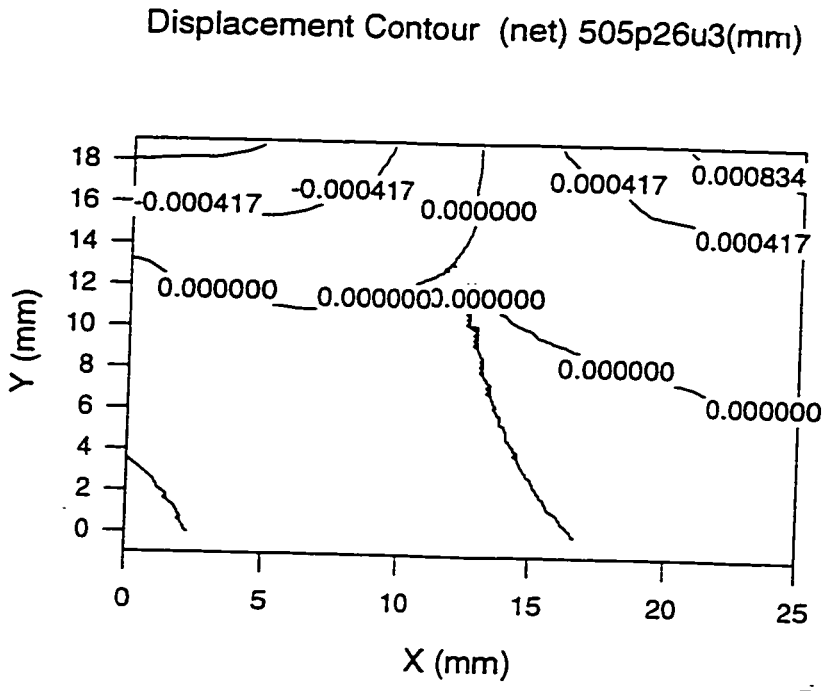

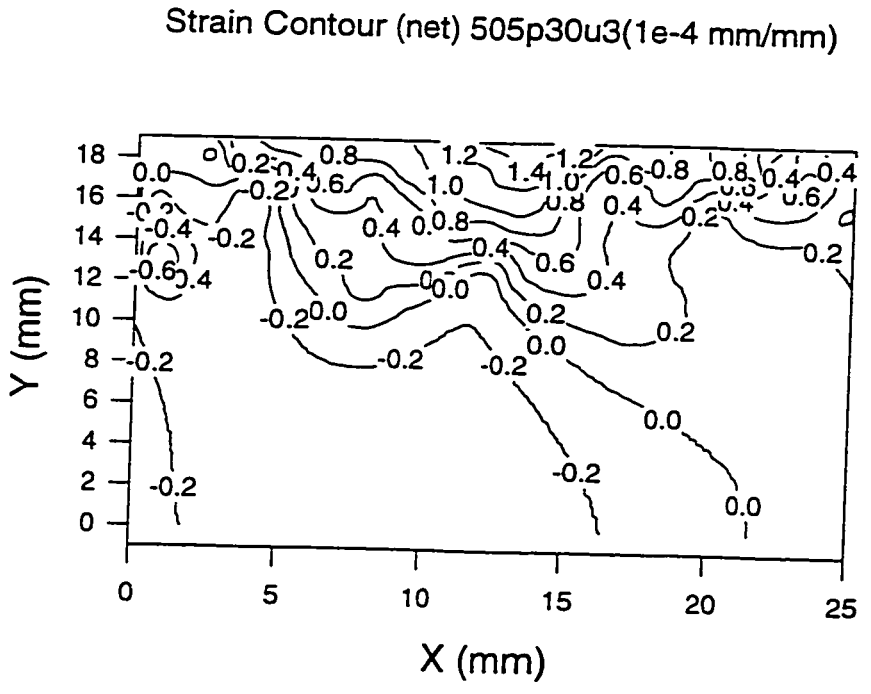

Figure H.15 *u*-field displacement and Strain contours for alumina at hole depth 1.7 mm (supply pressure 167 MPa, SOD 1 mm; garnet mesh 80; AFR 14 g/s)

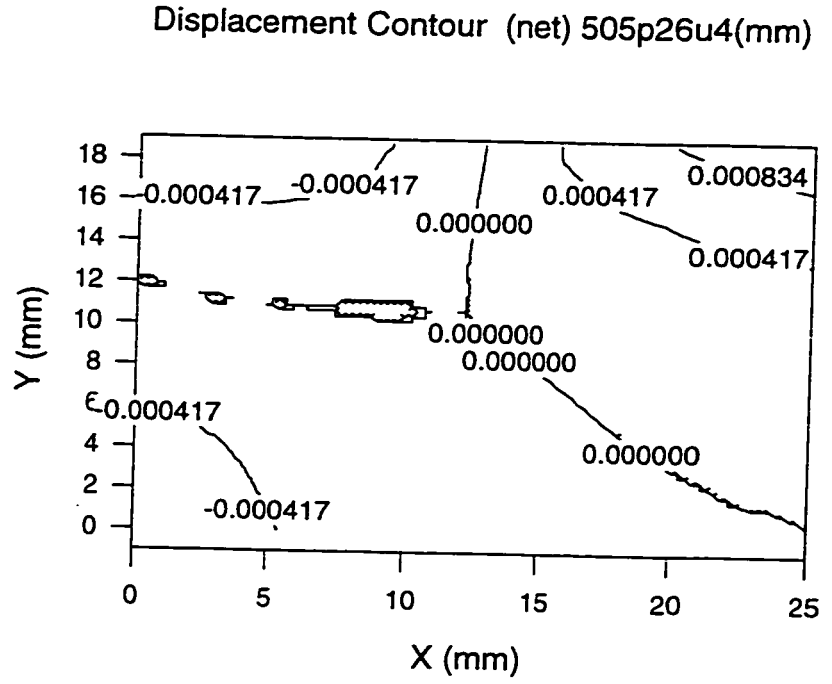

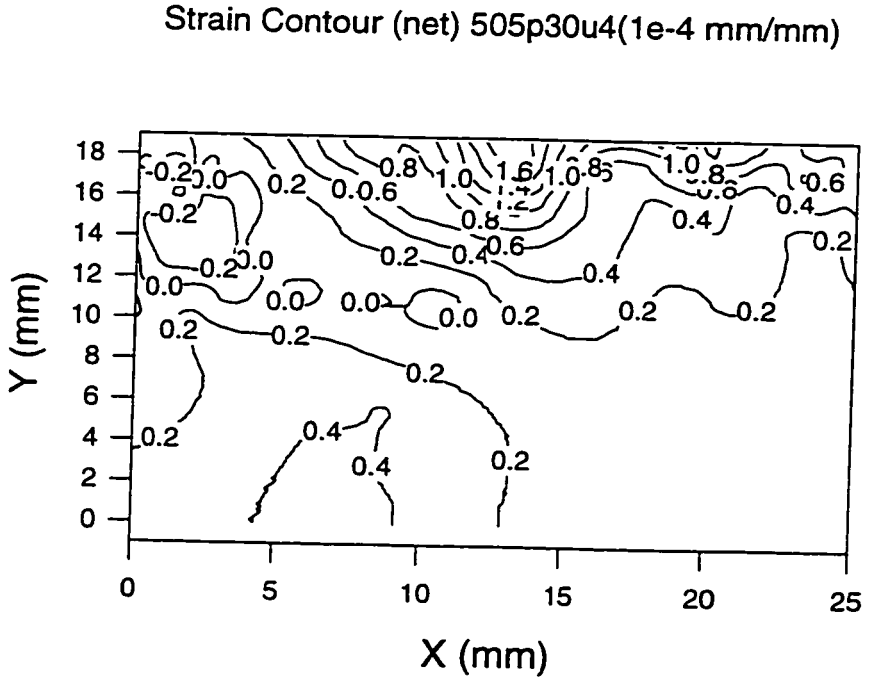

Figure H.16 *u*-field displacement and Strain contours for alumina at hole depth 2.01 mm (supply pressure 167 MPa, SOD 1 mm; garnet mesh 80; AFR 14 g/s)

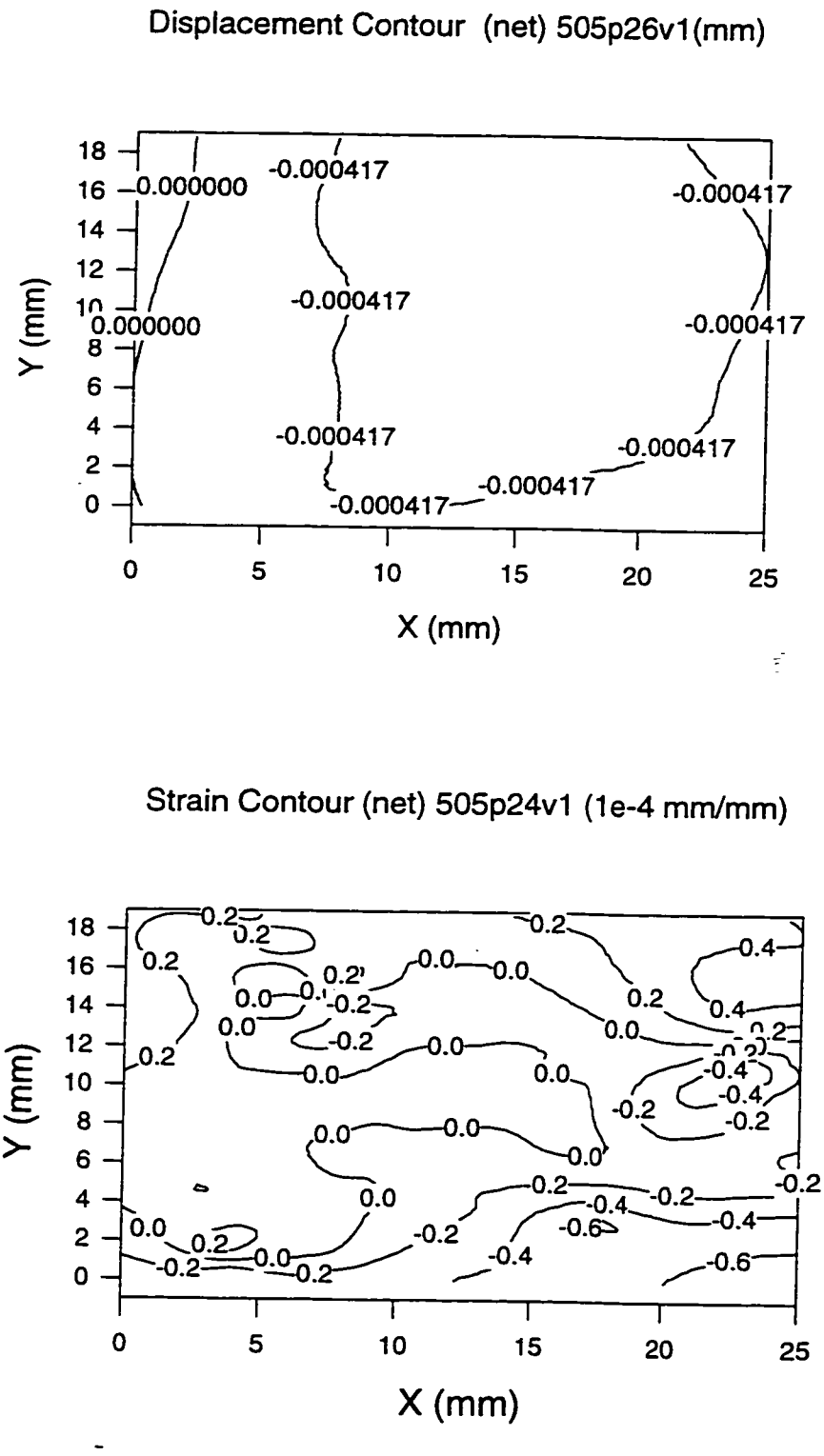

Figure H.17 *v*-field displacement and Strain contours for alumina at hole depth 0.94 mm (supply pressure 167 MPa, SOD 1 mm; garnet mesh 80; AFR 14 g/s)

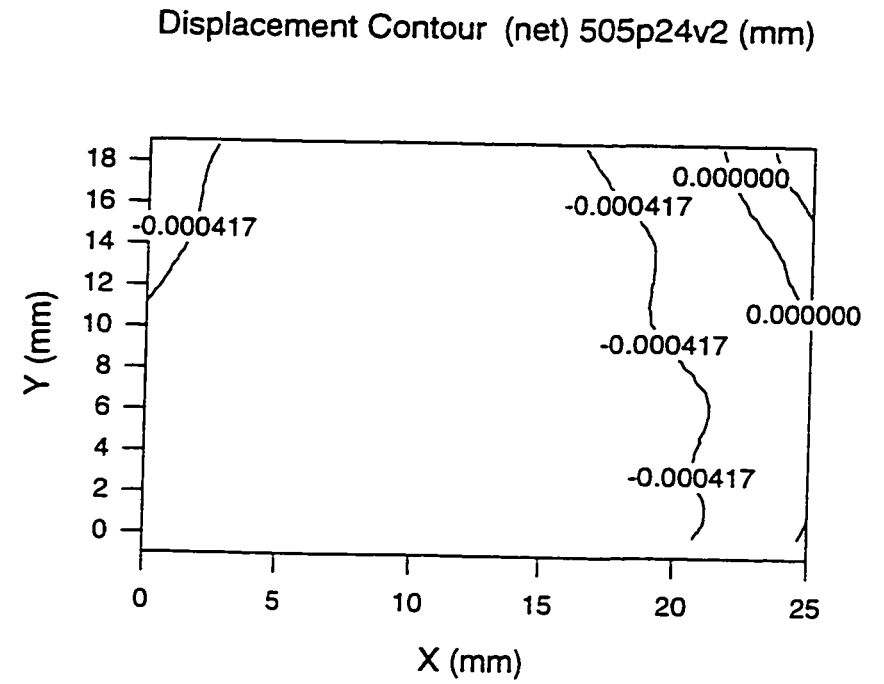

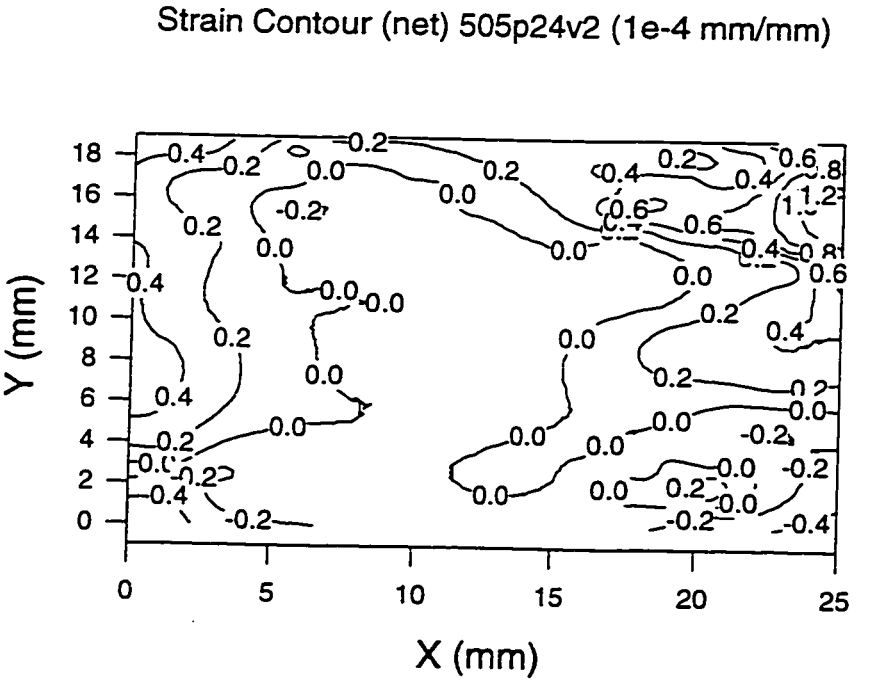

Figure H.18 ν-field displacement and Strain contours for alumina at hole depth 1.7 mm (supply pressure 167 MPa, SOD 1 mm; garnet mesh 80; AFR 14 g/s)

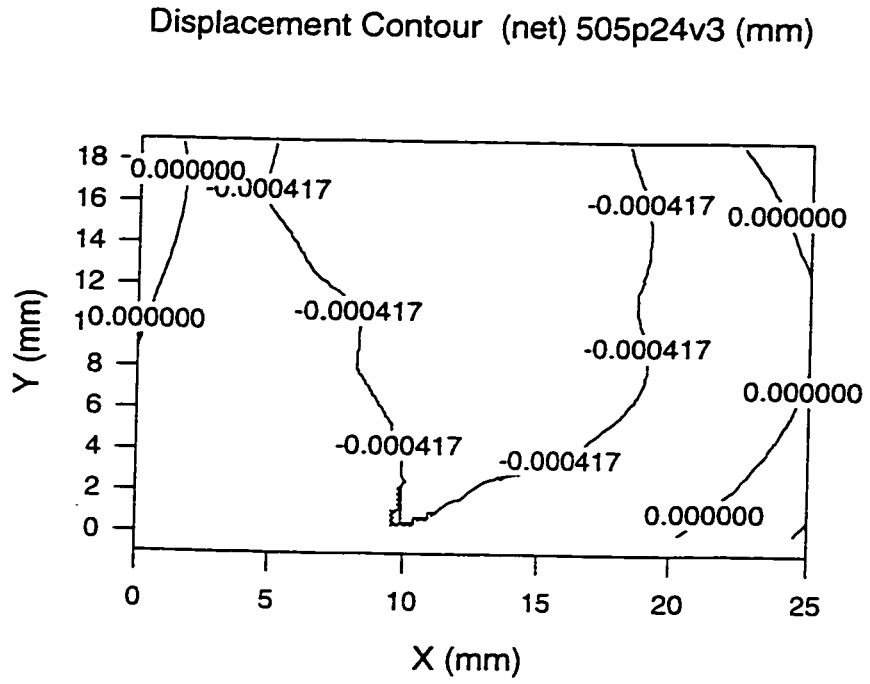

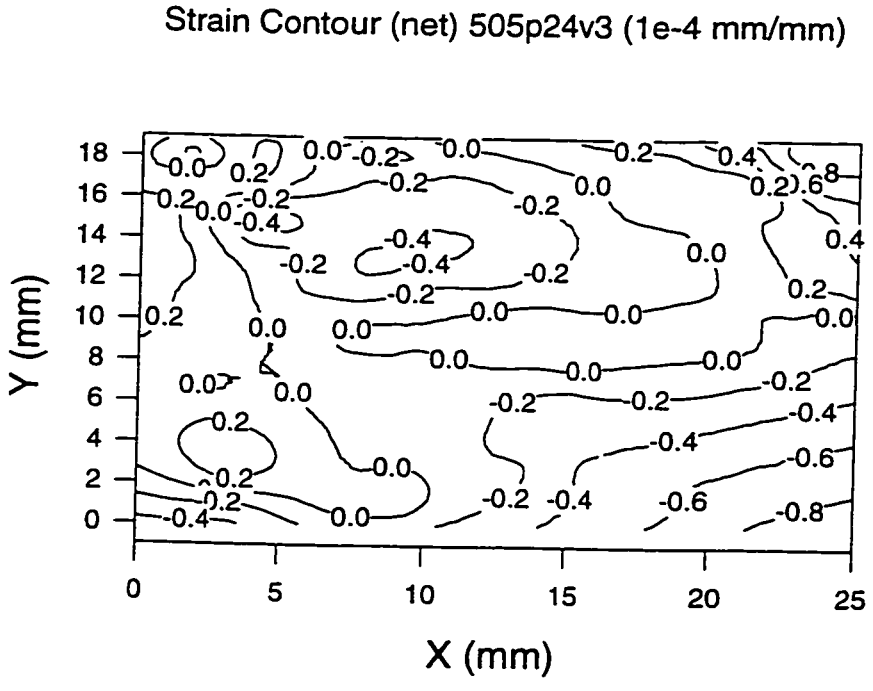

Figure H.19 ν-field displacement and Strain contours for alumina at hole depth 1.7 mm (supply pressure 167 MPa, SOD 1 mm; garnet mesh 80; AFR 14 g/s)

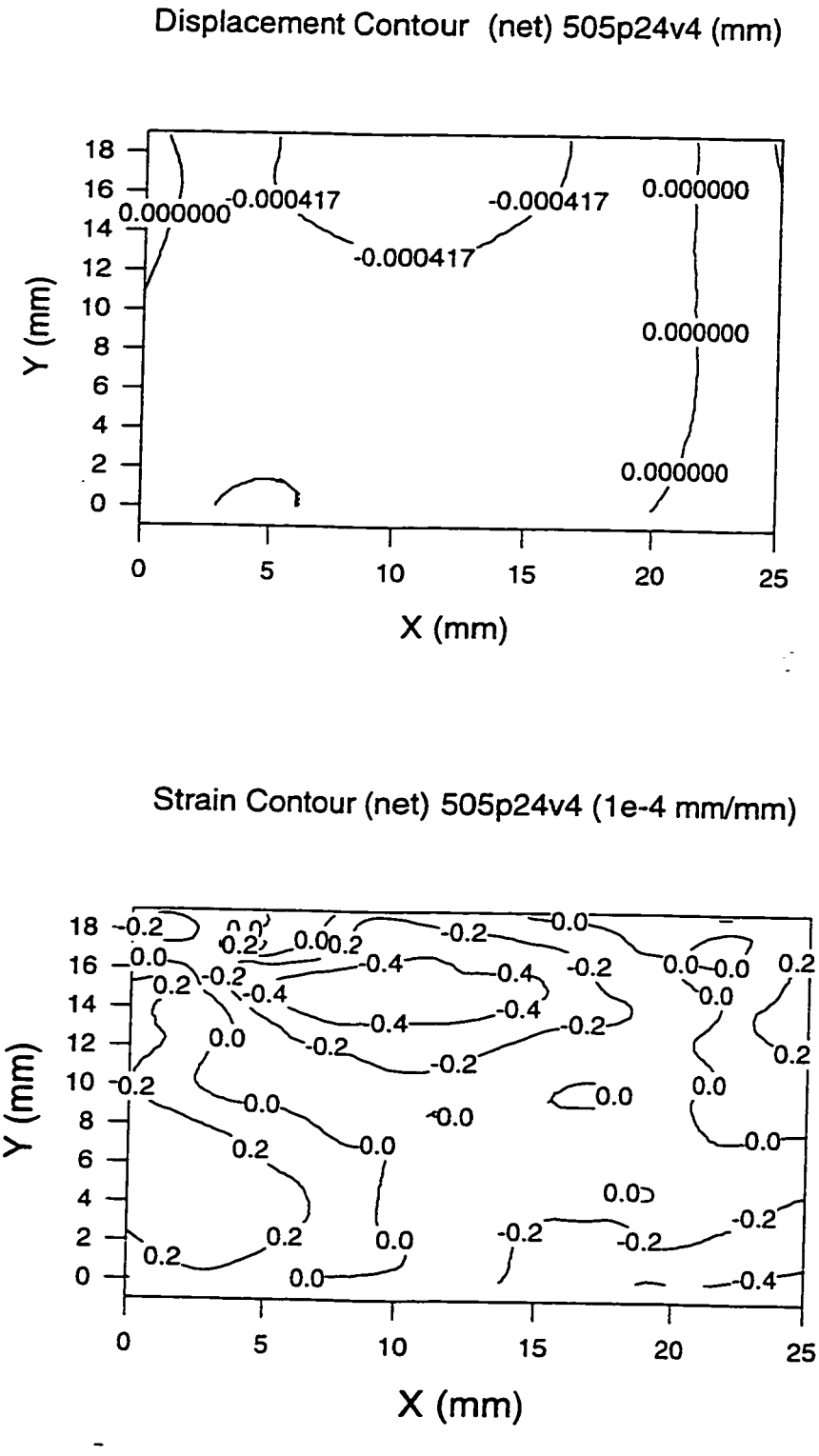

Figure H.20 ν-field displacement and Strain contours for alumina at hole depth 2.01 mm (supply pressure 167 MPa, SOD 1 mm; garnet mesh 80; AFR 14 g/s)

Vita

Zihong Guo
University of Washington
1998

EDUCATION:

Ph. D. in Mechanical Engineering — August 1998
University of Washington, Seattle WA
Dissertation: Experimental and Numerical Analysis of Abrasive Waterjet Drilling of Brittle Materials

M.S. in Aeronautics and Astronautics — June 1992
University of Washington, Seattle WA
Thesis: Deformations in a thin cylinder with an axial through crack

B.S. in Mechanical Engineering — July 1984
Nanjing University of Aeronautics and Astronautics, Nanjing, China

WORK EXPERIENCE:

Sr. Research and Development Engineer — 1993 - Present
Boston Scientific Corporation, Redmond WA

Research Associate — 1993 - Present
Department of Mechanical Engineering, Manufacturing Group
University of Washington, Seattle, WA

Research Assistant — 1990 - 1992
Department of Aeronautics & Astronautics, Structures Group
University of Washington, Seattle, WA

Engineer — 1988 - 1990
Boeing Commercial Airplane Group
Engine Installation Group, Renton, WA
Engine Cowling & Thrust Reverser, Kent, WA

Engineer — 1984 - 1988
Jingmen Airplane Research & Design Institute, Jingmen, Hubei, China

Professional Affiliation:

American Society of Mechanical Engineers
American Association of Water Jet Technology

IMAGE EVALUATION TEST TARGET (QA-3)

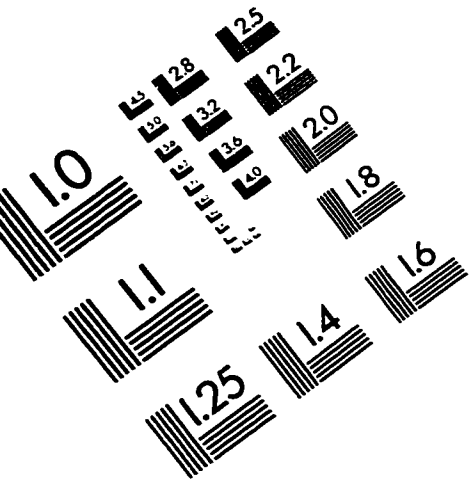

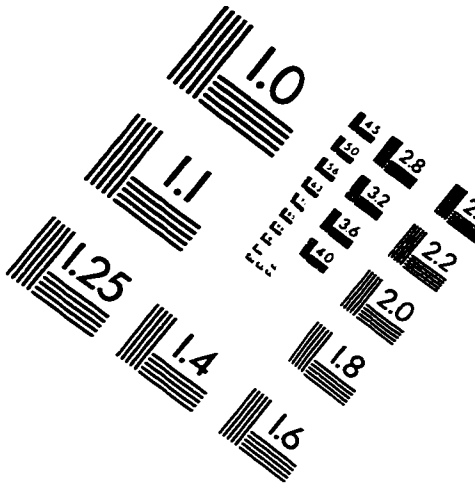

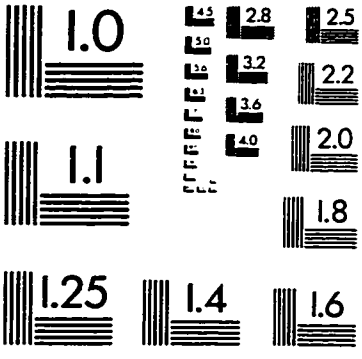

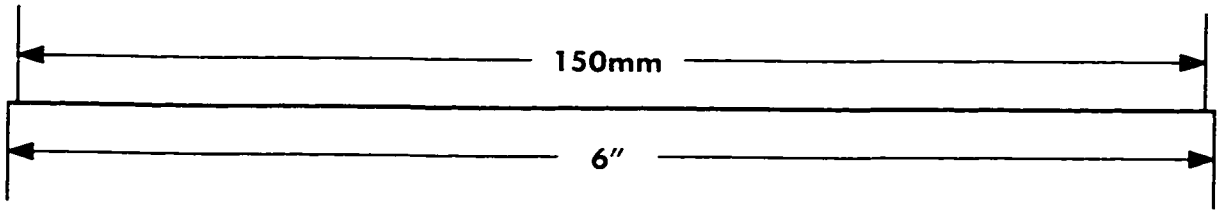

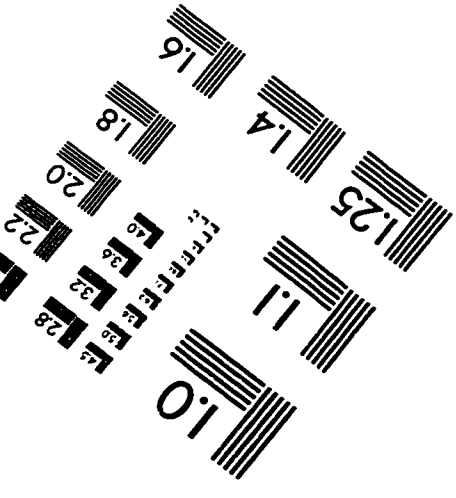

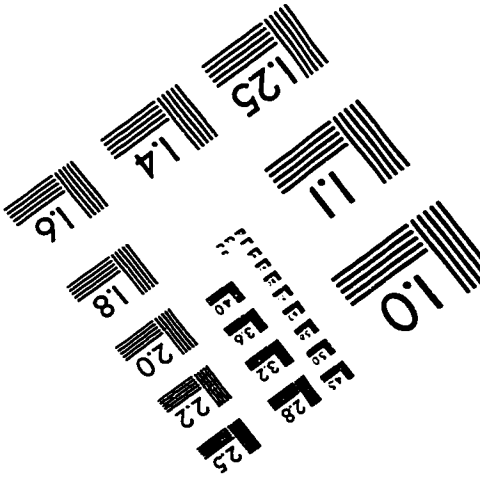

APPLIED IMAGE, Inc
1653 East Main Street
Rochester, NY 14609 USA
Phone: 716/482-0300
Fax: 716/288-5989